Measuring and modelling the crustal response to the 2011 eruption of Nabro volcano, Eritrea

Joanna Elizabeth Hamlyn

Submitted in accordance with the requirements for the degree of
Doctor of Philosophy

The University of Leeds
School of Earth and Environment
September 2015

Declaration

The candidate confirms that the work submitted is her own, except where work which has formed part of jointly authored publications has been included. The contribution of the candidate and the other authors to this work has been explicitly indicated below. The candidate confirms that appropriate credit has been given within the thesis where reference has been made to the work of others.

This copy has been supplied on the understanding that it is copyright material and that no quotation from the thesis may be published without proper acknowledgement.

The right of Joanna Elizabeth Hamlyn to be identified as Author of this work has been asserted by her in accordance with the Copyright, Designs and Patents act 1988.

Chapters 2, 3 and 5 contain work from the publication:

Hamlyn, J. E., D. Keir, T. J. Wright, J. W. Neuberg, B. Goitom, J. O. S. Hammond, C. Pagli, C. Oppenheimer, J. M. Kendall and R. Grandin (2014), Seismicity and subsidence following the 2011 Nabro Eruption, Eritrea: Insights into the plumbing system of an off-rift volcano, *J. Geophys. Res. Solid Earth*, doi:10.1002/2014JB011395

In this paper discussion of processing procedures to implement and interpretation was held with D. Keir, T.J. Wright, J.W. Neuberg, C. Pagli and J.M. Kendall. The project PI is C. Oppenheimer who provided feedback on the finalised manuscript. The collection of field data was completed by J. Hammond and B. Goitom. The grant proposal for InSAR data was helped by R. Grandin. J.E. Hamlyn completed the processing and modelling of the InSAR and seismic data, wrote the paper and created all of the figures.

Discussion and processing steps from Chapter 2 contributed to the publication:

Goitom, B., C. Oppenheimer, J. O. S. Hammond, R. Grandin, T. Barnie, A. Donovan, G. Ogubazghi, E. Yohannes, G. Kibrom, J. M. Kendall, S. A. Carn, D. Fee, C. Sealing, J. Blundy, J. Hamlyn, D. Keir, A. Ayele, T. Wright, S. Berhe (2015) First recorded eruption of Nabro volcano, Eritrea, 2011 *Bulletin of Volcanology*, doi:10.1007/s00445-015-0966-3

Acknowledgements

First and foremost I would like to thank my supervisors Tim Wright, Jurgen 'Locko' Neuberg and Derek Keir. Tim always pushed me do better, but encouraged me in a such away he never broke my resilience. Locko shared his knowledge, home, food and wine with me over the last 4 years. I am grateful for the opportunities he has given me to travel and to share my work with many different people across the the world. Derek's encouragement and belief in my ability made this PhD much more achievable. Without their collaborative effort and eternal patience this PhD would not have been possible. Additionally, Carolina Pagli has provided considerable support, especially through the final phases of the project, and Richard Walters took random and sometimes frequent breaks from his own work, to help me through problems often of my own making. Special thanks to Richard Rigby, you are Superman to the IT weak and vulnerable.

Thanks to all the members of the Volcanology and Tectonics research groups at the University of Leeds who have offered a friendly environment to practice talks and discuss results. An extended thanks to all of the staff along the IGT corridor, for making me feel like a valued member of the department.

Thanks to all those I have shared an office with during my time at Leeds, you guys made each day fun and enjoyable. A special thank you to Becky for sitting next to me on the rollercoaster that is PhD life, for grumbling with me through the low points and celebrating the highs. Hannah, Laura and Sandra thanks for the lunch time and corridor pep talks. Curls and his girls brought fun and laughter to every single day and made this experience richer for it.

Most of all I want to thank my parents for their unwavering love and support. For only encouraging me to be myself and helping me through with a hug, or food, or money, or washing. Jonny, I am not thanking you for pretending to fall asleep whenever I talked about my work, but for the camaraderie only a brother can provide. Lastly, thank you to India for being my side all the way, I can't wait to start the next adventure.

This PhD has been funded by a Natural Environment Research Council studentship.

Abstract

Nabro volcano, situated to the east of the Afar Rift Zone, erupted on 12 June 2011. Eruptions at such off-rift volcanoes are infrequent, and consequently the plumbing systems are poorly understood. In this thesis I present post-eruption InSAR and seismic data to delineate the plumbing system of Nabro. I also investigate the temporal evolution of the system. I discuss my findings in reference to the tectonics of the Afar Rift Zone, off-rift volcanism and compare the findings to volcanoes world wide.

I present 6 weeks of continuous seismic activity from an array of 7 seismic stations deployed following the eruption. For the analysis I locate and relocate hypocentres, determine focal mechanisms, calculate b-values and cross-correlate waveforms. I have relocated the hypocentres of 456 earthquakes and used the spatial pattern to interpret the local and regional crustal response to the eruption. The shallow earthquakes beneath Nabro's caldera delineate a NE-SW thrust fault which dips 45^{o} to the SE and extends across the caldera floor. This accommodates the stress change following the eruption, rather than movement on ring faults. The NE-SW fault plane is not associated with measurable surface deformation, indicating that it does not contribute much to the caldera deformation. A $\sim$10 km deep cluster highlights potential magma migration pathways directly beneath Nabro. On the flanks of the volcano, a linear pattern of earthquakes illuminate possible minor faults. There is also a cluster of earthquakes beneath Mallahle caldera at a depth of 6 km; the b-value for this cluster is 0.97 and is lower than that for clusters under Nabro (b =1.3). This implies that the earthquakes generated at Mallahle are not dominated by magmatic processes and occur in rock with a stronger rheology. Therefore, the seismicity I observed is likely due to changes in the stress field resulting from the subsidence at Nabro, and not caused by magma movement beneath Mallahle.

TerraSAR-X and COSMO-SkyMed were both tasked to prioritise the acquisition of SAR data over the volcanic centre. During the following 15 months, Nabro was imaged 129 times by these satellites, with an acquisition every 5 days on average. I processed the 25 images acquired by TerraSAR-X between 1 July 2011 and 5 October 2012 on descending orbit 046, to create 34 interferograms. I complemented these with 19 images from ascending orbit 130 spanning 6 July 2011 to 10 October 2012 from ascending orbit 130, which I used to create 21 interferograms. I produced velocity ratemaps and time series using π-RATE, showing subsidence of $\sim$25cm/yr offset by 2 km to the SW of Nabro's caldera. COSMO-SkyMed satellite also imaged the volcano

on a descending track between 26 June 2011 and 18 July 2012 within the Italian Space Agency project SAR4Volcanoes: a total of 64 images were acquired and used to produce 171 interferograms.

I combined the InSAR data sets using a modelling approach to produce a detailed time series of the deflation of a Mogi source at ∼6.4 km depth. The time series shows that the volcano continued to subside for the entire period of observation, with the most rapid subsidence in the first 12 weeks, followed by subsidence at a slowly declining rate. I assessed the impact of atmosphere delays, using the outputs from ERA-Interim (ERA-I), a global atmospheric model computed by the European Centre for Medium-range Weather Forecasting (ECMWF), to correct each SAR acquisition. The atmospheric correction noticeably reduced the scatter in the time series, and removed the two atmospheric artefacts apparent in the COSMO-SkyMed time series. This result highlighted the importance of applying atmospheric corrections using independent sources of information. This contrasts with a standard approach of filtering in space and time which did not completely remove these atmospheric errors. Without the ERA-I correction the time series appeared to show pulses of recharge; with the correction continued subsidence is observed.

I explore mechanisms that might explain the long-lived subsidence at Nabro volcano. In particular, I tested models of thermal contraction, degassing, fluid migration and viscoelasticity. Degassing is the most likely cause of deformation, although contraction due to cooling may also contribute. The long term post-eruption subsidence is unusual in comparison to other active volcanoes. I suggest that the low magma supply rate, combined with the high rate of passive degassing, induces an overall subsidence of the ground surface above Nabro.

Contents

List of Figures

List of Tables

Chapter 1

Introduction

The theory of plate tectonics, which describes the continuous recycling of Earth's lithosphere, began a revolution in geological sciences. The interaction between these plates is still being quantified today, one hundred years after Alfred Wegener proposed his innovative concept of continental drift. These plates move toward, past or away from each other; in some locations three individual plates meet, further complicating the geological structure at the surface. Where two or three continental plates diverge a rift valley is created, which may eventually form new oceanic crust. In response to plate stretching, decompression melting occurs. The magma is intruded into the rift zone to accommodate extension and may subsequently erupt from volcanic segments along the spreading axis. Counter-intuitively, volcanoes also form offset from the rift zone. These 'off-rift' or 'off-axis' volcanoes erupt infrequently, limiting opportunities to study their role in continental break-up and subsurface plumbing. The Afar Rift Zone (ARZ) marks the centre of a Rift-Rift-Rift triple junction between the Nubian, Somalian and Arabian plates; where the Main Ethiopian Rift (MER), Red Sea Rift (RSR) and Gulf Of Aden (GOA) meet. The Nabro Volcanic Range (NVR) is an off-axis volcanic lineament which trends oblique to the RSR towards the centre of the ARZ. Nabro volcano, the namesake of the lineament, erupted on 12 June 2011 providing the opportunity to study the crustal response at these volcanoes and to delineate the magmatic system in this unique tectonic setting. In this thesis, I measure the ground deformation following the eruption using InSAR and seismic techniques. I model the time dependent ground displacement which occurs in response to the eruption and interpret the subsequent brittle crustal response of the caldera. The findings of these studies will contribute knowledge to the plumbing of off-rift volcanoes and the continued splitting

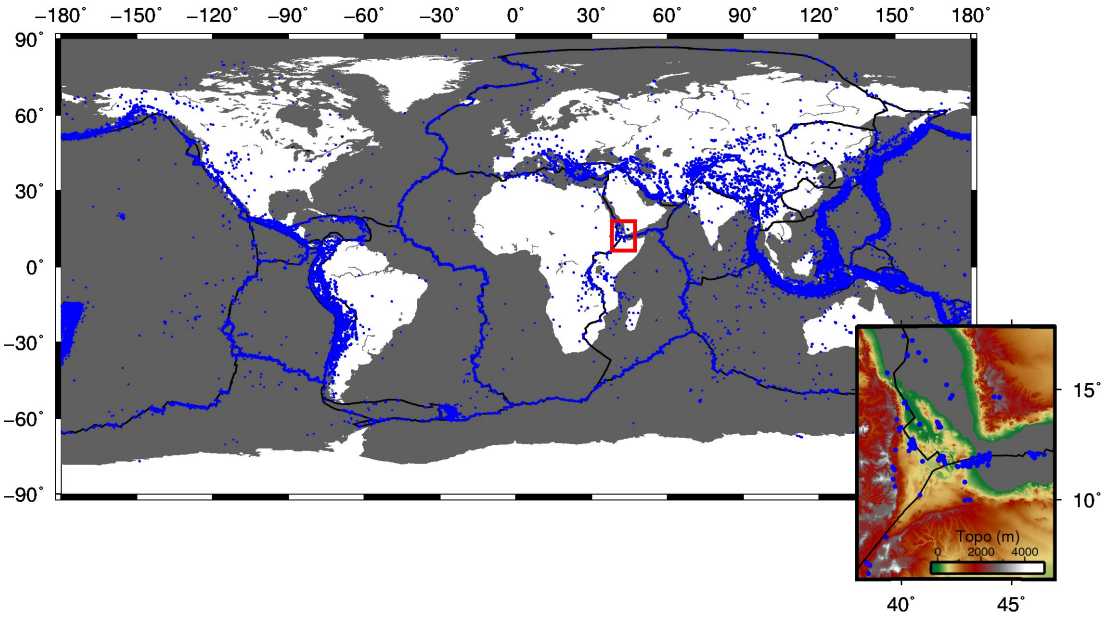

Figure 1.1: Worldwide distribution of magnitude 5 and above earthquakes since 1973 as recorded in the USGS catalogue (blue dots) and the plate boundaries (black lines). The inset map shows the plate boundaries and seismicity of the Afar region before 2014.

of the African continent.

1.1 Plate Tectonics

The theory of plate tectonics unifies observations from geology, geophysics and geochemistry which at one time seemed unrelated. The parental theories of plate tectonics: continental drift and seafloor spreading, are accredited to Alfred Wegener and Harry Hess in 1915 and 1962, respectively. These ideas provided the inception for plate tectonics which was quantified by Jason Morgan and Dan McKenzie in the late 1960's and 1970's. Fundamentally, plate tectonics requires that the lithosphere is fractured into plates due to convective cooling from the Earth's interior, which are rigid compared to the asthenosphere and mantle. There are 36 continental plates identified by Bird (2003) (Figure 1.1). This section will focus on divergent plate boundaries and triple junctions. A full history of plate tectonics can be found in books Condie (2013) or Cox and Hart (2009), for articles specific to the Afar region, see McKenzie and Morgan (1969a), McKenzie et al. (1970), McKenzie (1978), and Le Pichon and Francheteau (1978).

1.1.1 Divergent plate boundaries

Convective heat flow from Earth's interior force the tectonic plates to move relative to each other. Where two plates move apart is known as a 'divergent boundary'. This separation can occur through failure of the tensile strength of the rock as extensional forces are applied to the region (Turcotte and Emerman, 1983), for example by slab pull at a subduction zone. This is known as passive rifting (Sengör and Burke, 1978). Active rifting initiates when an upwelling of mantle material causes thermal erosion at the base of the lithosphere, generating a thinned crust which collapses under gravity and forces the plates to part (Morgan, 1972, Turcotte and Emerman, 1983). The three rift branches of the ARZ expose several stages of rift development during active continental plate separation (Wolfenden et al., 2004, Maguire et al., 2006). The Afar plume is discussed in more detail in section 1.2.

The volcanism and fault structure observed at a diverging plate boundary today is dependent on the stage of development (Hayward and Ebinger, 1996). Initially, the surface is scarred by normal faulting and half-grabens as the plates rift (e.g., Hayward and Ebinger, 1996). Following the mechanical stretching of the crust, magma intrusion and surface volcanism occur in segments at the axis of spreading (White and McKenzie, 1989), required to maintain the extension (Maguire et al., 2006). Dyke intrusions can occur in lower stress conditions than those required to break continental crust using only tensional forces (Buck, 2006). The transition from mechanical stretching to volcanism occurred within the MER approximately 3 Ma ago (Hayward and Ebinger, 1996, Beutel et al., 2010); and in the northern MER right laterally-stepping en-echelon volcanic ranges have accommodated extension during the last ∼2 Ma (Daly et al., 2008, Keir et al., 2006a)(Figure 1.2).

The thin lithosphere induces adiabatic decompression and can produce large volumes of melt (e.g., Turcotte and Emerman, 1983). The amount of melt produced is dependent on multiple factors; the amount of lithospheric thinning, the duration of extension, the rate of extension, the initial thickness of the lithosphere and the potential temperature of the asthenosphere (McKenzie and Bickle, 1988, Bown and White, 1995, Furlong and Fountain, 1986, Foucher et al., 1982). Additionally, the chemical composition of the mantle (Thompson et al., 2015) and the focusing of melt in the presence of a steep Lithosphere-Asthenosphere Boundary (LAB) (Holtzman et al., 2010) will effect the amount of melt produced.

Daniels et al. (2014) show that extensive dyke intrusion into a region allows aseismic ductile deformation to occur due to heating. This transfer from magma intrusion to ductile deformation is a late stage of rifting and is postulated as the present-day mechanism of deformation within the Danakil Depression (Bastow and Keir, 2011, Daniels et al., 2014). The continental plate separation is complete when the rift valley floods and new oceanic crust is formed from a mid-ocean ridge. The GOA began rifting 35 Ma ago and reached the stage of sea floor spreading during the early Miocene, between 16 to 18 Ma ago (Leroy et al., 2010, d'Acremont et al., 2010). The erupting magmas have a geochemical composition of Ocean Island Basalt (OIB) type (Cann, 1970). Similarly, volcanism on the axis of the Red Sea Rift (RSR) has also produced oceanic type basalts since the Miocene (Altherr et al., 1990).

Rift-Rift-Rift Triple Junctions

It is a geometrical requirement of plate tectonic theory that there will be locations where three individual plates meet. There are 16 combinations of transform, rift and thrust plate boundaries that are possible at these points, but not all are able to exist over an extended period of time (McKenzie and Morgan, 1969b). The most stable is a Rift-Rift-Rift (RRR) triple junction, in which the three plates are moving away from each other. Examples of this formation include the ARZ, the Galapagos Rift Zone and the Rodrigues Triple Point (McKenzie et al., 1970, Hey and Deffeyes, 1972, McKenzie and Sclater, 1971). However, the ARZ is the only one splitting continental crust. Burke and Dewey (1973) suggest that separation ceases on one arm of the rift and that the MER and ARZ is an example of a failed rift (an aulacogen). However, present day volcanism and crustal structure suggest that the rift is still active and has the potential to develop into an ocean basin (Keranen et al., 2004).

Off-Rift Volcanism

As discussed previously, magma often intrudes within the rift valley to accommodate extensional stresses. However, magma can also be erupted outside the border faults which delineate the rift zone. Volcanic centres outside the rift valley have been observed within the MER (Chernet et al., 1998) and the RSR (Bosworth et al., 2005). Maccaferri et al. (2014) found that the final location of ascending magma is controlled by the stress conditions of the region, the ratio between lithospheric unloading and tectonic

stretching, the nucleation depth of the dyke and the aspect ratio of the rift. Ascending magma which nucleated at a shallow depth relative to the width of the graben will be erupted or stored within the rift. In contrast, deep nucleation depths and narrow rift zones will result in off-rift volcanism. Maccaferri et al. (2014) use this theory to explain the locations of early syn rift volcanism related to the MER, the Baikal rift and the Chaines des Puys systems.

1.2 The Afar Rift Zone (ARZ)

The ARZ marks the location of the triple junction between the Nubian, Somalian and Arabian plates; where the MER, RSR and GOA meet (McKenzie and Morgan, 1969b). Geographically, it encompasses parts of Ethiopia, Eritrea and Djibouti and with air temperatures exceeding 40°, it is considered to be an exceptionally harsh environment to inhabit. The ARZ has drawn the attention of geologists and geophysicists since the inception of plate tectonic theory, as it is an ideal place to observe evolution from continental rifting to seafloor spreading.

1.2.1 Tectonic evolution

The formation of each branch of the triple junction has not been synchronous, nor has the location of the triple junction remained static since its initiation (Tesfaye et al., 2003, Wolfenden et al., 2004, McKenzie et al., 1970, McKenzie and Morgan, 1969b). The oldest branch is the GOA, where the onset of volcanism occurred approximately 35 Ma ago (Leroy et al., 2004). Later, extension began in the RSR 31 to 29 Ma ago (Wolfenden et al., 2004). This rift bifurcated at 13°N approximately 9 ±4 Ma ago; south of 13°N, extension is accommodated by both the ARZ (McClusky et al., 2010) and the southern RSR (Xu et al., 2015). The divergence of the RSR is thought to have been associated with a change in the rate of the Arabian plate motion around 13 Ma (McClusky et al., 2010) and was aided by the thinning of the Nubian lithosphere due to interaction with a thermal plume. Oceanic crust is evident in the GOA (Leroy et al., 2013) and within the RSR as far south as 15°N (Cochran and Martinez, 1988). In southern Ethiopia, rifting on the MER propagated northwards into Afar 11 Ma ago (Wolfenden et al., 2004). The MER terminates against the Tendaho-Goba'ad Discontinuity (TGD) which separates the MER from the onland branch of the RSR. Therefore, the fully formed triple junction has existed for approximately 11 million years, $\sim$ 20 Ma after rifting

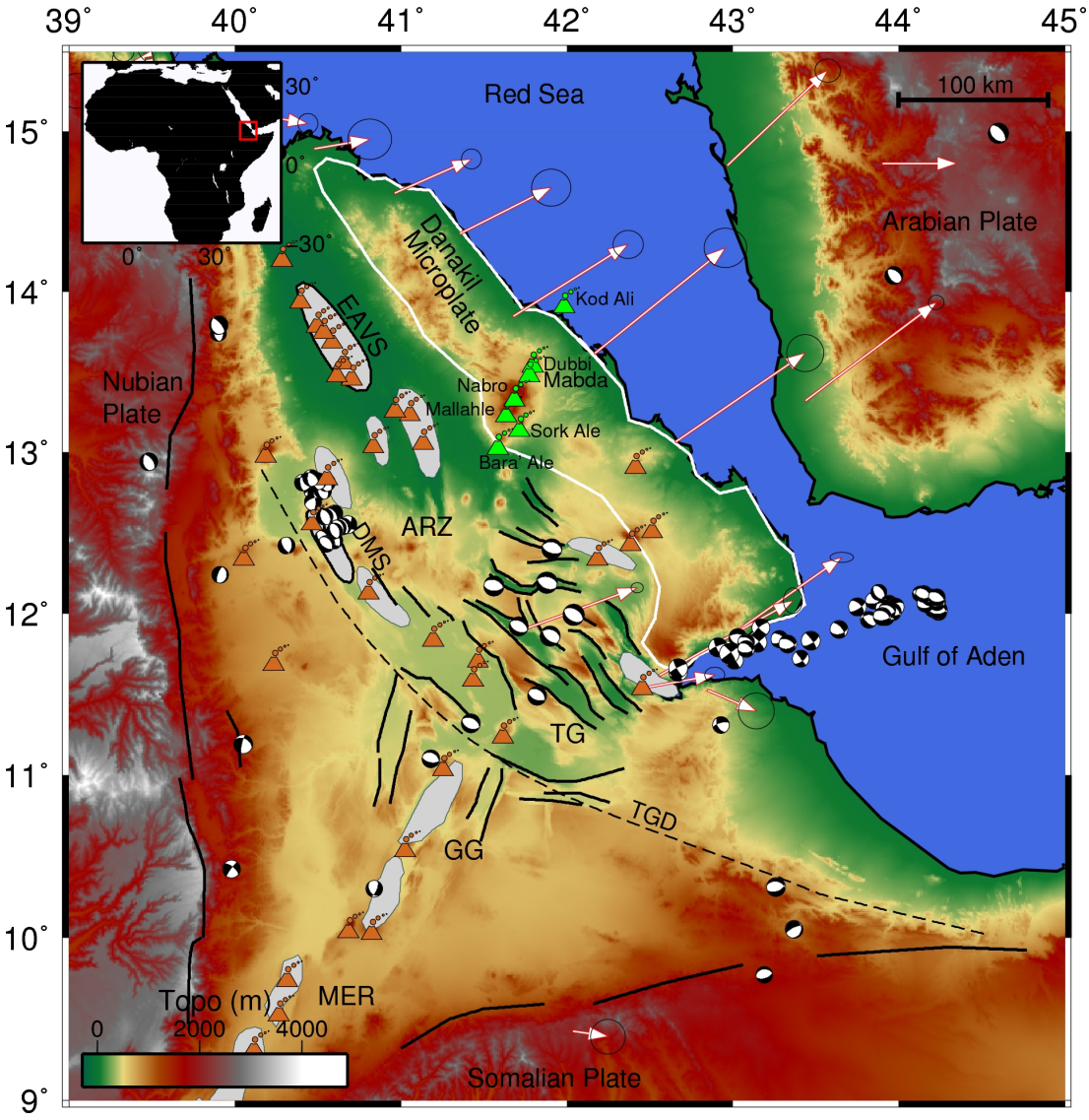

Figure 1.2: Topographic map of the Afar Rift Zone from the 90m SRTM. Black lines show the regional faults, black dashed line indicates the Tendaho Goba'ad Discontinuity (TGD) which separates the Tendaho (TG) and Goba'ad Grabens (GG), respectively. White arrows are measured horizontal GPS displacement relative to the Nubian plate (McCluskey 2010). White outline delineates the Danakil Microplate. The grey shading shows volcanic segments with the Erta Ale Volcanic Segment (EAVS) and the Dabbahu Magmatic Segment (DMS) outlined in black. The regional fault plane solutions, as defined by the Harvard CMT Project between 1979 and 16th March 2011, show the previous quiescence of the Nabro Volcanic Range (NVR). Orange triangles show positions of volcanoes in the region as defined by the Smithsonian catalogue, green triangle show the volcanoes which compose the NVR. The NVR is composed of several volcanoes; Sork' Ale, Bara' Ale, Mallahle and Nabro, as well as the silicic domes of Mabda, Dubbi, the Edd lava field and Kod Ali island, which is located significantly further north in the Red Sea. Upper Left inset: The position of the Afar Rift Zone (ARZ) on the African Continent.

initiated in the GOA. Tesfaye et al. (2003) suggest the TGD defines the centre of the triple junction. This tectonic structure is formed by the northwest striking Tendaho and southwest striking Goba'ad grabens, which separate the northwest tectonic trend in central Afar from the north north east MER tectonic fabric. Due to the different rifting rates of the plates, the triple junction has migrated approximately 160 km over the last 25 Ma (Tesfaye et al., 2003). This differential rifting has also forced the orientation of the RSR to alter since its initiation (Hammond et al., 2011, Wolfenden et al., 2004), originally north-south it has shifted to a NNW-SSE trend.

The structural geology of the ARZ is complicated by the fragments of continental crust which have become isolated within the Afar Depression (e.g., Eagles et al., 2002, Hammond et al., 2011). The most spectacular is the Danakil microplate, a suspected sliver of continental crust composed of Mesozoic sediments (Beyene and Abdelsalam, 2005) which separates the two branches of the RSR. It is rotating anti-clockwise at a rate of 1.9 $\pm$0.1°Ma around a pole located at 17.0 $\pm$0.2°N 39.7 $\pm$0.2°E. Assuming a linear rate the block began rotating coincident with a change in the Arabia-Nubia relative motion 11 Ma ago, associated with the ocean ridge spreading of the GOA. The Nabro Volcanic Range is Quaternary age volcanism present at the southern edge of the Danakil Alps, seemingly bisecting the Danakil Horst on a NE-SW trend as delineated by Eagles et al. (2002).

The Afar Plume

The onset of the Afar plume is often cited as a cause of rift initiation in East Africa (e.g., White and McKenzie, 1989), but the current influence of a mantle plume is still debated. Key components of hot spot tectonism; i.e. Continental flood basalts, plateau uplift, and transition from continental rifting to seafloor spreading, are all recognisable in the ARZ (Ebinger and Casey, 2001, Furman et al., 2006, Hofmann et al., 1997, Pik et al., 2008). However, the current presence of a lower mantle upwelling beneath Afar is unclear (e.g. Furman et al. (2006), Chang and Van der Lee (2011), Rychert et al. (2012), Hansen and Nyblade (2013), Ferguson et al. (2013), Thompson et al. (2015)). Ebinger and Casey (2001) argue that a single plume can account for the distribution and timing of magmatism, because of the strong controls the lithosphere can impart on the plume induced melt. Many seismic models support this, showing a broad region of low velocity material present in the upper mantle from Tanzania to Ethiopia (Bastow

et al., 2005, Benoit et al., 2006, Bastow et al., 2008, Hansen et al., 2012). However, Rogers et al. (2000) and Furman et al. (2006) expand on the single plume hypothesis, based on the geochemical evidence that the composition has remained stable over the past 30 million years. They suggest the Afar plume has multiple stems which are connected to the South African superplume. Adding to this debate, a number of other seismic models also support the multiple plume model, showing more local upwellings beneath Afar (Chang and Van der Lee, 2011, Thompson et al., 2015). Importantly, recent studies have suggested that local upwellings beneath Afar are different to classic plumes such as Hawaii. They may instead have a limited thermal anomaly (< 100K), be sourced directly below the transition zone and have a dependence on the composition of the mantle (Chang and Van der Lee, 2011, Thompson et al., 2015). This supports observations that the mantle beneath Afar is warm and that rifting and melting is largely driven by passive upwelling above a warm mantle (Ferguson et al., 2013, Armitage et al., 2015). Additionally, high resolution models of upper mantle structure beneath Afar show that localised diapiric upwellings may be present in the uppermost mantle that may relate to off-axis volcanism (Hammond et al., 2013).

1.2.2 Present day volcanism in Afar

As discussed previously a plume of hot mantle material initiated the continental rifting observed today. Flood basalts associated with the hot spot are found on the Nubian, Somalian and Arabian plates (White and McKenzie, 1989, Bertrand et al., 2003). The present day volcanism in Afar is associated with rift volcanism as described in section 1.1.1. Over the last decade numerous periods of magmatic rifting processes have occurred. The most notable of these is the 2005-2011 Dabbahu-Manda-Harraro rifting episode. In September 2005, a dyke fed from Dabbahu and Gabho stratovolcanoes propagated the entire length of the 60 km long Dabbahu magmatic segment (Wright et al., 2006). A new column of crust approximately 8 m wide formed (Wright et al., 2006). Following this initial emplacement 13 smaller intrusions have occurred between June 2006 and May 2010 (Hamling et al., 2009, Ebinger et al., 2010, Wright et al., 2012).

The Erta' Ale Volcanic Segment (EAVS) is composed of 4 volcanic centres: Erta' Ale, Dalafilla, Gada Ale and Tat Ale. The November 2008 fissure eruption on Alu Dalafilla illuminated the shallow magma storage systems which fed large eruptions. Pagli

et al. (2012) showed that lava was extruded from a 1 km deep sill, which strikes parallel to the range. Geochemical analysis of the November 2010 Erta' Ale eruption indicated a shallow storage chamber less than 1 km deep (Field et al., 2012a). Dallol volcano sits to the north east of the Erta' Ale range, InSAR analysis of the October 2004 eruption shows that the magma was sourced from a 2 km deep reservoir (Nobile et al., 2012).

The only documented eruption of an NVR volcano prior to the 2011 eruption of Nabro is the May-October 1861 eruption of Dubbi volcano (Wiart and Oppenheimer, 2000). Satellite images and geochemical analysis of lava and tephra deposits were used by Wiart and Oppenheimer (2000) to interpret the eruption. This study was contextualised through eye witness accounts, which were readily available due to the high level of maritime activity in the Red Sea. During the 6 month eruption the style transitioned from explosive to effusive. The explosive beginning of the eruption was accompanied by pyroclastic flows which reached at least 25 km from Dubbi (Wiart and Oppenheimer, 2000). The final volume of erupted lava is a minimum 3.5 km^3, ranking the event as the largest recorded eruption on the African continent (Wiart and Oppenheimer, 2000). Compared to rift volcanism, the off-rift volcanoes erupt infrequently but catastrophically; 175 people were killed by the Dubbi eruption (Wiart and Oppenheimer, 2000). This illustrates the need for a deeper understanding of off-rift volcanoes.

1.3 The Nabro Volcanic Range (NVR)

The NVR is composed of 7 volcanic centres; Bara Ale, Sork Ale, Mallahle, Nabro, Mabda, Dubbi, and Kod Ali. They form a lineament which trends SSW-NNE, extending approximately 110 km from the Afar Depression to the Red Sea, bisecting the Danakil Microplate (Wiart and Oppenheimer, 2005) (Figure 1.2). Nabro and Mallahle calderas lie in the middle of the NVR, together these volcanoes are known as the Bidu Volcanic complex (BVC). Despite the NVR being a major topographic feature within the ARZ, it has not been documented in great detail. The only geological study of Nabro volcano prior to its eruption in 2011, was published by Wiart and Oppenheimer (2005).

The NVR is not associated with the rift related volcanism observed elsewhere in Afar. The strongly alkaline composition of the NVR centres is distinct from the more transitional basalts from the on-rift volcanoes (Barberi et al., 1974). Additionally, the

lavas from the off-rift volcanoes contain ultramafic inclusions which are not observed elsewhere in Afar (Barberi et al., 1974). An explicit holistic theory for the magma supply, cause and role of the NVR has not yet been found. The stress regime mechanism for off-rift volcanism as discussed previously may not be sufficient as it explains sporadic volcanic centres and not a volcanic lineament. Further processes are required in addition to this theory or separate to it to explain the presence of the NVR. Hammond et al. (2013) resolved three thermal diapiric upwellings from the upper mantle using seismic tomography, one of which is located under Nabro. The deep upwelling may explain the geochemical variations across Afar (Pik et al., 2006, Rooney et al., 2012) and a direct magma supply to the volcano, but there is no direct link to the structural trend or the number of centres which create the lineament. The NVR has been recognised as a relic of the regional tectonic fabric (Tazieff and Varet, 1972), or an extension of the Wonji Fault Belt (Mohr, 1968), as well as the result of tensional forces acting on the Danakil microplate only (Barberi et al., 1972).

1.3.1 Nabro and Mallahle

Nabro is a stratovolcano with a horseshoe-shaped caldera reaching 8 km in diameter, the breach faces SW towards the smaller 6km diameter caldera of Mallahle volcano (Wiart and Oppenheimer, 2005)(Figure 1.3). The summit of Nabro is 2248 m a.s.l, making the BVC one of the largest massifs in the Afar region. Nabro's caldera walls form 400m high cliffs and within the caldera there are two additional collapse craters; the first is ∼400 m deep and ∼2 km across, the second is overprinted on the SW rim of the first crater, it is over 200 m deep and ∼1.4 km wide (Figure 1.3). This second crater proved to be the focus of the June 2011 eruption and is referred to as the SW pit in section 1.3.2. Based on satellite images, Goitom et al. (2015) note that the inner walls of this crater are lined with scoriaceous lavas, possibly from drain back from a previous eruption. The flanks of Nabro are scarred by numerous gullies and are largely composed of trachytic lava flows (Wiart and Oppenheimer, 2005).

Mallahle is a shorter volcano, reaching 1,800 m a.s.l. The complete, circular caldera has a dipping floor partly in-filled with pyroclastics. The only field evidence of activity since caldera collapse are several obsidian flows on the caldera floor. In comparison to the rest of the Afar, there is relatively dense vegetation cover in the southern part of the caldera (Wiart and Oppenheimer, 2005).

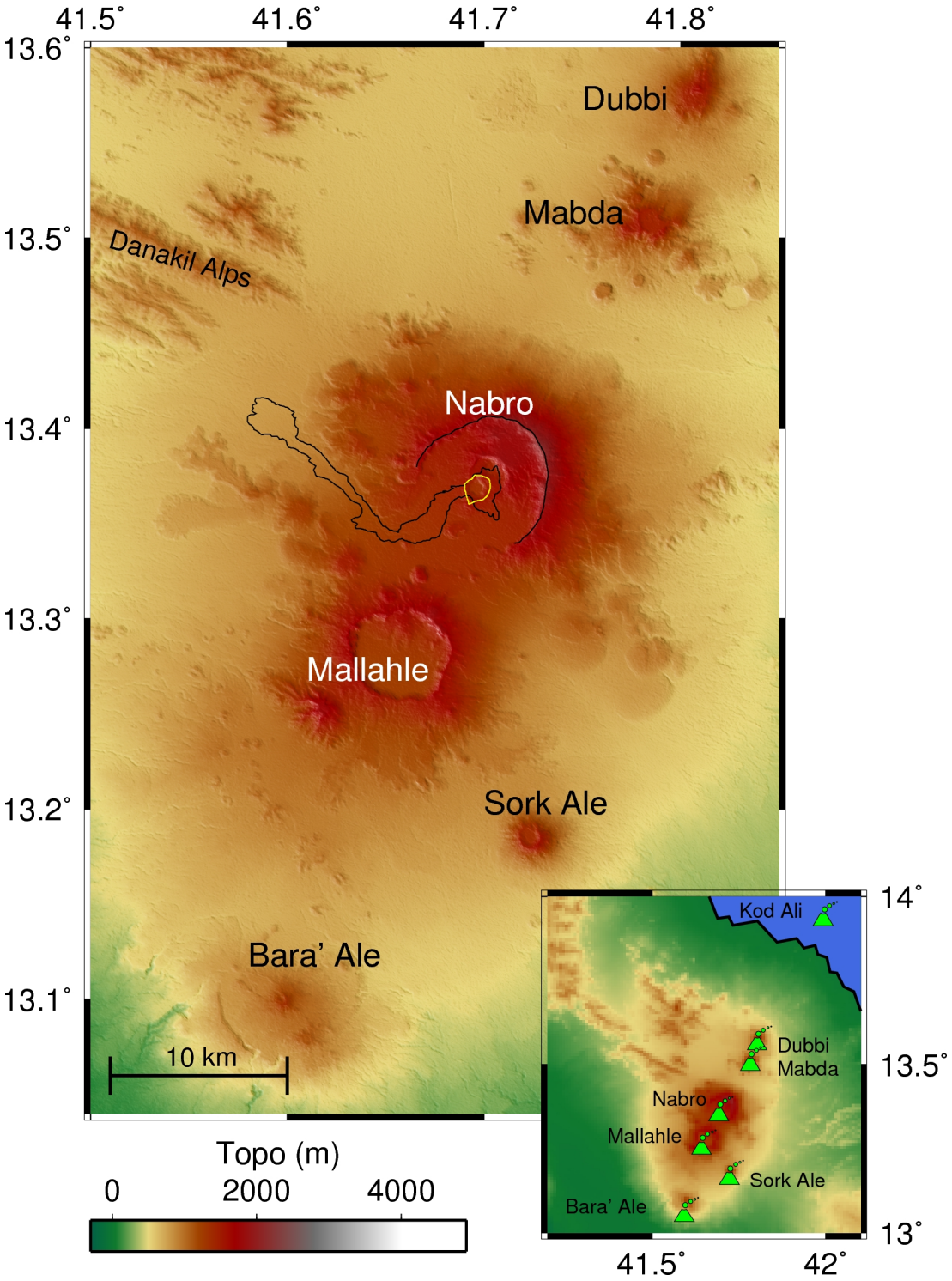

Figure 1.3: Zoom of the Nabro volcanic range. Components of the Bidu Volcanic Complex are labelled in white. Vent region is highlighted in yellow. The caldera walls and lava flow are outlined in black.

The geological map of the BVC (Figure 1.4) was produced by Wiart and Oppenheimer (2005) based on Landsat satellite imagery. It reveals that both Mallahle and Nabro calderas have a similar lithology and geomorphology. The calderas are primarily composed of trachytic lava flows, which were produced from 2 separate eruptions. Both structures also have domes and flows composed of rhyolitic obsidian. The most recent volcanics of the BVC include lavas with a more basaltic composition, which have erupted from fissures perpendicular to the NVR lineament, between the calderas. Wiart and Oppenheimer (2005) suggest these were produced from separate sources to those which fed the initial silic volcanism. The calderas are notably undeformed, due to the distance from the extensional forces which dominate volcanic structures in the centre of the ARZ.

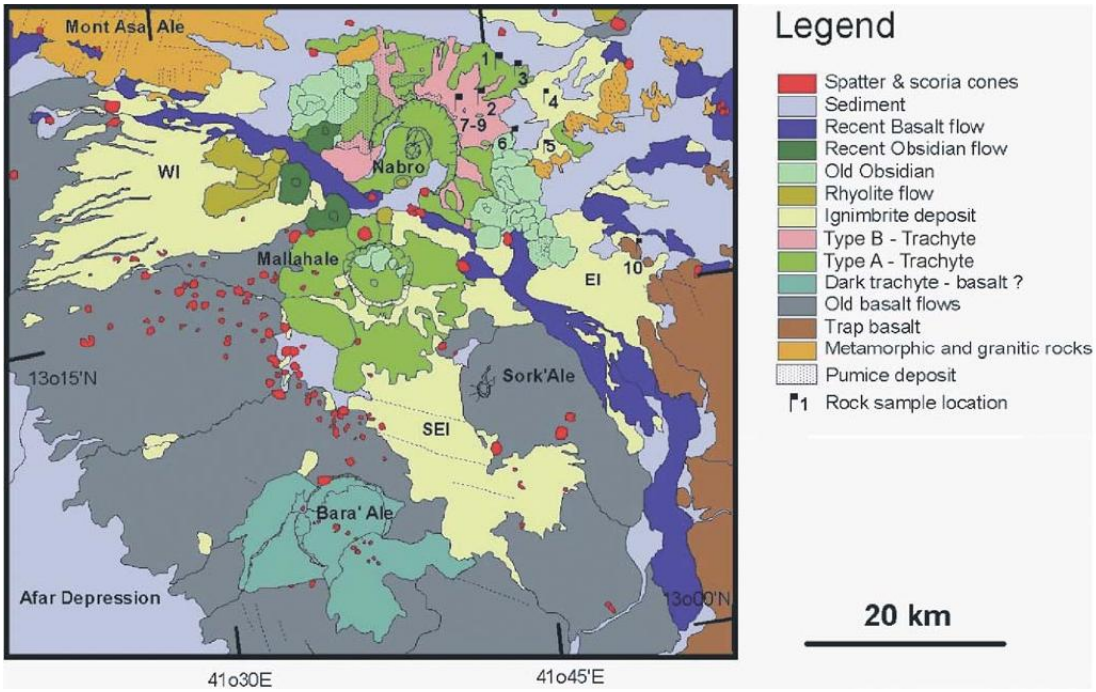

Figure 1.4: Extracted from Wiart and Oppenheimer (2005), geological map of the Bidu Volcanic complex and the associated west, southeastern and eastern ignimbrites, WI SEI and EI respectively. The image was produced from Landsat imagery.

1.3.2 2011 eruption synthesis

Here I give an overview of the pre- and co-eruption activity of the 12 June 2011 eruption of Nabro volcano. It is based on the synthesis study by Goitom et al. (2015), which describes the seismic, infrasound, petrological and geodetic data available following the eruption. There was no monitoring of Nabro prior to this eruption and no system

in-place to evacuate the people who lived in the caldera, but a rapid response from emergency services saved lives. In total, 7 people were killed and approximately 12000 were displaced. The total cost of the eruption was estimated at 3 million USD (Solomon, 2012).

Pre-eruption Activity: 23 Feb to 11 June 2011

The first major earthquake recorded in the region occurred on the 31 March 2011, it was originally located by the USGS to have an epicentre 25 km south east of the caldera, but subsequent field work and reanalysis of the regional seismic data by Goitom et al. (2015) relocated the hypocenter to within Nabro's caldera. The region was seismically quiet before the eruption; there were only 9 events on 8 separate days in the pre-eruptive period (23 February to 11 June 2011). Only the 31 March 2011 event had a large enough magnitude to be recorded by the USGS, the other events were catalogued by regional stations in Afar. The local magnitudes varied from 2.6 to 4.8, the largest being the 31 March event.

Co-eruption Activity: 12 June to 17 June 2011

On 12 June 2011 a seismic swarm began at 15:37 UTC. 5 hours later, between 20:27 and 20:42 UTC, the eruption began. Two large seismic events occurred before and after the eruption onset at 20:32 and 21:03 UTC. It was the most seismically active day with local earthquake magnitudes ranging from 2.8 to 5.8. Between 12 and 17 June seismicity recorded at a station 125 km away indicated high levels of volcanic tremor during this period. It remained at a high and steady rate before falling to almost no activity on the 16 June; the same day there were confirmed high levels of lava effusion at the main vent in the SW pit. On 17 June there were renewed earthquakes and the largest earthquake occurred, which was recorded to have a local magnitude (M_L) of 5.9. This second phase of activity is indicative of a renewed magma supply feeding the eruption Goitom et al. (2015). The seismicity during this period occurs under both Nabro and Mallahle calderas.

Topographic changes to the caldera were observable from a high resolution CSK image acquired on 18 June. Since the onset of the eruption a tephra cone was created in the SW pit, which sourced multiple lava flows including the longest flow that reached 17.5 km-long by 16 June. The image also shows an NW-SE alignment of pits which

opened up as they sourced smaller lava flows and remained active until 1 July. Satellite images also observed the tephra fallout, which settled during the first few days of the eruption. The deposit covers a 700 km^2, 130° segment from SSE to WNW of the vent.

The newly emplaced lava flows have a composition of trachybasalt to trachybasaltic andesite, which is more alkali rich than rocks in the centre of the Afar rift (Goitom et al., 2015). Overall, the lavas are highly crystalline. Some tephras are glassy indicating discrete batches of magma, with zoning patterns which suggest a complicated storage history. The petrology shows some magma was reheated before eruption and some rapidly ascending from depth.

An estimated 4.3 Tg of SO_2 were emitted to the atmosphere during the eruption (Theys et al., 2013), making this eruption the largest atmospheric aerosol perturbation since Mt Pinatubo, which emitted ∼20 Tg SO_2 to the atmosphere (Bluth et al., 1992). Related to African volcanism, this was the largest emission of SO_2 following the release of ∼4.11 Tg SO_2 during the 1981-1982 eruption of Nyamulagira (Bluth and Carn, 2008).

Co-eruption Activity: 18 June to October 2011

Following the intense seismicity on 17 June 2011, fluctuating levels of volcanic tremor was recorded over the following 30 days before ceasing on 14 July 2011. Frequent seismicity was recorded on regional stations from the 18 June to the beginning of September, some events were greater than M_L 4 and were mostly located beneath Mallahle caldera. Additionally, some earthquakes events occurred beneath Sork Ale.

An infrasound station in Djibouti recorded 3 days of explosive activity on 18, 21 and 22 June. This was accompanied by increase in seismic moment and small increase in the SO_2. SWIR channels of ALI images acquired on the 24 June and 12 July show intense thermal radiation in multiple locations; at the highest point within the SW crater, the source of the main lava flow, at the front of the main flow and along minor flows. The small lineament of vents which opened up during the main eruption do not appear to significantly contribute to the lava eruption after 20 June. By mid September the SWIR channels of ALI images show no thermal radiation from the lava flows, with only anomalous 'hot' patches around the SW crater. These were also observed by Clive Oppenheimer and colleagues during a field campaign in mid-October, at this time they also observed a weak plume (C. Oppenheimer, 2012 *person comm*).

1.4 Magma Chambers

The configuration of magma within the shallow crust has become widely debated over the past decade. Advances in petrological and geophysical analysis have provided new data incompatible with classic models of magma storage. The standard model of a magma chamber (labelled such by Gualda and Ghiorso (2013)), includes an isolated, long lived singular body of crystal poor melt that cools from the margins (Hildreth, 1979). The chamber is evacuated by a top down process which results in the deposition of zoned ignimbrites. However, geophysical studies can not determine large volumes of crystal-poor melt within the crust (e.g., Schilling and Partzsch, 2001, Chu et al., 2010). Also, large eruptions do not require a pre-existing large melt volume as eruptible magma can be assembled quickly (e.g., Charlier et al., 2005, Simon et al., 2014, Wotzlaw et al., 2014).

Recent studies suggest that magma storage regions are composed of crystal mush and intersital melt (i.e. not crystal poor (e.g., Lipman, 2007, Hildreth and Wilson, 2007, Walker et al., 2007)), with lenses of increased percentage of partial melt. These are distinct and large eruptions can tap multiple lenses (e.g., Cooper et al., 2012, Ellis and Wolff, 2012, Gualda and Ghiorso, 2013). The 2012 eruption of Eyjafjallajokull tapped vertically distributed lenses (Tarasewicz et al., 2012), whereas laterally isolated lenses contributed to the Bishop Tuff eruption from the Long Valley caldera (Hildreth and Wilson, 2007). These observations combined with low pyroclast vesicularity, multiple explosive episodes and variable melt and bulk compositions can not be reconciled with a model of magma from a single pressurised, well mixed, melt-dominated magma chamber.

Often analytical models of geodetically observed ground deformation at volcanoes use sources with clearly defined boundaries in a homogeneous, isotropic, elastic half space. As discussed, the plumbing of volcanoes has the potential to be a much more complex system of distinct lenses of partial melt in a crystallising mush. These differences and ambiguities are important to consider when interpreting seismic and geodetic data.

1.5 Volcanic Deformation

Observed ground deformation results from the mechanical properties of the crust which transfer a stress change at depth to the surface (Dzurisin and Mori, 2007). In a volcanic setting, the stress on an edifice may be induced by a range of processes including magma movement, degassing and hydrothermal systems (Caricchi et al., 2014). The pattern of the resulting deformation can be modelled to identify the depth and geometry of the source of the volume change, which can give insight to the subsurface structure of the volcano. Subsequently the process causing initial stress change can be investigated.

The cyclical nature of ground deformation at volcanoes can provide a basis for volcano monitoring (Dzurisin, 2003, Lu et al., 2003). Inflation leading to an eruption is well recorded in literature (e.g., Dvorak and Dzurisin, 1997). After a dike emplacement or an eruption, subsidence occurs due to a pressure decrease inside the volcanic edifice (Sigmundsson et al., 2014). It is common for a volcano to subsequently re-inflate following subsidence as the magma chamber recharges (e.g. Mt. Etna: Lanari et al. (1998)). This is an idealised scenario, not all periods of inflation culminate in an eruption and likewise, not all volcanoes inflate before erupting (Biggs et al., 2014). Also, periods of deflation do not have to be associated with an eruption (e.g. Medicine Lake Volcano: Parker et al. (2014) and Askja: Pagli et al. (2006)) and some volcanoes do not re-inflate following an eruption. The evolution of the cycle is complicated by complex magma evolution and cooling, and variations in the mechanical properties of the crust. Furthermore, my interpretation of the data can be biased by the length of the observation period.

InSAR monitoring has an unprecedented spatial resolution for observing the ground displacement, useful for inverting the observations for a source model. However, the model that is inverted for is often situated in a homogeneous elastic half-space. The simplification of the mechanical properties which are transmitting the stress to the surface will cause a misfit between the model and the true geometry. In reality, the subsurface will have a poroelasticity, thermoelasticity, viscosity, and be influenced by the presence of fluids and the topography of the free surface.

Once the source volume and geometry have been estimated, the processes causing the deformation can be investigated. In the case of subsidence following an eruption, the volume change will be composed of magmatic and gas components. If the subsidence

is not related to an eruption, the magma body may be losing volume through cooling and contraction. Inflation and deflation cycles due to hydrothermal systems have been observed at Campi Flegrei caldera in Italy. According to Battaglia et al. (2006), inflation is caused by the exsolution of brine and gas from a crystallising magma. When the brine and gas solution breach an overlying impermeable zone beneath an aquifer the solution to escapes and the ground surface subsides. Degassing of SO_2 is correlated with the ground deformation cycle on Montserrat based on tilt meter data (Watson et al., 2000).

1.6 Volcano Seismology

Diverse types of seismic signals are recorded by seismometers situated on volcanoes and their surrounding regions. The signals are caused by the brittle failure of rock and magma, due to the interaction of magmatic and hydrothermal fluids which lead to stress changes (Neuberg et al., 2006), pressure variations and fragmentation, all within the volcanic edifice (Gupta, 2011). Also, processes at the surface such as dome collapse, pyroclastic flows and smaller rock fall events, all produce seismic signals. Different volcanogenic processes create seismic signals by which volcanic processes can be identified, often in real time for volcano monitoring purposes (Chouet, 2003). Here I introduce the categories of seismic signals, the trigger mechanism and their defining characteristics.

Volcano-Tectonic events

Volcanoes create areas of complex tectonic stresses. The presence of an active volcano constantly adjusts the local stress field which is situated within a regional stress field dominated by plate tectonics. It is the superposition of the volcano related stresses on the regional tectonics that cause volcano-tectonic (VT) earthquakes (Roman, 2005).

The characteristics of VT earthquakes are the same as for local earthquakes because of a common source mechanism; the brittle fracture of rock. VT's are characterised by a clear P- wave and S- wave arrival and dominant frequencies range between $5-15$ Hz (McNutt, 2002), and typically have magnitude range between $1-3$ Mb (Gupta, 2011) (Figure 1.5). However, VT events of magnitude 5.5 M_w occurred during the 2005 Dabbahu (Ebinger et al., 2008) and the 2004 Dallol (Nobile et al., 2012) events. The location and focal mechanism of VT events illustrate how the local stress field is

changing based on magma movements (Roman, 2005). VT activity can be the first sign of a volcano reawakening (Chouet, 1996).

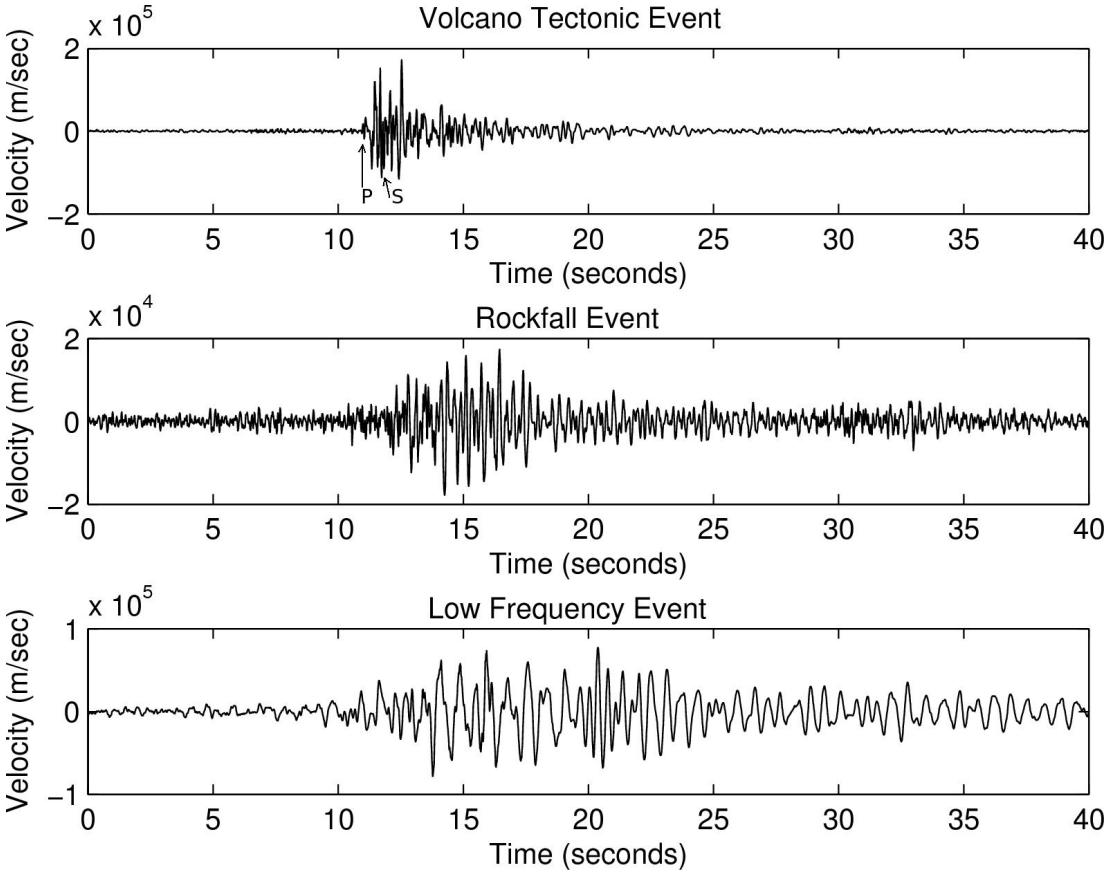

Figure 1.5: Example seismograms of volcano tectonic, rockfall and low frequency events. Recorded on Soufriere Hills Volcano (Montserrat) in 1997.

Rockfall events and pyroclastic flows

Seismic signals are generated by the impact of rocks falling on the volcanic edifice. A rockfall event creates a characteristic cigar shaped seismic signal (Figure 1.5), in which the amplitude increases as the volume of rock and acceleration increases. These events are common in explosive, dome building episodes which involve highly viscous magma (Neuberg, 2000). They can be placed on a continuum between small isolated rock avalanches and pyroclastic flows.

Low frequency earthquakes

Low frequency (LF) earthquakes are characterised by a spectral band between approximately 0.2-5Hz and are the broader term used for a continuum of events which range

from long period to hybrid events (Neuberg, 2000) (Figure 1.5). Low frequency events appear to be sourced from the walls of conduits, dykes or cracks containing gas or magma (Neuberg et al., 2006). Seismic energy becomes trapped in this scenario and therefore resonates within the system, with only a small amount of energy reaching the surface.

Long period earthquakes

Long Period (LP) events resemble small tectonic earthquakes in duration but differ in their characteristic frequency range and harmonic signature (Chouet, 1996). As these signals originate from the fluid contained in the magmatic system, they involve volumetric modes of deformation, unlike VT's which involve solid rock processes. VT earthquakes also tend to be more widely dissipated in space and time, whereas LP's and volcanic tremor are concentrated within the magma plumbing system where disturbances in the flow are encountered. LP events are characterised by a harmonic waveform, containing up to several dominant periods in the range of 0.2 to 2s, dependent on the length of flow with in the system.

Volcanic Tremor

Volcanic tremor can occur if the trigger mechanism for low frequency earthquakes is maintained, allowing LF events to merge through time. Therefore, the same source generates both events with the only difference being duration (Chouet, 1996). However, volcanic tremor can also occur as the general background noise emanating from volcanic processes. For example, volcanic tremor at Piton de la Fournaise, La Reunion, originates from turbulent magma and extruding lava flows. Similar sources of tremor involve degassing or hydrothermal activity (Neuberg et al., 2000). Tremor of this type is composed of a large variety of frequencies and does not have distinct seismic phases, so cannot be used to locate sources based on arrival times (Neuberg et al., 2000).

Hybrid events

So far two types of seismic signal have been discussed: those associated with fracture of brittle rock and those which have a volumetric component caused by fluid or gas. These signals are not two independent categories but should be considered end members of a continuum. The events that are representative of the transition between each end of

the spectrum are known as hybrids.

The onset of a hybrid is more distinct than an LP event, however the coda is still dominated by a non-dispersive harmonic wave train (Chouet, 1996). Hybrid and LP events can be distinguished from each other on the basis of wave polarity as it varies at each seismometer for VT and hybrids but remains fixed for LP events (Chouet, 1996). The model illustrating a trigger mechanism for hybrids has to contain both shear and volumetric components. A possible configuration for this scenario involves shear faulting along a plane which intersects a fluid filled crack (Chouet, 1996).

1.7 Thesis Overview

In this thesis I aim to delineate the plumbing system of Nabro volcano using seismic and InSAR data collected following the 12 June 2011 eruption. I also explain the main mechanisms causing my observations. The thesis is organised as follows:

In Chapter 2, I present the seismic data used for this study and develop an outline of Nabro's plumbing system.

In Chapter 3, I give a brief description of the InSAR method, for the benefit of seismologists and volcanologists not familiar with this geodetic technique. I introduce the data sets used for this study and go on to investigate the atmospheric corrections required.

In Chapter 4, I model the linear ground displacement as the result of Mogi and Okada source geometries.

In Chapter 5, I model the temporal variation of source volume change.

In Chapter 6, I discuss the implications of my results for the plumbing of Nabro volcano and its relation to the Afar Rift.

Finally, in Chapter 7 I summarise the conclusions and discuss future work.

Chapter 2

Seismic Analysis

VT earthquakes are commonly recorded pre-, co- and post-eruption (Hill, 1977, Umakoshi et al., 2001, Roman and Cashman, 2006, Roman et al., 2006, Vargas-Bracamontes and Neuberg, 2012). Ascending magma perturbs the local stressfield, fracturing the rock around the conduit as well as the edifice and causing numerous small-magnitude earthquakes (Sparks, 2003, Vargas-Bracamontes and Neuberg, 2012). Following an eruption, the crust adjusts to the new stress conditions by brittle fracture and aseismic deformation. Post eruption VT data, whilst not aiding early warning systems, are still critical to our understanding of volcanoes. This seismicity exposes a relationship between the crustal response after the eruption, and the magma release during the eruption (e.g., the 1975 eruption of New Tolbachik (Zobin, 2003), the 1980 eruption of Mt St. Helens (Weaver et al., 1981), the 1991 eruption of Mt. Pinatubo (Mori et al., 1996) and the 1991-1995 eruption of Unzen (Umakoshi et al., 2001)).

Relying on regional networks to locate VT earthquakes for detailed analysis of magma plumbing and associated fracturing is problematic (Anderson and Webb, 1994). If the nearest station to record an earthquake is further away than one focal depth, the resulting error in depth of the earthquake increases (Anderson and Webb, 1994). Therefore, deploying a temporary array of seismometers, which targets a specfic eruption, will increase the accuracy and precision of VT event locations, making it possible to delineate structures in the crust. Furthermore, the focal mechanism of an event can be more tightly constrained due to the proximity and aperture of the stations.

In this chapter, I present my analysis of the seismicity recorded at a local array following the 2011 eruption of Nabro. This includes calculating hypocentre locations following processing with relocation algorithm HypoDD, local magnitudes of events,

$b-$values of clusters, focal mechanisms and waveform correlation. This work has been published in article: Hamlyn et al. (2014), see Appendix E.

2.1 Data Catalogue

There were no operational seismometers in Eritrea before the eruption began (Goitom et al., 2015). However, the coincidental deployment of a regional array was completed on 16 June 2011. Following the eruption, NERC funded the urgency grant: NE/J012297/1, for a rapid deployment of a local seismometer array. To enable this, SEIS-UK loaned 8 broadband seismometers, five CMG6TD and three CMG40TD, for a period of 14 months. The stations were deployed in August 2011 by James Hammond and others through collaboration with Eritrea Institute of Technology, the Department of Mines and Energy and the Southern Red Sea Regional Administration. The stations were serviced twice over the following 18 months: in October 2011, and May 2012, before being decommissioned in October 2012. The stations were situated around Nabro with a 20 km array aperture. Choosing sites to the south west of Nabro was problematic due to the proximity to the disputed border with Ethiopia; close collaboration with the Eritrean government and regional agencies was essential for the safe and successful completion of the project.

The network was fully operational by 31 August 2011, 79 days after the eruption began. The first data download, completed on 7 October 2011, provided the 38 day data set used in this study. The total 14 months of data are now archived on the SEIS-UK system and will be publicly available from 14 October 2015. NAB6 (40TD site) was damaged due to flooding and at NAB5 (6TD site) the GPS failed, therefore data recorded at these stations were not used in this study. NAB7 also had timing issues, but data from this station was used for focal mechanism determination. In addition to the local network on Nabro, data recorded by FAME a Güralp 3ESP seismometer, installed in the nearby village of Afambo was also used. This seismometer is located approximately 35 km north west of the caldera and is part of the Eritrean regional array. The resulting array configuration is depicted in Figure 2.1.

All local array seismic stations have a natural response period of 30 s, whereas FAME has a natural response period of 60 s. The initial sampling rate of the station was 100 Hz, this was reduced to 50 Hz during the October 2011 servicing to decrease the memory required by the system. The data have a high signal to noise ratio due

to a favourable recording environment; the noise levels are low as the equipment was located in small villages, sheltered from the wind and far from ocean noise.

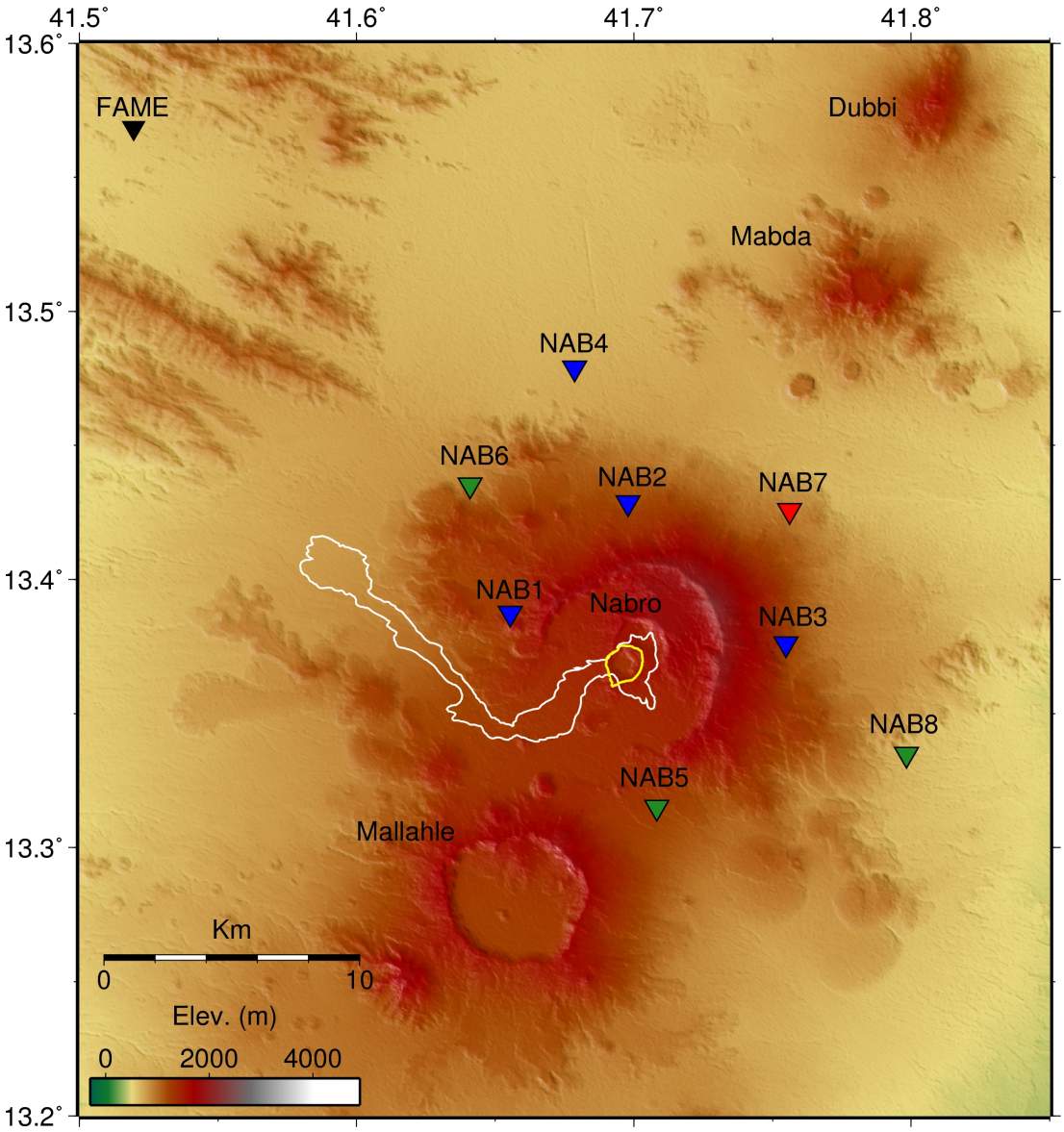

Figure 2.1: ASTER G-DEM topographic map of Nabro volcano. Inverted triangles show the configuration of seismic stations used for the analysis. Green: 40TD Güralp seismic stations. Blue: 6TD Güralp seismic stations. Red: 6TD Güralp seismic station used for focal mechanism analysis only. Black: 3ESP seismic station, part of a regional array. White outline: 2011 eruption lava flow. Yellow: 2011 eruption vent region.

2.2 Seismic Analysis

2.2.1 Hypocentre locations

I manually picked arrival times of P and S phases at every seismic station for each distinguishable earthquake using SAC software (Goldstein and Snoke, 2005). I found that the traces did not need to be filtered before analysis due to the high data quality. I assigned a quality value of 0, 1, 2, 3 to the measurement, based on an estimated P-wave arrival time error of 0.05, 0.1, 0.15 and 0.2 s, respectively. For S-waves, the 0 to 3 quality values were assigned to values of 0.1, 0.175, 0.25 and 0.3 s, for the estimated error in arrival time (Figure 2.2).

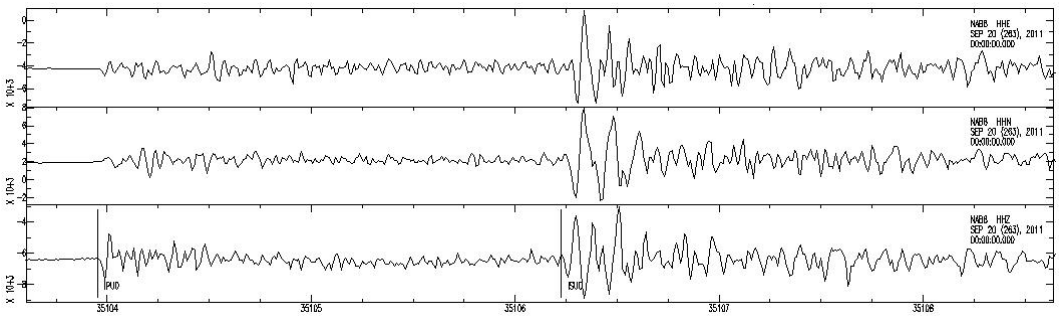

Figure 2.2: Trace display in SAC2000. One event at one seismic station is shown in the Z, N and E components. Both the P- and S- wave arrivals are picked on the Z component. However, the N and E components are used to help guide the position of the S- wave pick. This is an example of an event with a clear P- and S- wave onset, and have therefore been assigned a high weighting for the HYPOINVERSE program.

The assigned values were used as weights in the location inversion performed by the Hypo2000 algorithm (Klein, 2002) (Figure 2.4). All of the events recorded can be defined as VT earthquakes based on the criteria set by Lahr et al. (1994) as they have clear P and S wave arrivals, with an average peak frequency of 7 Hz. During the 38 day recording period I detected a total of 658 earthquakes on Nabro caldera and in the surrounding area.

I used the algorithm HYPOINVERSE2000 (Hypo2000) (Klein, 2002) to determine the hypocentre locations of each picked event. This program solves for the hypocentre locations by converging on a point which minimises the RMS travel-time residual. The program requires a 1D velocity model. I used values based on a controlled source, crustal scale reflection and refraction survey performed across the Danakil block by Makris and Ginzburg (1987). This homogenous layer velocity model is given in Table 2.1.

Layer	Depth (km)	Velocity (ms^{-1})
1	0-3	4.1
2	3-8	6.1
3	8-25	6.8
4	> 25	7.4

Table 2.1: 1D velocity model

The last layer in the model defines the homogeneous half space, which is the mantle in this case. I used TTGEN, a subprogram of Hypo2000, to create a travel time table so that the velocity smoothly increases between the defined boundaries (Lahr, 1989)(Figure 2.3). This removes the potential for artificial clustering of earthquakes at velocity discontinuities, an artefact often observed in velocity models with homogeneous stepped layers. The V_P/V_S velocity ratio is 1.8, which is slightly lower than that found in the centre of the ARZ where $V_P/V_S > 2.0$, indicative of abundant partial melt in the crust (Stuart et al., 2006).

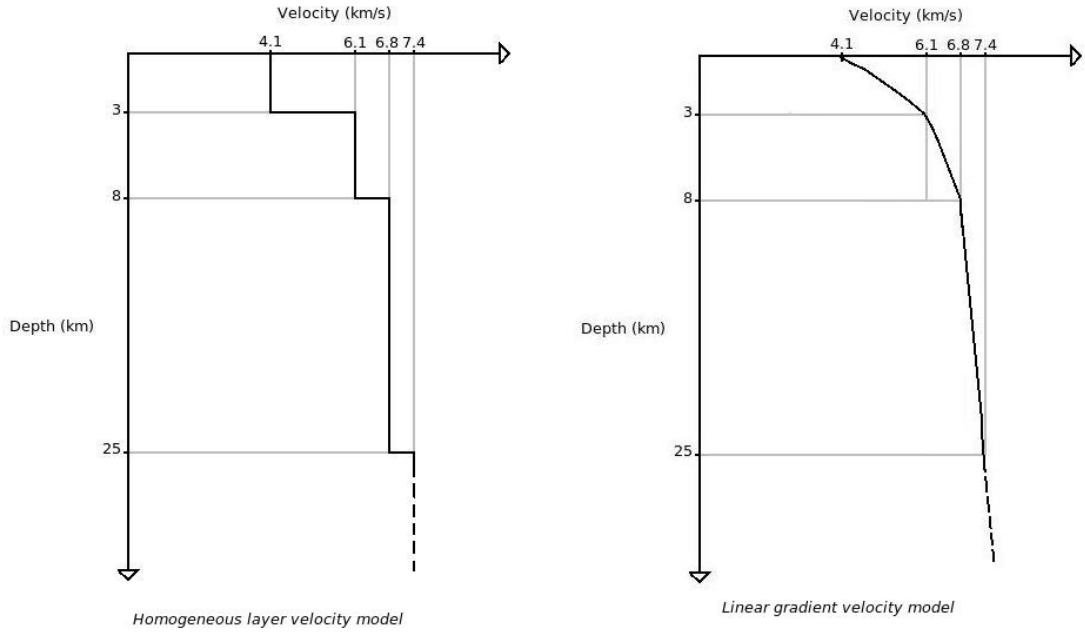

Figure 2.3: Illustration of the initial velocity model input into HYPOINVERSE (LHS), and a schematic of the velocity model output from the TTGEN computer program and subsequently input into HYPOINVERSE.

The depths calculated are referenced to 1035m a.s.l, the average elevation of the seismometers. The average location error using this technique is ±2 km in horizontal

directions, ±4 km in depth. The large errors reduce confidence in interpretations of features of the magmatic plumbing (Jones and Stewart, 1997). The errors result from a combination of factors including, the heights of the station locations, available phases, accuracy of the arrival time measurement and the validity of the velocity model (Waldhauser and Ellsworth, 2000). HypoDD assumes a flat earth, but there is an option to add delays to an individual station to simulate topography. I chose not to use station delays as the highest station is only 294 m above and the lowest station 380 m below the assumed surface, which will not make a significant difference to the overall locations. As I manually picked the arrival times, the measurements are susceptible to human error; such as the number of events seen and the arrival time picked. However, as I picked all the events myself I assume that the events were picked systematically. Also, in some instances it was not possible to pick both the P and S wave arrivals for every event at every station so some events will be better constrained than others. The velocity model is the governing parameter which controls the ultimate locations of the hypocentres. The velocity of a seismic wave beneath an active volcano varies in 3 dimensions due to changes in rock composition along the ray path and the presence of partially molten bodies. In addition, the subsurface velocity structure may also change through time as partially molten bodies evolve.

Relocations

I minimised the dependence of the hypocentre locations on the velocity model by relocating the events determined by Hypo2000 with the double differencing technique HypoDD (Waldhauser and Ellsworth, 2000, Waldhauser, 2001). Differencing techniques are based on the actuality that rays from two closely spaced hypocentres travel along near-identical paths to reach the seismometer, therefore the difference in their travel times is solely dependent on the spatial offset between the sources. The HypoDD algorithm additionally computes the residual between the theoretical and observed arrival times for a pair of earthquakes. The travel time residuals are then minimised using a weighted least squares method to alter the location and timing of each event (Waldhauser and Ellsworth, 2000) (Figure 2.5).

The paired events are controlled by parameters that describe the search area around an event which may link it to another. The pairs have to pass minimum thresholds, such as the minimum number of station observations, to be deemed stable to use in the

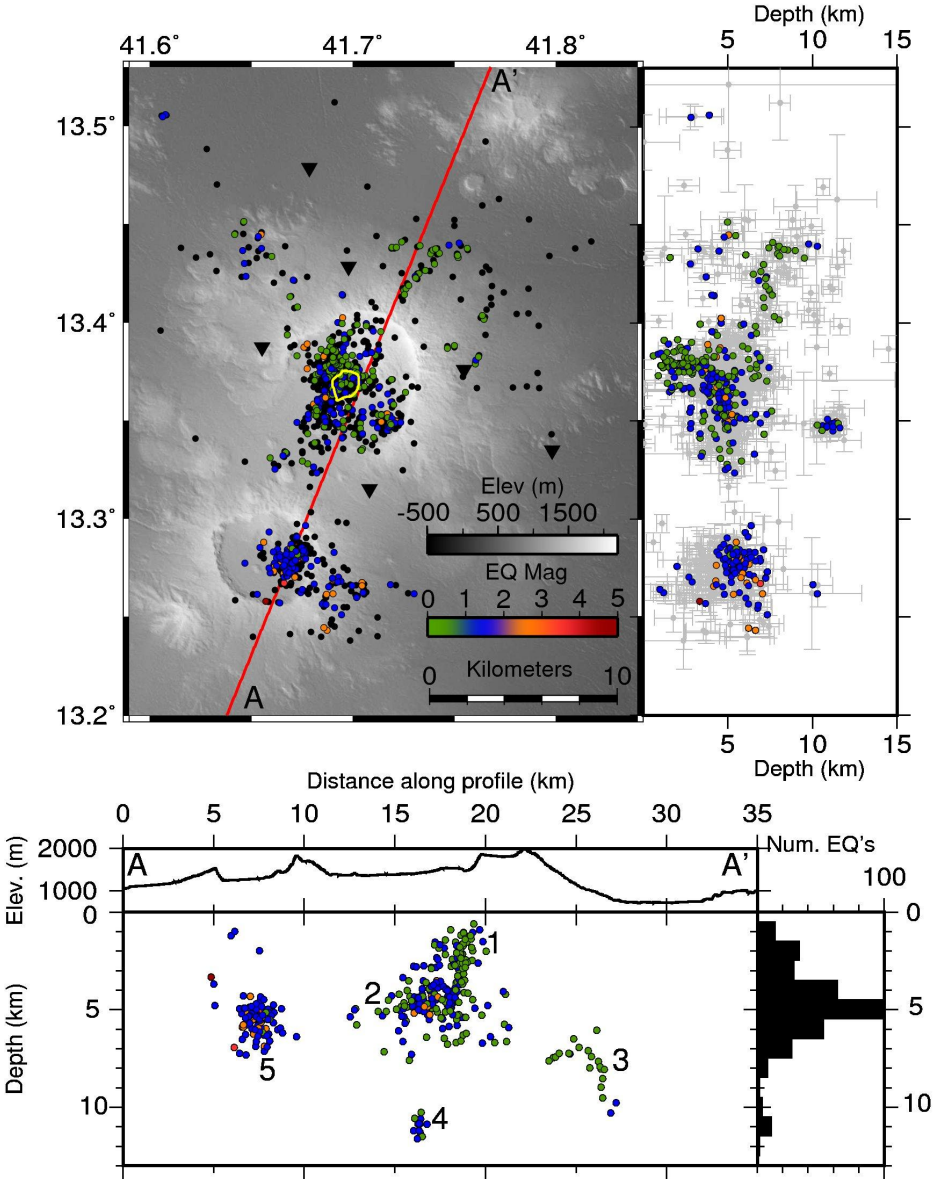

Figure 2.4: Top: Initial hypocentre locations determined using Hypo2000, for the 658 earthquakes detected during the period 31st August-7th October 2011, shown as black dots (map view) and grey dots with error bars (N-S depth profile). The position of 456 relocated hypocentres calculated by HypoDD are shown as coloured dots, dependent on M_L. Seismic stations used to locate the events are indicated by black triangles. Yellow outline highlights the vent region. Bottom: Topographic profile and hypocentres along transect A-A', determined by HypoDD within 1 km either side of the transect. The depths are given referenced to 1000m a.s.l. The histogram shows numbers of hypocentres at depth per 1km bin. Numbers indicate clusters as described in the text.

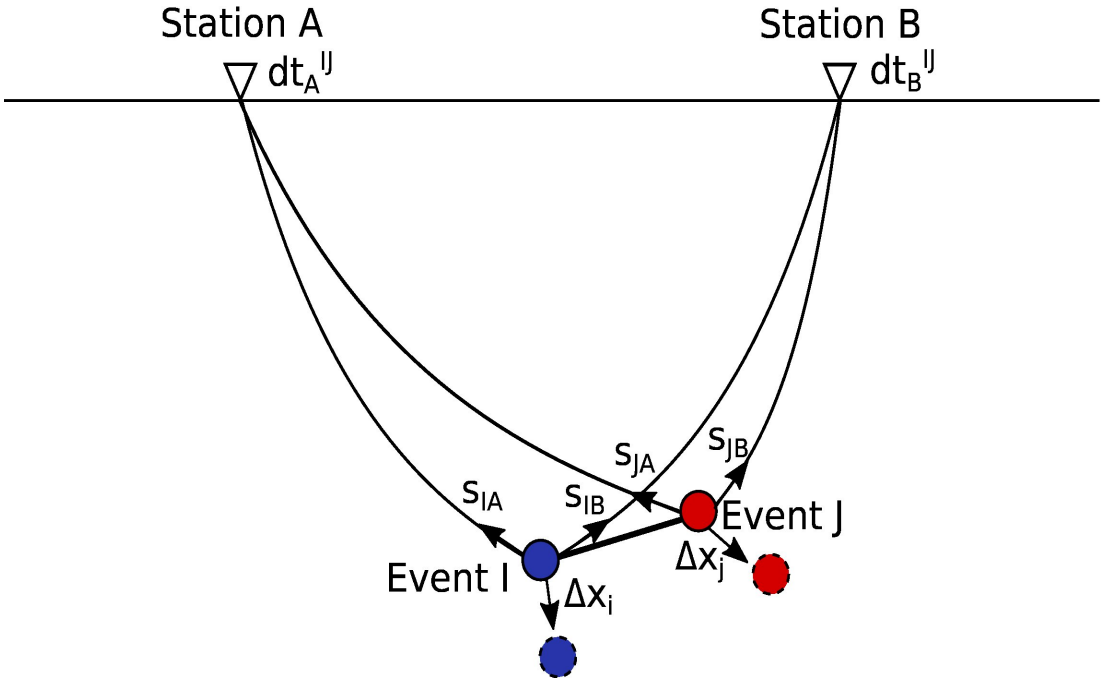

Figure 2.5: Schematic of the HypoDD algorithm after Waldhauser and Ellsworth (2000). The intial Events I and J (solid circles) are paired and each relocated (dashed circles) by Δx, based on their travel time difference at stations A and B (d_{AB}^{IJ}). The slowness (S) are also shown. For the full inversion formulae see Waldhauser and Ellsworth (2000).

subsequent inversion. These pairs are then grouped into clusters before the inversion which considers each cluster individually. I parametrised the relocation procedure in order to relocate the maximum number of events whilst minimising the allowed separation between the initial hypocentres. In this manner, 456 of the initial 658 earthquakes were relocated. 202 events were removed from the inversion because their initial location was too far away from the rest of the earthquakes or they could not be paired in accordance to the specified thresholds. See Appendix A for a full description of HypoDD and the inversion parameters used.

Event locations after relocating with HypoDD are overlain on the Hypo2000 results in Figure 2.4. The relative error of the relocated earthquakes is ± 40 m in depth and ± 16 m in the horizontal direction. Five clusters are visible in the spatial distribution of the earthquakes (Figure 2.4): (1) Directly beneath the vent, there is an elongate, sub-vertical cluster extending between 1-4 km depth. (2) Cluster is located beneath the central and southern part of the caldera, it is sub-horizontal with the seismicity deepening to the south-west, the cluster is ∼5 km long and between 4-5 km deep. (3) Beneath the NE flank of Nabro, there is a NE striking cluster which deepens to the

north, it is 6-11 km deep. (4) Beneath the SE caldera wall, 16 earthquakes are between 10 and 12 km deep. (5) Cluster lies directly beneath Mallahle, the hypocentres form a spherical cluster ranging between 4 km and 7 km deep. There is a noticeable aseismic zone between Nabro and Mallahle calderas.

2.2.2 Magnitude and *b*-value determination

Local magnitudes (M_{L}), as originally defined by Richter (1935), were computed using the maximum body wave amplitude of the horizontal component seismograms after they are convolved with the standard Wood-Anderson response (Anderson and Wood, 1925, Kanamori and Jennings, 1978). The computation also considers the distance between the earthquake and stations in a distance correction term, which allows for decrease in amplitude with distance due to geometrical spreading. I used the correction term derived for the Main Ethiopian Rift (MER) by Keir et al. (2006b). This correction is applicable to the high ground motion attenuation conditions, caused by high heat flow due to the presence of partial melt beneath the rift valleys in the region (Gass, 1970, Keir et al., 2011). I used M_{L} estimates to calculate the seismic moment release using empirical relationships, e.g. Kanamori (1977), following the method of Keir et al. (2011).

I determined $\mathrm{M_L}$ that range between -0.37 and 4.5, for all 658 earthquakes located using Hypo2000. The magnitudes of the relocated earthquakes are shown in Figure 2.4. The majority of earthquakes beneath Mallahle have a magnitude between 1 and 2, (Figure 2.6). Most of the events with a magnitude between 0 and 1 are located beneath Nabro. The lower magnitude threshold beneath Nabro is likely due to the fact that the stations are nearer to the hypocentre. In order to see how magnitudes are distributed and establish cut-off magnitudes, I used the Frequency-Magnitude Distribution (FMD) (Gutenberg and Richter, 1944):

$$\log N = a - bM_{\mathrm{c}}, \tag{2.1}$$

where N is the cumulative number of earthquakes with a magnitude equal to or greater than M, a is a constant describing the rate of seismic activity in the study area, and b is the gradient of the FMD plot (known as the b-value). M_{c}, also known as the 'cut-off' magnitude, is the smallest magnitude of earthquake to which the catalogue is complete, this is determined by the network sensitivity. As Equation (4.1) uses only the maxi-

mum observed magnitude, the resulting b-value tends to be an underestimate (Bender, 1983). Therefore, as the data only spans a short period, I used the maximum likelihood formula (2.2) as derived by Utsu (1965) to calculate the b-value,

$$b = \frac{\log_{10}\mathrm{e}}{M_\mathrm{a} - M_\mathrm{c}}, \tag{2.2}$$

where M_a is the average magnitude and M_c is the cut-off magnitude. Previous works by Bridges and Gao (2006) and Sanchez et al. (2004) show how spatial variations in b-values can provide constraints on the distribution of magma in the subsurface. Therefore, I found separate b-values for the events on Nabro and those on Mallahle (Figure 2.6). The b-value was determined for Nabro using values of M_a =1.86 and M_c =1.52, and for Mallahle using M_a =2.62 and M_c =1.82. For all detected seismicity on Nabro, b =1.3±0.08 and for the events beneath Mallahle b =0.97±0.15 (Figure 2.6). The difference in cut off magnitude between the two calderas is due to the siting of seismic stations solely on Nabro.

2.2.3 Focal mechanisms

Focal mechanisms describe the type of movement during an earthquake as a pair of planes at 90°. The mechanism is determined from the distribution of positive or negative initial particle motions of the P and S_h arrivals (Figure 2.7). Choosing between the actual fault plane and the auxillary plane requires additional observations and geological information. So far I have described the post eruption seismicity in terms of location and magnitude. By calculating the focal mechanisms of multiple events I will be able to interpret how the crust is responding to the changing stress conditions of the local region (Aspinall et al., 1998, Vargas-Bracamontes and Neuberg, 2012)..

I computed lower hemisphere projection focal mechanisms to constrain the orientation of crustal strains using FOCMEC (Snoke, 2003). The program uses the station location relative to the hypocentre, take off angles, and P- and S_H-wave polarities to perform a grid search for the best fit double couple solution (Snoke, 2003, Ebinger et al., 2008). Using an incremental step of 10°, all computed fault plane solutions have an error of $\leq \pm$ 20° in strike and dip of the nodal planes (See Appendix A for further details). I was able to estimate 46 fault plane solutions beneath Nabro's caldera. I could not determine solutions for events away from the caldera due to the configuration of seismic stations. Data from the seismic station with a failed GPS system (NAB7)

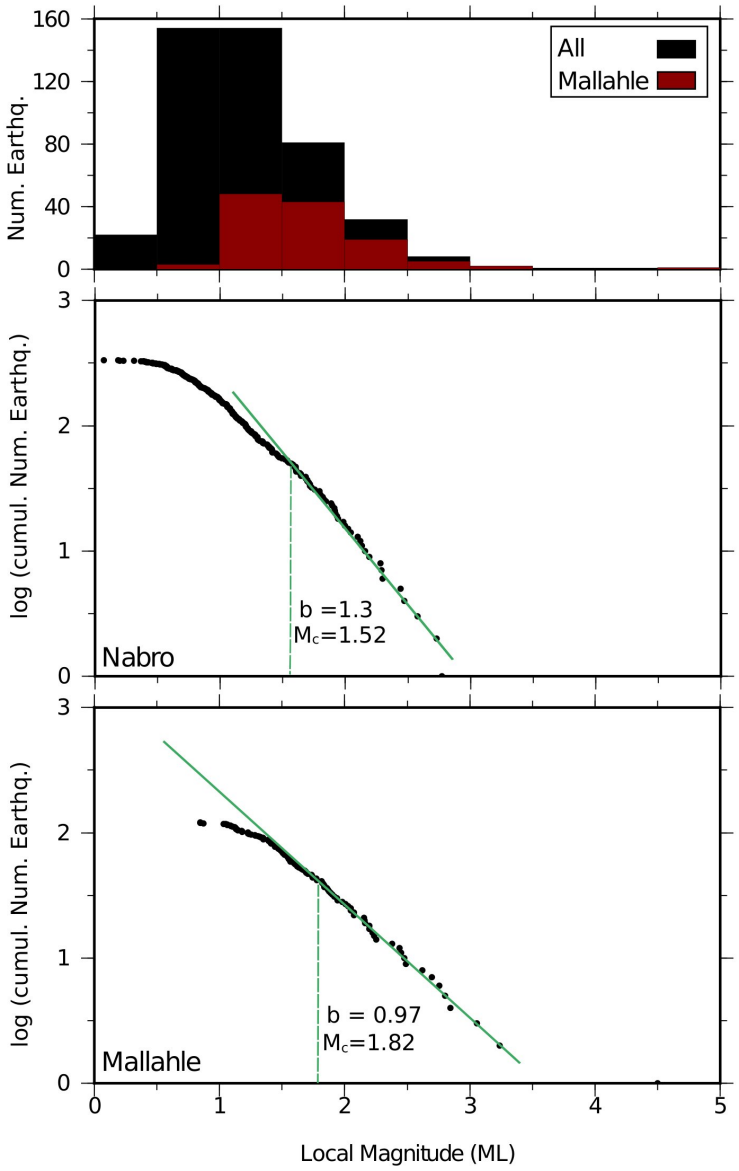

Figure 2.6: For all 658 events. Top: Distribution of the number of earthquakes with magnitude. Black shows the distribution for all hypocentres, red shows the distribution for those which occurred below the Mallahle caldera. Middle: Gutenberg-Richter distributions of the relocated earthquakes below Nabro. Bottom: Gutenberg-Richter distributions of the relocated earthquakes below Mallahle. Green line shows *b*-value. Dashed Line marks the cut-off magnitude.

were included in the data set as the arrival time of the wave was not relevant for this analysis, but the position of the station was useful for determining the strike of the nodal planes.

I computed focal mechanisms for 46 events beneath Nabro's caldera of which 6 were normal, 33 were thrust and 4 were largely strike slip motions (Figure 2.8). A prominent feature is a series of 18 thrust mechanisms with nodal planes striking NE-SW located in

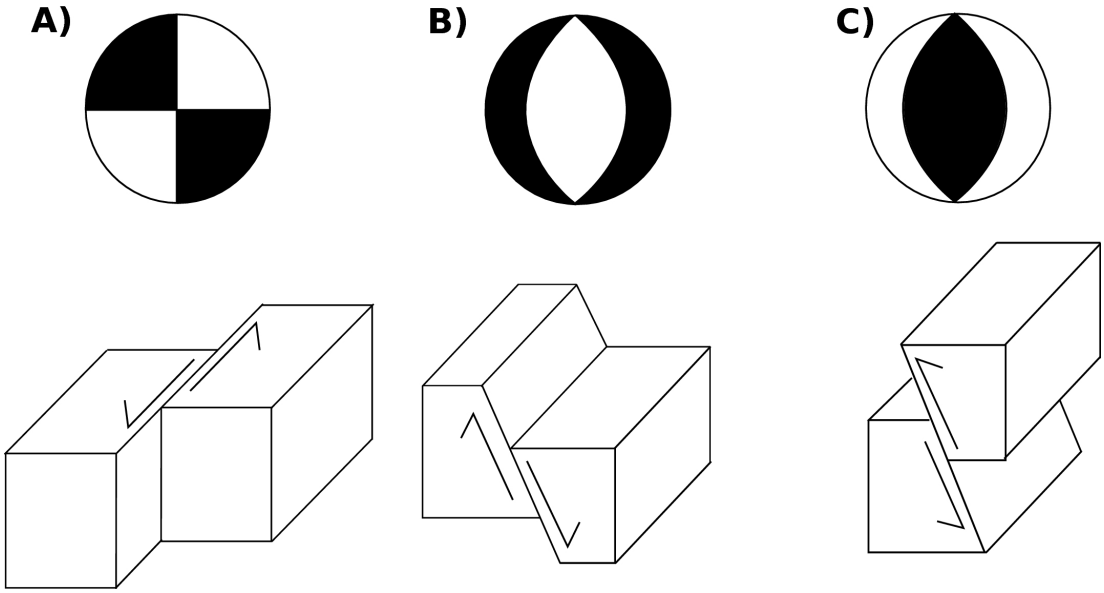

Figure 2.7: Focal mechanism (Top) which results from basic fault slip illustrated (Below), for A: strike-slip faulting, B: Normal faulting and C: Thrust faulting. The shaded segments indicate compression (postive first motion).

the centre of the caldera, under the vent, which occur throughout the recording period at a depth between 4 and 5 km (Figure 2.8 (highlighted in bold), and Figure 2.9). In this region, there are 3 thrust mechanisms with a variety of nodal plane orientations; one striking northwards and 2 with nodal planes striking ESE-WNW. Also in the centre of the caldera, only one solution indicates normal faulting, the nodal planes strike SE-NW. Away from the centre of the caldera, only 9 of the 46 focal mechanisms have a major normal faulting component, 4 of which are located within the deep seismic cluster (4)(Figure 2.4). Due to the seismic network configuration, the focal mechanism of events beneath Mallahle caldera could not be constrained.

2.2.4 Waveforms

In order to test whether different earthquakes located close to each other were generated by the same slip motion on the same fault, I used the criteria of waveform similarities of earthquake pairs. Earthquake waveform pairs that have a significant similarity, expressed by a correlation coefficient greater than 0.7, are produced by the same source mechanism (Pechmann and Kanamori, 1982) and located within a distance of a 1/4 wavelength of each other (Geller and Mueller, 1980). Also, the earthquakes must propagate through the same subsurface, so time-dependent correlation decreases can highlight changes in the shallow crust. I have chosen 8 pairs of earthquakes to per-

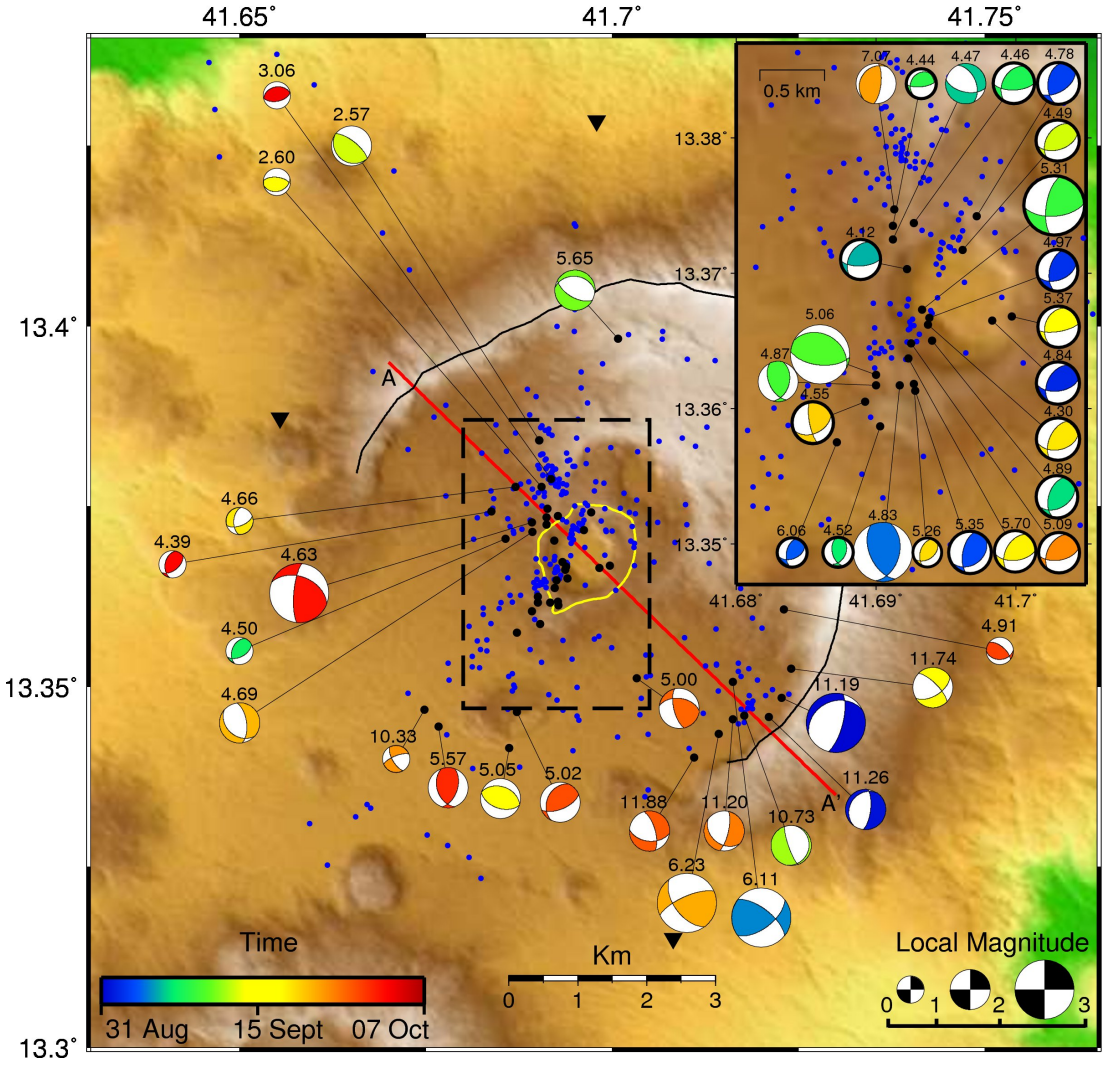

Figure 2.8: Lower hemisphere fault plane solutions for 46 earthquakes below Nabro; the location of the corresponding hypocentre is shown as a black dot. The size of the fault plane solution is scaled to the local magnitude of the event, and the depth at which it occurred is reported (in km) above the focal mechanism. All other earthquakes in the region are depicted with a blue dot. The colour of the compressional quadrant of the solution is related to the time of the event. The 2011 eruption vent region is outlined in yellow and the caldera rim is outlined in black. Inset: Zoom of the vent region with focal mechanisms. 18 thrust mechanisms are outlined in bold.

form the cross-correlation, whose hypocentres are located within 215 m of each other, which is a 1/4 wavelength distance for these waveforms and all have the same focal mechanism. I have summarised the time gap between each pair and the correlation coefficient at seismic stations NAB1 and NAB7 in Table 2.2. The table shows that waveforms recorded at NAB7 stay correlated for days to weeks before the correlation coefficient decreases significantly. This suggests that the shallow subsurface is evolving over time. However, the arrivals for the same events at NAB1 are not well correlated.

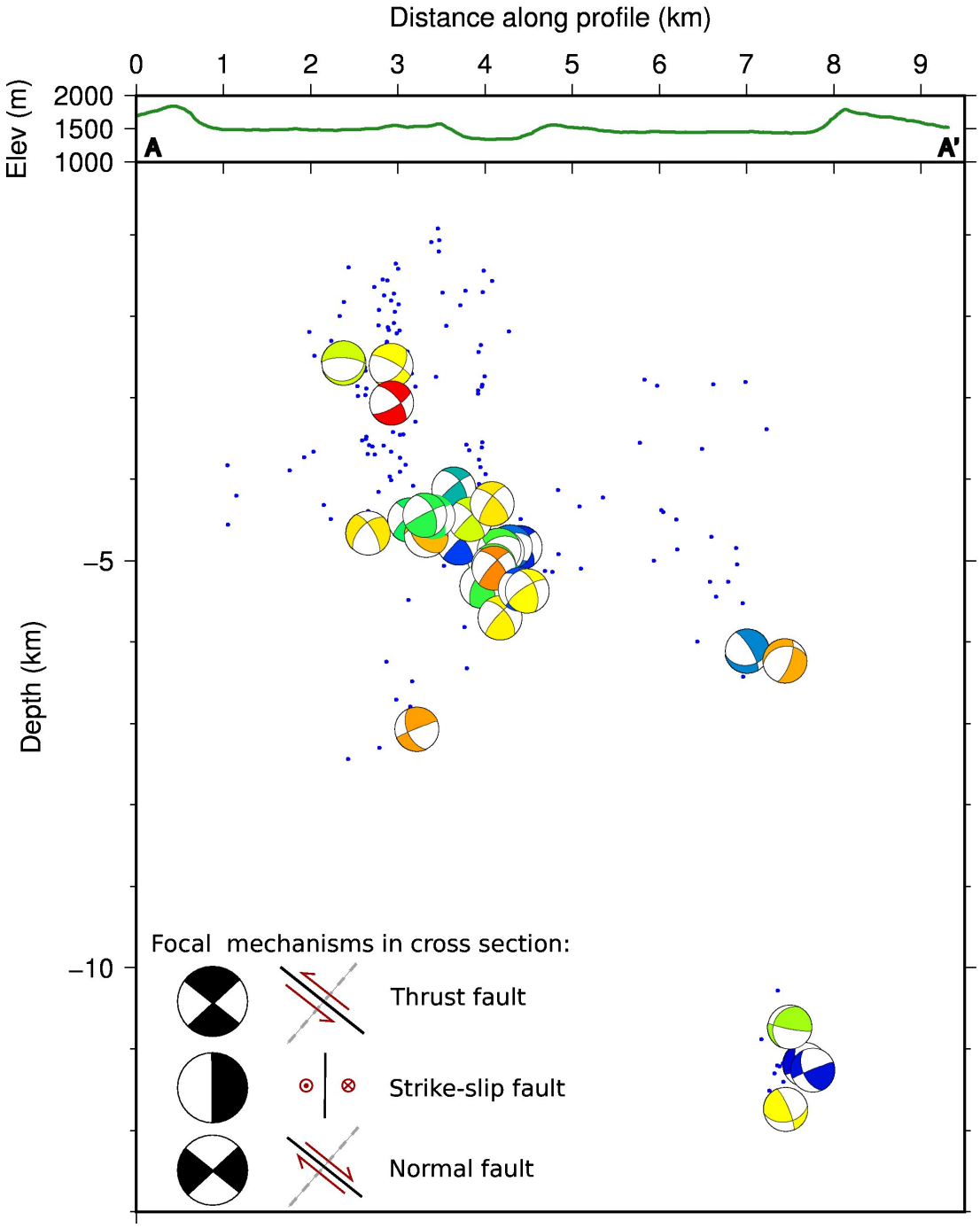

Figure 2.9: Top: Topography of Nabro along transect A-A'. Bottom: All focal mechanisms have been projected on to transect A-A' (Figure 2.9), then rotated to a side view, as viewed from south west to north east.

The significant decorrelation has occurred at NAB1 as it is located perpendicular to the trend of events, unlike NAB7 which is along strike. The relative locations of the earthquakes to the stations has caused large differences to the subsurface path each earthquakes takes despite meeting the criteria outlined by (Pechmann and Kanamori,

1982) and Geller and Mueller (1980).

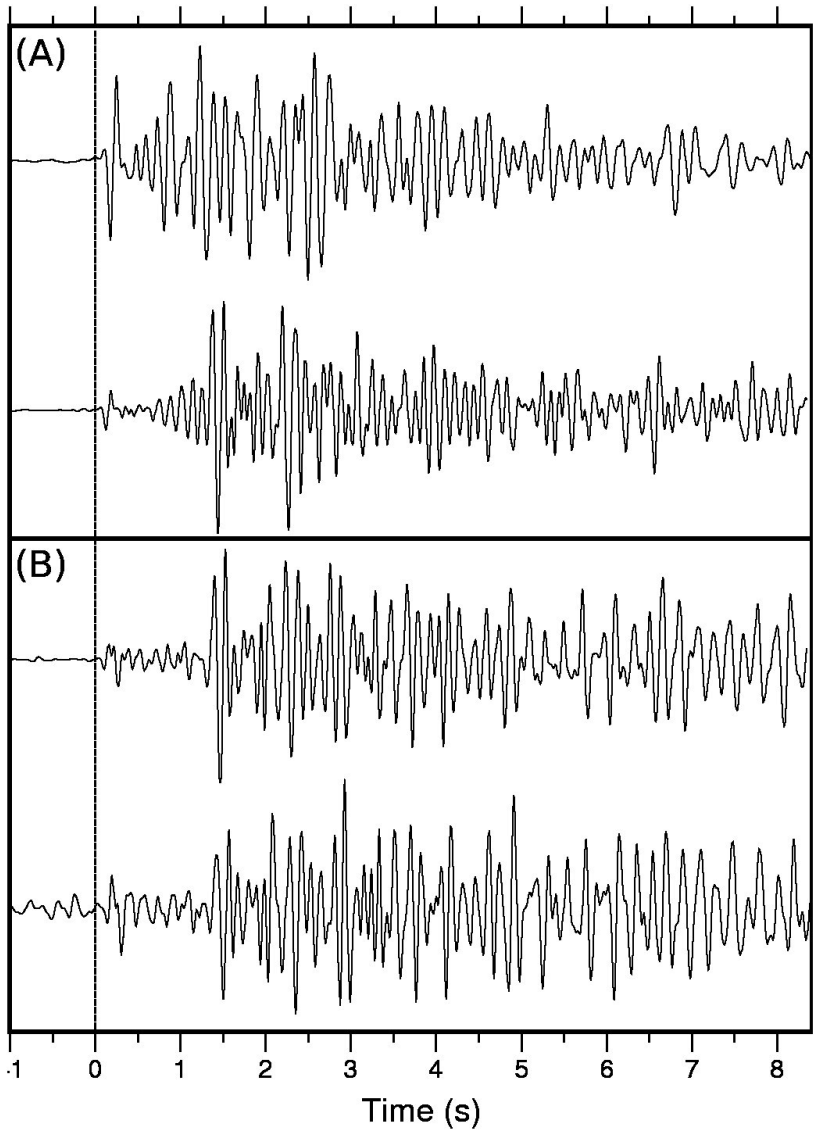

Figure 2.10: Examples of waveforms with a bandpass filter between 2 and 10 Hz applied. The hypocentres of the pairs are located within 215m of each other. A: Waveforms of earthquakes temporally separated by 22 days, with cross correlation of 0.20. B: Waveforms of earthquakes temporally separated by 10 min, with cross correlation of 0.84.

2.2.5 Temporal variations

The daily number of earthquakes (Figure 2.11A) varied between 4 and 33 during the 38 day recording period. Figure 2.11B shows the original 658 earthquakes, which contributed 76 $\times 10^{15}$ Nm seismic energy release. The largest release of seismic energy can be attributed to an event with a magnitude > 4. When this event is removed from the analysis (Figure 2.11C) it can be seen that the seismic moment release increased by

Time gap	NAB1 Coef.	Nab7 Coef.
10 minutes	0.5562	0.8
15 Hours	0.2451	0.9376
4 Days	0.3385	0.9602
4 Days	0.1839	0.9546
5 Days	0.2190	0.8454
8 Days	0.2609	0.7219
22 Days	0.1098	0.2073

Table 2.2: Correlation coefficients for earthquake pairs at NAB1 and NAB7.

between 0.2 and 0.4 $\times 10^{15}$ N m steps every 6 -10 days with a linearly increasing moment release between each step. These linear increases with discrete steps were observed on both Nabro and Mallahle calderas. These step increases in moment magnitude correspond to earthquakes with $M_L \geq 2.7$ (Figure 2.11). Figure 2.11D shows the seismic energy release from the events on Nabro only, these show the same trend as that observed in Figure 2.11C. There appears to be no consistent temporal pattern in the spatial distribution of events.

2.3 Summary

The spatial pattern and sporadic nature of the hypocentres located at shallow depths (less than 6 km) under Nabro, are likely caused by the episodic fracturing of brittle rocks within the volcanic edifice (Dzurisin et al., 1991, 2002), in response to the depletion of the magma chamber. The temporal pattern of earthquake hypocentres has previously been used to show the migration of magma preceding and during eruptions (Tarasewicz et al., 2012). However, beneath Nabro the seismicity recorded by the local array does not necessarily show this migration of magma to the surface, rather it shows the constant reactivation of already developed faults. Using the spatial distribution of the hypocentres, I assume the region of brittle failure is immediately above the magma chamber, which fractures to accommodate the volume change. Therefore, the residual magma body is situated in the aseismic zone immediately below centred at a depth of approximately 7 km. As discussed in section 1.4, the existence of a clearly defined magma chamber beneath volcanoes is debated. Seismicity only indicates those areas that are able to deform in a brittle manner and have been stressed appropriately. The aseimic zone under Nabro is indicative of a magma reservoir but the seismicity alone

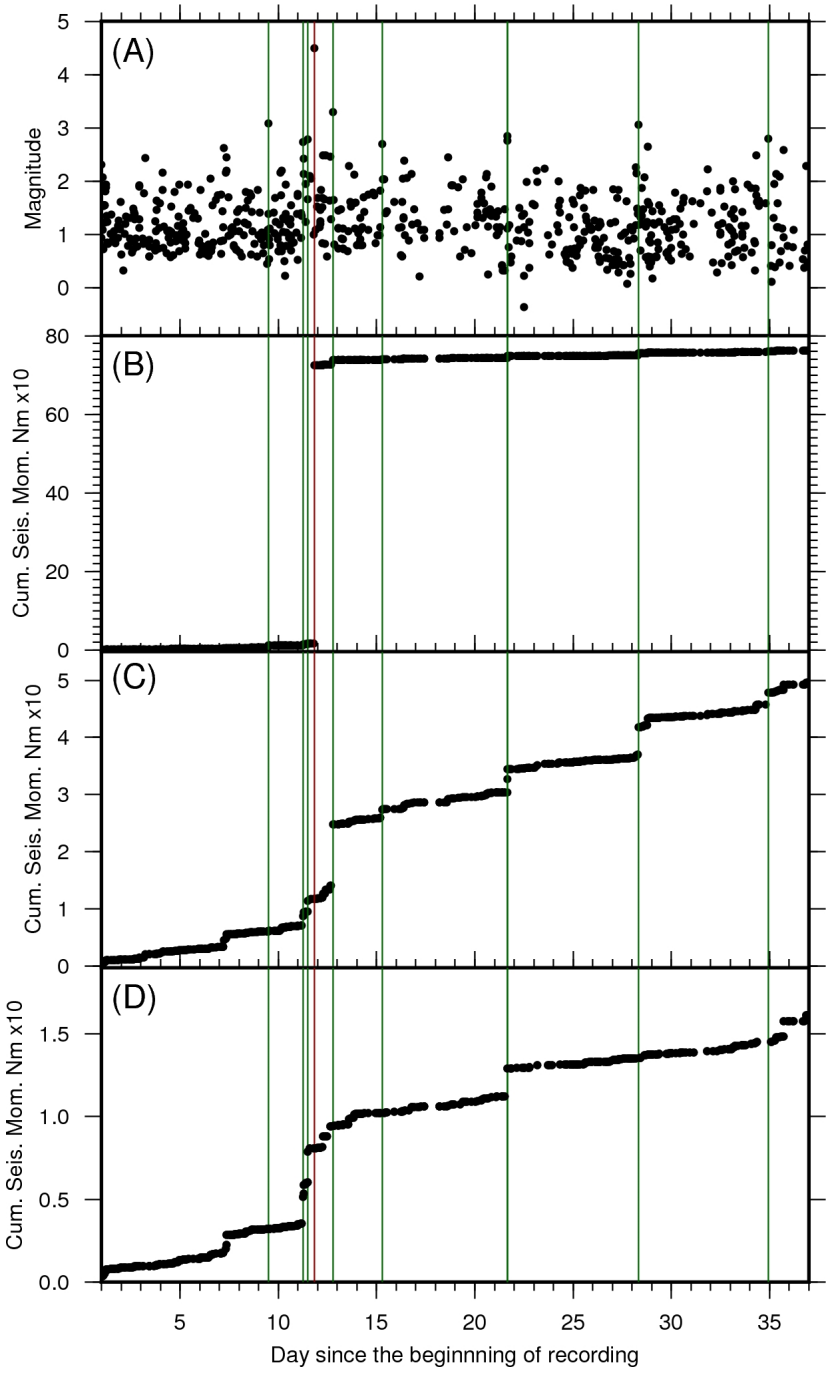

Figure 2.11: A: Magnitude of 650 Hypo2000 located earthquakes over the 38 day recording period. B: cumulative seismic moment release of all earthquakes over the recording period. C: cumulative seismic moment release with the largest event removed. D: Cumulative seismic moment for earthquakes under Nabro only. Red line highlights time of M_L4.5 event which was removed from the analysis in C and D. Green lines highlight times of earthquakes with $M_L \geq 2.7$.

can not delineate the geometry of the magma source. Perhaps the the lack of seismicity in this region suggest magmatic mush and multiple storage zones which can not be

delineated. The deep cluster of seismicity (cluster 4 Figure 2.4) directly beneath this region may be related to small-scale fracturing around a constricted part of the plumbing system, potentially linking the shallow sources to a deeper reservoir, similar to an interpretation of lower-mid crustal seismicity at Eyjafjallajökull volcano (Tarasewicz et al., 2012).

b-values describe a region's ability to accumulate stress and the average global *b*-value is approximately 1.0 (Richter, 1958). However, *b*-values can vary between regions as different geomechanical properties influence the ability of rock to accumulate stress. Low *b*-values indicate that a region is capable of accumulating significant stresses, which can result in large earthquakes. Areas with an increased thermal gradient (Warren and Latham, 1970) can be associated with a weak rheology, which cause small magnitude stress changes that tend to favour small magnitude earthquakes. The lower *b*-value for Mallahle implies that the earthquakes generated here are not dominated by magmatic processes and occur in rock with a stronger rheology. Therefore, the seismicity I observed is due to changes in the stress field resulting from the subsidence at Nabro, and not caused by magma movement beneath Mallahle. However, a connection between the two calderas may have existed in the past. Also, the large magnitude ($M < 4$) VT earthquakes which occurred beneath Mallahle suggest that pre-existing faults have been brought closer to failure, due to stress changes following the magma reservoir depressurisation (Wauthier et al., 2013a). I interpret seismic cluster 3 to also be a result of the stress change, where the linear structure implies a fault which has been created or reactivated due to the new distribution of stress. I cannot constrain the focal mechanisms of these events as they are located outside the seismic array. The *b*-value I calculated on Nabro is higher, likely due to a relatively weaker rheology, the presence of fluids and melt, the presence of highly fractured rock typical of heavily faulted calderas and a higher geothermal gradient associated with the magma reservoir.

2.3.1 Modes of caldera subsidence

The structure and evolution of calderas provide information on the behaviour of the magma reservoir, and therefore understanding their geometries is crucial for predicting future activity (Cole et al., 2005, Acocella, 2007). I can compare the mode of subsidence implied by the focal mechanisms to models of caldera response. The seismic data reveal fault structures in the shallow subsurface (less than 6 km deep), the magnitudes of the

earthquakes which delineate the fault have a maximum magnitude of 3. I also assess the temporal evolution of these faults through interpretation of the cross-correlated waveforms. In Figure 2.9 a thrust fault is observed to cross cut the caldera floor, 1 km above the centre of the magma source. Since the focal mechanisms define a 45^{o} dip along one of the nodal planes (Figure 2.9), I infer that a fault plane strikes NE-SW, dipping 45^{o} to the SE. I can compare this faulting to both numerical modelling performed by Holohan et al. (2011) and analogue models (Lavallée et al., 2004, Kennedy et al., 2004, Roche et al., 2000) to provide further insights into the mechanisms of subsidence. Holohan et al. (2011) used a 2-dimensional finite element method to model the caldera subsidence in a half space with a range of geomechanical properties. I qualitatively compared Figure 2.9 to Figure 5c in Holohan et al. (2011) (shown here as Figure 2.12), and found similarities such as the dip and motion of the fault plane and its position relative to the magmatic body. Using the terminology of Holohan et al. (2011), my results could also be described as 'reverse fault that separates two inward rotated roof blocks'. Quantitatively, the model I refer to would require the ratio between the thickness and diameter of the roof to be less than 0.33. Assuming the seismicity under Nabro highlights the brittle failure of the roof, I find this ratio is between 0.69 and 0.88. As Nabro's caldera is already well established, the fault plane I observe may have existed prior to the eruption and has been re-activated. This may explain the presence of the fault despite the higher ratio between the thickness and diameter of the roof. Furthermore, I observe a linear increase in the seismic energy release interrupted by large instantaneous releases from higher magnitude ($M_L \geq 2.7$) events that occur on a week time scale under Nabro, which is consistent with the findings of Ruch et al. (2012) that incremental collapses can occur on mature faults during caldera collapse. In the absence of appropriate measurements for bulk porosity, bulk density and Youngs modulus for rocks at Nabro, the benefit of further quantitative application models such as that of Holohan et al. (2011) is limited.

Ring faults are a common feature of a caldera collapse (Marti et al., 1994, Cole et al., 2005). However, the hypocentres I located are not concentrated on the caldera walls, implying that these structures may not have been activated during the eruption, which is not uncommon (Kennedy et al., 2004). In addition, the fault plane solutions of those found in the vicinity of the caldera walls are not tensional (Figure 2.9). The modelling by Holohan et al. (2011) shows an upwards migration of faulting, therefore the

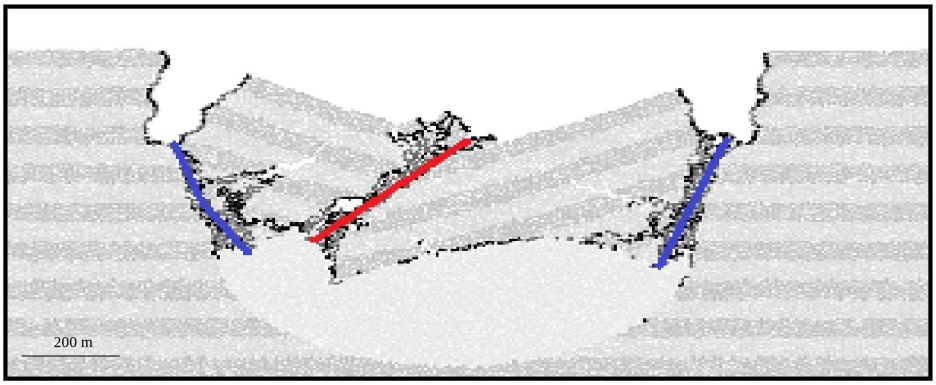

Figure 2.12: Adapted from Holohan et al. (2011). 2D finite discrete element method model of caldera collapse following 50% magma chamber depletion. Striped region: simulated crust isotropic homogeneous medium with no pre-existing near surface structure. Light grey: simulated magma chamber which undergoes depressurisation. Blue: Induced Normal faulting. Red: Induced reverse faulting.

hypocentre locations are expected to migrate towards the surface over time. However, as no such pattern is observed within seismic cluster 1, the faults are assumed to have been formed before the local seismic array was deployed, and I only observe their sustained reactivation as the caldera relaxes. By comparing the waveforms of two pairs of earthquakes with adjacent hypocentres on the same fault plane, but with each pair having a different temporal separation, I find a distinct decrease in correlation over time. This suggests that subsurface structures were evolving, even during the recording period.

Chapter 3

Measuring post eruptive ground deformation using InSAR

Over the last 20 years Interferometric Synthetic Aperture RADAR (InSAR) has become an established remote sensing tool for quantifying ground displacement (Bürgmann et al., 2000). Satellite mounted SAR can measure ground displacement with millimetric precision at high resolution, with an extensive spatial coverage, making InSAR a unique tool for geophysical monitoring. Combined with the ability to task satellites to monitor suddenly active areas, these qualities have enabled InSAR to aid the interpretation of magma plumbing systems at volcanoes across the world. Biggs et al. (2014) reported that 198 volcanoes have been systematically monitored by InSAR between 1992 to present, four times more than the number of similar deformation studies undertaken before the late 1990s (Dvorak and Dzurisin, 1997, Pinel et al., 2014). SAR capable satellites provide systematic observations of volcanic edifices which can inform hazard decisions and strategic development (Biggs et al., 2014). Few active volcanoes are monitored so frequently by other methods such as GPS, seismology and geochemistry (Dzurisin, 2003). The deployment of equipment for these studies is a finite resource and is also expensive and potentially logistically challenging. Additionally, deployment may be hazardous and equipment might be damaged or destroyed by an eruption. InSAR can either provide supplementary information for multiparameter studies which aim for a holistic understanding of volcanoes, or can be used independently providing detection of magma processes which may otherwise have gone unnoticed (Biggs et al., 2009).

In this chapter I briefly outline the InSAR method including the acquisition of SAR

images, the satellite viewing geometry and the processing procedure. Additionally, I present the data sets and corrections used in the remainder of this thesis, which includes SAR images from both the TerraSAR-X and COSMO-SkyMed missions. I have incuded a glossary of commonly used InSAR terms in Appendix D. More detailed descriptions of InSAR methodology have been published previously, and if required, I refer the reader to the following articles: Massonnet and Feigl (1998), Bürgmann et al. (2000) and Hanssen (2001).

3.1 InSAR Method

3.1.1 SAR acquisition and imaging geometry

A SAR capable satellite actively transmits pulses of microwaves in the 1-10 GHz frequency range from an onboard microwave antenna. The RADAR beam travels in a plane perpendicular to the orbit, emitted to one side of the direction of travel. The wavelength of the emitted pulse is dependent on the application of the satellite. Short wavelengths (∼3 cm, X-band) have a higher precision when detecting ground deformation, however longer wavelengths, between ∼6 cm (C-band) and ∼24 cm (L-band), are required to monitor ground deformation beneath dense vegetation. As an active instrument emitting EM waves, SAR capable satellites can observe the Earth's surface through a range of atmospheric media at any time. SAR satellites usually operate in a sun-synchronous orbit, collecting data on a descending path during daylight hours and on the ascending path during the night.

The inherent resolution of the radar is dependent upon the height of the orbit and the ratio of the emitted wavelength to the aperture. For a satellite orbiting 1000 km above the Earth the raw resolution is typically 10 km on the ground (Massonnet and Feigl, 1998). To increase the ground resolution to 10's of meters an antenna of an impractical length would be required to focus the transmitted and received energy. To solve this, the RADAR pulse return is processed as if it came from a physically large antenna, known as the Synthetic Aperture. This is possible because the same ground point will be illuminated multiple times by successive RADAR pulses. First the returning signals are sorted according to their total travel time. Second, the Doppler frequency shift is used to sort samples in the along track direction (Massonnet and Feigl, 1998).

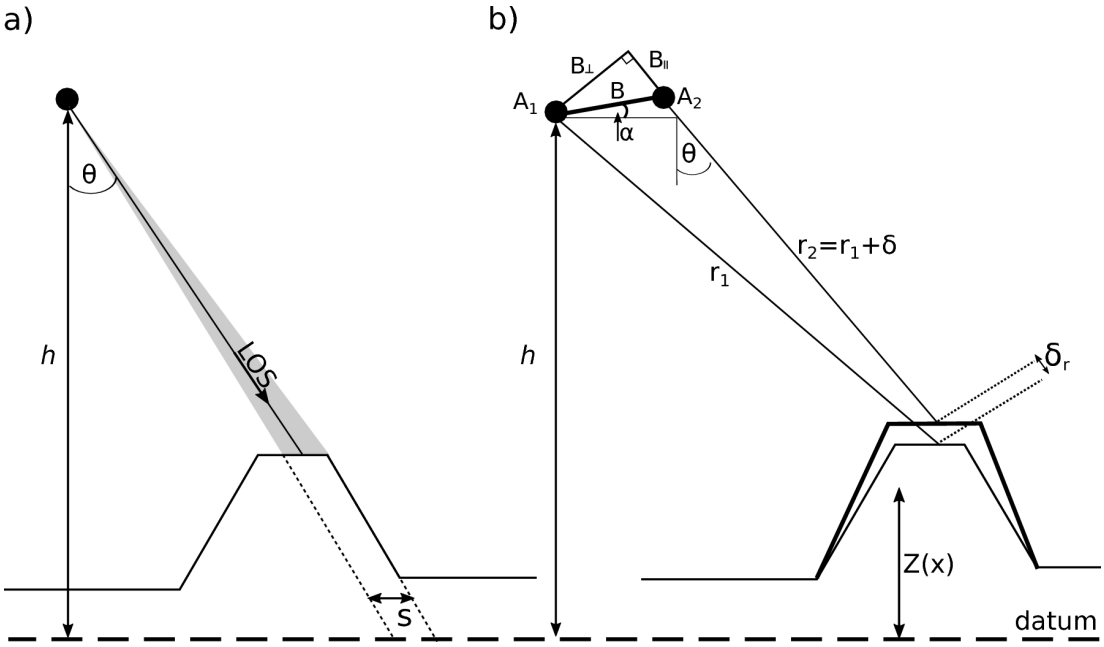

Figure 3.1: Viewing geometry for a) SAR image b) InSAR image, adapted from Garthwaite (2011), Walters (2012) and Peyret et al. (2011). The flight direction of the satellite (black circles) is into the page. The satellite is at height, h, above a datum, imaging a swath with width, S, with radar pulses. The angle of incidence of the RADAR wave, θ, varies across the swath. δ_r is the change in range between the satellite and ground between the first (A_1) and second (A_2) acquisition, due to ground movement shown by the bold black line. B is the baseline separation, which can be split into two components, the perpendicular and parallel baselines, $B_\perp$ and $B_\parallel$, respectively. The topography in a scene is Z(x) above a datum. r_1 and r_2 are the range distances from the ground to the satellite along the Line of Sight (LOS).

From the viewing geometry given in Figure 3.1, the satellite orbits the Earth at a height (h) above a reference datum, and illuminates a swath to one side of the satellite with radar waves. The incidence angle (θ) of these waves varies across the swath, which has a defined width (S). The combined radar signals returned for a given pixel are encoded as a complex number, $Z = Ae^{i\phi}$. A is the amplitude, or brightness, of the cell and is a measure of the combined reflectivity of the scattering elements within the cell. It is dependent on dielectric constants and the roughness of the surface. The phase (ϕ) has values between 0 and 2π, and is a function of the distance travelled and atmospheric and ground interactions. In a single SAR image the returned phase is random between neighbouring pixels; only after subtracting the phase values of two successive images can the relative phase change be observed. An interferogram is the resulting map of the phase values after this subtraction. This phase depends on the change in the time (δ_t) it takes the back scattered RADAR pulse to reach the satellite: $\Delta\phi = \frac{C\delta_{\text{time}}}{\lambda}2\pi$, where C is the speed of light and λ is the wavelength of the pulse. This difference might be caused by changes in the slant range (r) between acquisitions, or because of different atmospheric conditions. The measurement is relative between the two acquisitions; determining absolute displacements requires external data, for example from GPS. SAR Images from the ascending and descending tracks cannot be interfered as the direction of the radar beam must be similar.

3.1.2 SAR Satellites

Below I introduce the two SAR capable satellites which acquired the radar images used in this thesis.

COSMO-SkyMed

COSMO-SkyMed (COnstellation of small Satellites for the Mediterranean basin Observation) (or CSK) is an Earth Observation System composed of 4 satellites conceived by the Italian Space Agency (ASI) and funded by the Italian Ministry of Defence and the Italian Ministry of Research. The configuration of the four satellites reduces the revisit period to as little as 1 day for some targets. The satellites follow the same sun-synchronous polar orbit at a height of ∼620 km above the Earth's surface. They were launched over a period of three years between 2007 and 2010, with the constellation becoming fully operational in April 2011.

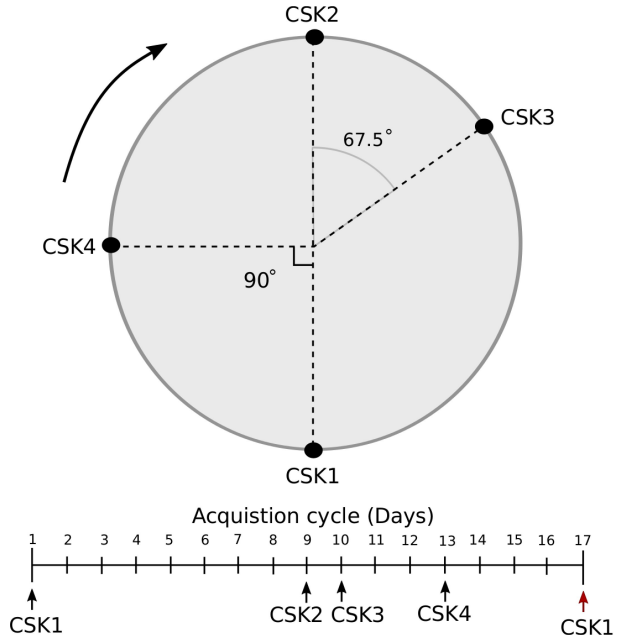

Figure 3.2: Top: COSMO-SkyMed orbital configuration in 2011 and 2012, shaded disk represents the orbital plane. Bottom: Image acquisition cycle. Redrawn from (Pietranera et al., 2011).

The identical satellites have the same orbit direction and incidence angle allowing for interferograms to be created regardless of which satellite acquired the separate SAR images. During the time period of interest, June 2011- end 2012, the CSK satellites were positioned in non-symmetric configuration (Figure 3.2). Consequently, in a 16-day cycle there are 4 interferometric acquisitions: On day 1, day 9, day 10 and day 13. The SAR sensors operate in the X-band, emitting a radar pulse with a ∼31 mm wavelength. The Stripmap (HIMAGE) mode acquisitions used to observe Nabro have a swath 40 km wide with a spatial resolution between 3 and 15 m.

TerraSAR-X

TerraSAR-X is a single Earth observation satellite which is co-owned by the German Aerospace Center (DLR) and EADS Astrium, as a joint public-private venture. It was launched on 15 June 2007 and operates at an altitude of 514 km, travelling on a dusk-dawn near-polar orbit within a 250 m radius orbiting tube (Yoon et al., 2009). The satellite repeats the ground track every 11 days. TerraSAR-X has a range of imaging modes: Spotlight, StripMap and ScanSAR. For this study, I use StripMap mode images. In this mode, the swath width is 30 km, the full performance incidence angle range is

20°-45°, and the pixel resolution is 3.3 m in the azimuth direction and 1.7 m to 3.5 m in the ground range directions, as it is dependent on the incidence angle. The emitted radar pulse has a ∼31 mm wavelength and a frequency of 9.65 GHz. Therefore, each fringe within a TSX interferogram corresponds to a change in range of ∼15 mm between the ground and the satellite.

3.1.3 Repeat-Pass Interferometry

The phase component of 2 SAR acquisitions are subtracted to create an interferogram, traditionally a later image (known as the slave) is resampled into the geometry of an earlier image (the master) for the subtraction. The interferogram, shows the interference pattern as coloured cycles of phase which has a cyclic quantity of modulo 2π. The measured phase difference observed in a interferogram ($\Delta\phi_{int}$) has contributions from multiple sources:

$$\Delta\phi_{int} = \Delta\phi_{def} + \Delta\phi_{cor} + \Delta\phi_{orb} + \Delta\phi_{topo} + \Delta\phi_{atm} + \Delta\phi_{other} \tag{3.1}$$

where Δ refers to the differencing of the master and slave acquisitions, ϕ_{def} is phase change due to ground displacement, ϕ_{cor} is noise introduced by decorrelation, ϕ_{orb} is contribution associated with the orbit geometry of the satellite, ϕ_{topo} is the topographic phase , ϕ_{atm} is atmospheric contribution, and ϕ_{other} includes any other sources of noise including unwrapping errors and instrument noise. These terms are desrcibed in the following text. To isolate the signal of interest, ϕ_{def}, the other components must be removed during interferogram processing or accounted for in the error budget. The $\Delta\phi_{atm}$ contribution is removed separately following the interferogram formation.

Decorrelation $\Delta\phi_{cor}$

The correlation function (γ_i) for pixel i, describes the relationship of the two radar waves after an interferogram has been formed (Bürgmann et al., 2000):

$$\gamma_i = \frac{\langle \Gamma_1 \Gamma_2^* \rangle}{\sqrt{\langle |\Gamma_1|^2 \rangle \langle |\Gamma_2|^2 \rangle}}, \tag{3.2}$$

where Γ_k is the reflectivity of acquisition k and the angular brackets denote the averaging of the speckle in a resolution cell over the master and slave images. The correlation is a measure of the constructive phases within an area of the interferogram;

if the phase sum is $\gamma = 1$ the area is completely correlated, when $\gamma = 0$ complete decorrelation has occurred. The magnitude of the correlation, $|\gamma|$, is often referred to as the 'coherence' in the literature. The correlation will comprise contribution from a number of effects (Simons and Rosen, 2007):

$$\gamma_i = \gamma_{\mathrm{G}}\gamma_{\mathrm{Z}}\gamma_{\mathrm{T}}\gamma_{\mathrm{N}} \tag{3.3}$$

where γ_{G} is the noise caused by different viewing geometries for each acquisition, γ_{Z} is the effect caused by the vertical extent of the scatterers, γ_{T} is the temporal redistribution of scatterers over time, γ_{N} is the noise introduced by the radar system. It is easier to discuss each of these factors in terms of decorrelation which is defined as $\delta_X = 1 - \gamma_j$, where j is G,Z,T or N (Simons and Rosen, 2007).

Complete geometrical decorrelation (δ_G=1) occurs if the phase change over a resolution element between each acquisition is greater than 2π: $\Delta\phi_1 - \Delta\phi_2 \geq 2\pi$ (Simons and Rosen, 2007). This is dependent on the perpendicular baseline. If the perpendicular baseline is larger than a critical value ($B_{\perp crit}$) it causes the phase to change by greater than 2π per resolution element. This critical baseline provides a limit on the spatial separation between acquisitions (Rosen et al., 2000), and provides a criteria to select image pairs. The ($B_{\perp crit}$) is proportional to the wavelength, λ, and the resolution element projected into the look direction, $\Delta\rho$ (Simons and Rosen, 2007):

$$B_{\perp crit} \propto \frac{\lambda}{\Delta\rho}. \tag{3.4}$$

For TSX $B_{\perp crit}$ can be several kilometres dependent on the incidence angle, assuming a flat terrain. For the CSK satellites the critical baseline is around 5 kilometres, again dependent on the terrain. These are theoretical thresholds and due to terrain and atmospheric noise, I find that significant decorrelation occurs over more than 500 m.

Volume scattering, γ_{Z} is a contribution to the correlation if the radiating ground resolution element changes size due to a change in the volume above it, for example vegetation canopy (Rosen et al., 2000). In addition, multiple reflections can occur within this volume, causing significant decorrelation over short revisit periods (Schepanski et al., 2012). Temporal decorrelation, γ_{T}, occurs when there is a change in the scattering characteristics of the reflectors inside a resolution cell between two acqui-

sitions. As the scatterers inside the resolution cell become randomly reorganised the speckle of the second acquisition varies from the first, so the images no longer correlate (Rosen et al., 2000). Some surfaces are more stable than others, for example bare rock and urban areas tend to stay correlated through seasons, a circumstance exploited by Persistent Scatterer (PS) InSAR methods (Hooper et al., 2004). However, heavily vegetated areas and regions prone to snow can lose correlations due to the dynamic nature of the surface. A longer wavelength radar antenna is less prone to decorrelation of this type. This is because the X-band will be scattered by small objects such as leaves and branches, which are constantly changing. Longer wavelengths will penetrate the vegetation canopy and be back scattered by the tree trunk and ground surface which are inherently more stable. Lastly, the system noise effects the correlation. Noise (γ_{N}) has multiple sources; thermal noise in each SAR acquisition introduces phase noise in the interferogram (Rosen et al., 2000) and it can be defined as:

$$\gamma_N = \frac{1}{\sqrt{1+\mathrm{SNR}_1^{-1}}\sqrt{1+\mathrm{SNR}_2^{-1}}}, \tag{3.5}$$

where SNR_i is the signal to noise ratio for each acquisition. Each image will also have Doppler and range ambiguities (Rosen et al., 2000).

Decorrelation is observed as patches of pixels that have a seemingly random phase in comparison to their neighbour. These areas create problems when 'unwrapping' an interferogram. This is the process which converts the 2 π modulo signal into a continuous measurement of relative displacement by integrating the phase gradient across pixels. The integration used is the branch cut algorithm, where the integration follows a route across the interferogram where the integrals are zero (Goldstein et al., 1988). If non-zero regions are found the area is cut, and another route is found. The unwrapping errors will then have to be fixed manually. For a full description of phase unwrapping see Ghiglia and Pritt (1998). If patches are only decorrelated sporadically, then processing algorithms such as π-RATE (Section 3.3.1) can use sporadically coherent pixels whilst stacking interferograms to increase coherence. Correlation can be increased by 'multilooking' which averages pixels together. This increases coherence across the scene at the expense of resolution. The processing software ROI_PAC, which I use to create the interferograms can flag pixels which are 'unwrappable'. I calculate these pixels as a percentage of the total interferogram and use this a as a proxy for the coherence of

each interferogram (Figure 3.10).

Orbital trajectories $\Delta\phi_{orb}$

A satellite's orbit, which is well determined by conservative gravitational forces, is also perturbed by an unconservative field that is more difficult to quantify. The forces that contribute to this field include solar radiation pressure, anisotropic re-radiation, atmospheric drag and effects due to satellite signal emission (Ziebart et al., 2005). The combination of these effects can modify the orbit by 100-200 m per orbit in some instances (Ziebart et al., 2005). Therefore, the SAR images are not acquired from the same location on each pass, and an accurate and precise location may not be known.

The baseline, B, can be decomposed into a parallel baseline and perpendicular baseline distances (Figure 3.1). The latter has a strong influence on the phase component of an interferogram as follows. The change in path length between A_1 and A_2 is (Walters, 2012)

$$\delta = B_{||}\cos(90 - \theta + \alpha) = B\sin(\theta - \alpha), \tag{3.6}$$

where $\theta =$ is the incidence angle and α is angle between the baseline and the horizontal. Therefore, there is a phase contribution caused by this additional path length equal to

$$\Delta\phi_{orb} = \frac{4\pi B\sin(\theta - \alpha)}{\lambda}. \tag{3.7}$$

This phase contribution changes across the interferogram swath as:

$$\frac{\partial(\Delta\phi_{orb})}{\partial\theta} = \frac{4\phi B\cos(\theta - \alpha)}{\lambda} = \frac{4\pi}{\lambda}\cdot B_{\perp}. \tag{3.8}$$

Therefore, the phase varies based on the perpendicular baseline. This artefact is observed as fringes aligned with the azimuthal direction of the interferogram. The perpendicular baseline effect is removed during interferometric processing using precise models of the satellite's orbit. If the satellite acquired images from the exact same location, this effect is zero but keeping each orbit identical is not feasible. As the satellite drifts, orbit control manoeuvres can be performed to correct the orbit, however this uses fuel which ultimately decreases the life of the mission. Any error in the precise orbit models will cause residual fringes. TerraSAR-X is kept within an orbit tube with a radius of 250m (Yoon et al., 2009). As mentioned residual orbit fringes exist due to uncertain-

ties in the satellite orbit. The processing algorithm π-RATE can remove the error by inverse modelling the orbital signal as a ramp in the interferogram and then removing this plane. The size of the ramp in the TSX data set used for this study, in terms of north and east components of the plane fitted to the data is displayed in Figure 3.3. The small correction required shows the advantage of a small orbital tube. There is also a phase ramp in the azimuthal direction by uncertainties along track variation in $B_{parallel}$ and if the satellite rocks as it orbits the Earth. Note that these ramps will also include long wavelength atmospheric signals.

Topography $\Delta\phi_{topo}$

The different viewing geometries of each SAR acquisition creates fringes which delineate the topography. The effect is caused by different relative path lengths between pixels due to the ground height. The change in altitude required to produce one 2π fringe is known as the altitude of ambiguity (Hanssen, 2001):

$$h_a = \frac{R_s \lambda \sin\theta}{2B_\perp}, \tag{3.9}$$

where, R_s is the range from the slave image, θ is the incidence angle, λ is the wavelength, $B_\perp$ is the perpendicular baseline. h_a will be infinite if the images were acquired from exactly the same position, removing the topographic effect. However, the larger the perpendicular baseline the more fringes will result from a topographic feature, the fringes will be spaced at intervals in elevation of h_a. The effects of topography are removed by using a Digital Elevation Model (DEM) during processing, but errors in the DEM will leave a residual topographic phase. For the TSX data I use a ~90 m DEM derived by the 3-arc-second Shuttle RADAR Topography Mission (SRTM). For processing this was 'upsampled' to a resolution of 9×9 m for a smooth elevation correction for processing full resolution interferograms. Additionally, this will prevent a high phase gradient becoming aliased. Significantly upsampling the DEM can create some signal artefacts in the interferogram, but these were not observed. Additionally, the output is downsampled for the inversions performed in Chapter 4 onwards, so the effect is minimal. The SRTM has an average absolute height error of 5.6 m across Africa (Farr et al., 2007). The DEM induced topographic errors will be small if h_a is much greater than the DEM error. Topographically correlated fringes can be removed with linear phase-topography estimation, or by removing the topography as a function

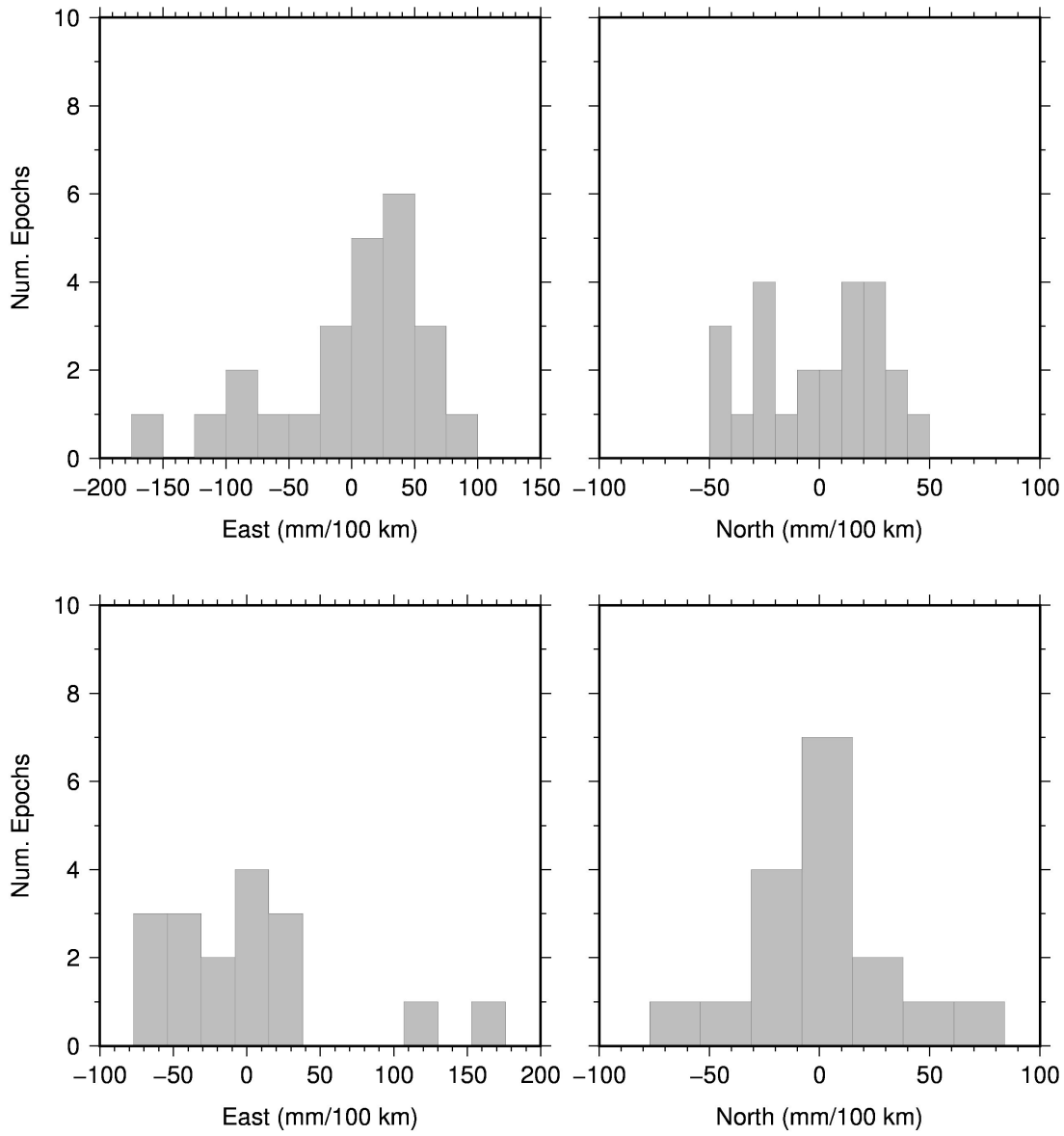

Figure 3.3: TSX orbital tilt correction calculated by π-RATE (see Section 3.3.1) for each epoch. Top: Descending track. Bottom: Ascending track.

of perpendicular baselines.

Atmosphere $\Delta\phi_{atm}$

As the emitted radar waves pass through Earth's atmosphere the signal is affected by the refractivity of the troposphere. The atmospheric refractivity will vary between image acquisitions, so on differencing 2 SAR images a phase change is apparent. The refractive index (n) of a medium is the ratio of the speed of light through a vacuum to the speed of light through the medium. Radar waves propagate slower through the atmosphere than in a vacuum and on a curved, rather than straight path. This is due to the variation of n with height from the Earth's surface. This additional path length is (Bevis et al., 1992)

$$\Delta L = \int_L n(s)\mathrm{ds} - \mathrm{G}, \tag{3.10}$$

where $n(s)$ is the refractive index at point s along the ray path, and G is the equivalent straight line path if the atmosphere was a vacuum. This is equivalent to two separate terms for these effects (Bevis et al., 1992):

$$\Delta L = \int_L (n(s) - 1))\mathrm{ds} + (\mathrm{S} - \mathrm{G}), \tag{3.11}$$

where S is the path length along L. The first term is the slowing effect and the second term, $(S - G)$ is the bending term. Along the zenith, the bending term is removed because it is negligible for small incidence angles (Bevis et al., 1992). This condition is valid for InSAR as the curvature between the locations of the first and second acquisitions is insignificant (Zebker et al., 1997). Thus the bending term is removed and Eq. 3.11 is written in terms of atmospheric refractivity, N (Bevis et al., 1992):

$$N = 10^6(n - 1) \tag{3.12}$$

as

$$\Delta L = 10^{-6} \int_L N(s)\mathrm{ds}. \tag{3.13}$$

Temperature, pressure and partial pressure of water vapour control the refractivity of the atmosphere (Bevis et al., 1992). Thayer (1974) developed the following empirical

formula for N:

$$N = k_1 \frac{P_d}{T} Z_d^{-1} + k_2 \frac{P_w}{T} Z_w^{-1} + k_3 \frac{P_w}{T^2} Z_w^{-1}, \tag{3.14}$$

where k_1 =(77.604 ± 0.014) K hPa^{-1}, k_2 =(64.79 ± 0.08) K hPa^{-1}, k_3 =(3.776 ± 0.004)×10^5 K^2 hPa^{-1}, P_d and P_w are the partial pressure of dry air and water vapour in hPa (hectoPascals), respectively, and Z_d^{-1} and Z_w^{-1} are the inverse compressibility factors for dry air and water vapour, respectively (Bevis et al., 1992). Z_d^{-1} and Z_w^{-1} represent non-ideal gas behaviour and are very close to unity (Owens, 1967, Bevis et al., 1992) so can be neglected (Doin et al., 2009). The first and second term in Eq 3.14 refer to the induced dipole moment of the dry constituents and water vapour, respectively. Whereas the third term is the dipole orientation effects of the permanent dipole moment of the water molecule (Davis et al., 1985). Equation 3.14 was rewritten by Davis et al. (1985) to:

$$N = \underbrace{k_1 R_{d\rho}}_{\text{Dry}} + \underbrace{k_2' \frac{P_w}{T} Z_w^{-1} + k_3 \frac{P_w}{T^2} Z_w^{-1}}_{\text{Wet}}, \tag{3.15}$$

where $k_2' = k_2 - [k_1(R_d/R_w)]$, ρ is the density of the atmosphere and R_d and R_w are the specific gas constants for dry air and water vapour respectively. The first term is the hydrostatic delay (often known as the 'dry' delay), whereas the second and third terms collectively are the 'wet' component of delay. The integration of N along the zenith, to give the Zenith Total Delay (ZTD), was derived by Baby et al. (1988):

$$\mathrm{ZTD} = 10^{-6} \left[\underbrace{k_1 R_d \int_{Z_0}^{\infty} \rho \mathrm{dz}}_{\mathrm{ZHD}} + \underbrace{\int_{Z_0}^{\infty} \left(k_2' \frac{P_w}{T} Z_w^{-1} + k_3 \frac{P_w}{T^2} Z_w^{-1} \right) \mathrm{dz}}_{\mathrm{ZWD}} \right]. \tag{3.16}$$

By integrating with respect to height, z, the expression is composed of the Zenith Hydrostatic Delay (ZHD) and Zenith Wet Delay (ZWD). Doin et al. (2009) expresses the atmospheric delay along the look direction, Slant Total Delay (STD), as:

$$\mathrm{STD} = \frac{10^{-6}}{\cos(\theta)} \left[\frac{\mathrm{k_1 R_d}}{\mathrm{g_0}} \mathrm{P(z_0)} + \int_{\mathrm{Z_0}}^{\infty} \left(\mathrm{k_2'} \frac{\mathrm{P_w}}{\mathrm{T}} \mathrm{Z_w^{-1}} + \mathrm{k_3} \frac{\mathrm{P_w}}{\mathrm{T^2}} \mathrm{Z_w^{-1}} \right) \mathrm{dz} \right]. \tag{3.17}$$

where, $\mathrm{g_0}$ is acceleration due to gravity at the surface. In addition the ionosphere will

contribute to the phase, as the presence of charged particles will delay the radar pulse in a dispersive manner. The ionosphere has two main effects on the signal: a phase shift and a Farady rotation (Meyer and Nicoll, 2008).The ionospheric path delay along the LOS is (Breit et al., 2010)

$$\Delta R_{iono}(i) \approx \frac{K \cdot TEC}{f^2 \cdot \cos(\theta)} \tag{3.18}$$

where K is the refractive constant, TEC is the Total Electron Content and f is the center frequency (9.65 GHZ for TerraSAR-X) (Breit et al., 2010). As the delay is inversely proportional to frequency, X-band is less disrupted than L-band by the ionosphere due to the smaller wavelength (Meyer, 2011). The delay is of the order of $\sim$2 cm for TerraSAR-X (Breit et al., 2010). For X-band the tropospheric signals are larger than those originating from the ionosphere, so do not need to be corrected for here.

There are two types of atmospheric signal, those coming from turbulent mixing, random in space and those that are topographically correlated (Hanssen, 2001). Turbulent mixing arises due to a 3-dimensional heterogeneity in the refractivity of the atmosphere, and can occur in both flat and mountainous regions. It has two components: a 'hydrostatic' and a 'wet' delay. The dry delay is a long wavelength signal dependent on temperature and pressure variations within the troposphere. Even though this signal can be large, on an order of 2-3 m, the signal is not very spatially variable. Therefore, it is not commonly disruptive to InSAR-derived ground motions. The wet delay is based on the amount of water held in the lower troposphere. It has a much smaller magnitude (around 30 cm) than the dry delay, but it has a short spatial wavelength so it can be detrimental to the retrieval of surface deformation measurements through InSAR. The atmosphere will also contain a component which is correlated with topography as the presence of high relief features will reduce the distance the radar pulse travels through the troposphere. The removal of this component of the atmospheric phase contribution is discussed in section 3.2.1.

The tropospheric phase can be mitigated from the interferogram using independent data such as Spectrometer measurements (Li et al., 2006), weather models (Foster et al., 2006), Global Navigation Satellite Systems (GNSS) (Onn and Zebker, 2006) or a combination of these data (e.g, Li et al., 2005, Walters et al., 2013). These methods can reduce the topographic signal but are limited by the resolution of the auxiliary data (Bekaert et al., 2015). Without additional data, atmospheric signals can be cor-

rected by calculating the topography-phase relationship over the study area (Elliott et al., 2008, Bekaert et al., 2015), or by filtering the interferogram in time and space to calculate an Atmospheric Phase Screen (APS) (e.g., Biggs et al., 2007). Weather models and the topography-phase relationship are discussed further in section 3.2.1 and APS estimation is discussed in section 3.3.2.

Other phase contributions $\delta\phi_{other}$

Phase contributions from miscellaneous sources such as instrument noise, filtering noise and unwrapping errors are also contained within interferograms. Unwrapping errors are observed as patches of phase jumps with a value of $n2\pi$ after a summing a loop of at least 3 interferograms, where n is an interger. For example, if interferograms AB, BC and AC have no unwrapping errors the summation $AB + BC - AC$ should equal 0. The observed errors can then be checked in the individual interferograms, this is known as a loop closure technique (Biggs et al., 2007). Other miscellaneous sources of phase are assumed to be negligible.

Deformation signal $\delta\phi_{def}$

If $\delta\phi_{orb}$, $\delta\phi_{topo}$ and $\delta\phi_{atm}$ have been adequately removed, and $\delta\phi_{other}$ is negligible, the fringes observed in the differential interferogram are due to any ground movement between the two acquisitions. This range change, $\delta\phi_{def}$ (or $2\delta r$ in terms of path length change) is:

$$\delta\phi_{def} = \frac{4\pi\delta r}{\lambda} = -\left(\frac{4\pi}{\lambda}\right)\hat{\mathbf{l}}\cdot\mathbf{u}. \tag{3.19}$$

The range change is given in the LOS of the satellite, $\mathbf{u}$ is the ground displacement vector and $\hat{\mathbf{l}}$ is the unit vector between the ground target and the satellite. Therefore, one fringe is created by a range change equal to half the radar wavelength.

3.1.4 Interferometric processing procedure

I used the Repeat Orbit Interferometry PACkage (ROI_PAC) developed at JPL and Caltech to process the raw images from TerraSAR-X into interferograms (Rosen et al., 2004). ROI_PAC comprises a collection of Fortran and C programs within perl scripts to process raw SAR data into an interferogram. A detailed discussion of the algorithms

and processing steps involved is not given here, for this I refer the reader to the following publications: Rosen et al. (2000) and Elliott (2009).

3.2 CSK Data

The CSK data set is composed of 64 SAR images acquired on a descending track between 26 June 2011 and 18 July 2012 within the Italian Space Agency project: SAR4Volcanoes. In total, 171 interferograms were produced by Eugenio Sansosti and colleagues at the Istituto per il Rilevamento Elettromagnetico dell'Ambiente (IREA) in Naples. They used a Small BAseline Subset (SBAS) approach (Berardino et al., 2002) to create a map of average velocity (ratemap) and a time series for each pixel (Figure 3.4). The resolution is ∼30 m in both the azimuth and ground range directions. The coherence of the image is high, after multilooking there are approximately 3.5 million pixels in the ratemap. During processing, the team at IREA observed an orbital phase ramp in the velocity map which was subsequently removed using a linear fit. It was also removed from the time series after integrating over the corresponding time intervals. The initial data set that was supplied by IREA consists of a smoothed ratemap and time series. The spatiotemporal filter used by the IREA has a temporal window of 70 days and a spatial window of several km. The temporal window implies that about 10 samples in time are averaged, similar to a moving average.

The ratemap shows a roughly circular signal centred on the south-east edge of the caldera, which is slightly elongated on the east flank of the volcano. The LOS displacement shows the volcano moving away from the satellite at a rate of approximately 300 mm a year. The lava that partially filled the caldera and flowed to the west is evident as an incoherent grey elongate lobe, outlined in Figure 3.4. Other patches have also lost coherence probably due to steep topographic relief, for example on Nabro's caldera walls, the slopes of Mabda volcano and the Danakil Alps. The summit of Mallahle is significantly less coherent than Nabro, and this may be due to loose ash deposits from the June 2011 eruption (Goitom et al., 2015). However, there is no significant subsidence on neighbouring Mallahle caldera or at Mabda volcano to the north.

The time series of a given pixel shows two periods of reversed LOS displacement during the observation period. There is also a small indication that the overall gradient of LOS displacement decreases after the first of these 'pulses'. If these pulses are real and distinct it will have important ramifications for modelling and interpretation of

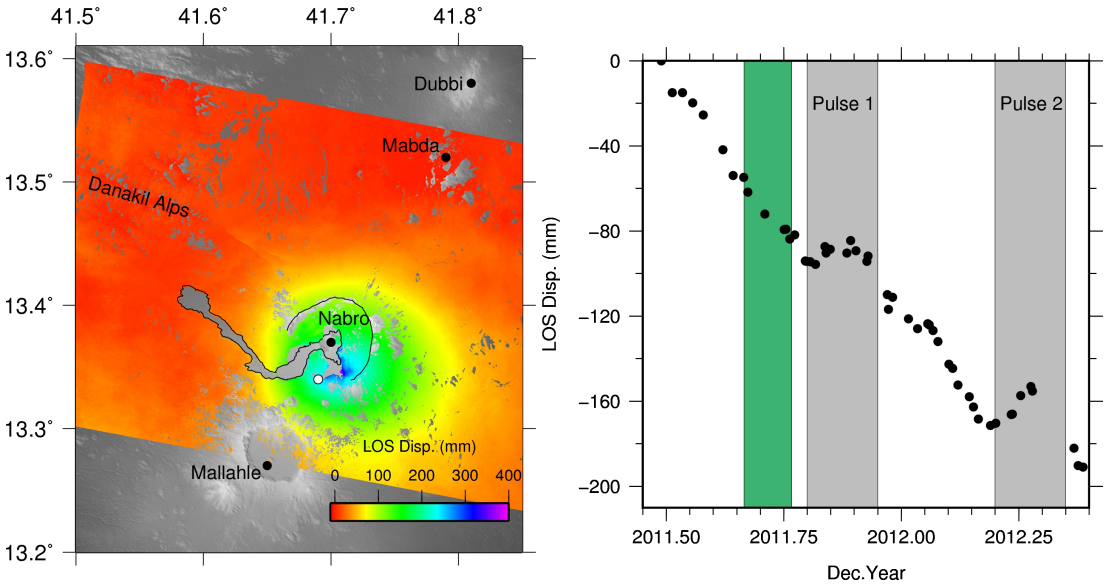

Figure 3.4: LHS: Filtered CSK ratemap of range increase from SAR acquisitions between 26 June 2011 and 18 July 2012, calculated using 171 interferograms. RHS: Filtered time series of displacement of the pixel highlighted in white. The grey shaded area highlights the pulses described in text. The green shaded region is the time period of the seismic analysis in Chapter 1. Data from E.Sansosti and colleagues at IREA, Naples.

Nabro's plumbing system. Therefore, I will apply atmospheric corrections to the raw data (Figure 3.5) to test if these are artefacts or authentic observations of ground displacement.

3.2.1 Atmospheric Phase Correction

Global weather models

The filtered time series of deformation shows 2 periods in which the range between the satellite and the volcano reverses, against the overall trend of decreasing LOS displacement. Before interpreting this signal and reconciling it with TerraSAR-X and seismic data, I used the outputs from ERA-Interim (ERA-I), a global atmospheric model computed by the European Centre for Medium-range Weather Forecasting (ECMWF), to correct each epoch for the atmospheric effects over Nabro.

The ERA-I model provides estimates of an array of atmospheric parameters since 1 January 1989. The parameters are calculated daily at 00:00, 06:00, 12:00, 18:00 UTC for grid nodes at approximately 80 km apart and at 37 vertical levels based on atmospheric pressure (Dee et al., 2011). Using the method described by Jolivet

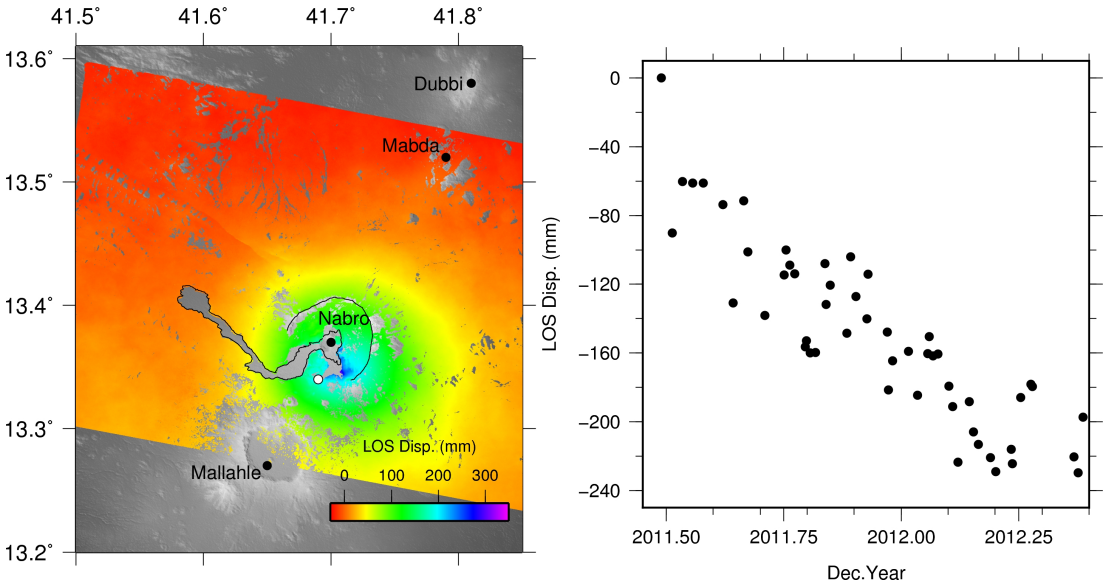

Figure 3.5: LHS: Raw CSK ratemap of LOS displacement based on SAR acquisitions between 26 June 2011 and 18 July 2012, calculated using 171 interferograms. RHS: Raw time series of displacement of the pixel highlighted in white. Data from E.Sansosti and colleagues at IREA, Naples.

et al. (2011) and Walters et al. (2013), I use the measurements for temperature, water vapour and pressure provided by the model from the closest model output locations, before and after the time of the SAR acquisition. The values of these parameters are then interpolated between each pressure level and then the phase delay as a function of elevation (STD(z), Eq 3.17) can be calculated. A bilinear interpolation between spatially separated node points and a spline interpolation between nodes at different altitudes yields a map of predicted delay. This is performed for the model outputs either side of the SAR acquisition, then interpolated in time to the moment of acquisition. A Digital Elevation Model (DEM) is used to select the data points at the ground surface and therefore the resulting phase maps have a resolution that is the same as the DEM. The wet and hydrostatic phase delay are calculated separately and then summed. I have displayed the wet and hydrostatic phase delay for three dates which correspond to the second pulse of deformation (Figure 3.6). I also show the wet and dry correction over the full observation period for one pixel. The hydrostatic delay has a large absolute value but has a much smaller variation over time than the wet delay.

I have applied the corrections to the 64 epochs of raw data I attained from IREA (Figure 3.5). I have also applied a spatio-temporal filter to the corrected data set.

The filtered ECMWF corrected CSK data shows no periods of LOS displacement reversal (Figure 3.7). This implies that the original timeseries determined by IREA had significant atmospheric artefacts.

Linear correction with height

It is also possible to correct the atmospheric component in interferograms with a simpler empirical approach, rather than by using independent data. An established method is to find a linear relationship between phase and elevation on a interferogram-by-interferogram basis (Cavalié et al., 2007). Elliott et al. (2008) used an epoch-by-epoch approach instead which takes into account the covariance of the correction between interferograms that share common acquisition dates. Using this method I found a linear phase-elevation relationship for the CSK data and removed this from the time series (Figure 3.7). The linear correction overcorrects the signal towards the end of the observation period. A significant disadvantage of this correction is that the atmospheric correction will trade-off with the tectonic signal as in this scenario the topography is correlated with the ground displacement signal. Additionally, spatially varying meteorological conditions are not taken into account, for example the differing hydrostatic and wet components on the leeward and windward sides of mountains (Puysségur et al., 2007). Figure 3.8 compares this correction to the ECMWF corrected time series. Elliott et al. (2008) and Doin et al. (2009) compare this empirical phase-elevation correction to that derived from the ERA-I ECMWF correction, and find good agreement. However, I find a disagreement between the two; the linear correction has a long term trend and this is not expected for atmospheric conditions on this timescale. This results in an overcorrection of the data toward the end of the observation period. I find that the ECMWF correction removes artefacts from the observed signal such that no pulses of displacement toward the satellite can be seen. I have therefore used the ECMWF corrected data from this point onwards.

3.3 TSX Data

The TSX satellite acquired 'StripMap' images on both ascending and descending orbits as it traversed over the BVC. The incidence angle of the beam is between 25.1° and 30.5° and 31.7° to 34.8° for the ascending and descending tracks, respectively (Figure 3.9). Each SAR scene is 30 km wide and 50 km long, large enough to cover the BVC and the

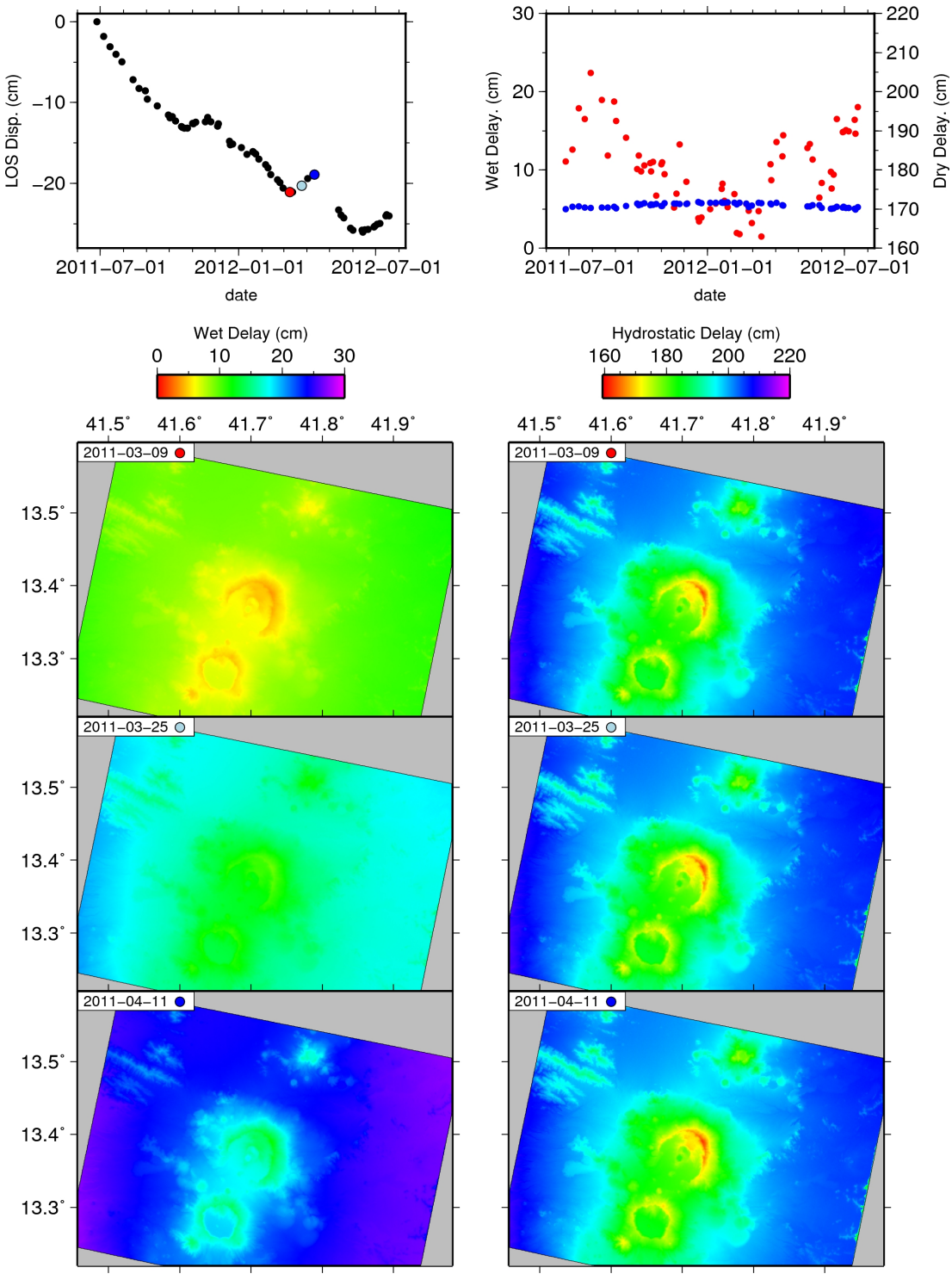

Figure 3.6: Top left: Uncorrected, filtered time series of range change for the CSK satellite, supplied by colleagues at the IREA. Top right: Time series of wet (blue) and hydrostatic (red) delay applied. Left column: Example wet phase delay maps. Right column: Example hydrostatic phase delay maps determined from the ECMWF weather model for the CSK acquisition date highlighted with the corresponding colour.

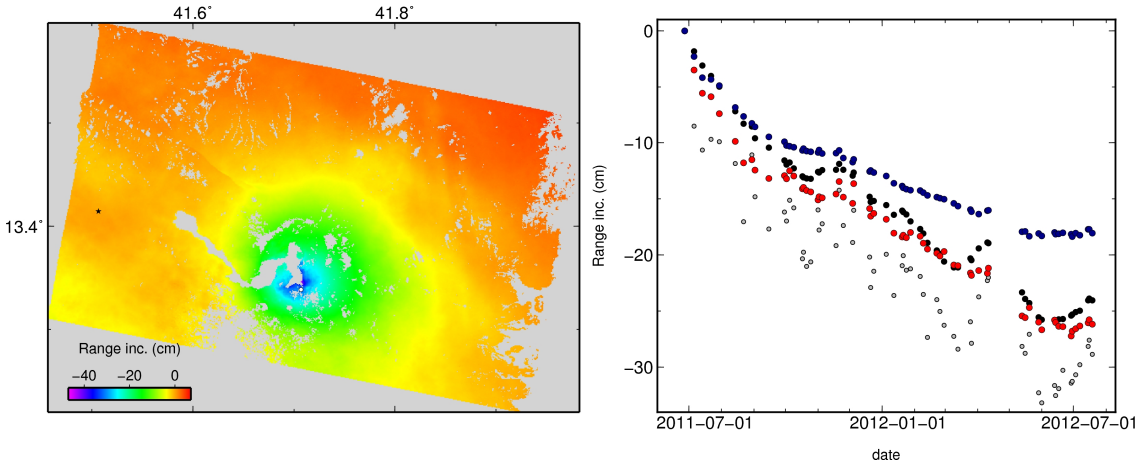

Figure 3.7: LHS: ECMWF corrected CSK ratemap, the reference pixel (black star) and pixel location of time series (white dot) are shown. RHS: Time series of range increase corrected using the ECMWF data (red), from the raw data (grey) compared to the IREA provided filtered series (black). The Linear-with-height correction is also shown(blue).

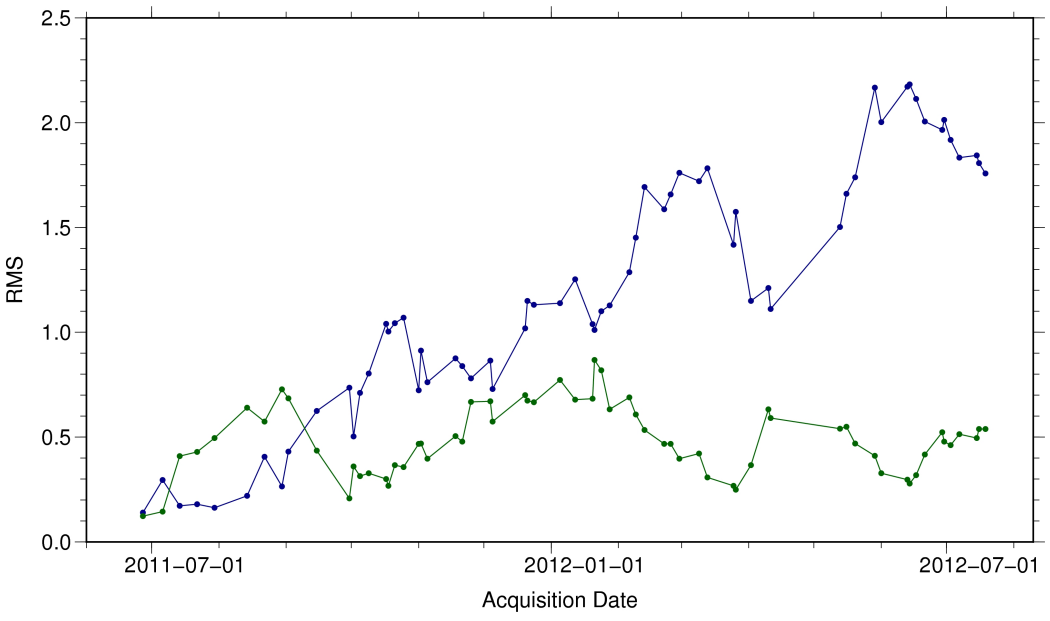

Figure 3.8: RMS Difference between the raw observation data and the ECMWF correction (green) and the observation data and the linear height correction (blue). The growing trend in the linear correction shows that the correction is getting worse as the signal increases.

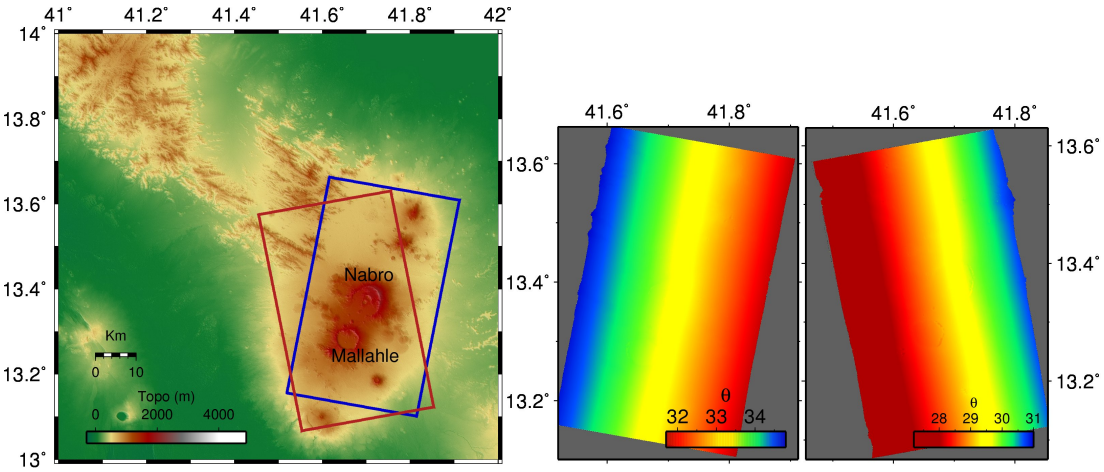

Figure 3.9: LHS: Example footprints of the descending (blue) and ascending (red) TSX coverage of Nabro volcano. Swaths are 30 km wide and 50 km long. RHS: Incidence angles across the descending and ascending swaths, respectively.

surrounding area (Figure 3.9). Through proposal GEO1206 (DLR, 2011) to the TSX science team, I obtained 36 images between the 1st July 2011 to the 5th October 2012 on descending orbit 046, and 27 images spanning the period between 6 July 2011 and the 10 October 2012 on ascending orbit 130.

Images were paired in order to keep baseline separation to a minimum (Figure 3.10). Large baselines between some images meant that a couple of acquisitions couls not be used. Using ROI_PAC I created 34 interferograms from the descending data set and 21 interferograms from the ascending data set. The interferograms have a maximum perpendicular baseline of 200 m and temporal baseline between 11 and 390 days. I used a connected network of interferograms which had at least 90% of the image unwrapped.

3.3.1 π-RATE

I subsequently input the interferograms in to the Poly-Interferogram Rate and Time-series Estimator (π-RATE) software package. This is a collection of Matlab scripts which estimates a constant displacement rate and time series of ground displacement from a set of geocoded unwrapped interferograms (Wang et al., 2010, Biggs et al., 2007, Elliott et al., 2008, Wang et al., 2009). See Garthwaite (2011) for a comprehensive description and synthetic testing of π-RATE software.

π-RATE calculates a map of ground displacement per pixel assuming a linear trend, known as a ratemap. A pixel does not have to be coherent in all interferograms to be

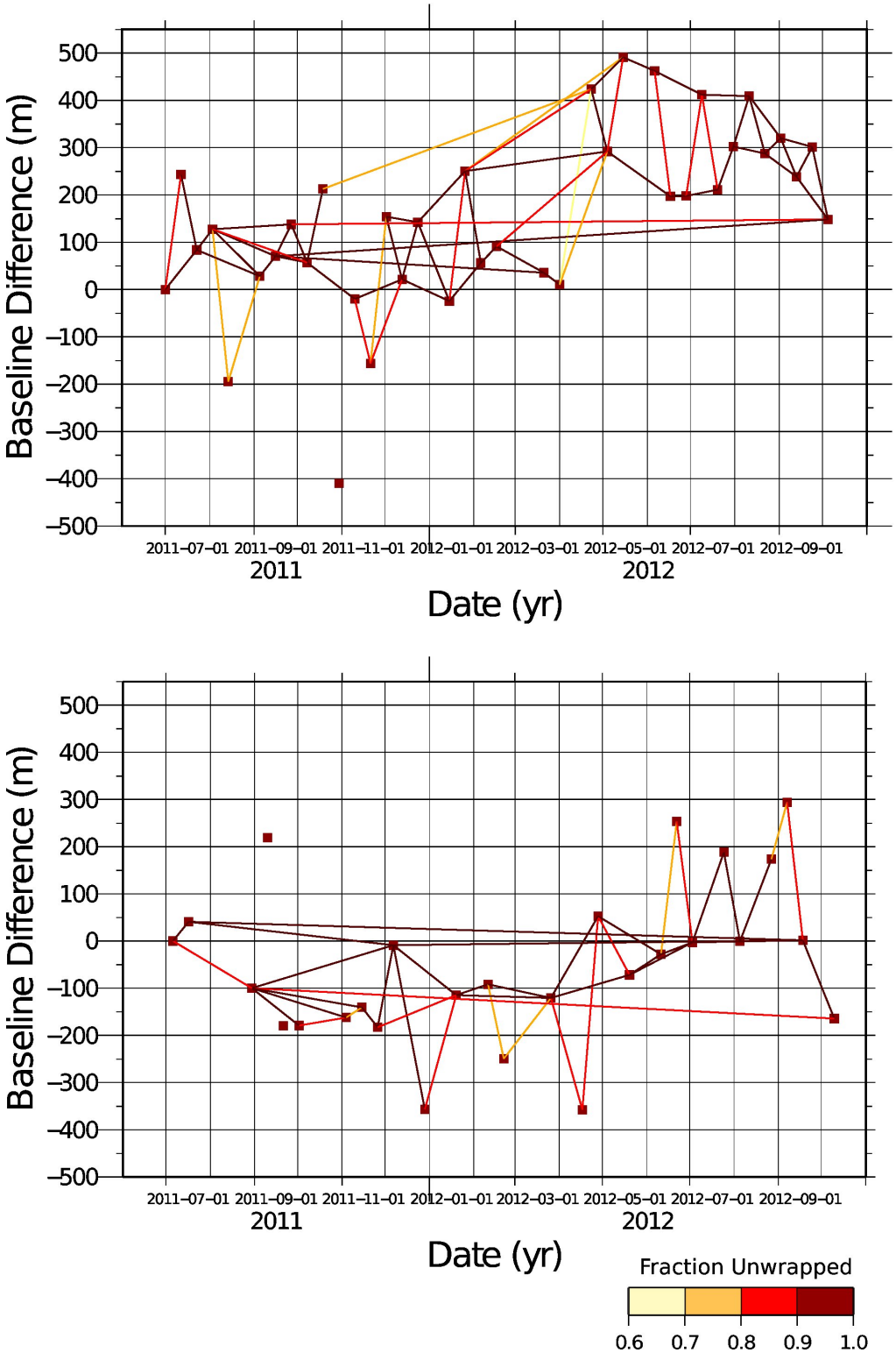

Figure 3.10: Perpendicular baseline vs. time plot for descending track 046 (top) and ascending track 130 (bottom), showing acquisitions (red squares) following the eruption. Solid lines represent interferograms which were created, the colour of the line is dependent of the percentage of the image which was unwrapped and is analogous with the coherence of the interferogram.

included in the analysis, as it can still provide a constraint on the inversion. However, a pixel does have to be coherent in interferograms more times than a specified threshold Ψ. The inversion is described in the following set of equations:

$$\Phi = \mathbf{T} \cdot \upsilon_k \tag{3.20}$$

where $\Phi = [\phi_{12}, \phi_{23}, \phi_{34} ... \phi_{lm}]^T$ are the observed displacements, $T = [t_{12}, t_{23}, t_{34 ... t_{lm}}]^T$ are the epochs and the υ_k is the LOS displacement rate for pixel (k). A weighted least-squares inversion is used to determine the best fitting υ_k and corresponding errors:

$$\upsilon_k = \Sigma_k T^T \sigma_\phi^{-1} \phi \tag{3.21}$$

$$\Sigma_k = [T^T \sigma_\phi^{-1} T]^{-1} \tag{3.22}$$

The inversion is weighted by σ_ϕ^{-1}, the inverse of a Variance-Covariance Matrix (VCM) which accounts for the temporal correlation which occurs when using the same epochs in multiple interferograms. When any ratio of a residual and its associated a priori standard deviation from the VCM is more than a given threshold,the pixel is deemed to have an unreliable phase observation so the observation is removed and the value recalculated. However, if the number of observations falls below the given threshold Ψ, it is removed from the ratemap. Additionally, if the standard deviation of a pixel's estimated rate is greater than a specified threshold the pixel is removed from the final ratemap.

π-RATE also generates a time series for each pixel within the velocity ratemap. The time series is required to remove the atmospheric phase contribution to the ratemap. The time series is determined using a Small BAseline Subset (SBAS) approach which inverts for a time series using Singular Value Decomposition (SVD). This method allows for the inclusion of interferograms offset by large baselines that are not connected to a large network of interferograms. For the inversion set-up see Berardino et al. (2002).

3.3.2 Atmospheric Phase Correction

The atmospheric artefacts within the unwrapped interferograms must be addressed (see section 3.1.3). As shown by the CSK data set (Section 3.2.1), it is important to apply an atmospheric correction. I tested two different techniques; applying a spatio-

temporal filter included within π-RATE (i.e. removing an Atmospheric Phase Screen (APS)) and using independent data to approximate the correction.

APS Estimation and removal with π-RATE

π-RATE includes an APS estimation method which can remove phase contributions from the atmosphere (ϕ_{atm}). The atmospheric noise has a high spatial correlation and low temporal correlation, whereas volcanic deformation is highly correlated through both space and time. Therefore the volcanic signal can be separated from noise using an appropriately designed filter.

π-RATE uses a three-stage algorithm. First, the raw time series is obtained at each pixel using a least squares inversion. Second, a Gaussian high-pass temporal filter removes the volcanic deformation signal. This is removed from each epoch leaving the signals with a low temporal correlation. Third, a spatial filter is applied to each epoch with a low-pass Butterworth filter. The size of the filter is determined by the width parameter (α), which describes the temporal variability of the atmospheric noise. Subsequently, the estimated APS for each epoch is subtracted from the raw time series and the interferograms are re-computed from the corresponding master and slave epochs. I tested a range of APS filter sizes and found the optimum to be a temporal window of 4 days. This provided enough smoothing but did not significantly alter the natural variation in the data set.

ECMWF correction

As with the CSK data I have also used ECMWF data to remove atmospheric noise. However, for the TSX data I have applied the ECMWF derived correction to each interferogram before creating the ratemap and time series with π-RATE processing.

3.3.3 Stackmap and Time series

The ratemaps that result from both the π-RATE and ECMWF derived atmospheric corrections are shown in Figure 3.11. The ECMWF corrected ratemap shows a larger magnitude signal and a more coherent map. The increased coherence from the ECMWF correction is because the APS model in π-RATE requires a linear rate of ground displacement. Pixels with a non-linear rate of displacement will be removed, and this can lead to the removal of many pixels depending on threshold values.

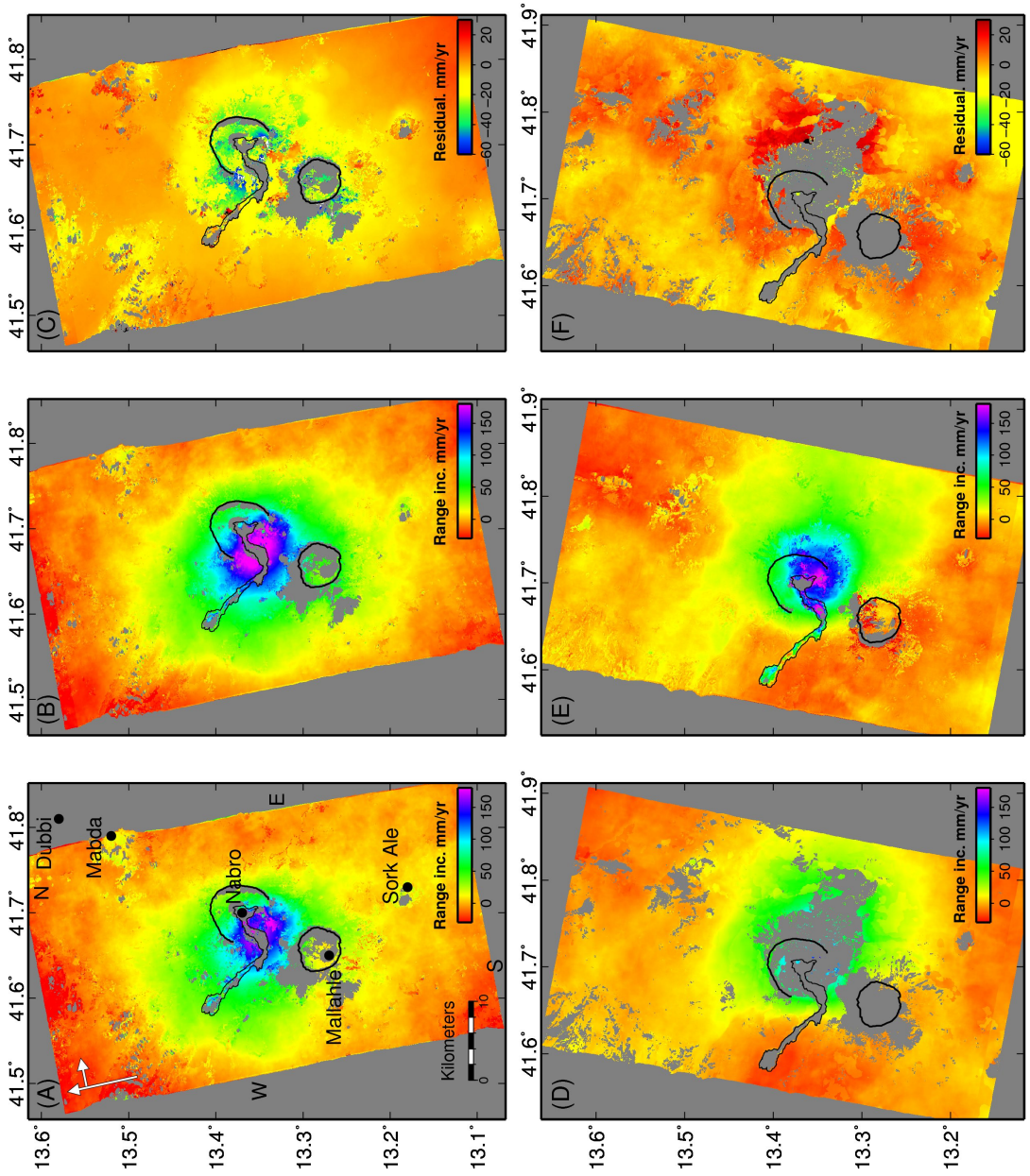

Figure 3.11: π-RATE calculated ratemap of displacement with a spatiotemporal filter applied to the ascending and descending tracks (A and D). B and E show the ratemaps corrected for atmosphere with ECMWF model used for correction, for the ascending and descending tracks, respectively. The difference between the corrected ratemaps.

In both ascending and descending data sets, I observe a nearly circular, ∼12-km-wide range increase, which is centred on the south west region of Nabro's caldera (Figure 3.11). As the signal is a range increase in both data sets, the volcano is subsiding following the eruption. The extent of the 17 km-long lava flow emplaced by the eruption is clearly distinguishable as a sliver of subsidence originating from the south-west opening of the caldera. There is no observable ground deformation at neighbouring volcanoes. However, the ascending ratemap does show some change from the far field measurement on Mabda volcano, this is likely to be atmospheric noise as it is not visible in the descending data set. The other possibility is that it is moving in a direction to which the ascending viewing geometry is insensitive. The time series of ground displacement with the ECMWF correction are shown in 3.12 and 3.13.

3.4 Summary

In all ratemaps I observe a nearly circular, ∼12-km-wide range increase, which is centred on the south west region of Nabro's caldera (Figures 3.7 and 3.11). As the signal is a range increase in both data sets the ground surface is moving away from the satellite. Therefore, the volcano is subsiding following the eruption. The maximum subsidence rate is ∼30 cm/yr which was observed by the CSK satellite around the south east side of the smaller caldera-bound lava flow. The descending TSX track shows the extent of the 17 km-long lava flow emplaced by the eruption as a clearly distinguishable region of subsidence which originates from the caldera and extends toward the west. The lava flow is subsiding because of thermal contraction and compaction. There is no clear signal of ground deformation at Mabda, Mallahle and Sork 'Ale volcanoes observable from either the CSK or TSX data sets.

On Nabro, the most significant artefact was caused by temporal and spatial variations of the atmospheric conditions over the observation period. This is somewhat surprising due to the low relief of Nabro and the arid climate of the Afar region. To remove this signal from the true ground deformation observed by the TSX satellite, I tried using both a spatio-temporal filter, and by using auxiliary data from the ERA-Interim ECMWF model. I found that by using the ECMWF model I was able to keep more pixels coherent over the vent region, especially in the descending track. High coherence ratemaps are vital to constrain the inversions performed in future chapters. The importance of the ECMWF correction is highlighted by the CSK timeseries. The

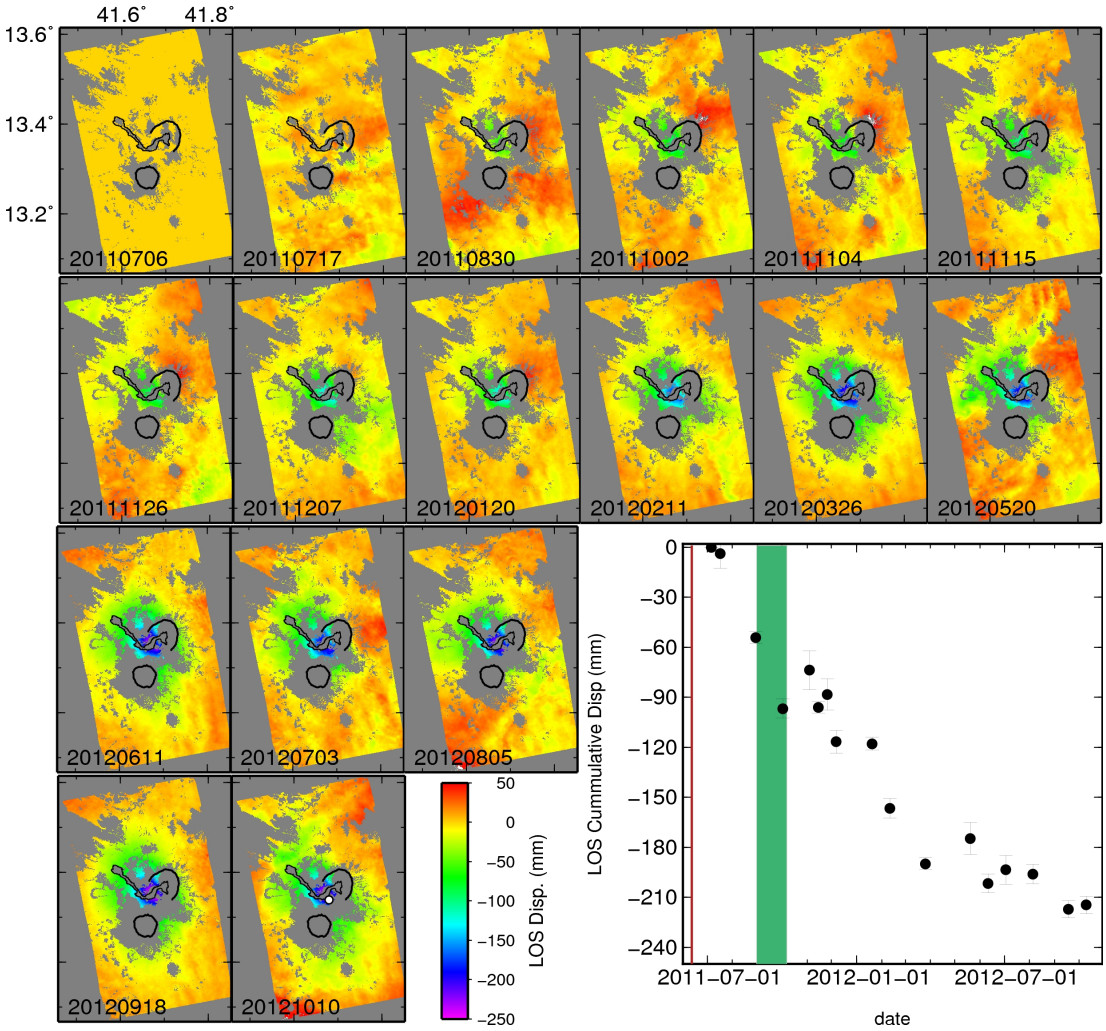

Figure 3.12: Cumulative displacement for each epoch (yyymmdd) in the TSX ascending time series. The graph shows the displacement over the observation period for the example pixel highlighted in white on date 20121010. The red line highlights the eruption date. The green shaded region is the time period of the seismic analysis in Chapter 2.

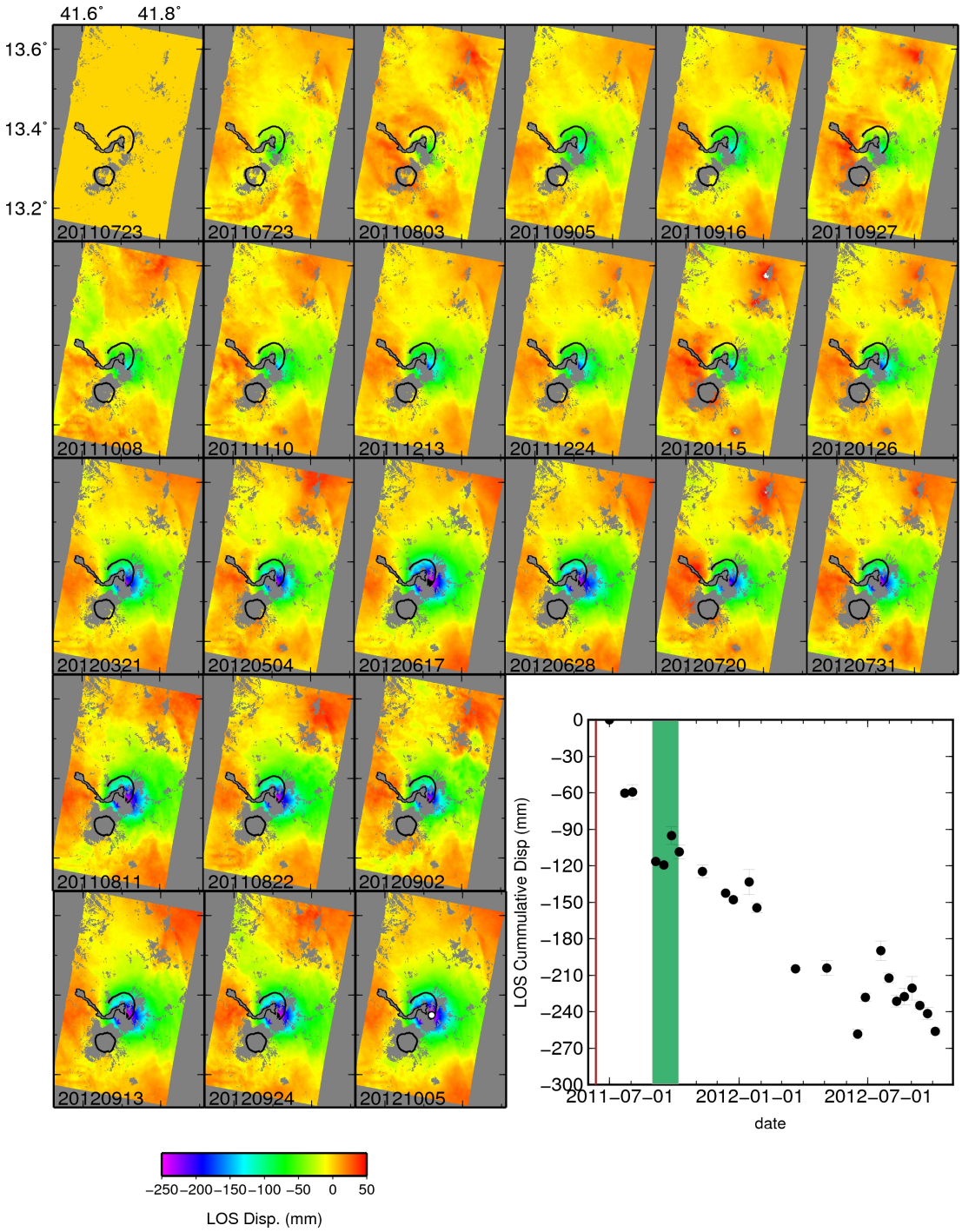

Figure 3.13: Cumulative displacement for each epoch (yyymmdd) in the TSX descending time series. The graph shows the displacement over the observation period for the example pixel highlighted in white on date 20121010. The red line highlights the eruption date. The green shaded region is the time period of the seismic analysis in Chapter 2.

atmospheric artefacts make it appear that episodic range change reversals have occurred. This would have had implications for the interpretation of volcanic processes, such as magma chamber recharge. However, after the correction has been applied, these reversals are removed. Although the ECMWF correction requires additional processing steps to create the delay maps, I find significant benefits using this independent data set. Furthermore, π-RATE has an in-built function to apply this correction, so it easy to implement either pre- or post- time series estimation.

I do not observe any ground displacement in the surrounding region. The circular subsidence signal does not extend laterally toward Mallahle volcano where one might suggest a magmatic or at least hydraulic link to exist, e.g. similar to that observed at Mauna Loa and Kiluea (Rhodes et al., 1989, Klein, 1982) or at Fernandina Volcano (Bagnardi and Amelung, 2012). It is important to note that this does not rule out the existence of magma pockets within the surrounding region, rather if they are present they have not been perturbed by the eruption and exist in isolation.

In this Chapter I have processed TSX data from SAR images to interferograms which were subsequently used to generate ratemaps of ground displacement. I applied two different atmospheric corrections to this data set to find the best solution for the removal of noisy signal. I also corrected the CSK ratemap from IREA for atmospheric signal. I now have 3 ratemaps and timeseries: CSK descending, TSX ascending and TSX descending that are corrected for atmospheric effects. In the following chapter I will investigate analytical models to quantify the source of the displacement observed.

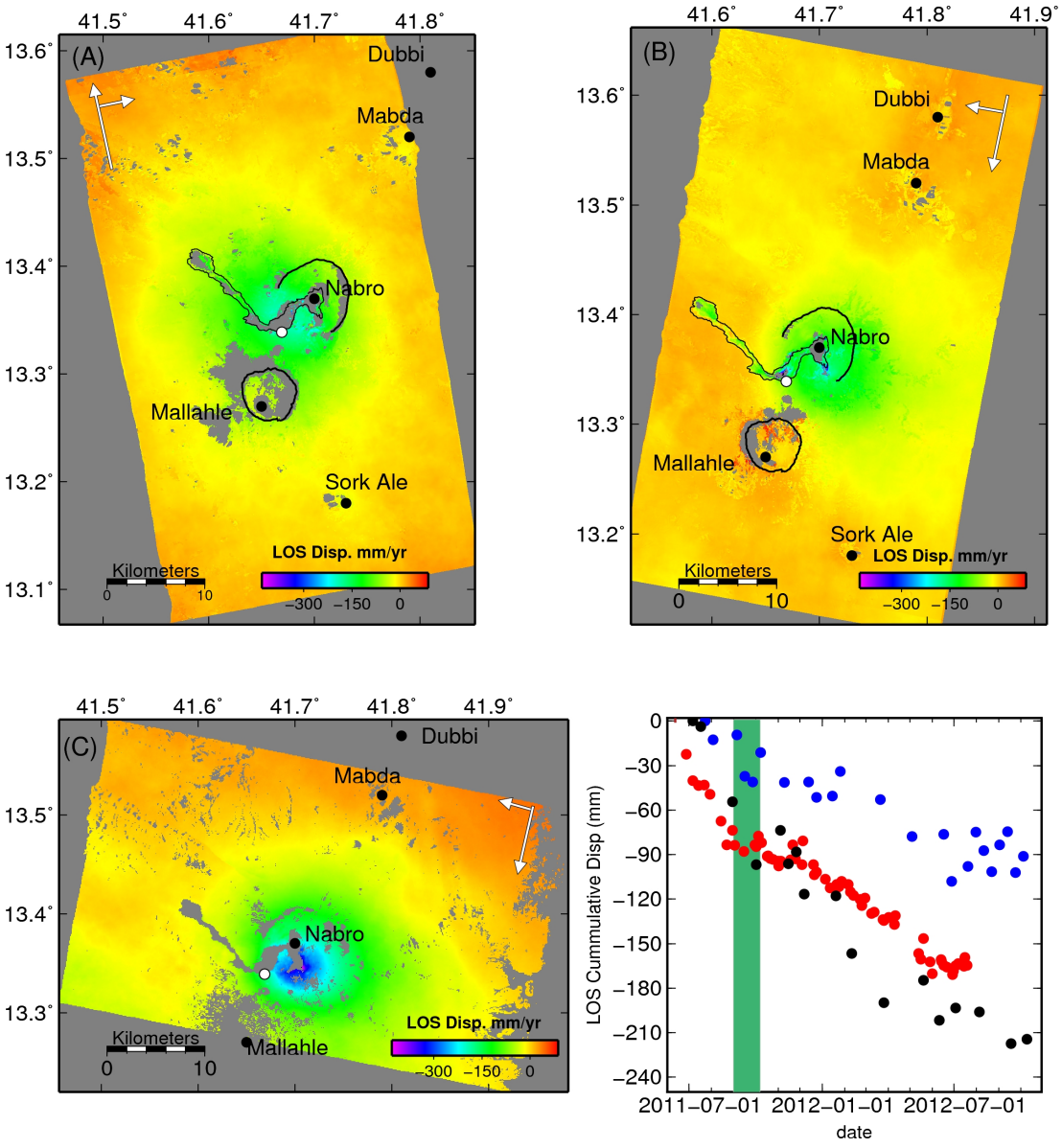

Figure 3.14: A) TSX ascending ratemap produced with π-RATE, with ECMWF atmospheric correction. B) TSX descending ratemap produced with π-RATE, with ECMWF atmospheric correction. C) CSK ratemap with ECMWF atmospheric correction. Lower right graph: LOS displacement for TSX ascending (black), TSX descending (blue), CSK (red), for the point highlight in white on A), B) and C).The green shaded region is the time period of the seismic analysis in Chapter 2

Chapter 4

Analytical modelling of linear rate ground displacement

4.1 Introduction

Ground deformation observed at active volcanoes is caused by magmatic and tectonic processes occurring at depth. The parameters of the source causing the deformation (i.e. the source depth, geometry and its volume change) can be estimated by fitting the observed surface displacement to predictions from analytical solutions, assuming the Earth can be approximated as an isotropic homogeneous elastic medium. The most commonly used analytical solutions in volcanic settings are those of Mogi (1958), Okada (1985), Fialko et al. (2001) and Yang et al. (1988). The success these models is based on their ability to match the observed deformation at a wide variety of different volcanoes across the globe as well as their computational simplicity (e.g. Unzendake volcano, Japan (Nishi et al., 1999); Gada Ale Volcano, Afar (Amelung et al., 2000); Mt. Etna, Italy (Puglisi et al., 2001); Okmok volcano, Alaska (Mann et al., 2002); and Three Sisters, Oregon (Riddick and Schmidt, 2011)). The Mogi and Okada models are applied here to explain the ground deformation observed by InSAR at Nabro, with further discussion of Fialko and Yang models.

4.2 The Mogi Model: A classic magma chamber

Mogi (1958) found that surface displacements observed around volcanoes can be explained as the inflation and/or deflation of a magma chamber at depth. He formulated an analytical solution of surface deformation induced by a point source buried at depth

within an elastic homogeneous isotropic half space. Figure 4.1 shows the coordinate system, geometric relationships and displacement predictions used for the Mogi geometry (as well as the finite pressure source, a small sphere). I give a brief overview of the solution here, but a full derivation can be found in Segall (2010).

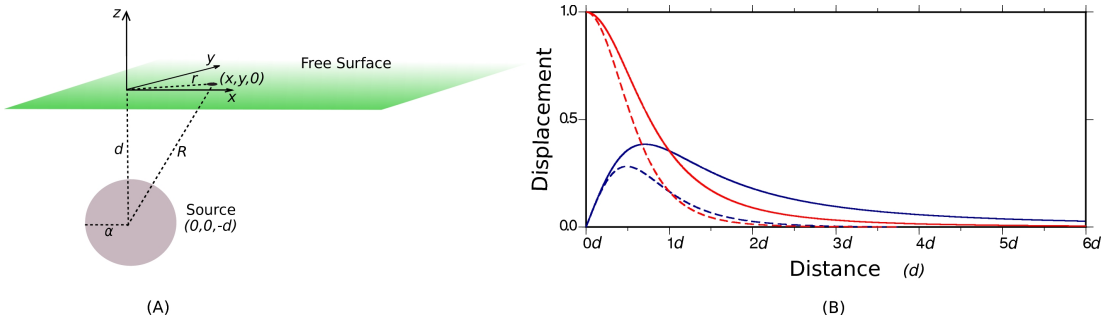

Figure 4.1: A) Mogi and Finite Pressure source (McTigue 1987 solution) coordinate system and geometric relationships which predict surface displacements from a point source in an elastic, homogeneous, isotropic half-space, after Lisowski (2006). B) Normalised profiles of vertical (red) and horizontal (blue) displacements for a Mogi (solid) and Finite pressure (dashed) sources with distance in terms of source depth (d). The displacements of the Mogi and Finite pressure sources are normalised by $\alpha^3\Delta P((1-\delta\nu)/Gd^2)$. The maximum horizontal displacement is found at a distance of $\simeq 0.5d$ for the Mogi source and at $\simeq 0.7d$ for th Finite, and the horizontal displacement becomes greater than the vertical at distances along the free surface larger than $1d$.

For a deep magma chamber (radius-to-depth ratio of $\alpha/d << 1$,) buried in an elastic medium (i.e. the Earth's crust) with a Poisson's ratio of $\nu = 0.25$, the horizontal and vertical surface displacements are given by

$$\begin{pmatrix} U_x \\ U_y \\ U_z \end{pmatrix} = \frac{3\alpha^3\Delta P}{4\mathrm{GR}^3} \begin{pmatrix} x \\ y \\ d \end{pmatrix}, \tag{4.1}$$

where, U_x, U_y, U_z are the horizontal and vertical surface displacements at the point $(x, y, 0)$, R is the distance to the centre of the source, G is the shear modulus of the surrounding medium and ΔP is the pressure difference between the medium and the interior of the source. The surface displacements are axisymmetric with the maximum vertical displacement (U_z) centred directly above the source, whereas the maximum horizontal displacement occurs at $\pm(1/\sqrt{2})d$ and exceeds the vertical displacement at distances larger than $\pm d$ from the origin (Figure 4.1B). The strength of the source (C) is:

$$C = \frac{3\alpha^3\Delta P}{4GR^3}. \tag{4.2}$$

The magnitude of the surface displacement is proportional to the source volume and pressure change, and inversely proportional to its depth and the shear modulus of the surrounding medium. Since the pressure and radius of the source contribute to the scaling coefficient, their individual contribution to the surface displacement cannot be defined. By comparing observations with predictions I can estimate the location and strength parameter of the magma chamber.

The deformation field observed at the surface is related to the amount of magma entering or leaving the magma chamber (ΔV_{magma}). For a magma chamber modelled with a Mogi source, the simplest estimate of the volume at depth is the integrated volume of surface change, referred to the edifice volume change ($\Delta V_{edifice}$),

$$\Delta V_{edifice} = \int_{z=0}^{\infty} u_z 2\pi r \text{ dr} = 2\pi \text{C}. \tag{4.3}$$

The volume change of the Mogi source can be calculated as

$$\Delta V_{Mogi} = \frac{4}{3}\pi C. \tag{4.4}$$

Therefore, combining equations 4.3 and 4.4 shows that the edifice volume change is 3/2 times the volume change of the Mogi source,

$$\Delta V_{Mogi} = \frac{2}{3}\Delta V_{edifice}. \tag{4.5}$$

The difference between these two volumes is due to dilation of the crust above the Mogi source (Delaney and McTigue, 1994). When magma is injected in a solidified magma chamber the volume of magma entering the chamber, ΔV_{magma}, is equal to ΔV_{Mogi}. However, if magma is injected frequently in a chamber where magma is already ponding, the effect of the compression of the pre-existing magma must be considered in order to obtain a correct estimate of ΔV_{magma}.

4.2.1 Magma compressibility

$\Delta V_{magma} \neq \Delta V_{mogi}$ because magma is compressible. As magma flows out of the system, the magma which remains in the chamber will expand; conversely if magma enters the chamber the initial magma will compress. The volume change (ΔV) of a material following a pressure change ΔP is

$$\Delta V = V \frac{1}{K*} \Delta P \tag{4.6}$$

where $K*$ is the effective bulk modulus (incompressibility) of the material. Therefore, ΔV_{magma} and $\Delta V_{edifice}$ are related by (Johnson et al., 2000),

$$\Delta V_{magma} = \frac{2}{3}\left(1 + \frac{4\mu}{3K*}\right) V_{edifice} \tag{4.7}$$

where μ is the shear modulus of the crust. As it is the mass, rather than volume, which needs to be conserved when considering a magma plumbing system, the discrepancies between ΔV_{magma} and $\Delta V_{edifice}$ will also be affected by the strength of the crust (Rivalta and Segall, 2008). The effective bulk modulus, $K*$, of the magma in the reservoir is dependent on several factors:

$$K^* = K \text{ for } \mathrm{N} < \mathrm{N_s} \tag{4.8a}$$

$$K^* = \frac{K}{1 + \frac{KN\rho_m RT}{P^2\omega}} \text{ for } \mathrm{N} > \mathrm{N_s}, \tag{4.8b}$$

where K is the gas-free melt bulk modulus, ρ_m is the bulk magma density, $R = 8.314\mathrm{m^3Pa/mol°K}$ is the gas constant, T is the absolute temperature (K), P is the average pressure assumed to be lithostatic and ω is the molar mass of gas. N is the total weight fraction of a gas phase in the magma and N_s is the maximum amount of this gas phase which can be dissolved. The gas plays an important role as exsolution will increase compressibility (Rivalta and Segall, 2008).

Rivalta and Segall (2008) provide the following formula for the compressibility of magma related to the ratio (r_v) of the erupted volume (V_E) and the measured magma chamber volume change (ΔV),

$$r_v = \frac{V_E}{\Delta V} = 1 + \left(\frac{4}{3}\mu\beta_m\right). \tag{4.9}$$

Using the co-eruption volumes from Goitom et al. (2015), I have calculated an estimate of the magma compressibility under Nabro:

$$\beta_m = \frac{3}{4\mu}\left(\frac{V_E}{\Delta V} - 1\right) = \frac{3}{4\times 3}\left(\frac{0.1}{0.07} - 1\right) = 1.07 \times 10^{-10}\mathrm{Pa^{-1}}. \tag{4.10}$$

This is lies within the $0.4 - 2 \times 10^{-10}$ range given by Spera (2000) for degassing

Basalts.

4.3 The Yang Model: Dipping Prolate Spheroid

It is unlikely that an actual magma chamber is perfectly spherical. A progression from the Mogi geomtery is that of a three-dimensional ellipsoidal cavity. Yang et al. (1988) determined an accurate solution of a dipping prolate spheroid in an elastic, homogeneous half-space. In this scenario, the magnitude of the three components of deformation are dependent on 7 parameters: pressure change ($\Delta P/\mu$), the aspect ratio (b/a), the source location (x_0, y_0, z_0), the dip andle θ and the strike (ϕ) (Battaglia et al., 2013) (Figure 4.2). The Greens functions which relate these parameters to displacement are complex and are not given here, see Yang et al. (1988), Segall (2010), Battaglia et al. (2013).

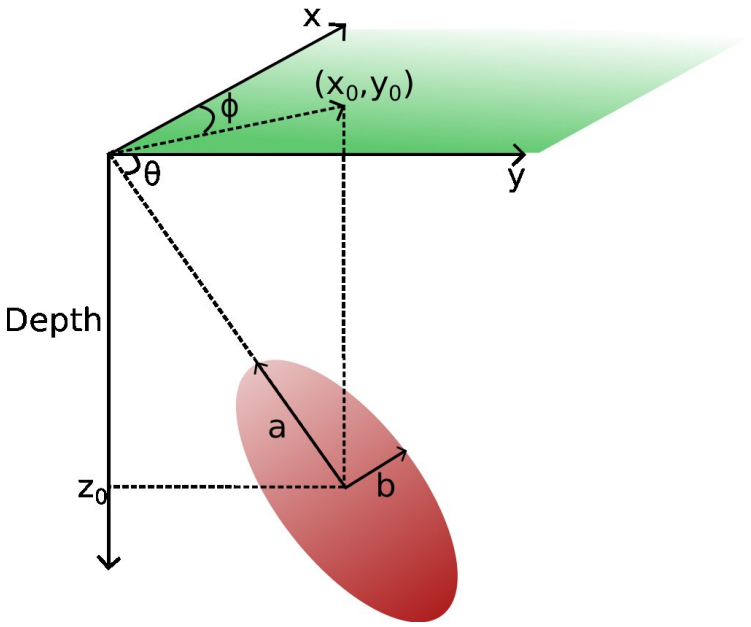

Figure 4.2: After Battaglia et al.,(2013). the set-up of the spheroida; source formulated by Yang et al., 1988. x, y, z are local cartesian coordinates, with the source located at x_0, y_0, z_0), a and b are semimajor and semiminor axes respectively. The spheroid has a dip and strike of θ and ϕ respectively. The shear stress acting on the surface of the ellipsoid is assumed to be 0 and the normal stress is equal to the pressure change ΔP.

I inverted the ground displacement oberserved by InSAR at Nabro using the Yang model geometry. I found that the major and minor axis of the elliposid were approximately equivalent, effectively producing a Mogi source. This has also been observed at Okmok (Lu et al., 2010), therefore for simplicity I continued with only Okada and

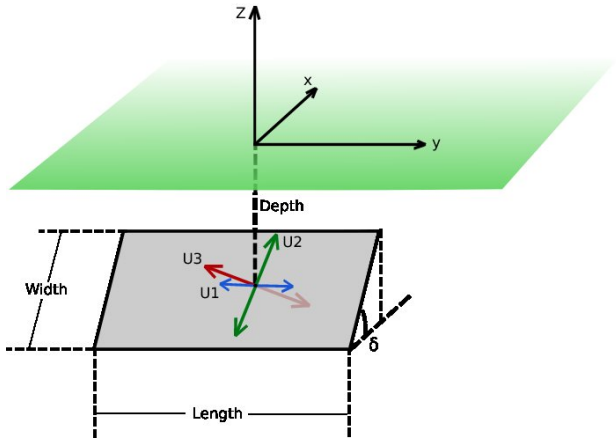

Figure 4.3: The Okada model coordinate system and geometric relationships which predict the surface deformation due to a rectangular tensile dislocation in an elastic, homogeneous, isotropic half-space, after Lisowski (2006). The crack strikes parallel to the x axis and dips at angle δ from the horizontal. For sill sources the crack is horizontal,δ=0.

Mogi geometries.

4.4 The Okada Model: Sill

Sills are horizontal magma bodies in which the length and width are many times greater than its thickness. These shapes are often modelled as a uniform tensile dislocation on a rectangular surface (Okada, 1985), which is buried at depth in an elastic, isotropic, homogeneous halfspace. The 'Okada' model has a total of ten source parameters: the length, width, strike and dip (δ) of the rectanglular sill, its location (x, y, depth) as well as opening ((U_3), strike-slip (U_1) and (U_2)). Here, I use a purely tensile opening (U_1 and U_2 equal 0) on a horizontal sill ($\delta = 0$) (Figure 4.3). In this case the surface displacement profiles are axisymmetric and very similar to a Mogi source, but the vertical surface displacements are 20% greater and the horizontal displacements are 10% smaller (Lisowski, 2006). I have used the solutions of Okada (1985) to calculate the surface displacement caused by a given horizontal sill ($\cos\delta \neq 0$), they are shown in Appendix D. The vertical and horizontal displacements predicted by an Okada tensile dislocation using different source parameters such as source size, depth and opening are described in Figure 4.4.

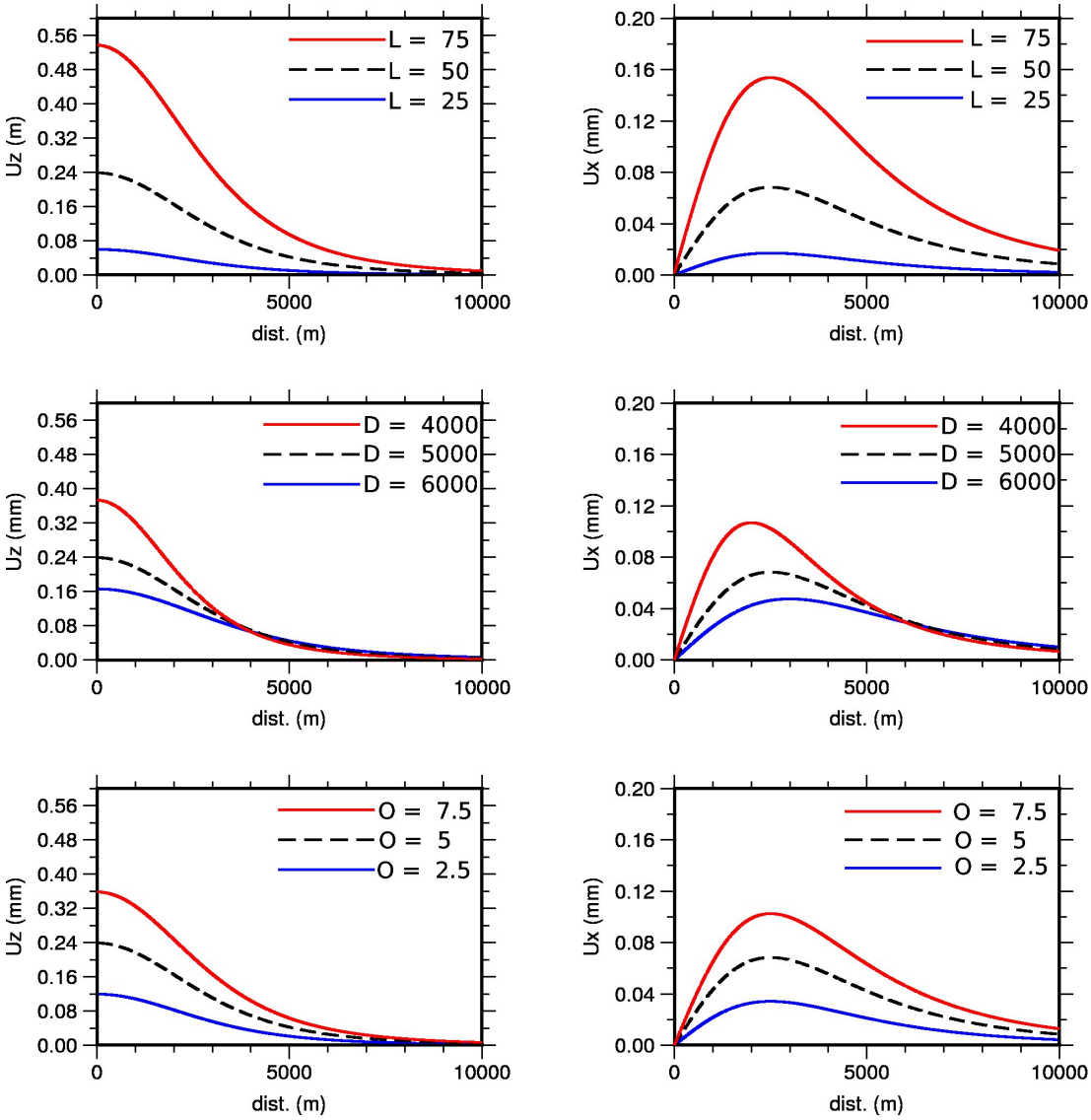

Figure 4.4: Vertical (U_z) and horizontal (U_x) surface displacements in mm for different values of parameters in the source term for an Okada dislocation. The dip and strike were both set to 0 to create a horizontal opening which simulates a sill. Parameters tested are the source size W, where $W = L$, source depth (d), and source opening (O). The dashed black line is the displacement for the original source with values: W= 500 m (L=500), d= 5 km, opening = 5 m. Poissons ratio remained constant ($\nu = 0.25$).

4.5 The Fialko Model: Penny Shaped Crack

Sills can also be modelled as a finite pressurised horizontal circular cracks (Figure 4.5). For the full solution see Fialko et al. (2001). The penny shaped crack adequately models the ground displacement at Alutu and Bora volcanoes located within the MER and at Menengai, Suswa, Longonot and Paka further south in Kenya (Biggs et al., 2009, 2011). Similar to an Okada solution, this model has a large vertical to horizontal displacement ratio and also produces a symmetric displacement. However, the Fialko model calculates a pressure, rather than a volume change, which makes the inversion computationally expensive. When only volume change is required the Okada model is much more time efficient. From map view, an Okada model is rectangular and the penny shaped Fialko crack model is circular, which at shallow depths generates different displacement patterns at the surface. It is common practise to solve for two Okada models offset by 45° for a computationally simple inversion, but without square edges. Then if a measurement for pressure is required, the displacements can be inverted using the Fialko model whilst searching for only this parameter, which will be computationally faster. However, I find that edge effects are not significant in my modelling of Nabro, due to a deep source and I will work interms of volume rather than pressure change, so I will invert for an Okada rather than Fialko geometry.

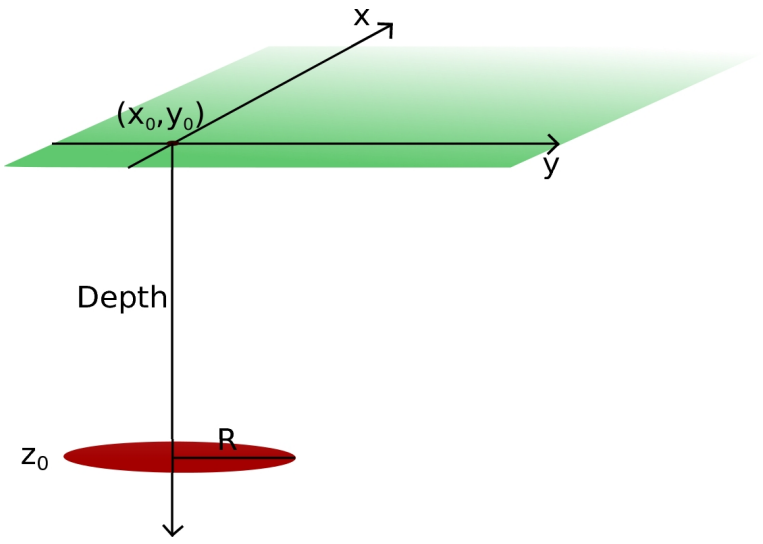

Figure 4.5: Schematic of the Fialko model, which examines the surface displacement resulting from a horizontal circular crack in a homogeneous half spcae.

4.6 Potential Limitations

Analytical solutions such as the Mogi, Yang, Okada and Fialko formulations are widely applied to volcanic deformation studies (Nishi et al., 1999, Amelung et al., 2000, Puglisi et al., 2001, Mann et al., 2002, Biggs et al., 2009, Riddick and Schmidt, 2011, Biggs et al., 2011), as the equations require few input parameters and predictions have been shown to provide a good fit to observations. These models assume an isotropic, homogeneous elastic half space with a horizontal free surface and a Poisson's ratio of 0.25. The reliability of my Mogi and Okada model predictions depends on how well these models approximate the real conditions of the Nabro magma chamber (i.e. (Wang and Anderson, 1995, Masterlark, 2007)). Here I discuss potential limitations of a relatively simple approximation of a plumbing system and crust.

Conceptual models of volcanoes based on field observations, geochemistry and geophysics often describe these structures as layers of inhomogeneous erupted materials with varying degrees of crystallisation, alteration and fracturing (Trasatti et al., 2003). Furthermore, the layering of materials will create a medium with some degree of anisotropy, as the medium stiffness will vary in the different directions. The Poisson's ratio for the bulk crustal representation of rocks is often $0.25< \nu <0.32$ (Christensen, 1996). Therefore, ν used here (0.25) is the lower bound rather than the bulk average for volcanic rock. The displacements predicted by a Mogi source in a homogeneous isotropic elastic half space differ by 30% between the upper ($\nu = 0.32$) and lower bounds ($\nu = 0.25$) (Masterlark, 2007). Additionally, the presence of pore fluid can alter the sensitivity of the displacements to the Poisson's ratio. The Poisson's ratio can have a large effect on the ability of the model to match observations, therefore if the Poissons ratio is known through existing petrophysical data then this should be used. Masterlark (2007) gives a linear correction which can annul the errors introduced by using an incorrect Poisson's ratio, but it requires a priori knowledge about the source strength.

The global topography is well known through the Shuttle Radar Topography Mission (SRTM) and the Advanced Spaceborne Thermal Emission and Reflection Radiometer (ASTER) Global Digital Elevation Model (GDEM) mission. Topography alters the distance to the source and may have a greater impact for shallower sources, suggesting that the flat surface assumption is invalid. Steep sided (10°), cone shaped topography, causes vertical displacements to flattened at the summit (Cayol and Cornet, 1998). This

can potentially lead to assuming an incorrect source geometry and pressure change if the topography is not taken into account. Cayol and Cornet (1998) over estimate a source volume change by 50% for a slope of 30°. However, Masterlark (2007) shows that of the 'isotropic, homogeneous elastic half space with a horizontal free surface and a Poisson's ratio of 0.25' assumptions, topography, along with heterogeneity, have the smallest effects on the Mogi solutions. Masterlark (2007) comments that in the absence of information other than ground displacement, the elastic, isotropic, homogeneous half space with a horizontal free surface and a Poisson's ratio of 0.25 fits the observations as well as the more complex models such as for Okmok volcano (Masterlark, 2007). Measurements of the geomechanical and anisotropic properties at Nabro volcano are lacking and the presence of an extensive fracture system or geothermal activity has not been reported. Furthermore, I do not have any a priori knowledge about the depth and geometry of the Nabro magma chamber: no previous deformation studies have been conducted in the area. Therefore, I find that modelling the Nabro chamber with relatively simple Mogi and Okada models assuming a homogeneous isotropic elastic half-space with a Poisson's ratio of 0.25 is an adequate assumption at Nabro.

4.7 InSAR inversion

4.7.1 Data

To find the model that best fits the InSAR observed subsidence, I performed a non-linear inversion (see section 4.7.2) of the deformation ratemaps as obtained in Chaper 3. Initially, I obtained ratemaps using the longest time-series of acquisitions available for each TSX and CSK dataset (Figure 3.13, 3.12 and 3.7, Chaper 3). However, as the acquisitions made by the TSX and CSK satellites span slightly different time periods I recalculated the ratemaps using only data spanning the same time period-from 06/07/2011 to 19/07/2012. The two sets of ratemaps are not significantly different, indicating that the rate of deformation was the same during the different time periods spanned by the TSX and CSK acquisitions. Therefore, in my inversion I used the ratemaps calculated by including the full data sets for each satellites, as using more extensive data in each ratemap minimised the sources of error.

For each data set the components of the unit vector, n_x, n_y, n_z pointing from the ground to the satellite were calculated by the following formulae:

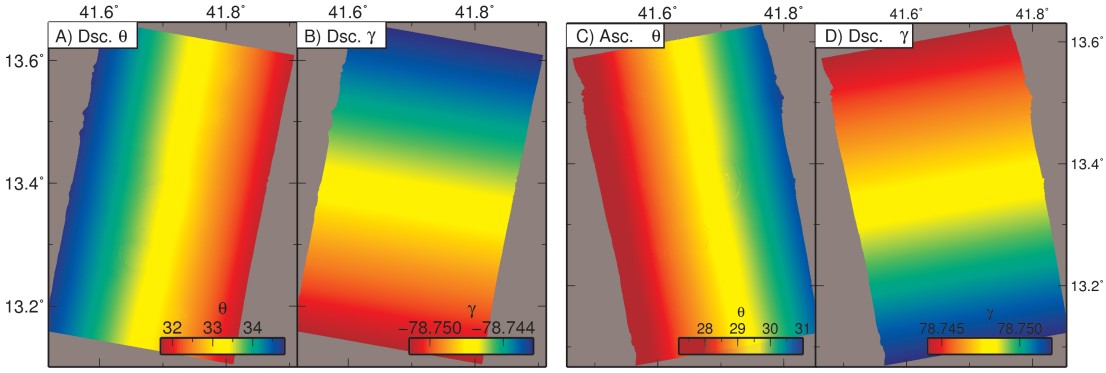

Figure 4.6: Contours of A) Descending incidence angle, B) Descending azimuth angle, C) Ascending incidence angle and D) Ascending azimuth angle.

$$n_x = \cos\gamma \cdot \sin\theta \tag{4.11a}$$

$$n_y = -\sin\gamma \cdot \sin\theta \tag{4.11b}$$

$$n_z = -\cos\theta, \tag{4.11c}$$

where n_i is the look vector for each direction, γ is the azimuth and θ is the incidence angle, both in radians (Figure 4.6). Before the inversion, I also downsampled the two sets of InSAR ratemaps to 1 ×1 km pixels using a nearest neighbour algorithm (Cover and Hart, 1967) and changed the projection from decimal degrees to UTM using ERMAPPER (ERDAS, 2008). The TSX data used in the inversion is shown in Figure 4.7. The ascending data set was also masked out in the far field, to reduce the total number of observations input into the inversion algorithm.

4.7.2 Okinv and Oksar

I used the inversion code 'Okinv' developed by Clarke (1996) and Wright et al. (1999) to find the best fit parameters assuming a Mogi or Okada model of the Nabro magma chamber. The code uses a downhill simplex inversion; the parameter space contains a simplex (a multidimensional generalisation of a triangle) with one more vertex than the number of parameters to be estimated. Initial values for the vertices are chosen by the user. Each parameter is altered in turn, creating a new vertex. The vertex has a penalty value associated with it, determined by the RMS misfit for that particular

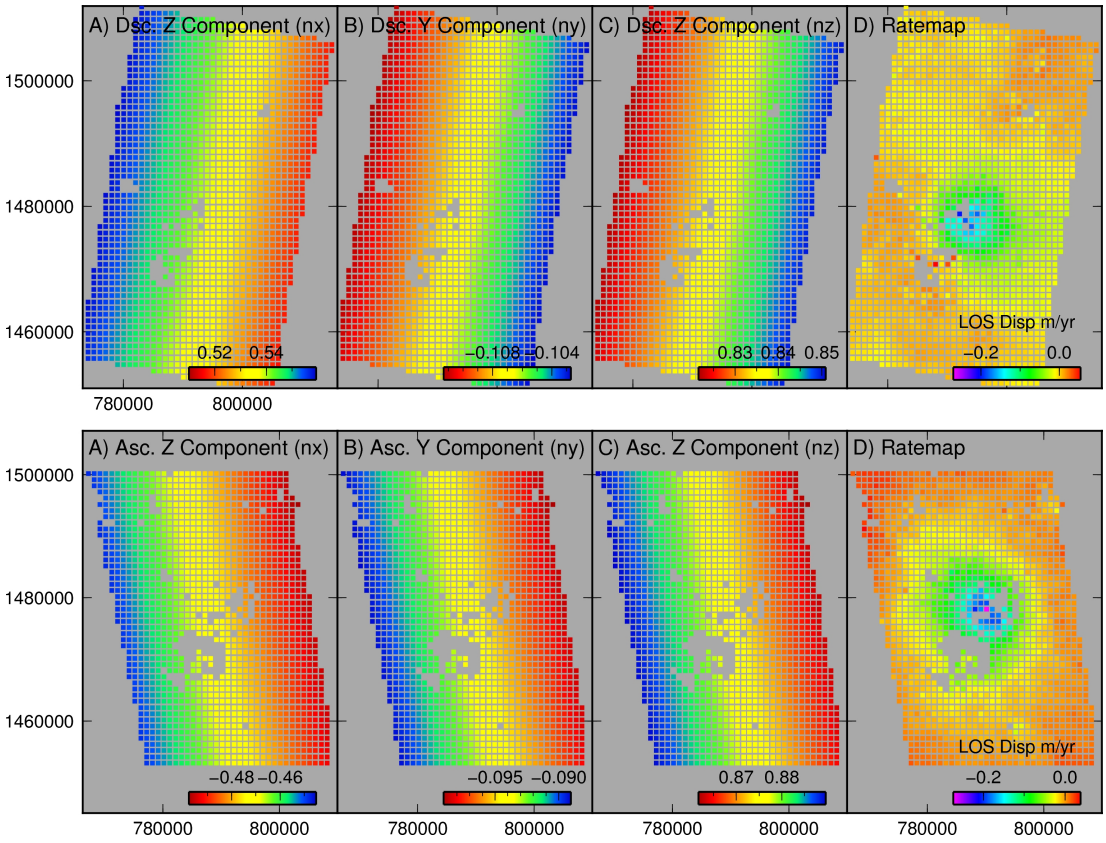

Figure 4.7: Data used as input to the inversion. Top: Descending, downsampled components of the unit vector: (A) X component, (B) Y component, (C) Z component and (D) LOS ratemap. Lower: Ascending, downsampled components of the ascending unit vector: (A) X component, (B) Y component, (C) Z component, (D) LOS ratemap. The ascending data set was cropped in the far field as not to exceed the maximum number of data points for the inversion.

solution. The process of inversion replaces the highest penalty value with a new one, determined by reflecting the point then contracting or expanding the edges of the simplex. The process is referred to as 'downhill' as the RMS misfit of the solution always decreases to a minimum. To ensure this is the global, rather than local minima, the Okinv program restarts the search from different initial values which have been specified. The best-fit model is found when the inversion finds the same solution three times. The Okinv program can solve for a range of linear and nonlinear parameters assuming either a Mogi or Okada model, or a combination of the two. Subsequently, I then used a forward model to generate the LOS displacement which results from the best fit model defined by Okinv.

4.7.3 Mogi solution

Initially, I tried to jointly invert the CSK and TSX data sets together. I used Okinv to solve for the location (latitude and longitude), depth and volume decrease of a Mogi source using the ratemaps obtained in Chapter 3. The best fit model is situated at 6.66 depth, and located at 13.35°N and 41.70°E, with a volume decrease of 0.05 km^3. For the TSX data this model fits the data well and has a RMS misfit of 1.3 cm/yr and 1.5 cm/yr for the ascending and descending tracks respectively. However, this model does not fit the CSK data equally well, giving an RMS residual of 2.8 cm/yr. The outputs from this one-step Mogi model inversion are shown in Figures D.1 and D.2, which can be found in Appendix D. In order to determine the reasons of the different goodness of fit I analyzed the data set separately and I have approached the inversion in two steps. First I invert the ascending and descending TSX dataset jointly, then I fix the resulting geometry and invert the CSK data for the volume change only. This method still allows me to exploit the different looking geometries inherent in the TSX ascending and descending tracks, so my final best fit model will be fairly well constrained (Yun et al., 2006).

Using this two step approach, I find the best-fitting Mogi source based on the TSX data is situated at 6.4 ±0.3 km depth, and located within ∼200 m of 13.356°N and 41.695°E, with a volume decrease of 0.036±0.003 x10^{-3} km^3, analogous to the results from the joint inversion of CSK and TSX. This model has an RMS misfit of 1.3 cm/yr and 1.5 cm/yr for the TSX ascending and descending tracks respectively. The best fitting CSK source has a somewhat higher volume reduction of 0.06±0.006 x10^{-3} km^3

and a somewhat improved RMS misfit of 2.7cm/yr. The residuals from this two step approach are very similar, but I think this approach is better because the two TSX geometries guaranties a good constraint on the model geometry and I can still make use of the CSK data as well. The volume differences may be a result of atmospheric noise which has not been removed at the processing step described in 3.2.1.

The Mogi model fits the data well (Figure 4.8). For the ascending data set, the RMS of the null model is 3.7 cm/yr, modelling the deformation field reduces this to 1.3 cm/yr, which is similar to the RMS of the farfield (1.1 cm/yr) and is a similar magnitude to that introduced by the atmosphere (1 cm/yr) (section 4.8). Both tracks have the highest residuals over the new lava flow and this is to be expected since cooling and contraction of the lava flow is not related to the deformation sources being modelled. Additionally, I suggest that lava loading is causing high residuals within the caldera adjacent to the incoherent lava flow seen in the CSK data set. Therefore these high residuals can be ignored. As the magma source is quite deep the model meets the specification that the magma chamber needs to be small relative to its depth ($\alpha/d \rightarrow 0$) McTigue (1987).

Furthermore, I took north-south and east-west cross-sections of the InSAR data and predictions based on the Mogi model to further visualise the match between the observations and my best-fit model (Figure 4.9 and 4.10). The cross-sections show that the model fits the NS and EW shape and magnitude of the data set well. On the descending track the NS transect shows the largest misfit to data, this is likely due to some unwrapping errors caused by the high incoherence on Mallahle caldera. The EW transects show that the model fits shape and magnitude of the TSX data set well. Modeling of the CSK data shows that local residual subsidence remains on top of the caldera, suggesting that some atmospheric noise may still affect the CSK data (Figure 4.10F).

4.7.4 Sill solution

I also used Okinv to invert the InSAR data assuming a sill geometry. Again, I used the TSX data to solve for the depth, location, geometry and opening of the sill. I fixed the length of the sill to 1 km as initial runs of the inversion with large bounds on the sill parameters would lead to models with unrealistically small sills and a large opening. I tested different lengths of the sill, between 500 m and 2 km and found that 1 km gave

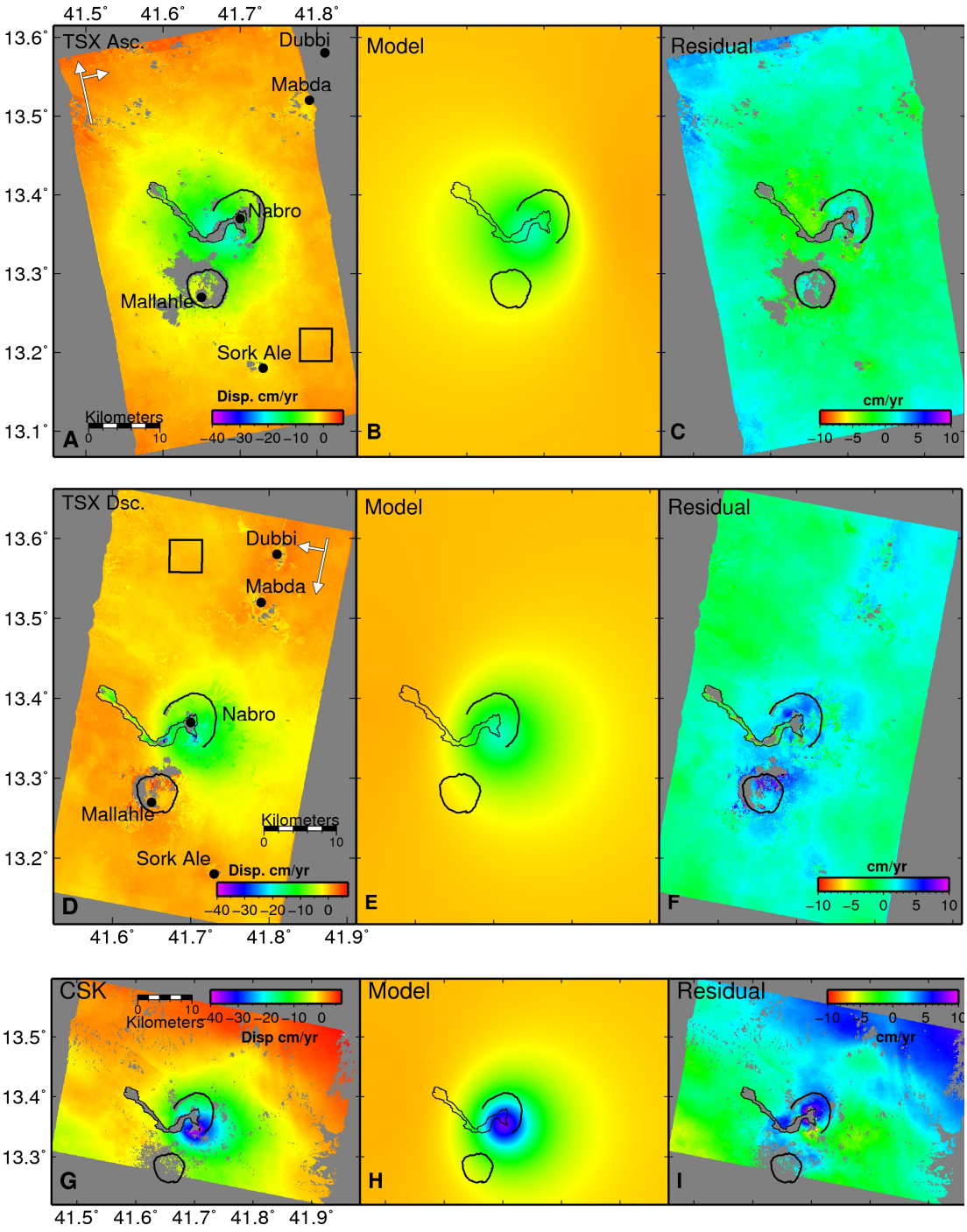

Figure 4.8: Ratemaps, the LOS displacement from the best-fit Mogi model and the resulting residuals: A) Observed TSX ascending rate map, B) Mogi model of deformation for ascending track, C) Residual motion, D) Observed TSX descending ratemap, E) Mogi model of deformation for descending track, F) Residual ground motion, G) Observed CSK ratemap of ground displacement, H) Mogi model of deformation for CSK track and I) Residual ground motion.

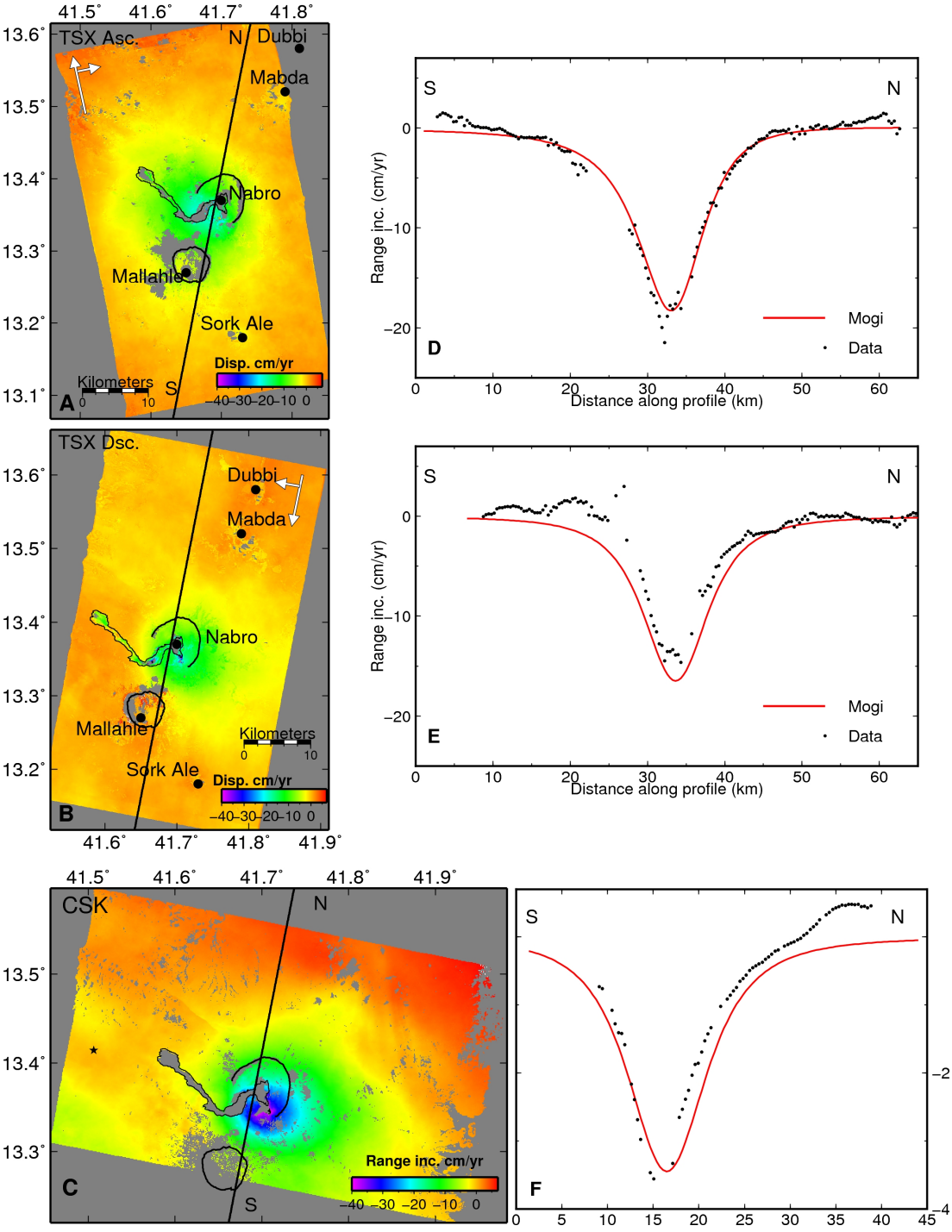

Figure 4.9: The position of the N-S transect on each ratemap, and corresponding graph of that displacement and the results from the Mogi model. A) Observed TSX ascending rate map of ground movement. B) Observed TSX descending rate map of ground movement. C) Observed CSK ratemap of ground movement. D) Profile of ground displacement along transect N-S on A) and from the Mogi model. E) Profile of ground displacement along transect NS on B) and Mogi model. F) Profile of ground displacement along transect N-S on C) and Mogi model.

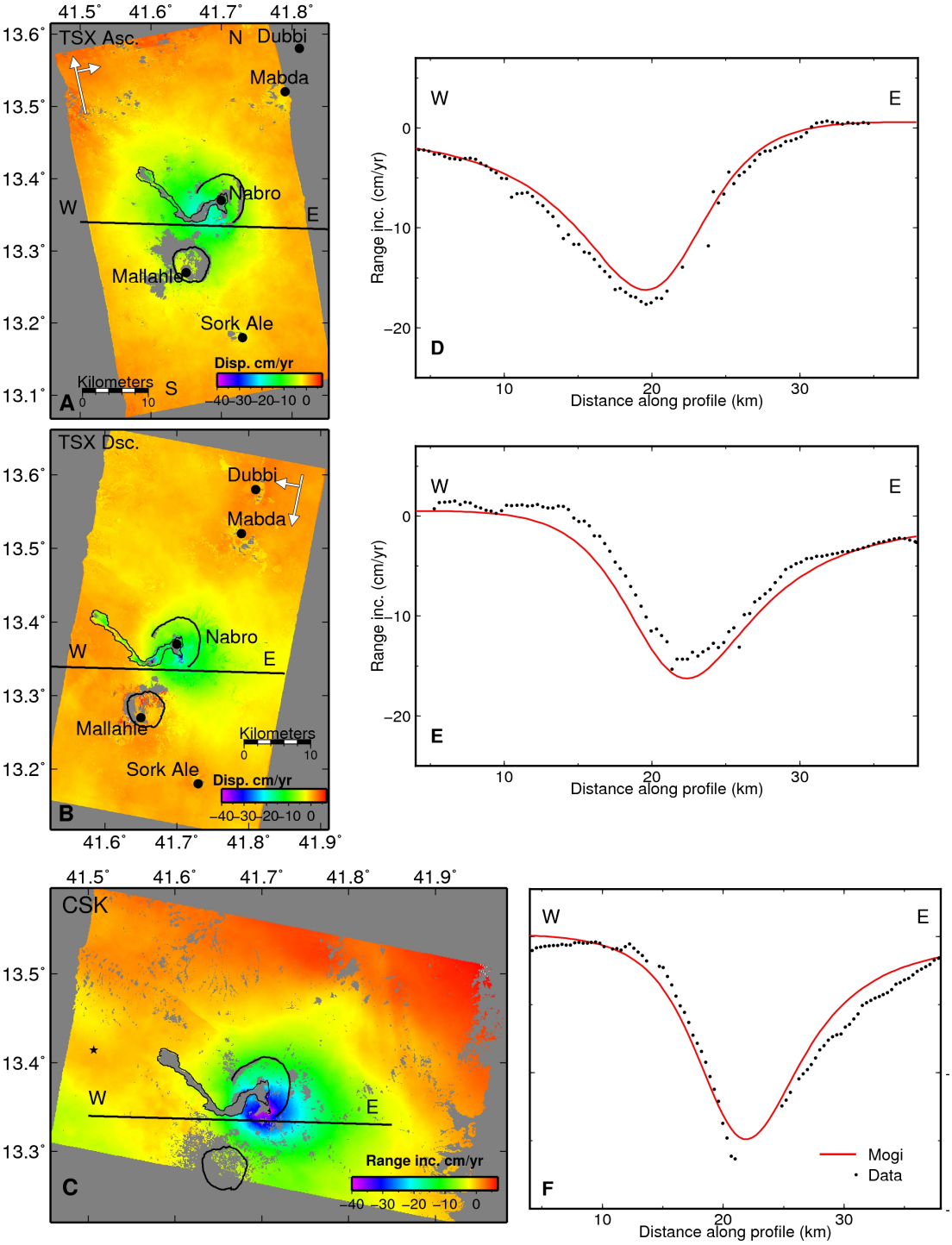

Figure 4.10: The position of the E-W transect on each ratemap, and corresponding graph of that displacement and the results from the Mogi model. A) Observed TSX ascending rate map of ground movement. B) Observed TSX descending rate map of ground movement. C) Observed CSK ratemap of ground movement. D) Profile of ground displacement along transect E-W on A) and from the Mogi model. E) Profile of ground displacement along transect E-W on B) and Mogi model. F) Profile of ground displacement along transect E-W on C) and Mogi model.

the lowest RMS misfits. Again, I performed a joint inversion of the TSX ascending and descending data, then I fixed the depth and location of the sill according to the TSX inversion results and I inverted the CSK data for the volume change.

I find the best fitting solution for the TSX data is a horizontal square sill, with 1 km long sides, located within ∼200 m of 13.347°N and 41.701°E, at a depth of 10 ±0.5 km, undergoing 39±3 m of contraction. While the best fit model for the CSK data gives a contraction of 76 m ± 6 m. The ground displacement modelled by the sill has an RMS misfit of 1.4 cm/yr, 1.5 cm/yr and 2.6 cm/yr, for the TSX ascending, descending and CSK tracks respectively.

As in the Mogi case, maps of the residuals show good agreement between the TSX models and the observations (Figure 4.11). The CSK observed subsidence is again over predicted on the northern half of the caldera and at the summit, which is not apparent in the TSX data, and not modelled by the sill source. Therefore, this signal is probably not related to the magma source, but a result of atmospheric noise which is not entirely removed during preprocessing. Again, I plotted the WE and NS transects to show the model fit to the data (Figure 4.12 and 4.13).

The Mogi and Okada solutions provide a comparable fit to the data but have different depth of the source, 6.6 km and 10 km respectively. In terms of RMS, the Mogi model appears to fit the data marginally better than the sill, furthermore the Mogi model is a simpler explanation than the sill as the Mogi requires less model parameters than the sill model. Additional data is required to distinguish which of the 2 model geometries is most plausible at Nabro.

4.8 Error Analysis

To determine the parameter errors for the non-linear inversions I performed a Monte Carlo simulation of correlated noise using the same method as Parsons et al. (2006); the method accounts for spatially correlated atmospheric noise. I found the best fit 1-D covariance function that approximates the atmospheric noise in a region of the output ratemaps where no significant displacements occurred. Second, I extracted an area nearly 8×8 km^2 large in both the TSX and CSK ratemaps using ERMAPPER. The exponential function

$$C(r) = \sigma^2 \exp^{-\alpha r} \tag{4.12}$$

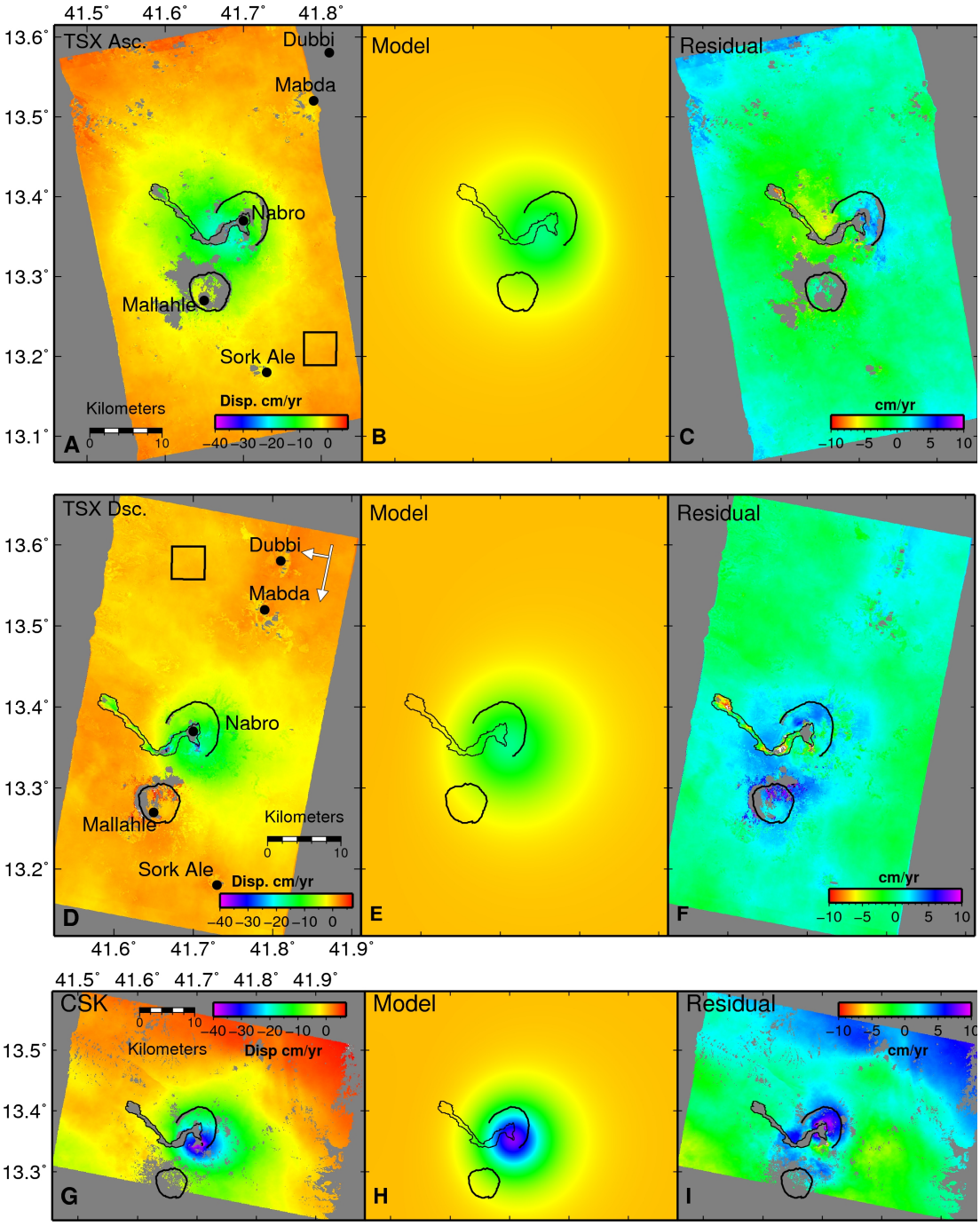

Figure 4.11: Ratemaps, the LOS displacement from the best-fit Sill model and the resulting residuals: A) Observed TSX ascending rate map, B) Sill model of deformation for ascending track, C) Residual motion, D) Observed TSX descending ratemap, E) Sill model of deformation for descending track, F) Residual ground motion, G) Observed CSK ratemap of ground displacement, H) Mogi model of deformation for CSK track and I) Residual ground motion.

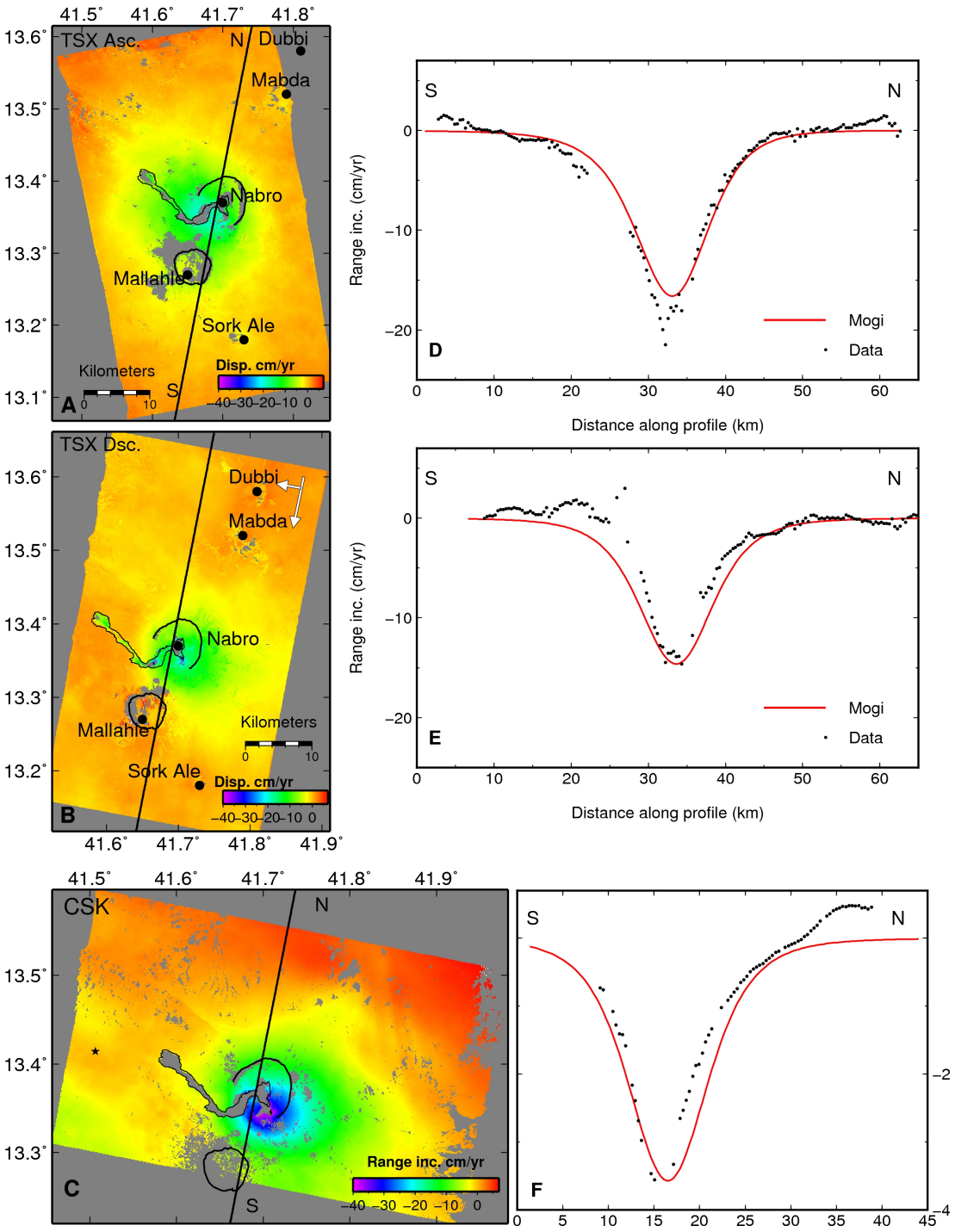

Figure 4.12: The position of the N-S transect on each ratemap, and corresponding graph of that displacement and results from the sill model. A) Observed TSX ascending rate map of ground movement, B) Observed TSX descending rate map of ground movement, C) Observed CSK ratemap of ground movement, D) Profile of ground displacement along transect N-S on A) and from the sill model, E) Profile of ground displacement along transect N-S on B) and Mogi model, F) Profile of ground displacement along transect N-S on C) and sill model.

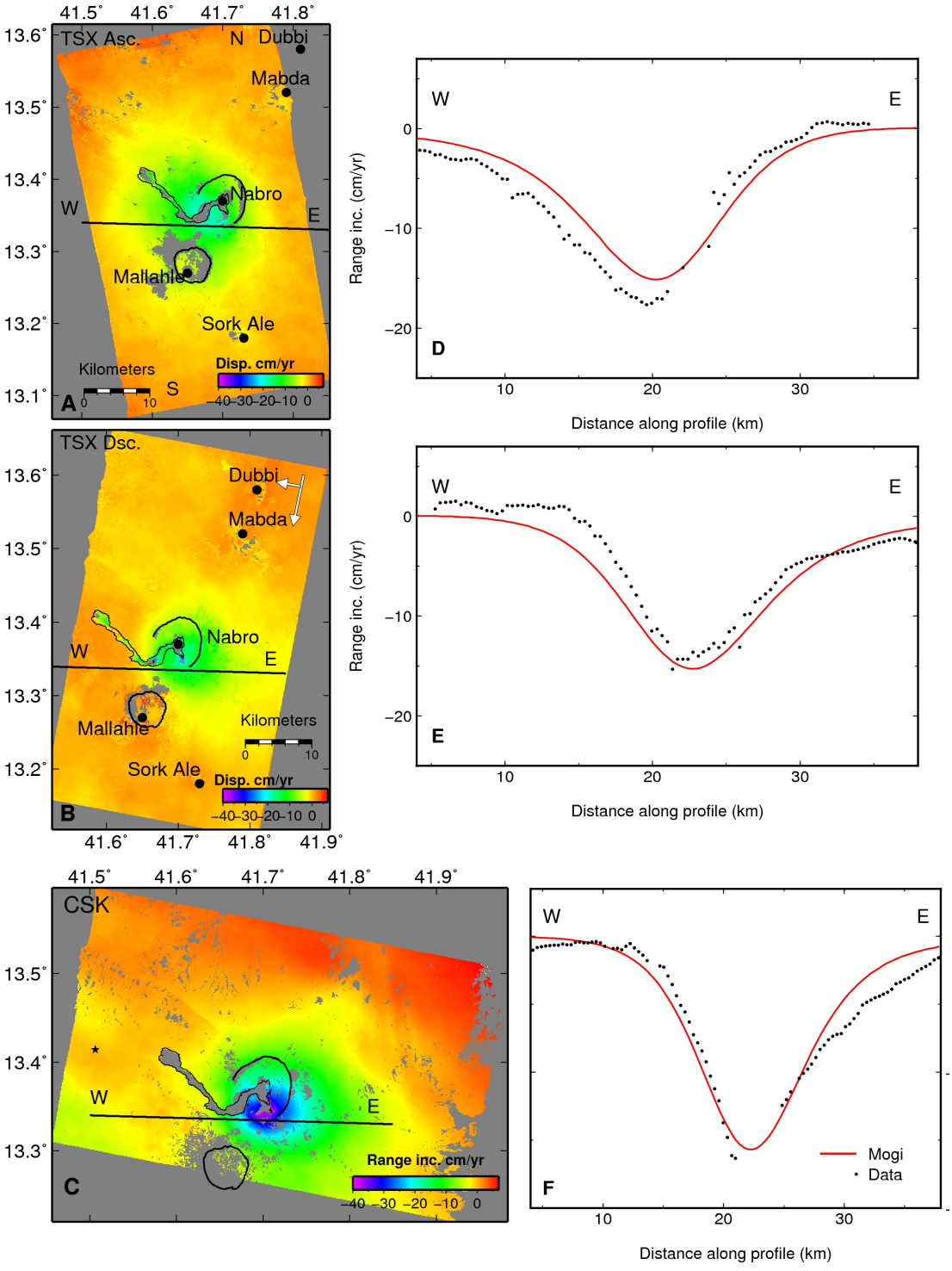

Figure 4.13: The position of the E-W transect on each ratemap and a graph of that displacement and that which results from the sill model. A) Observed TSX ascending rate map of ground movement. B) Observed TSX descending rate map of ground movement. C) Observed CSK ratemap of ground movement. D) Profile of ground displacement along transect EW on A) and from the Mogi model. E) Profile of ground displacement along transect EW on B) and sill model. F) Profile of ground displacement along transect E-W on C) and Mogi model.

is used to approximate the observed covariance function in these regions, where σ^2 is the variance, r is the separation of the observations in kilometers and α determines the correlation length scale of the atmospheric length scale. For the TSX ascending track, $\alpha = 0.233$ which is equivalent to a length scale of ∼4.3 km and for the TSX descending track $\alpha = 0.221$ which is equivalent to a length scale of ∼4.5 km. For the CSK data $\alpha = 0.307$ which is equivalent to a length scale of ∼3.2 km. For all data sets σ is approximately 1 cm. Assuming the noise structure is isotropic and identical throughout the image, I created a full variance-covariance matrix, Σ, for the extracted region. A vector of spatially correlated noise, y, is calculated from x, a vector of Gaussian, uncorrelated noise, by

$$\mathrm{y} = \mathrm{Lx}, \tag{4.13}$$

with a mean of zero and a standard deviation of 1, where L is the Cholesky Decomposition of the variance-covariance matrix (Rubinstein, 2006). This correlated noise is then added back to the original data to create a new noisy data set (Figure 4.14). The added noise is within a range of ±3 cm. This procedure was repeated 100 times to create 100 noisy data sets. Lastly, the noisy data sets were inverted for the same model parameters. The distribution of these results determined the uncertainties in the model parameters. This method was performed for both the ascending and descending tracks and applied to both the Mogi and sill models. This technique also illuminates any trade-offs between different model parameters. In Figure 4.15 and Figure 4.16, I have plotted the parameters against each other, illustrating a strong trade-off between the volume change or opening of the source and its depth.

4.9 Discussion

I have found that the depth, location and volume of the Nabro magma chamber can be successfully estimated by inverting the InSAR ratemaps assuming analytical models. However, the depth of the chamber varies depending on whether a Mogi or the sill (Okada) model is assumed. The Mogi solution suggests a depth of 6.4±0.3 km, whereas the sill solution yields a depth of 10±0.5 km. The RMS misfit of the Mogi model is only a slightly better fit to the data (TSX ascending RMS: Mogi=1.3 cm/yr Okada=1.4 cm/yr). Based on this measurement both models are plausible. Therefore,

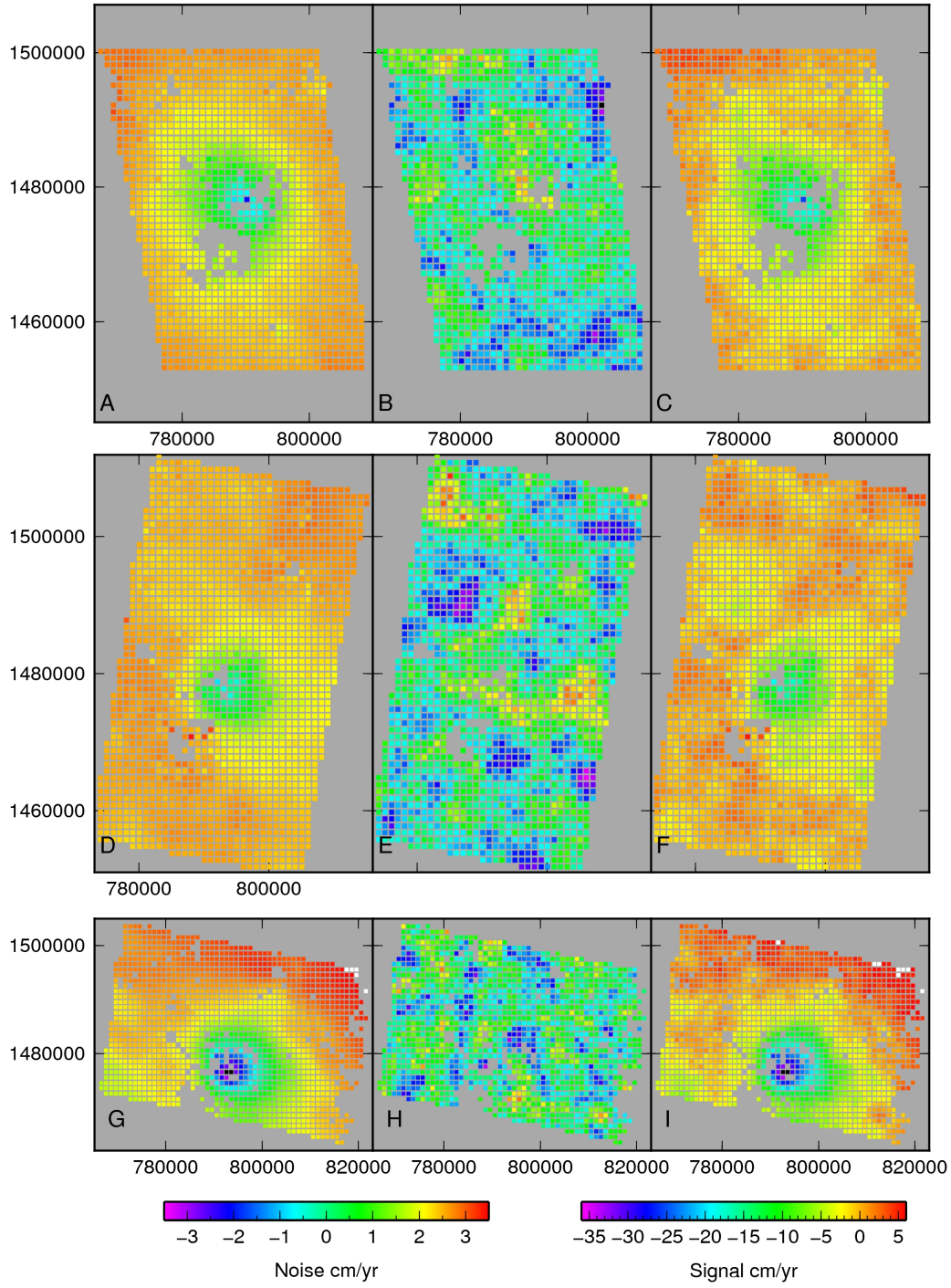

Figure 4.14: Examples of random noise, in cm/yr, added to the observed TSX and CSK ratemaps.

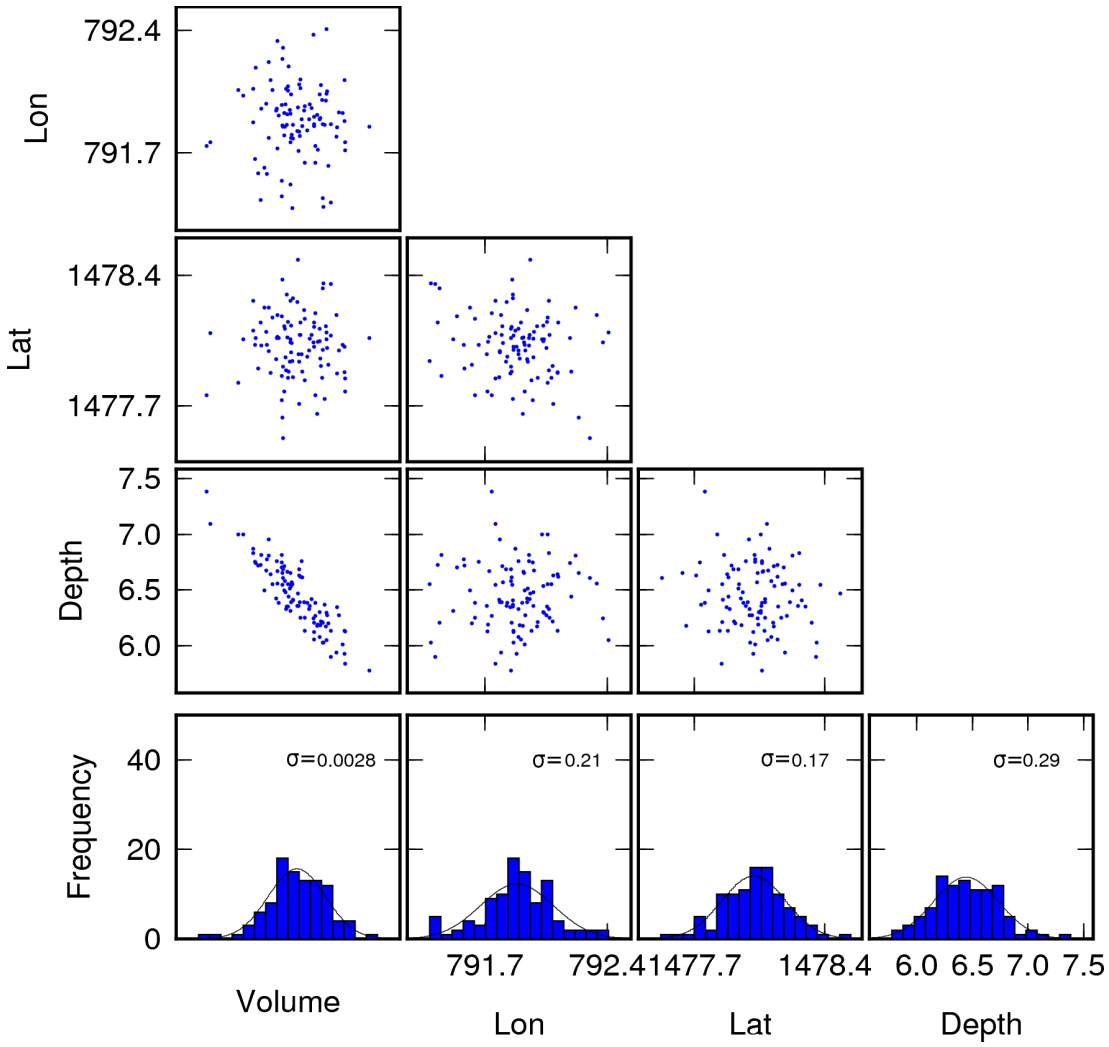

Figure 4.15: TSX Mogi inversion tradeoffs for parameters latitude, longitude, depth and volume change.

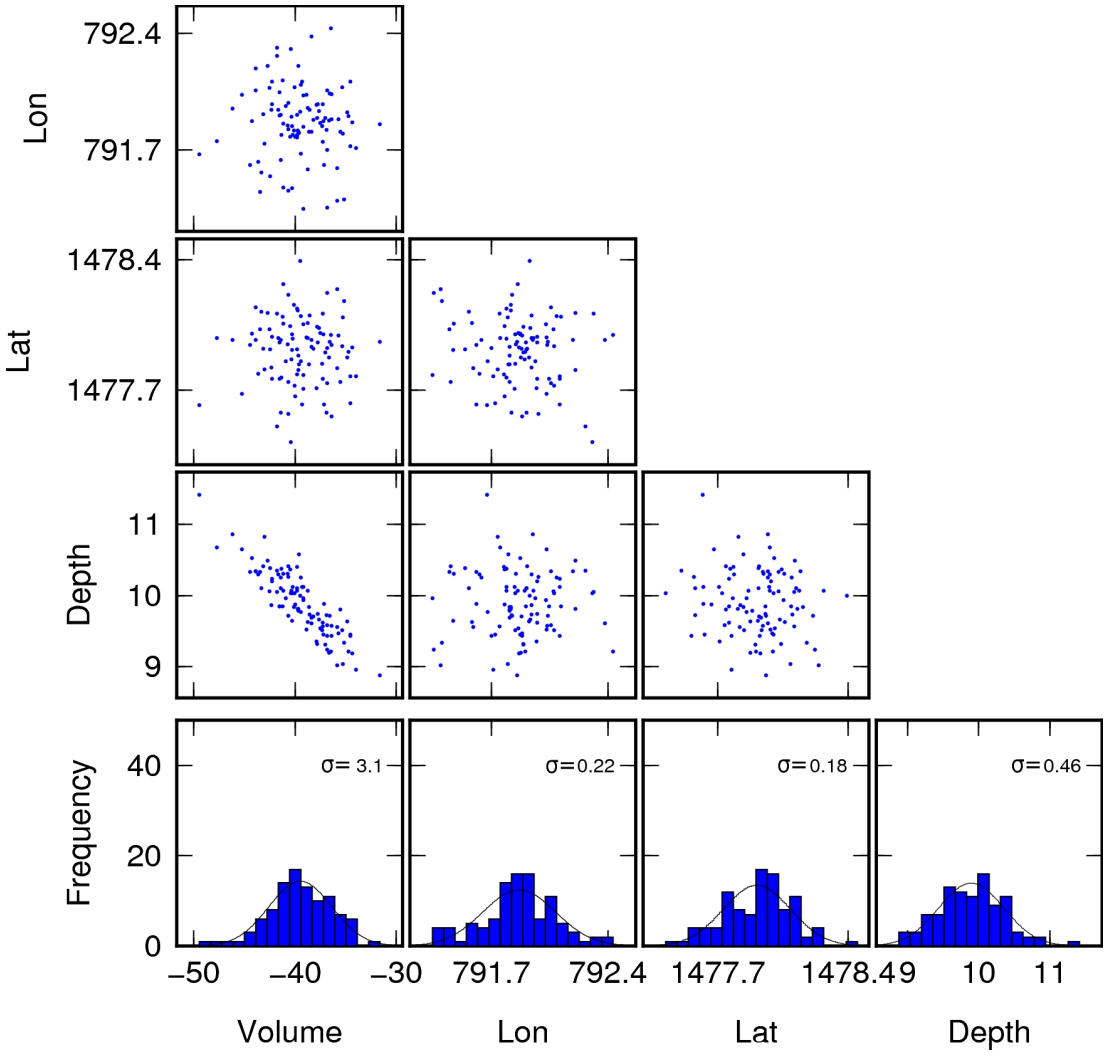

Figure 4.16: TSX Okada inversion tradeoffs for parameters latitude, longitude, depth and volume change.

	Latitude	Longitude	Depth (km)	Closing
Mogi	13.356°N ±200 m	41.695°E ±200 m	6.4 ±0.3	0.036±0.003x$10^{-3}$$km^3$
Sill	13.347°N ±200 m	41.701°E ±200 m	10 ±0.5	39±3 m

Table 4.1: Best fit Mogi and Sill models following inversion of TSX data acquired on an ascending track between 6 July 2011 and 10 october 2012, and on descending track between 1 July 2011 and 5 october 2012. The source change output from the CSK inversion with was a volume decrease of 0.06±0.006 x10^{-3} km^3 from a Mogi model, or a closing of 76 m ± 6 m from an Okada model. The CSK data between 6 July 2011 and 19 July 2012 was used. Note this removes the first date of the total CSK acquisition.

I have separated the observed displacement and model predictions into their vertical and horizontal components. As mentioned previously, the Mogi and Okada models produce similar vertical displacements, but the horizontal displacements produced by the Mogi source are much larger. Figure 4.17 shows that the Mogi model fits the data only slightly better in the vertical component. However, the Mogi model does a significantly better fitting the large horizontal displacement. I had difficulty reconciling the magnitude of the TSX and CSK data displacements. The CSK data observed a larger displacement than the TSX and CSK data which meant I had invert the CSK only for volume change after fixing the geometry using the outputs from the TSX inversion. When I go on to invert the displacement at each time step the volume decrease for on at each epoch the models coincide, which suggests that the discrepancy is due to residual atmospheric noise on the initial acquisition dates which have been included in the ratemaps. Otherwise, the datatsets should be reprocessed using the same workflow. Also the early signal may have contained some co-eruption displacement that is not related to the post eruption signal analysed in this study. Table 4.1 summarises the inversions inputs and outputs.

Using the spatial distribution of the earthquake hypocentres and the horziontal component of displacement, my preferred source model is the Mogi solution, as I interpret seismic cluster 2 (Figure 2.4) as the region of brittle failure immediately above the magma chamber, which has fractured to accommodate the volume change. In this interpretation, the magma chamber is situated in the shadow zone immediately below this cluster. However, it is likely that the Mogi model is an oversimplification of the geometry of the magma chamber. The magma chamber under Nabro could be a more complex system of numerous lenses and dykes of partial melt across a depth range of 6

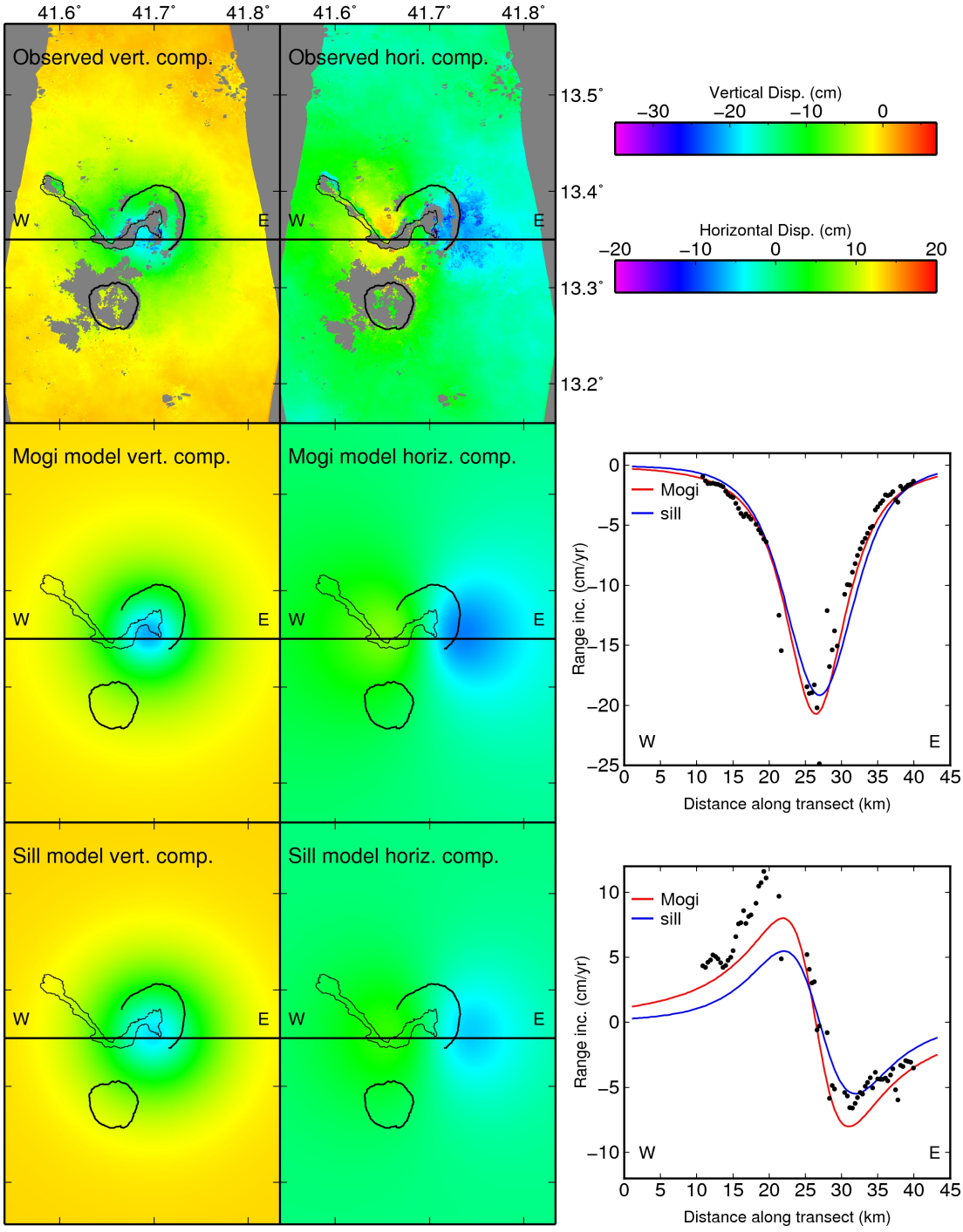

Figure 4.17: Left column: Vertical component of displacement for the observed TSX data (top), Mogi model (middle), and Okada model (bottom). Middle column: Horizontal component of displacement for the observed TSX data (top), Mogi model (middle), and Okada model (bottom). Right Column, top: Transect of vertical displacememnt for the observed data (black dots), Mogi (red) and Okada (blue). Right Column: Transect of vertical displacememnt for the observed data (black dots), Mogi (red) and Okada (blue). Right Column, bottom: Transect of horizontal displacememnt for the observed data (black dots), Mogi (red) and Okada (blue).

to 10 km, which together approximate a single point source. A similar magmatic system has been inferred for Dabbahu from analyses of seismic, petrological and geodetic data (Field et al., 2012b). The deep cluster of seismicity (cluster 4 Figure 2.4) directly beneath this region may be related to small-scale fracturing around a pipe where magma flows, potentially linking a deeper reservoir to shallower sources, similar to an interpretation of lower-mid crustal seismicity at Eyjafjallajökull volcano (Tarasewicz et al., 2012). Future joint inversion of seismicity and InSAR may clarify the details of the Nabro plumbing system.

The model used in this chapter assumed a clearly defined boundary between the mechanical properties of the magma chamber and those of the crust. However, when a magma body resides in the crust the properties of the medium are modified by the heat emitted from the emplaced magma body. In more evolved models of magma chambers the reservoir is encompassed in a thermo-metamorphosed shell which is viscoelastic rather than elastic. This produces a time dependence on the rate of subsidence. This issue is addressed fully in chapter 5, where the time series and causes of subsidence are discussed. In the following chapter I will use the CSK and TSX data sets from Chapter 3 to model the timeseries of deformation. I assume the best-fit Mogi model as found in this chapter and invert for the volume of contraction for the TSX and CSK data sets. I will then model the time varying contraction using thermal contraction, degassing and discuss viscoelastic contraction.

Chapter 5

Time Dependent Volcanic Deformation

Ground deformation at active volcanoes is not steady in time and space (Segall and Matthews, 1997). The rate and shape of deformation at a specific location can be controlled by changes in the source geometry, through processes within the magma chamber, through time dependent geomechanical properties of the surrounding crust, or by a combination of these processes (e.g., Segall, 2006, Dzurisin, 2006). The previous chapter presented models of the magma chambers assuming a linear subsidence during the observation period. In this chapter, I will investigate the changes in deformation rate during the observation period assuming the Mogi geometry defined in Chapter 4. I will then investigate the possible causes of the time-varying signal.

5.1 Data

I used both incremental and cumulative displacements to evaluate time-dependent source parameters. As in Chapter 4, I calculated the horizontal and vertical components of the LOS vector and downsampled the data to 1 km spacing. The dense time sampling of the CSK data set is particularly useful for observing changes in the source geometry and size. However, it was not possible to perform joint inversions as data was acquired on different dates.

5.1.1 Uncertainties

The uncertainties in the model parameters for each date are found by using a Monte Carlo analysis as described in Chapter 4, a total of 100 different noisy atmospheres was

added to each date, with the 1σ uncertainty given by one standard deviation of the results for each parameter. Examples of the cumulative data, the added noise and the resulting noisy data set are shown in Figure 5.1.

In section 5.3 I perform grid searches as an inversion technique to find the best-fitting parameters for the thermal model. I use the time series of the volume change as input data, and search for the solution with the smallest weighted RMS misfit,

$$WRMS = \xi Q_y^{-1} \xi^T, \tag{5.1}$$

where ξ is the residual and Q_y is a diagonal matrix of the variance σ_1^2. By weighting the misfit for each data point the results will not be skewed by noise.

5.2 Source Geometry

Previously, I found that the Mogi geometry best fitted the linear displacement rate calculated for the TSX and CSK data. However, over time the magma chamber may evolve and change shape, for example by feeding shallow intrusions. Therefore, to check the stability of the Mogi source I performed an inversion to find the depth and surface position of the Mogi model, at each time step for the TSX descending data. I used the observed incremental displacement to prevent any time dependent changes being overprinted by previous displacements that are contained in a cumulative data set. The incremental time series of each parameter will have a low signal to noise ratio because of the small window of time between each SAR observation.

The surface position and depth of the source does not show any time-dependent trend, indicating that the location of the source is permanent (Figure 5.2). Therefore, as the source geometry is stable, I can investigate the time dependent volume change of the source. I used the average values for each location parameter and solved only for the volume change as a function of time (Lu et al., 2010). For this step I used the cumulative data as there will be a higher signal to noise ratio and I know that only the volume change is time dependent (Figure 5.3). To plot the TSX data relative to first CSK SAR acquisition, I calculated the linear displacement rate between the first and second CSK acquisition dates an offset the TSX data accordingly (the same method as Pagli et al. (2012)).

When all other parameters are fixed, the time series of the cumulative source volume

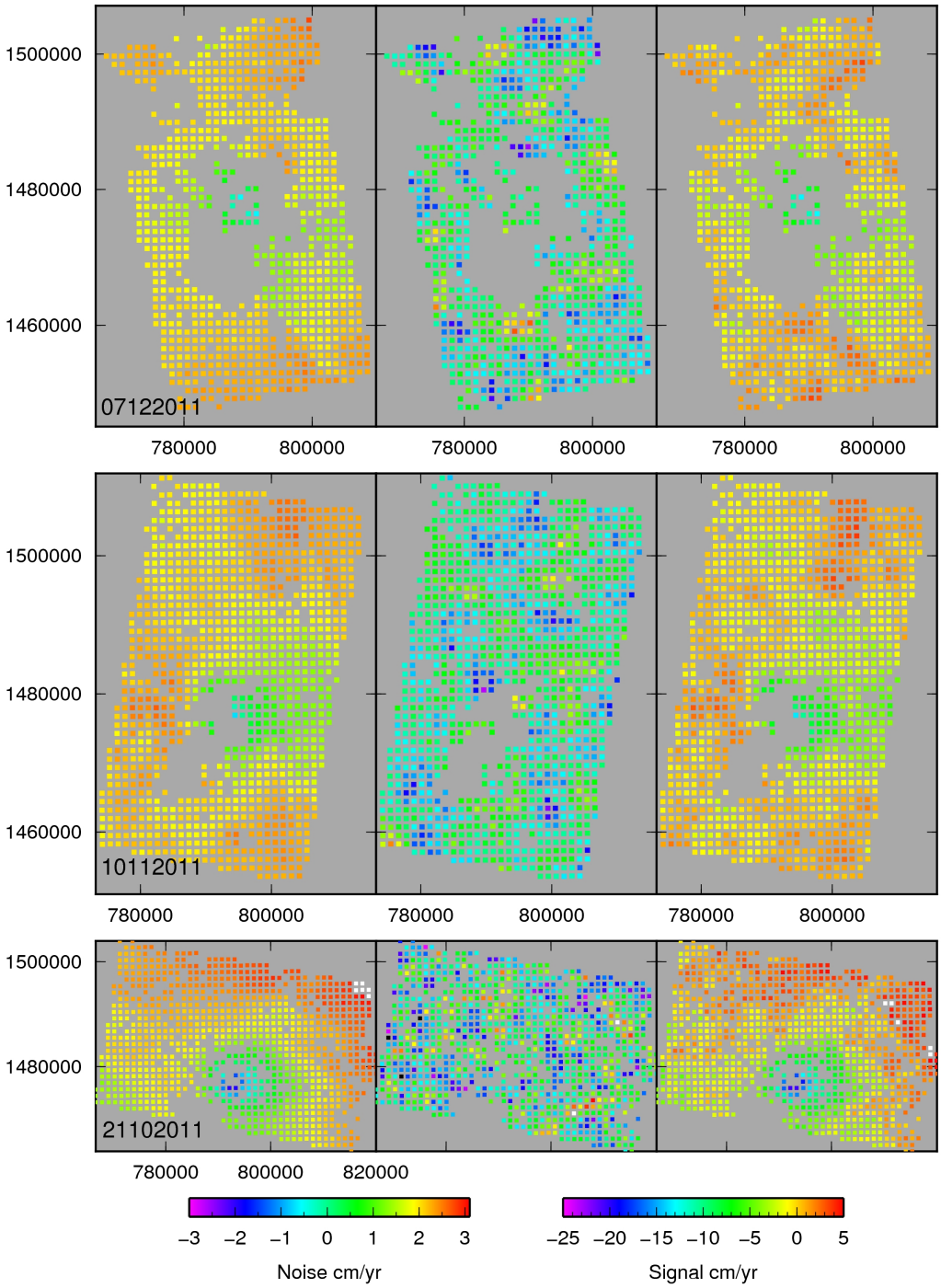

Figure 5.1: Left: The observed signal sampled at 1 km. Middle: Example noisy data set. Right: Observed signal plus noise. For three example dates. The 'Signal' colour scale applies to the left and right columns. The 'Noise' colour scale is applied to the middle column.

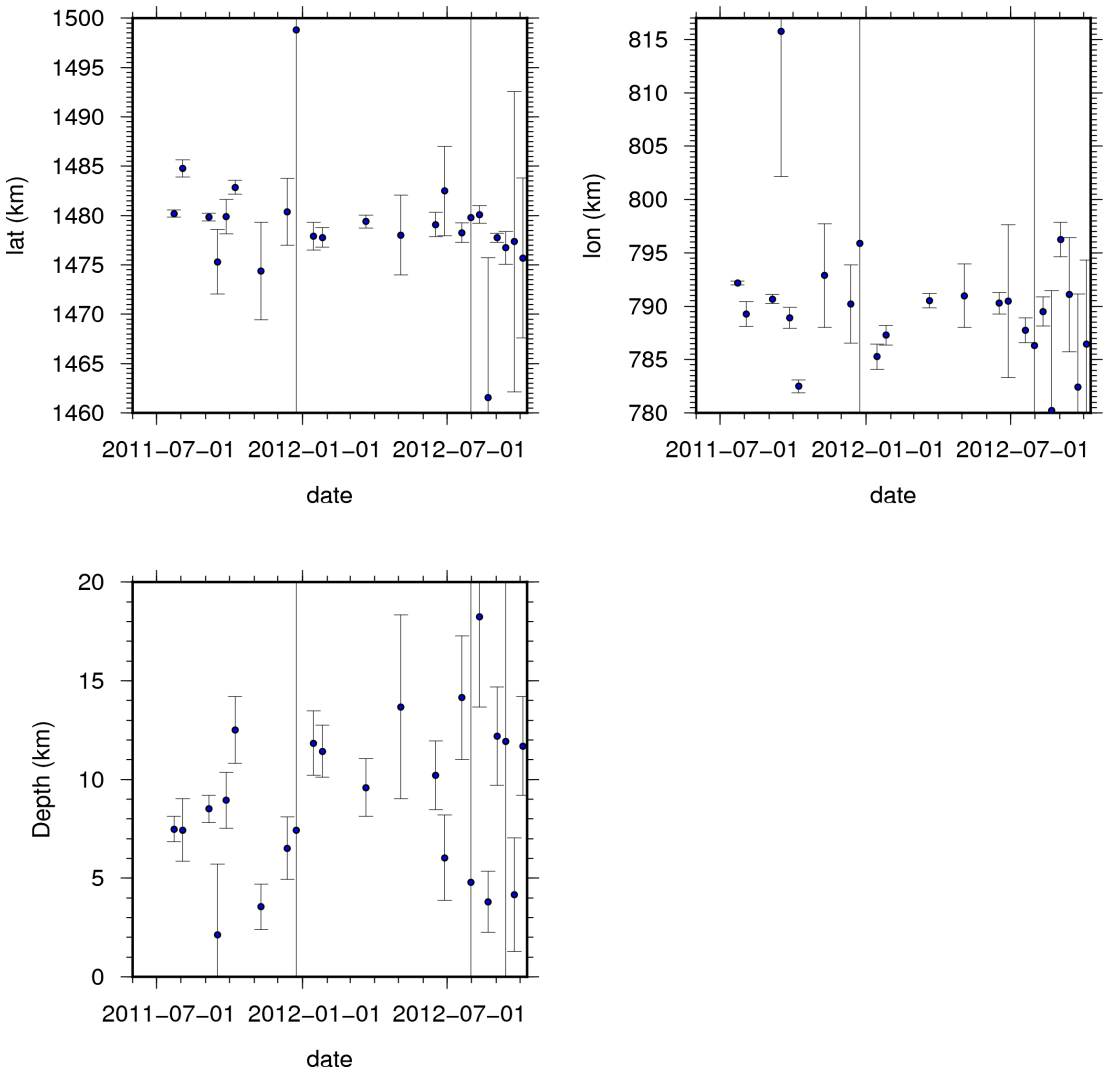

Figure 5.2: Time series of inverted source geometry parameters for longitude (top left), latitude (top right) and depth (bottom left). Incremental data were used for the inversion.

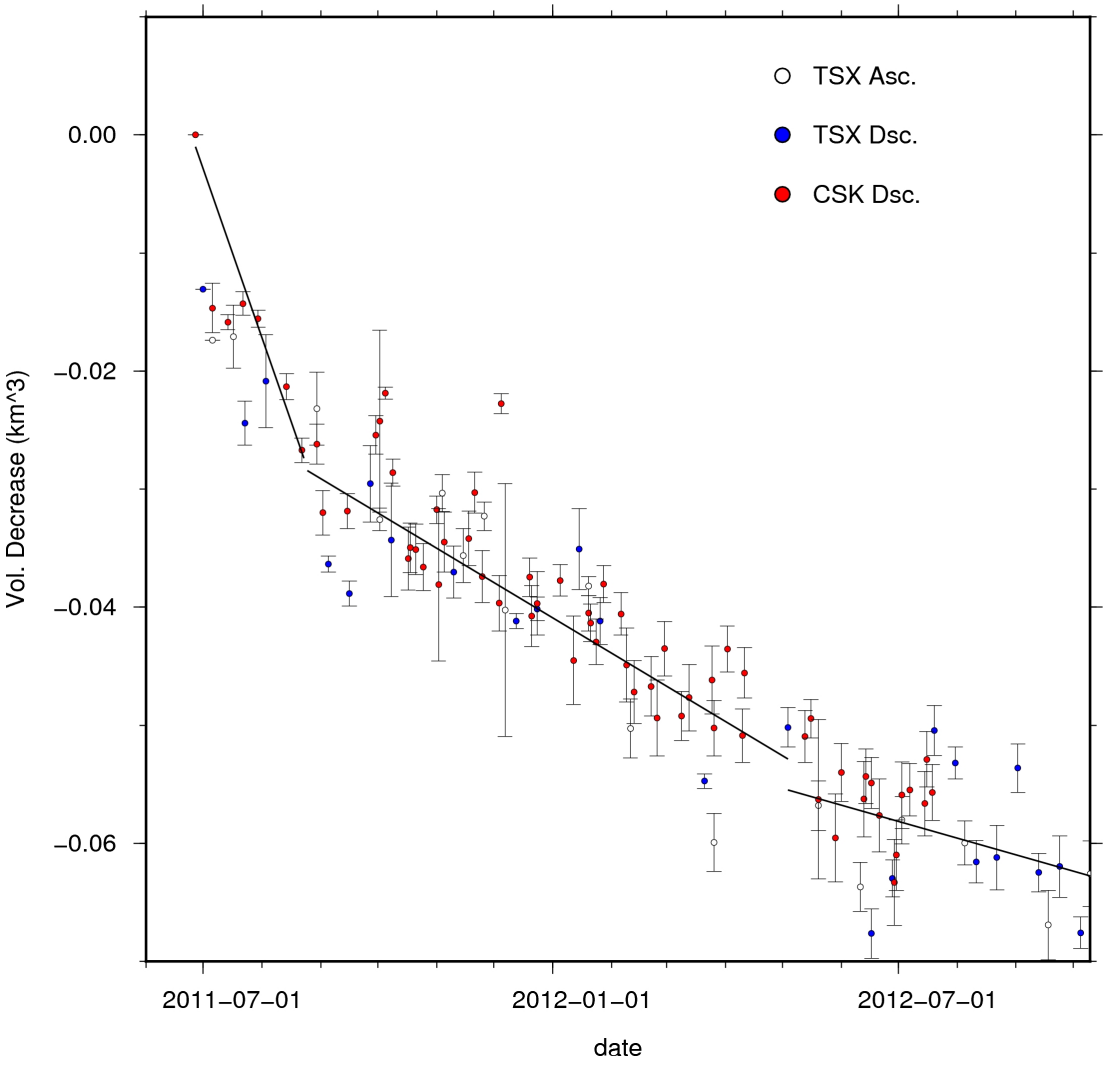

Figure 5.3: Time series of volume change. Assuming a fixed geometry a Mogi Source at a depth of 6.4 km at 41.69°(Lon) 13.36°(Lat). Cumulative data was used for the inversion. Black lines indicate the best-fit displacement rates, highlighting the non-linearity of the subsidence.

change shows a decrease of 0.013 km^3 in the initial 2 weeks of observation, between the 27 June 2011 and 10 July 2011. During this time there is no increase in lava flux but there is intense thermal radiation from the main lava flow (Goitom et al., 2015). Furthermore, just before this period there was a small increase in SO_2 release (Goitom et al., 2015). Therefore, I suggest that within this period the volcano is still within in a co-eruption phase. The volume then decreases steadily from 0.013 km^3 to ∼0.055 km^3 over a period of 50 weeks. After this point the CSK data ends. The TSX data sets imply that the volume decrease starts to slow after 15 months of observations. I have solved for the best fit decrease rates for the whole period and each separate period discussed and find that there are three different deflation rates during the period, clearly showing a non linearity within the observation period (Figure 5.3). There is no suggestion of deflation pauses or recharge over the observation period. A total volume decrease of approximately 0.06 km^3 is significantly smaller 0.15 km^3 of subsidence following the 1960 collapse of Kilauea Volcano (Delaney and McTigue, 1994). But is comparable to that of Lliama (Bathke et al., 2011) and larger than the 0.001 km^3 that observed at Galeras.

Having found that the volume change at the source is the only time dependent parameter, I explore models for this observation. Post eruption subsidence is rare compared to post eruption uplift (e.g., Moran, 1994, Nakada et al., 1999, Ruiz et al., 2007, Pagli et al., 2012, Girona et al., 2014)(see section 6.4 for further discussion), several mechanisms have been proposed to account for time varying deformation at volcanoes. In volcanic settings, subsidence has been explained by thermal cooling (e.g. Medicine Lake Volcano (Poland et al., 2006, Parker et al., 2014), Basilizzo Island (Tallarico et al., 2003)), passive degassing (e.g. Liama volcano Girona et al. (2014)), magma migration (e.g. Askja (de Zeeuw-van Dalfsen et al., 2005)) and viscoelastic relaxation (Newman et al., 2001). Here, I investigate or discuss each process in relation to the ground displacement observed at Nabro.

5.3 Thermal contraction

Subsidence of the ground surface above a suspected cooling magma chamber has been observed at numerous volcanoes across the world [e.g. Medicine Lake Volcano, California (Poland et al., 2006), Okmok, Aleutians (Caricchi et al., 2014), Askja, Iceland (Sturkell and Sigmundsson, 2000), Basiluzzo Island, Aeolian Islands (Tallarico

et al., 2003) and Volcan Alcedo, Galapagos (Hooper et al., 2007)]. The subsidence measured in these studies is thought to have persisted from yearly to centenial timescales, with the geodetic record beginning during the subsidence, after the intrusions occurred. Caricchi et al. (2014) showed that subsidence due to thermal cooling is visible on an interannual time scale; however only a small volume change of 0.003 km^3 was observed.

Pagli et al. (2014) obtained a timeseries of cumulative displacement between 2007 and 2010 over the Afar region. There is no surface displacement at Nabro during this period. Therefore, if thermal contraction is a plausible mechanism to explain the subsidence at Nabro, cooling would have had to have begun in early 2011 or inconjunction with the eruption. Thermal contraction was observed following the 1663 eruption of Usu volcano (Tomiya and Takahashi, 1995). During the Usu eruption, mechanical mixing of hot newly injected magma was forced by the eruption itself (Figure 5.4). As the hot, newly injected magma mixed it cooled quicker than if it had remained stratified at the base of the chamber. The cooling induced crystallisation that caused an accelerated rate of thermal contraction. Donovan and Pyle (*in prep.*) performed whole rock and melt inclusion analysis on samples taken from Nabro and the surrounding region during a field expedition in October 2011. The authors suggest that the arrival of new batches of magma into the chamber in the beginning of 2011 triggered the eruption in June (Sparks and Sigurdsson, 1977). I have chosen to investigate the thermal contraction of the magma chamber as a reason for absent pre-eruption subsidence and ongoing post-eruption subsidence at Nabro.

I use an analytical model to invert the ground displacement observed for the thermal state and size of the chamber at the point of the eruption. I assume that the magma will begin to cool through conduction to the surrounding crust as in Tallarico et al. (2003). This will induce a volume change and a corresponding subsidence of the Earth's surface. This hypothesis is dependent on Nabro being a closed system during the observation period. Tallarico et al. (2003) proposed a simplified first order model of the volume change induced by a cooling spherical magma chamber. The model accounts for internal magma chamber processes such as thermal convection and its interaction with crystallisation and chemical differentiation, by allowing the radius of the chamber to change over time. The volume of contraction ($\Delta V'(t)$) after time t since the beginning of cooling is

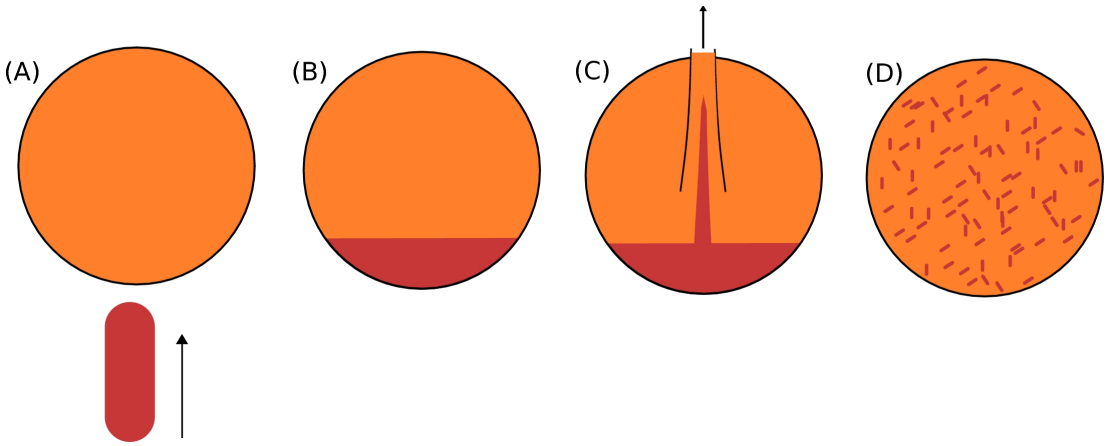

Figure 5.4: Thermal model hypothesis. A) New, hot magma is injected into the base of the magma chamber. B) The new magma is stratified at the base of the magma chamber. C) The eruption evacuates the original and new magma. D) The eruption has induced mechanical mixing within the chamber, the newly injected magma is mixed and cools quickly due to an increase in surface area.

$$\Delta V'(t) = -\frac{4}{3}\pi\frac{\Delta\rho}{\rho_s}\left(\frac{t^{\frac{3}{2}}}{\Lambda^3} - 3R_0\frac{t}{\Lambda^2} + 3R_0^2\frac{\sqrt{t}}{\Lambda}\right), \tag{5.2}$$

where the controlling parameters are the starting radius before contraction (R_0), ρ_s is the density of solid magma, $\Delta\rho$ is density difference between the solid and liquid magma (ρ_l) and Λ is a dimensionless parameter that describes the state of heat within the magma chamber and the efficiency of cooling. Λ is defined as follows:

$$\Lambda = \frac{\rho_l\sqrt{\pi\chi}(C_p\Delta T + fQ_l)}{2kT_s}, \tag{5.3}$$

where C_p is the specific heat capacity, ΔT is the temperature change, χ is the thermal diffusivity, f is the percentage of magma within the chamber that crystallises, Q_l is the latent heat of crystallisation, k is the thermal conductivity of the crust and T_s is the temperature of the boundary through which the heat is passing. In this scenario the temperature decrease induces the growth of crystals and contraction of the magma body.

The numerator in Eq. 5.3 represents the amount heat in the system, the efficiency of the heat diffusion and the density of the material to be cooled down. The denominator represents the conductivity of the material (k) and so measures how much heat will flow in the material. This contrasts with χ, which describes how rapidly this heat will flow. Note that the temperature of the boundary through which the heat is passing (T_s) will

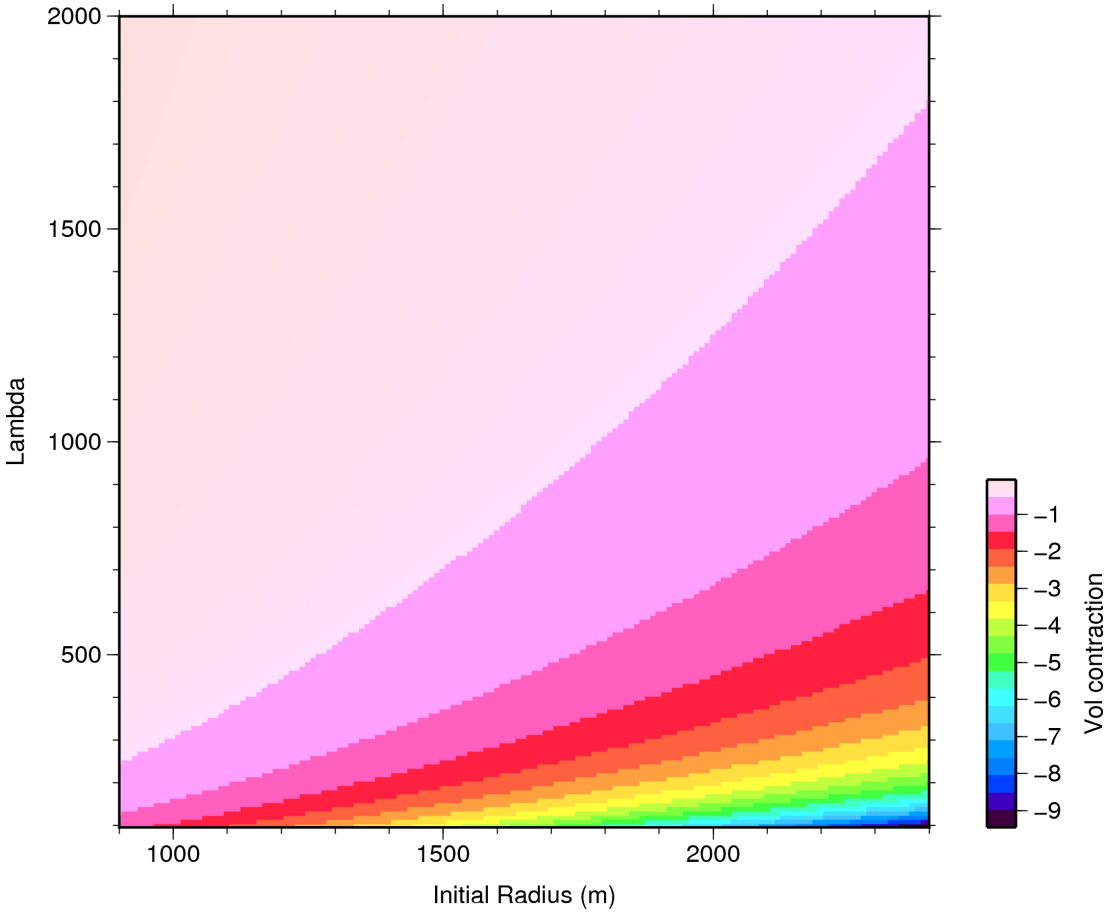

Figure 5.5: Illustration of the tradeoff between the initial radius (R_0) and the value of Λ, defined in Eq.5.2.

also affect the conductivity of the material due to atomic scale heat interaction.

Eq. 5.2 shows that the volume of contraction involves a tradeoff between Λ and the initial radius R_0 (Figure 5.5). For example, if I know the magma chamber at Nabro had an initial radius of 1500 m, a small value of Λ will induce a large volumetric contraction because it is inversely proportional to the conductivity, allowing the heat to be lost efficiently. Conversely, for the same radius a large value of Λ will induce a small volumetric change because the initial heat in the system is high and/or the mass of the material is high, whilst the conductivity is low.

To find an appropriate value of Λ, I assumed the values for the constituent parameters discussed above, based on values used in previous studies (Table 5.1). Using these values, I calculated a maximum and minimum Λ, then I inverted for the best fitting $\Delta V'$ over the observed time period by performing a grid search for the value of R_0.

For the maximum value of Λ (Λ=1095) the required initial radius is 2.39±0.005

Param.	Units	Max Value	Reference	Min Value	Reference
C_p	J Kg^{-1} K^1	1100	Martin et al. (1987)	1047	Armienti et al. (1984)
f		0.9	Tallarico et al. (2003)	0.6	Armienti et al. (1984)
k	W m^{-1} K^{-1}	3	Chapman (1986)	2.3	Armienti et al. (1984)
Q_l	J Kg^{-1}	800000	Armienti et al. (1984)	334944	Tallarico et al. (2003)
T_s	K	1130	Donovan *pers. comm.*	1030	Donovan *pers. comm.*
ΔT	K	350	Armienti et al. (1984)	150	Huppert and Sparks (1981)
ρ_s	kg m^{-3}	3300	Scandone and Giacomelli (1998)	3084	Scandone and Giacomelli (1998)
ρ_l	kg m^{-3}	2750	Sparks and Huppert (1984)	2570	Armienti et al. (1984)

Table 5.1: Example minimum and maximum values for the thermal characteristics of a magma chamber.

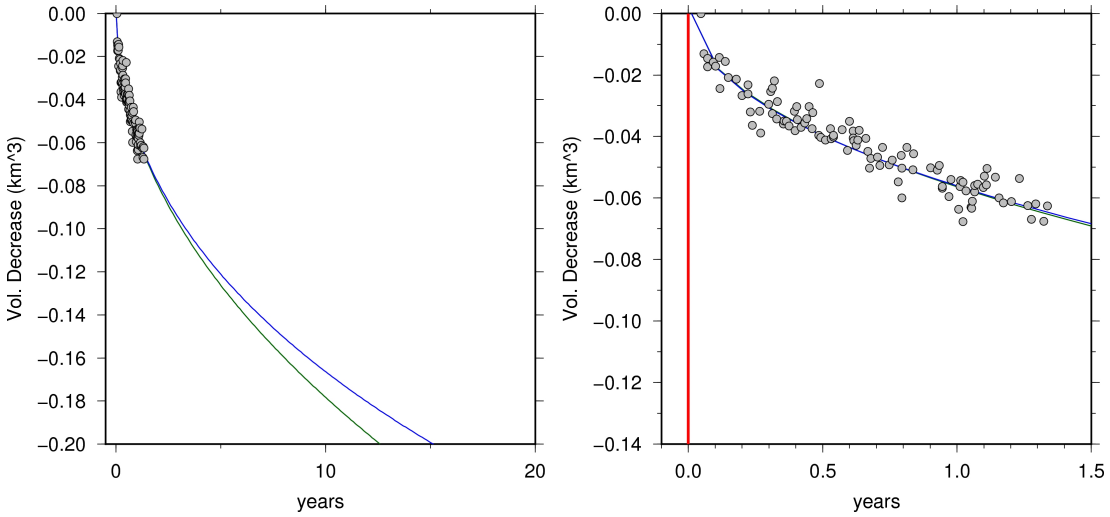

Figure 5.6: The volume of contraction calculated from the maximum value of Λ is shown in blue and the volume of contraction assuming a minimum is shown in green. Using Λ_{min} requires an initial starting radius of 0.944 km and Λ_{max} results in an initial radius 2.386 km. LHS: trend over 20 years. RHS: trend over observation period.

km, whereas for the minimum value of Λ (Λ=191) the required radius is 0.95±0.002 km (Figure 5.6). Both models fit the data well; however, the tradeoff between Λ and R_0 allows for a large range of initial radii. The model with the smaller initial radius reaches equilibrium such that contraction ceases at approximately 1000 years from the eruption date, whereas for the larger body this equilibrium is reached after approximately 10,000 years. The long term differences in subsidence rate will help differentiate between the models if more SAR images are acquired in the future.

The Tallarico et al. (2003) model used here only considers the heat generated by crystal nucleation and growth (Brandeis and Jaupart, 1986). There is no consideration for heat generated by newly arriving magma during the cooling period, as the model is a closed system. For the model to be compatible with observations the system would become closed following eruption otherwise subsidence would have occurred prior to

eruption. Currently, it is not possible to confirm whether the magma chamber became isolated post eruption for cooling to occur. Alternatively, the entire magma chamber would have to have been injected prior to the eruption.

The subsidence rate determined by the Tallarico et al. (2003) model is a minimum. There is no consideration for accelerated cooling by convection of fluids in the country rock. Additionally, Tallarico et al. (2003) only consider the density changes from crystallisation, and do not consider the exsolved gases generated by this process (Tait et al., 1989). If the gas phase can escape from the system (e.g. Medicine Lake volcano (Dzurisin et al., 2002)), the volume of subsidence would increase (Girona et al., 2014).

The simple analytical model used here ignores time dependent temperature feedback. As the surrounding rock heats up, the conductivity changes creating a thermal insulator around the magma chamber. This results in a large initial radius of the magma chamber. Applying this model requires a radius of 0.9 km to 2.4 km, depending on Λ, giving a volume range of $\sim$3.5 km^3 to $\sim$60 km^3. To overcome the simplifications implicit in analytical models numerical models of thermal contraction can be used, but these require additional petrological information. However, these models are unlikely to change the result that a large magma body ($<<$ 1 km^3) would be required to produce the observed contraction rate. It seems unlikely that this could have been injected prior to eruption. If it was cooling before the eruption there would have been a geodetic signal. Additionally, injecting an entire magma chamber would be implausible at this scale.

5.4 Post-eruption Degassing

In collaboration with Marie Edmonds and Brendan McCormick at the University of Cambridge, I investigate if degassing is a plausible mechanism to induce subsidence at the surface. They used the model D-Compress$_2$ to generate a database of gas compositions for a magma in the system C-S-O-H-Fe, during decompression. At each pressure increment the proportion of exsolved gas, composition and densities were calculated. The model was constrained using the co-eruption InSAR derived volume change and the co-eruption SO_2 emissions observed by Theys et al. (2013). SO_2 is an abundant volcanic gas that is more easily detectable and can be measured from space (Theys et al., 2013). The ratio of CO_2 to SO_2 is variable from 0.5 to $\sim$7 (Williams et al.,

1992). The calculations found a very gaseous magma, which is 9.68% exsolved gas at a depth of 6.4 km. Therefore, if I assume the volume loss of 0.06 km^3 (Figure 5.3) is encapsulated within this gas phase, then 0.06 km^3 of gas will reside in a magma chamber with a volume of 0.62 km^3. I assume that this gas is a pure CO_2 phase at 6.4 km depth, as CO_2 is the least soluble gas and SO_2 and H_2O exsolve much shallower depths (Gerlach, 1986). To calculate the flux of CO_2 during my observation period, I use the Ideal Gas Law (Eq. 5.4) to convert this volume of CO_2 in to a mass:

$$PV = nRT\,, \tag{5.4}$$

where, P is pressure, V is volume, n is the number of moles, T is temperature and R is the Ideal Gas Constant. I used a pressure of 173.6 MPa (equivalent to a depth of 6.4 km), a temperature of 1273 K based on petrology data (Donovan,*pers. comm.*) and the ideal gas constant of 8.3145 m^3 Pa mol^{-1} K^{-1}. I rearrange Eq. 5.4 for the number of moles,

$$n = \frac{PV}{RT} = \frac{173.556 \times 10^6 \times 0.06 \times 10^9}{8.3145 \times 1273.15} \simeq 1 \times 10^{12}\text{moles}\,. \tag{5.5}$$

Then, as I am assuming a pure CO_2 phase, I calculate the mass as $\sim 4.4 \times 10^{13}$g (44 Mt). If I assume this mass of gas is removed from the system at a linear rate over 10 years, the CO_2 flux leaving the magma chamber is 12 kt day^{-1}. Note that this is the rate CO_2 outgassed from the chamber and not necessarily the flux that would be measured at the surface.

The flux of CO_2 I have calculated is a maximum. The model assumes that the magma is instantaneously emplaced at a certain depth and subsequently determines the resulting composition and fluid volume fractions. The model does not simulate the exsolution of CO_2 as the magma migrates from depth to the storage zone. The amount of CO_2 exsolved before this point is dependent on the time taken for the magma to reach the given depth.

The relationship of the CO_2 flux at depth to that at the surface is difficult to define. Scrubbing of volatiles from magmatic sources is at a high rate for soluble gases such as SO_2 (Gerlach et al., 2008, Dzurisin et al., 2005). Less soluble gases such as CO_2 are removed from the gas phase to a lesser degree, but scrubbing of these compounds can still be significant (Gislason et al., 2010). At Hekla volcano,

comparison of the CO_2 content of ground water to the CO_2 content of volcanic plumes suggest that as much as 94% to 99% of the total CO_2 from the volcano is removed by hydrothermal systems. Yohannes (2012) suggests there is evidence of a potentially significant hydrothermal system beneath Nabro. Additionally, one of the seismometers deployed for this study was destroyed by flooding. This implies that there is the potential to remove a significant proportion of the CO_2 flux that I have calculated through scrubbing at Nabro. This would reduce the flux to the atmosphere significantly.

The 12 kt d^{-1} CO_2 flux leaving the magma chamber at Nabro is comparable to outgassing measured at the surface at active volcanoes worldwide. In periods of quiescent passive degassing, Stromboli releases 6-12 kt d^{-1} CO_2, Mt. Etna releases 21 kt d^{-1} CO_2 and Masaya releases 14-16 kt d^{-1} CO_2 (Allard et al., 1994, Aiuppa et al., 2008, Burton et al., 2000). Girona et al. (2014) showed that passive degassing induced depressurisation and subsequent subsidence at Lliama Volcano, Chilie.

When comparing the CO_2 flux between volcanoes it is important to differentiate between total and crater emissions. As CO_2 can be un-reactive compared to other gas phases, it will leave solution and not necessarily outgas at the crater but instead leave the system through fractures across a broad area. Diffusion and high background atmospheric levels makes it difficult to measure the total gas release at a volcano (Burton et al., 2000). On Etna the same magnitude of CO_2 emission is recorded on the flanks as from the crater (Allard et al., 1991).

The hyperspectral Infra-red Atmospheric Sounding Interferometer (IASI) instrument is on-board satellite MetOp-A, which was launched in 2006 and measures trace gas content in the atmosphere. IASI measurements of SO_2 over Nabro, processed by Elisa Carboni at the University of Oxford, show some continued degassing at least until the end of December 2011. The satellite based measurements of SO_2 above Nabro show significant plumes of SO_2 in June and July. Unfortunately, the data in August and September are noisy due to circulating stratospheric SO_2 from the eruption. The SO_2 measured in October and December is higher over Nabro than background noise, but it is not quantifiable. This additional data set furthers the argument that outgassing is occurring at Nabro. I suggest that outgassing of a CO_2 rich magma at depth is the most plausible mechanism for continued subsidence at Nabro.

5.5 Fluid Migration

Subsidence in some instances has been attributed to volume loss following the outflow of hydrothermal fluids or drainage of magma. The magma chamber beneath Askja volcano has been losing volume since at least 1983 (Pagli et al., 2006); this has been interpreted as a combination of magma drainage and thermal contraction (de Zeeuw-van Dalfsen et al., 2005). From the timeseries of ground displacement and ratemaps of spatial displacement in the Nabro region if magma drainage is occurring beneath Nabro following the eruption it must be flowing to deeper levels that mask detection. The seismic data presented in Chapter 2 does highlight potential linkages between the shallow chamber and deeper potential sources. Based on the volume loss of 0.12 km^3, and assuming another Mogi geometry the reservoir would need be at a depth of ∼30 km. At this depth the resulting surface displacements will be 3 mm, which is less than the level of noise detected in the interferograms, making the reservoir invisible to InSAR. This is a maximum depth as I have assumed an elastic halfspace. If the magma was drawn down to a depth where the crust was more ductile, the magma and deformation will be distributed across a wide area.

The fluid migration hypothesis does not require a temporal trend of source deepening. If the magma was draining through a narrow conduit to a deeper reservoir, the Mogi source will contract and its depth will not change. Additionally, the depth estimated here is a maximum, as magma will not migrate a single coherent body and magma may become dissipated dependent on the plumbing system. Based on the deep seismicity I observed, the brittle-ductile transition is at a depth of ∼12 km under Nabro. Therefore, the magma would not have to migrate as deep as 30 km before becoming hidden in the ductile layer. At Askja Pagli et al. (2006) suggest that the draining is caused by the need to accommodate the extension of the European and North American tectonic plates. Unlike the axial volcanoes which are known to accommodate the extensional forces observed elsewhere in the Afar Rift (Ebinger et al., 2008), Nabro's off-rift location means it is unlikely to be accommodating significant extension.

5.6 Viscoelasticity

An eruption will cause a volume decrease within the magma chamber to which the crust will respond. Previously, I have assumed that the response has propagated through a

purely elastic medium. Analytical models apply this simplification as a sharp discontinuity between the elastic homogeneous half space and the magma chamber. However, when magma is injected into the shallow crust the heat perturbs the geothermal gradient and can increase the temperature of the crustal rocks beyond the brittle-ductile transition (Del Negro et al., 2009). Therefore, it may be more appropriate to define the mechanical characteristics of the country rock as viscoelastic (Del Negro et al., 2009). A shell of partially molten material surrounding a magma chamber has been suggested by several thermal models (Hodge, 1974, Spera, 1980). The thickness of the shell is dependent on the size of the magma chamber and the temperature of the magma and the surrounding rock. Bonafede et al. (1986) describe the solution for displacements induced by a Mogi source in a viscoelastic halfspace. Dragoni and Magnanensi (1989) extend the calculations to a spherical magma body with a shell of viscoelastic properties embedded in an elastic full space. The solution given in Newman et al. (2001), extends the work by Dragoni and Magnanensi (1989) to give solutions from an elastic halfspace (Figure 5.7). As the magma chamber establishes a new equilibrium, the surface displacement through time is given by Segall (2010) as:

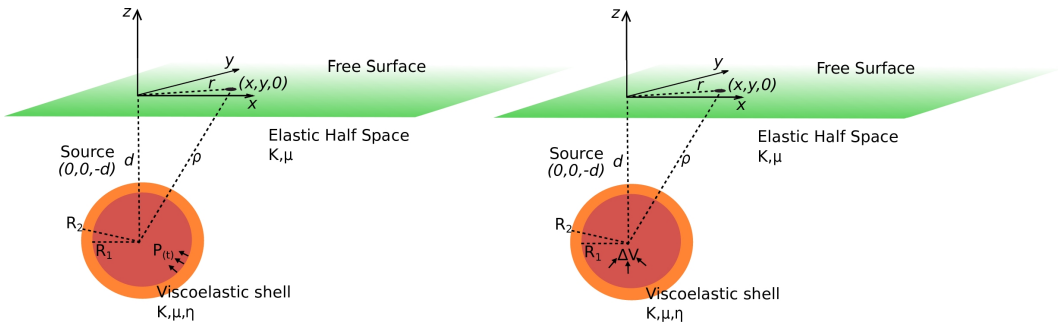

Figure 5.7: Spherical magma chamber with a viscoelastic shell, with a radii of R_1 and R_2 respectively. LHS: The system is perturbed by a pressure drop. RHS: The system is perturbed by a volume change.

$$U_z(\rho, z=0, t) = \frac{(1-\nu)P_0R_1^3}{\mu d^2}\left[e^{\frac{-t}{t_R}} + \frac{R_2^3}{R_1^3}(1-e^{\frac{-t}{t_R}})\right]\frac{1}{(1+\rho^2)^{\frac{3}{2}}} \tag{5.6a}$$

$$U_\rho(\rho, z=0, t) = \frac{(1-\nu)P_0R_1^3}{\mu d^2}\left[e^{\frac{-t}{t_R}} + \frac{R_2^3}{R_1^3}(1-e^{\frac{-t}{t_R}})\right]\frac{\rho}{(1+\rho^2)^{\frac{3}{2}}} \tag{5.6b}$$

The solution for the surface displacement is a scaled time dependent version of the Mogi source in an elastic half space. The characteristic relaxation time (t_R) is

$$t_R = \frac{3\eta(1-\nu)R_2^3}{\mu(1+\nu)R_1^3} \tag{5.7}$$

where ν is the Poisson's ratio (often 0.25), P_0 is the initial pressure drop (MPa), μ is the shear modulus (GPa), R_1 is the radius of the magma chamber and R_2 is the radius (km) of the viscoelastic shell which has a viscosity (η) in Pa s. The pressure is perturbed using a Heavyside function. The solution above assumes that pressure is held constant throughout time. Del Negro et al. (2009) further investigated the viscoelastic shell model by allowing the local geotherm caused by the presence of the magma chamber to allow for a spatial dependence of the viscosity of the shell as a function of temperature. They also used a trapezoidal pressure source history instead of the stepped Heavyside function.

The presence of the viscoelastic shell will damp the subsidence at the surface over time if the instantaneous removal of volume within the inner shell is not maintained. As the pressure between the inner and outer shells respond to the effects of the eruption. Therefore, I suggest that further processes would be required to maintain the large on subsidence signal at Nabro.

The effect of including a viscoelasticity in the subsurface is highly dependent on the model geometry. Following an eruption the volcanoes often will re-inflate, as observed at Grìmsvötn following the 1998 eruption (Sturkell et al., 2003a), following the 1991-93, 1991, 2001, 2002-03 and 2004-05 eruptions of Mt. Etna (Bonforte et al., 2008), and after the 2005 eruption of Fernandina Volcano (Chadwick Jr et al., 2011). Viscoelastic models can be used to model uplift, Nooner and Chadwick (2009) explain post eruption uplift at the Axial Seamount using a model with a different geometry. Their model has a viscoelastic medium is present beneath the sill, with the top edge of the sill bounded against an elastic layer which extends to the surface. Nooner and Chadwick (2009) argue that the hydrothermal processes will mitigate the temperature affects of the magma chamber and the material above the sill can be considered as elastic rather than viscoelastic. Therefore, the post eruption stresses are relieved below the chamber and cause uplift. In the post eruptive period, the material beneath the chamber flows back, allowing the elastic stress in the upper elastic layer to completely recover. This causes a gradual uplift, until the co-eruptive subsidence has disappeared.

5.7 Summary

In this chapter I proposed mechanisms to explain the time varying subsidence observed at Nabro volcano following the 12 June 2011 eruption. First, I investigated a time dependent geometry. I found that the only time dependent parameter of the source geometry is the volume change as the location of the source and fit to a Mogi model remains stable over time. Therefore, I tried to account for the volume change using an analytical model for thermal contraction. This model introduced large tradeoffs between the state of heat within the chamber and its initial radius, making it difficult to constrain. Additionally, the instantaneous emplacement of the magma chamber or the closing of the system prior to cooling is difficult to justify. I then investigated fluid migration and continued degassing. Through collaboration with Marie Edmonds and Brendon McCormick at University of Cambridge and Elisa Carboni at the University of Oxford, I found that degassing is a plausible and most likely explanation for the continued volume loss at Nabro.

Chapter 6

Discussion

6.1 Nabro's Plumbing System

In this study I have measured the crustal response to the 2011 eruption of Nabro volcano. Through my modelling of the high resolution InSAR data and in conjunction with seismicity, I have combined my interpretation of the seismic and InSAR data to create a working model of the magmatic plumbing system and how it interacts with faults (Figure 6.1). I observe a circular subsidence signal which is offset to the SW of the caldera topography and the vent region, suggesting the magma reservoir is not located directly beneath the eruption centre. The time series of subsidence suggests there is ongoing volume reduction of the magma chamber following the eruption. The subsidence is accompanied by earthquakes which have been caused by the depletion of the magma chamber.

I find that the depth of the magma body, estimated by inverting the InSAR deformation field, is dependent on whether I choose a Mogi or sill source. The best fit Mogi solution is at a depth of $\sim$ 6 km which is shallower than the best fit sill solution at $\sim$ 11 km depth. The hypocentres located between 1 km to 4 km depth (that delineate the thrust fault shown in Figure 6.1), are in the region of brittle failure immediately above the magma chamber which fracture to accommodate the volume change. Therefore, I suggest the more likely geometry of the source is a $\sim$6 km deep Mogi type solution, as this implies that the magma body is situated in the shadow zone immediately below this cluster.

I have been able to model the ground displacement using a single Mogi source and consequently interpret a single magma chamber residing at a depth of 6 km. However,

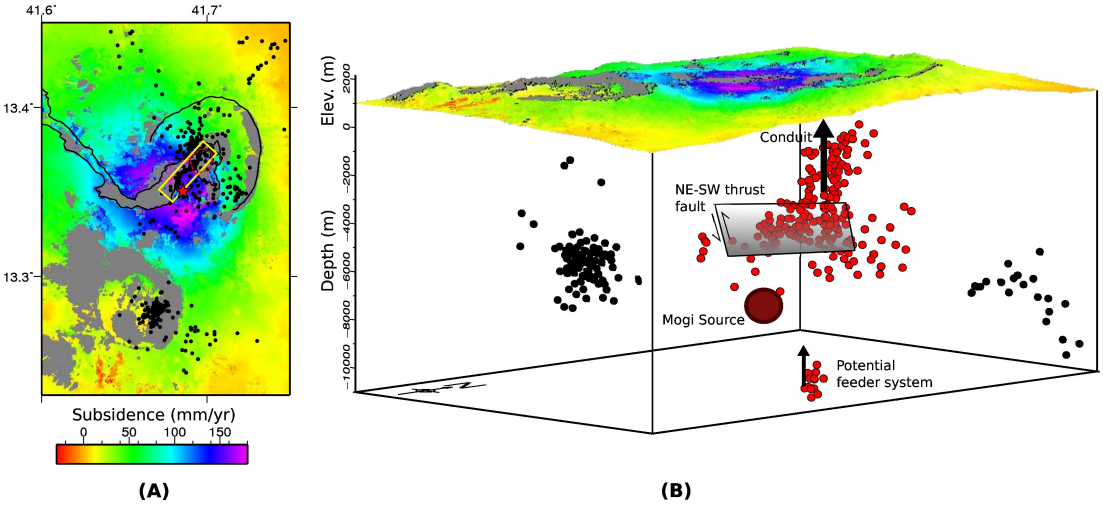

Figure 6.1: Working model of the magma plumbing system beneath Nabro. A) Map view of the observed subsidence from the ascending InSAR data. Black outlines: caldera rim and lava flow. Red dashed line: vent region. Black dots: relocated hypocentres. Red star: Mogi model centre. Yellow rectangle: NE-SW thrust fault outline at the surface. B) 3D view of the proposed working model. Top plane: the observed subsidence from the ascending InSAR data draped on topography. Lower volume: hypocentre locations at depth. Red: earthquakes induced directly by the eruption. Black: regional earthquakes induced by changes to the stress field. The proposed Mogi source (dark red spot), conduit (large black arrow), thrust fault (grey plane) and potential magma supply system (small black arrow) are also highlighted.

a number of studies suggest that magma plumbing systems that resemble Mogi sources in geodetic modelling are in fact more complex and may be stacked sills (e.g. Zellmer and Annen (2008), Macdonald et al. (1995) and Yun et al. (2006)). For example, a magma plumbing configuration of closely stacked sills was inferred from joint analysis of seismic, petrological and geodetic data for Dabbahu volcano (Field et al., 2012b). The geodetic data alone in Field et al. (2012b) was not able to distinguish whether a simple one source model or a multiple stacked sills model was most suitable. The more complex geometry was required based on the petrological evidence. At Nabro, it is possible that the Mogi approximation is an oversimplification of the geometry of the magma source. The magma reservoir under Nabro may also constitute numerous lenses and dykes of partial melt across a depth range of 6 km to 10 km, which together approximate a single point source ground deformation signal. However, based on the geodetic data alone it would not be possible to discriminate more complex models because the deformation pattern is too similar.

Earthquakes which occur prior to an eruption have been observed to migrate upwards toward the surface and have been used to delineate magma pathways (e.g. Battaglia et al. (2005), Patanè et al. (2008), Aspinall et al. (1998), Tarasewicz et al. (2012)

and Umakoshi et al. (2001)). These earthquakes are either generated at high strain rates when magma moves against the conduit walls or in the surrounding crust in response to stress changes (Lavallée et al., 2008, Roman et al., 2004). Following an eruption shallow VT seismicity often ceases (Roman et al., 2008). Roman et al. (2008) suggest that leading up to an eruption the conduit becomes pressurised and the stress is transferred on to local fractures causing seismicity. During the eruption, the stress drops or remains steady and no further stress is transferred, halting shallow VT events. The level of post-eruption VT seismicty at Nabro is high, and a column of seismicity extends from ∼2 km depth to the surface (Figure 6.1). I suggest that the continuing subsidence at Nabro is a mechanism for ongoing stress transfer around the conduit, allowing high levels of VT seismicity to remain post eruption. Therefore, this vertical column of seismicity highlights Nabro's vent area and conduit. Alternatively, shallow seismicity may be driven by hydrothermal systems (e.g Nishi et al., 1996, Crawford et al., 2013). Additionally, I have proposed that Nabro is extensively outgassing, a process which can induce seismicity (e.g White et al., 1998).

The geodetic data does not constrain deep plumbing, but anomalously deep earthquakes commonly occur in response to magma motion and are therefore useful in illuminating lower crustal magma pathways. Beneath volcanoes, deep seismicity in small spatial areas is suggestive of a bottleneck in the plumbing system (Tarasewicz et al., 2012). Magma flow in either direction through this bottleneck would induce seismicity by creating high strain rates (Lavallée et al., 2008). This has been observed through lower-mid crustal seismicity at Eyjafjallajökull volcano (Tarasewicz et al., 2012). Under Nabro, the deep cluster of seismicity directly beneath the modelled Mogi source (Figure 6.1) may be related to small-scale fracturing around a constricted part of the plumbing system, potentially linking the shallow sources to a deeper reservoir. The presence for deeper reservoirs is consisent with the off-rift setting assuming the magma supply is low, this is discussed further in section 6.3.

6.1.1 Stress changes caused by Nabro's plumbing system

In rift settings the regional maximum compressive stress is vertical (Illies, 1981, Bosworth et al., 1992). On Nabro we expect the regional stress field to produce a vertical P-axis and a NE striking T-axis. However, our post-eruption focal mechanisms show a

horizontal NW striking P-axis, revealing a local 90° shift from the expected regional orientation. Studies of VT earthquake swarms have documented a ∼90° rotation of the P-axis on volcanoes prior to and during eruptions, due to the propagation or inflation of dikes (Roman and Cashman, 2006, Lehto et al., 2010). However, on Nabro I find the 90° shift is present during the post-eruptive episode while the volcano is subsiding, with the NE-SW striking thrust fault being the geological expression of this stress field. I propose that this post-eruption rotation observed on Nabro, is due to the stress field induced by magma reservoir depressurization, as also suggested for Soufriere Hills Volcano by (Vargas-Bracamontes and Neuberg, 2012). However, the fault geometry may also be influenced by the geomechanical structure of the caldera. Additionally, the edifice will induce a local stress field which is decoupled from the regional stressfiel (e.g., Biggs et al., 2013, Xu and Jónsson, 2014).

The eruption of Nabro has implications for the regional geological structures. The InSAR subsidence signal is centred on Nabro caldera and does not extend laterally towards Mallahle, which implies that there is no current subsurface magmatic connection between the two calderas. Therefore, the seismicity we observe at Mallahle is due to changes in the stress field resulting from the subsidence at Nabro, and not caused by magma movement beneath Mallahle. This is further supported by the *b*-value analysis (Section 2.2.2), with a relatively low *b*-value beneath Mallahle suggesting non magmatic activity. However, a connection between the two calderas may have existed in the past. Also, the large magnitude ($M < 4$) VT earthquakes which occurred beneath Mallahle suggest that pre-existing faults have been brought closer to failure, due to stress changes following the magma reservoir depressurization (Wauthier et al., 2013a) (Hamiel 2012 personn comm.).

Seismicity is also observed on the NE flank of Nabro. I interpret this to be a result of the stress change, where the linear structure implies a fault which has been created or reactivated due to the new distribution of stress. I cannot constrain the focal mechanisms of these events as they are located outside of the local seismic array. The earthquakes that illuminate this proposed fault have a maximum M_L of 2 and are situated at a depth of ∼8 km. If I assume the fault to have a 90° dip and a thrust or normal mechanism (to give a maximum surface diplacement), the surface deformation resulting from earthquakes on this inferred structure is less than 0.5 mm, which is not large enough to be observed using InSAR.

6.1.2 A time dependent system

By modelling the InSAR time series, I was able to observe how the plumbing system evolved following the eruption. Repressurisation of a magma chamber can lead to horizontal magma migration. For example, at El Hierro repressurisation of the source following the 2011 eruption has created sills extending from a spherical magma chamber (González et al., 2013). Furthermore, the 2005 Dabbahu eruption was succeeded by emplacement of thirteen dikes over the next 5 years, due to remaining tectonic extensional stress in the rift (Hamling et al., 2010). However, beneath Nabro, I find no such modification of the source of deformation as the horizontal and vertical location is stable through time. This is consistent with the subsiding signal, as horizontal magma migration of this type requires recharging of the magma chamber.

At Nabro, I have found the only time dependent change is the source volume decrease. In order to explore this I have investigated both thermal, viscoelastic and degassing models in Chapter 5. All models require a long term volumetric change of $\sim$0.1 km^3. I have been able to reconcile some of this volume loss with post eruption degassing through fractures, similar to that observed at Miyakejima following the November 2000 eruption of Miyakejima (Geshi et al., 2002). I have also considered additional volume loss by fluid migration, but this is dependent on the tectonic setting of Nabro and is discussed further in Section 6.3. Additionally, I presented an argument for accelerated cooling as occurred at Usu volcano. However, the effect of this process will be damped by small temperature variations between initial and injected magma. Evidence for this model would exist in the petrology of magma released at future eruptions. To get a better constraint on the time dependent processes I would require a longer time series of the subsidence.

6.2 Comparison to Co-eruption InSAR analysis

The co-eruption InSAR analysis performed by Goitom et al. (2015) used TSX acquired images between 11 June 2011 to 1 July 2011 on a descending orbit and 14 May 2010 to 6 July 2011 on an ascending orbit. They found a complex pattern of ground deformation (Figure 6.2) that included broad scale subsidence of up to 20 cm to the north, east and south east of Nabro and a localised uplift that reached a maximum of 75 cm within the vent region. A subsidence signal of up to 50 cm centred on Mallahle is also observed.

To reproduce this pattern of displacement Goitom et al. (2015) found the best fitting model required 3 components: a Mogi source at 6 km depth, a NW-SE striking 8 km long dike that extends from 0.3 km to 4.3 km depth and inflates by 0.04 km^3, and a normal fault striking 320° that slips by 0.7 m. Hamiel et al. (2013) also investigated this complex deformation pattern. They were able to model the TSX InSAR data using 2 components: a strike strip and a normal fault (Hamiel et al., 2013).

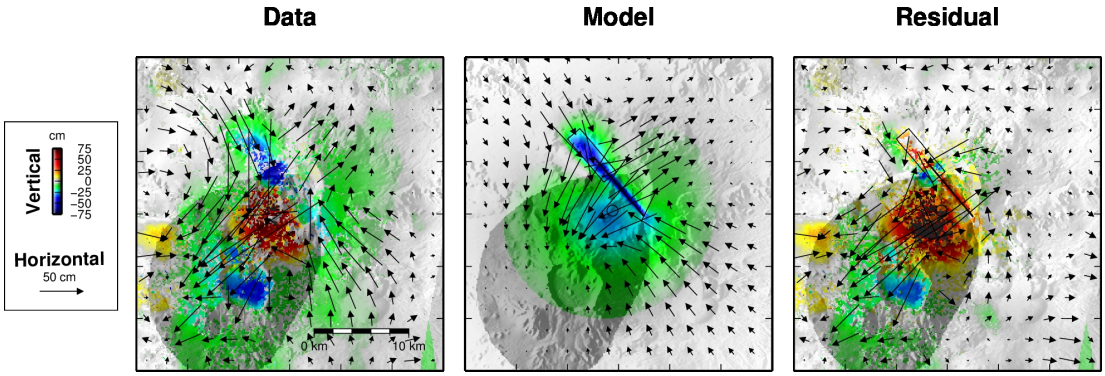

Figure 6.2: Co-eruption ground motion of the 12 June 2011 eruption of Nabro and the model used to explain the observations, extracted from Goitom et al.,(2015). LHS: Observation, resolved into vertical and horizontal movement. Middle: Model presidiction. RHS: Residual displacement.

Contrary to the co-eruption data, both the temporal and spatial pattern of the post-eruption ground displacement is relatively simple. Spatially, I observe a roughly circular pattern of subsidence that can be modelled with a single Mogi source. Analysis of InSAR time series reveals on going subsidence through out the observation period. However, despite quantifying the changing rate of subsidence in terms of volume change, the main processes causing this displacement have been difficult to quantify (Section 6.1.2). Based on the contrasting surface displacements between the co-eruptive and post eruptive deformation patterns, the processes controlling these phases of the eruption cycle are very different. This study and that of the co eruption data both find a Mogi source at ∼6 km deep. I suggest that this source controls the post eruption deformation despite only playing a minor role in the co-eruption deformation. This shows significant independence between the co-eruption and post-eruption processes at Nabro, contrasting findings at many other volcanoes (e.g., Fernandina (Chadwick Jr et al., 2011), Okmok (Lu et al., 2010), Stromboli (Métrich et al., 2010)).

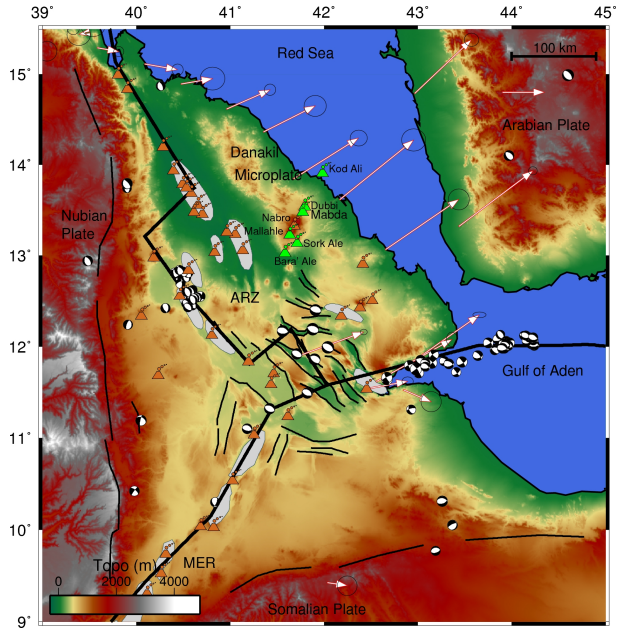

Figure 6.3: Heavy black lines show plate boundaries defined by Bird (2003). The NVR (Green trangles), lie off the rift compared too other regional volcanoes (orange triangles). Topographic map of the Afar Rift Zone from the 90m SRTM. Black lines show the regional faults, grey shading shows volcanic segments, white arrows are measured horizontal GPS displacement relative to the Nubian plate (McCluskey).

6.3 Off-rift volcanism

As described in the introduction, Nabro is an off-rift volcano. Off-rift volcanism is a common phenomenon that has also been observed in the Virunga Volcanic Province (Ebinger, 1989), in the Red Sea Rift (Bosworth et al., 2005), Iceland (Sturkell et al., 2003b) and the Baikal Rift (Kiselev, 1987). Above the rift axis of the ARZ lie large volcanic provinces constructed from magma generated by decompression melting due to lithospheric thinning (Hammond et al., 2013). Pagli et al. (2012) use InSAR to model shallow magma chambers beneath the Afar rift axis, for example the <2.5 km deep chambers under Alu-Dalafilla and Dallol volcanoes (Pagli et al., 2012, Nobile et al., 2012). Pagli et al. (2012) suggest the high rate of magma supply counteracts cooling to allow for shallow magma chambers, similar to those found at fast spreading mid-ocean ridges. The deeper magma chamber at Nabro implies that the off-rift volcanoes of the Danakil depression are fundamentally different to those in the rift axis. The deep chamber is consistent with the prediction of Pagli et al. (2012) with lower magma supply beneath off-rift volcanoes causing magma reservoirs to form deeper in the crust.

The orientation and cause of the NVR is uncertain. The NVR strikes oblique to

the Red Sea Rift, bisecting the Danakil microplate which is considered a relatively un-rifted, coherent block (McClusky et al., 2010, Hammond et al., 2013). Hammond et al. (2013) suggest a thermal anomaly may be present and some argue that increased melt production coincides with steep gradients in the lithosphere-asthenosphere boundary (Holtzman et al., 2010, Rychert et al., 2012). However, these arguments do not explain the strike and position of the NVR as a near continuous lineament from the ARZ to the Red Sea. Barberi et al. (1974) hypothesised that the NVR is a transverse structure, which developed through the rejuvenation of tectonically weak zones that proceeded rift formation. The global CMT catalogue shows that the majority of magnitude >4 earthquakes along the NVR have strike slip and normal fault mechanisms. In addition to fault slip and style, the NEIC catalogue of earthquakes shows that the NVR is also well delineated by a NE-SW striking alignment of earthquakes. The combination of fault slip style and earthquake locations on a regional scale show that the NVR has a transtensional motion, somewhat consistent with the previous interpretation in Barberi et al. (1974). In addition, all of our focal mechanisms, which I use to constrain the NE-SW thrust fault crossing the caldera floor, have a strike slip component. The orientation and strike slip could be due to a pre-existing structural fabric created by regional transverse motions, which was subsequently exploited during subsidence (Holohan et al., 2008). Pre-existing faults oblique to the rift have been shown to control caldera orientation to the south of Afar, in the Kenyan Rift (Robertson et al., 2015). At Nyamulagira volcano a cross-cutting caldera fault has also been observed during inter-eruptive periods, and it is considered to be a result of regional stresses (Wadge and Burt, 2011, Toombs and Wadge, 2012, Wauthier et al., 2013b). However, on Nabro I cannot differentiate between this cause of strike slip motion and that produced by the caldera collapse itself. Horizontal motions caused by the interactions of numerous faults on the caldera floor can produce oblique-slip faults (Holohan et al., 2013). The global CMT catalogue of normal fault mechanisms and presence of volcanoes along the line suggest that the transform motion is accommodated by opening, partly accommodated by magma intrusion. Joint geological and geophysical data therefore show that the NVR may be analogous to a 'leaky' transform fault, common on the magma-rich ocean ridge system (Gregg et al., 2007). Our interpretation implies that the Danakil block may experience internal deformation and may be better approximated as two microplates either side of the NVR. Extension accross these two microplates may drive

fluid migration from shallow to deep sources, as observed at Askja (Pagli et al., 2006).

6.4 Modes of Post-eruption deformation

Through my study of Nabro volcano I have been able to quantify and interpret the post-eruption process acting on the volcanic edifice. The high temporal resolution of the InSAR data has allowed me to create a data set which does not contain signal from the co-eruptive phase, but allows analysis of deformation that occurred immediately after the eruption ceased. In some studies it is impossible to separate the pre-eruptive, co-eruptive and post-eruptive phases, due to the temporal sampling of data and the behaviour of the volcano, so this study creates an opportunity to find mechanisms which control the post-eruption phase. In the post-eruption phase a volcanic edifice will either uplift, remain at a given height or subside. At Nabro I find ongoing subsidence. Here, I discuss the processes which can cause each of these scenarios to identify any systematic controlling factors. In this section I link my findings of the post-eruptive phase to other volcanoes across the world to try and identify systematic factors which control the post eruption deformation.

After an eruption a volcanic edifice may uplift. During an eruption removal of material from a shallow magma chamber will cause a pressure drop. The depressurisation creates a pressure gradient between the shallow and deep sources, drawing magma upwards from deeper levels. As the shallow magma chamber is recharged, the chamber becomes repressurised and once it reaches an equilibrium with deeper sources, the magma migration will slow and then stop. This requires a closed conduit system to allow pressure to accumulate. This process will be observed at the surface as ground surface uplift and has been observed at numerous volcanoes, such as following the 2005 eruption of Sierra Negra volcano (Ruiz et al., 2007, Geist et al., 2014), after the May 1980 activity at Mt. St. Helens (Moran, 1994), after the 1991 eruption of Unzen volcano (Nakada et al., 1999), at Redoubt after the 2009 eruption (Grapenthin et al., 2013), at Alu-Dalafilla volcano following the 2008 eruption (Pagli et al., 2012) at Gabho and Dabbahu following the 2005 Manda Hararo diking episode (Wright et al., 2006, Grandin et al., 2010). Figure 6.4 shows GPS, degassing and seismicity rates at Soufriere Hills Volcano between 1995 and 2012, published in Cole et al. (2012). The data collected from Soufriere hills shows a distinct relationship between uplift and subsidence in comparison to eruptive periods. At Nabro this process is not significant

compared to the processes causing subsidence.

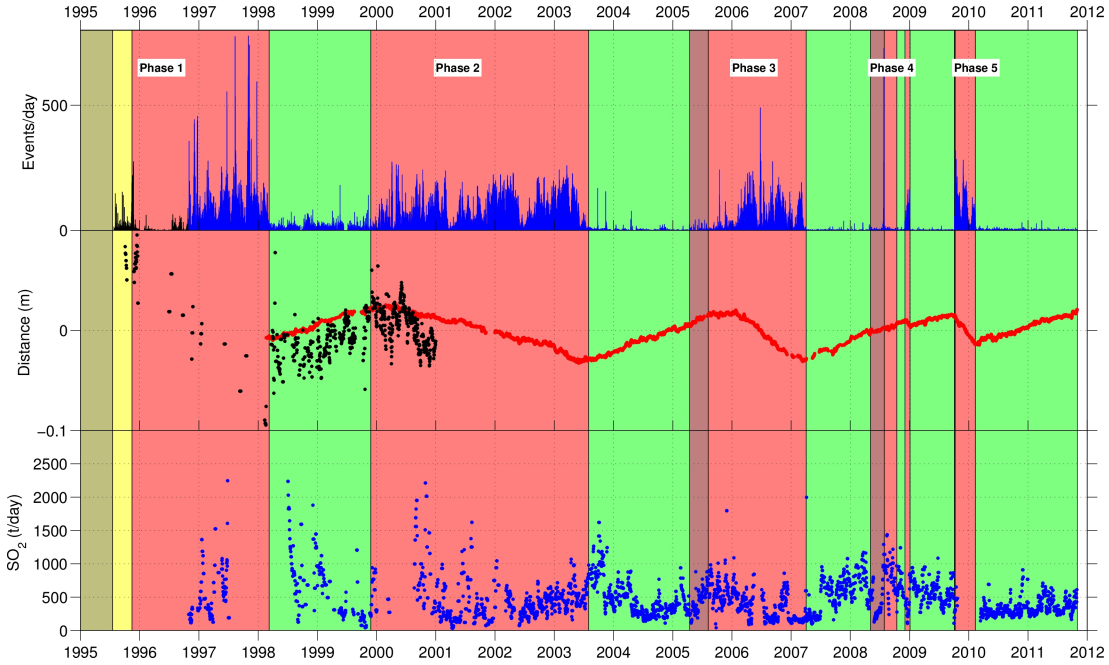

Figure 6.4: Summary of seismic (top), GPS (middle), SO_2 emission (bottom) monitoring by the MVO (figure from the 2012 MVO report). Eruption time periods are highlighted in red and pauses are shown in green (the first instruments were installed during the period highlighted in yellow). Seismicity shown in events per day (blue). GPs measurements are radial (red) and vertical (black), radial displacements are smoothed with a 7 day moving average.

In contrast, some volcanoes show a long-lived subsidence following an eruption. This can be caused by both magmatic and non-magmatic processes. Fluid migration from the magma chamber to deeper levels is a direct way to remove volume from the shallow source and induce subsidence at the surface. This has been observed at Askja volcano as magma is drawn downwards to accommodate rifting of the North American and European plates (de Zeeuw-van Dalfsen et al., 2005). Caricchi et al. (2014) demonstrated how the thermal regime can influence petrological processes and causing volume change and ultimately deformation at the surface. Alternatively, passively degassing magma can depressurise a magma chamber and cause subsidence (Girona et al., 2014). Liama volcano (Chilie) subsided through a volume of contraction of 0.1 km^3 over 3.5 years (Bathke et al., 2011) which was accounted for by degassing (Girona et al., 2014). This is the same order of magnitude as that lost at Nabro and I conclude this is the most likely mechanism for subsidence at Nabro.

Long term subsidence has also been the result of non-magmatic processes. At Nyamuragira volcano post eruption subsidence is due to aseismic slip along normal fault

zones that bound the western branch of the East African Rift system in which the volcano sits (Toombs and Wadge, 2012). Therefore, this is a tectonic control rather than magmatic process. Kiska Volcano erupted in 1990 and InSAR analysis of ground deformation between 1995-2001 showed an ongoing subsidence signal here. The source of the surface subsidence is successfully explained by pore fluid pressure decrease within a shallow hydrothermal system, with the source of this being very shallow at ∼1 km depth (Lu et al., 2002). Loading of the volcanic edifice with voluminous lava flows will also result in long term subsidence. Modelling of flows on Nea Kameni, as loads on a elastic lid overlying a viscoelastic halfspace, have shown that this process is an important influence on the geodetic signal observed there (Parks et al., 2015). Additionally, creep of unstable slopes will be observed as long term subsidence on the volcanic edifice, for example that observed on Volcan Arenal (Costa Rica) (Ebmeier et al., 2010).

Some post-eruption magmatic processes do not result in a geodetic signal at the surface. Magma migration at depth might not result in a geodetic signal with a magnitude greater than the interferogram noise, effectively becoming 'invisible' to InSAR (Pagli et al., 2006). In open conduit systems, it is not possible to build up stresses during magma chamber recharge therefore large surface displacements do not develop. In these circumstances, there will be small surface displacements that can now be observed with very high resolution tiltmeters and ground based InSAR like those used to monitor Stromboli volcano (Genco and Ripepe, 2010, Casagli et al., 2009). Lastly, if two processes are acting simultaneously, their contribution to ground displacement can cancel out, producing no net effect. At Okmok the time series of ground displacement showed periods of inflation (due to magma supply), deflation (due to degassing) and no ground movement, if the inflation and deflation processes where balanced no ground deformation will result (Lu et al., 2010). Sometimes the process may be missed if the temporal resolution is low (e.g. Chiten, Chilie (Fournier et al., 2010)) and the magmatic processes are rapid and ascend from depth below InSAR detection e.g. Shishaldin Volcano, Alaska (Moran et al., 2006)). Furthermore, ground deformation might not be observed as surface processes such as contraction of lava flows or ash deposits may mask subsurface processes (Toombs and Wadge, 2012, Whelley et al., 2012).

From the scenarios given here, it is clear that there are numerous controls on volcanic edifices following an eruption. I find that post eruption uplift is the most common process, especially at historically active volcanoes. Post eruption subsidence is much

more uncommon and is only related to magma migration in extensional tectonic setting e.g. at Askja. It is more likely to be controlled by degassing from deeper chambers or hydrothermal processes for very shallow sources of deformation. As degassing is controlling the subsidence at Nabro, the pressure in the magma chamber is low implying that there is no imminent future eruption. If in the future there is a reversal of the subsidence at Nabro there will be important implications for the state of the magma chamber. Future uplift of the edifice would suggest that the chamber is no longer being depressurised by gas loss, but is repressurising with an influx of new magma. This will have serious implications for the possibility of a future eruption. Some volcanoes show extended periods of inflation and do not erupt (Biggs et al., 2011), but Nabro has not been monitored prior to the eruption so it is difficult to understand the eruption cycle here. Pagli et al. (2014) created Afar wide interferograms between 2007 and end-2010 and observed no uplift at Nabro. This suggests that there was no uplift prior to the eruption or that uplift was rapid during the first 6 months of 2011. I propose that rapid uplift would have been the more likely scenario, based on the petrological evidence that new batches of magma were arriving into the system.

Chapter 7

Conclusions

The main findings of my thesis are:

- I have produced a model of the plumbing system at Nabro volcano using InSAR and seismic methods. Interferometric analysis of SAR acquisitions acquired by the TSX satellite on ascending and descending paths and the CSK satellite on a descending path between the 27 June 2011 and 10 October 2012, shows a concentric subsidence signal centred to the SW of Nabro's caldera. I have successfully modelled this with a Mogi geometry centred within 200 m of 13.356°N and 41.695°E with a depth of 6.4±0.3 km and a volume of contraction of 0.036±0.003 x10^{-3} km^3. However, this may be an oversimplified model of magma reservoir geometry.

- I have relocated the hypocentres of 456 earthquakes and used the spatial pattern to interpret the local and regional crustal response to the eruption. The shallow earthquakes beneath Nabro's caldera delineate a thrust fault that strikes NE-SW which dips 45° to the SE and extends across the caldera floor. This accommodates the stress change following the eruption, rather than movement on ring faults. A ∼10 km deep cluster highlights potential magma migration pathways directly beneath Nabro. On the flanks of the volcano, a linear pattern of earthquakes illuminate possible minor faults.

- A cluster of earthquakes is located beneath Mallahle caldera at a depth of 6 km, the b-value for this cluster is 0.97 and is lower than that for clusters under Nabro (b =1.3). This implies that the earthquakes generated at Mallahle occur in rock with a stronger rheology. This finding, inconjunction with the observa-

tion that InSAR measured ground displacement does not extend toward Mallahle, suggests that seismicity here is due to changes in the stress field resulting from the subsidence at Nabro. Therefore, there has not been magma movement beneath Mallahle during this observation period, but a connection between the two calderas may have existed in the past.

- I found that applying an empirical correction to the CSK data in order to remove atmospheric signals significantly underestimates the rate of subsidence because signal correlates with topography. Using data from the ERA-I ECMWF to correct the data was necessary to adequately remove the artefacts.

- Analysis of the time series shows how the subsidence does not occur at a linear rate over time. I have been able to model this time dependence as a function of a viscoelastic relaxation of a shell surrounding the magma chamber. This model requires an additional volume decrease during the post eruption period aproximately equal to the co-eruption volume. I have found that this is likely the result of passive degassing of a CO_2 rich magma. The high temporal resolution provided by systematic SAR acquisitions has allowed me to reveal these additional features of the plumbing system and forcing mechanisms.

- The long-term post-eruption subsidence at Nabro is unusual. I suggest that the low magma supply rate which causes the deep magma chamber is also controlling the post-eruption ground displacement, is superceeded by the rate of passive degassing of a CO_2 rich magma. The overall effect on the magma chamber is depressurisation, which induces subsidence.

- A future reversal of the subsidence at Nabro will have important implications for potential future eruptions. Future uplift of the edifice would suggest that outgassing is no longer the main mechanism controlling ground displacement and a new influx magma is pressurising the system.

7.1 Future Work

The 12 June 2011 eruption of Nabro volcano resulted in the collection of a rich geophysical data set. This study has only utilised the first available 6 weeks of seismic data after the eruption. The study of Nabro would be improved by analysing the full data

set with the methods used here. This would potentially show more details of magma pathways beneath the volcano and help understand the causes of the ongoing subsidence. I predict that the rate of seismicity will decrease as the volume change slows. Additionally, this work provides the first constraints on the plumbing system beneath Nabro and therefore provides a benchmark which to understand future activity. Acquiring more SAR images of Nabro and extending the InSAR time series presented here will help constrain the mechanisms of the time dependent processes. I also recommend ground based gas monitoring following a second eruption.

Monitoring Nabro in the future for potential uplift is important. If the volcano was to start inflating it should raise concerns. Nabro has the potential to cause millions of dollars worth of damage to grazing land and property, disrupt aviation and potentially to take lives. If the potential of Sentinel-1 for large scale automatic monitoring is realised this would be a great aid for volcanic hazard management in Eritrea.

References

Acocella, V. (2007), Understanding caldera structure and development: An overview of analogue models compared to natural calderas, *Earth-Science Reviews*, *85*(3), 125–160. 2.3.1

Aiuppa, A., G. Giudice, S. Gurrieri, M. Liuzzo, M. Burton, T. Caltabiano, A. McGonigle, G. Salerno, H. Shinohara, and M. Valenza (2008), Total volatile flux from Mount Etna, *Geophysical Research Letters*, *35*(24). 5.4

Allard, P., J. Carbonnelle, D. Dajlevic, J. Le Bronec, P. Morel, M. Robe, J. Maurenas, R. Faivre-Pierret, D. Martin, J. Sabroux, et al. (1991), Eruptive and diffuse emissions of co2 from Mount Etna, *Nature*, *351*(6325), 387–391. 5.4

Allard, P., J. Carbonnelle, N. Metrich, H. Loyer, and P. Zettwoog (1994), Sulphur output and magma degassing budget of Stromboli volcano, *Nature*, *368*(6469), 326–330. 5.4

Altherr, R., F. Henjes-Kunst, and A. Baumann (1990), Asthenosphere versus lithosphere as possible sources for basaltic magmas erupted during formation of the Red Sea: constraints from Sr, Pb and Nd isotopes, *Earth and Planetary Science Letters*, *96*(3), 269–286. 1.1.1

Amelung, F., C. Oppenheimer, P. Segall, and H. Zebker (2000), Ground deformation near Gada 'Ale Volcano, Afar, observed by radar interferometry, *Geophysical research letters*, *27*(19), 3093–3096. 4.1, 4.6

Anderson, H., and T. Webb (1994), New Zealand seismicity: patterns revealed by the upgraded National Seismograph Network, *New Zealand journal of geology and geophysics*, *37*(4), 477–493. 2

Anderson, J., and H. Wood (1925), Description and theory of the torsion seismometer, *Bulletin of the Seismological Society of America*, *15*(1), 1–72. 2.2.2

Armienti, P., F. Barberi, and F. Innocenti (1984), A model of the Phlegraean Fields magma chamber in the last 10,500 years, *Bulletin volcanologique*, *47*(2), 349–358. 5.3

Armitage, J. J., D. J. Ferguson, S. Goes, J. O. Hammond, E. Calais, C. A. Rychert, and N. Harmon (2015), Upper mantle temperature and the onset of extension and break-up in Afar, Africa, *Earth and Planetary Science Letters*, *418*, 78–90. 1.2.1

Aspinall, W., A. Miller, L. Lynch, J. Latchman, R. Stewart, R. White, and J. Power (1998), Soufrière Hills eruption, Montserrat, 1995–1997: Volcanic earthquake locations and fault plane solutions, *Geophysical Research Letters*, *25*(18), 3397–3400. 2.2.3, 6.1

Baby, H., P. Gole, and J. Lavergnat (1988), A model for the tropospheric excess path length of radio waves from surface meteorological measurements, *Radio science*, *23*(6), 1023–1038. 3.1.3

Bagnardi, M., and F. Amelung (2012), Space-geodetic evidence for multiple magma reservoirs and subvolcanic lateral intrusions at Fernandina Volcano, Galápagos Islands, *Journal of Geophysical Research: Solid Earth (1978–2012)*, *117*(B10). 3.4

Barberi, F., H. Tazieff, and J. Varet (1972), Volcanism in the Afar depression: its tectonic and magmatic significance, *Tectonophysics*, *15*(1), 19–29. 1.3

Barberi, F., E. Bonatti, G. Marinelli, and J. Varet (1974), Transverse tectonics during the split of a continent: data from the Afar rift, *Tectonophysics*, *23*(1), 17–29. 1.3, 6.3

Bastow, I., A. Nyblade, G. Stuart, T. Rooney, and M. Benoit (2008), Upper mantle seismic structure beneath the Ethiopian hot spot: Rifting at the edge of the African low-velocity anomaly, *Geochemistry, Geophysics, Geosystems*, *9*(12). 1.2.1

Bastow, I. D., and D. Keir (2011), The protracted development of the continent-ocean transition in Afar, *Nature Geoscience*, *4*(4), 248–250. 1.1.1

Bastow, I. D., G. W. Stuart, J.-M. Kendall, and C. J. Ebinger (2005), Upper-mantle seismic structure in a region of incipient continental breakup: northern Ethiopian rift, *Geophysical Journal International*, *162*(2), 479–493. 1.2.1

Bathke, H., M. Shirzaei, and T. Walter (2011), Inflation and deflation at the steep-sided Llaima stratovolcano (Chile) detected by using InSAR, *Geophysical Research Letters*, *38*(10). 5.2, 6.4

Battaglia, J., V. Ferrazzini, T. Staudacher, K. Aki, and J.-L. Cheminée (2005), Pre-eruptive migration of earthquakes at the Piton de la Fournaise volcano (Réunion Island), *Geophysical Journal International*, *161*(2), 549–558. 6.1

Battaglia, M., C. Troise, F. Obrizzo, F. Pingue, and G. De Natale (2006), Evidence for fluid migration as the source of deformation at Campi Flegrei caldera (Italy), *Geophysical Research Letters*, *33*(1). 1.5

Battaglia, M., P. F. Cervelli, and J. R. Murray (2013), Modeling crustal deformation near active faults and volcanic center: a catalog of deformation models, *US Geological Survey Techniques and Methods*, pp. 13–B1. 4.3

Bekaert, D., A. Hooper, and T. Wright (2015), A spatially-variable power-law tropospheric correction technique for InSAR data, *Journal of Geophysical Research: Solid Earth*. 3.1.3

Bender, B. (1983), Maximum likelihood estimation of b values for magnitude grouped data, *Bulletin of the Seismological Society of America*, *73*(3), 831–851. 2.2.2

Benoit, M. H., A. A. Nyblade, and J. C. VanDecar (2006), Upper mantle P-wave speed variations beneath Ethiopia and the origin of the Afar hotspot, *Geology*, *34*(5), 329–332. 1.2.1

Berardino, P., G. Fornaro, R. Lanari, and E. Sansosti (2002), A new algorithm for surface deformation monitoring based on small baseline differential SAR interferograms, *Geoscience and Remote Sensing, IEEE Transactions on*, *40*(11), 2375–2383. 3.2, 3.3.1

Bertrand, H., G. Chazot, J. Blichert-Toft, and S. Thoral (2003), Implications of widespread high-μ volcanism on the Arabian Plate for Afar mantle plume and lithosphere composition, *Chemical Geology*, *198*(1), 47–61. 1.2.2

Beutel, E., J. van Wijk, C. Ebinger, D. Keir, and A. Agostini (2010), Formation and stability of magmatic segments in the Main Ethiopian and Afar rifts, *Earth and Planetary Science Letters*, *293*(3), 225–235. 1.1.1

Bevis, M., S. Businger, T. A. Herring, C. Rocken, R. A. Anthes, and R. H. Ware (1992), GPS meteorology: Remote sensing of atmospheric water vapor using the Global Positioning System, *Journal of Geophysical Research: Atmospheres (1984–2012)*, *97*(D14), 15,787–15,801. 3.1.3, 3.1.3, 3.1.3, 3.1.3, 3.1.3

Beyene, A., and M. G. Abdelsalam (2005), Tectonics of the Afar Depression: A review and synthesis, *Journal of African Earth Sciences*, *41*(1), 41–59. 1.2.1

Biggs, J., T. Wright, Z. Lu, and B. Parsons (2007), Multi-interferogram method for measuring interseismic deformation: Denali fault, Alaska, *Geophysical Journal International*, *170*(3), 1165–1179. 3.1.3, 3.1.3, 3.3.1

Biggs, J., E. Anthony, and C. Ebinger (2009), Multiple inflation and deflation events at Kenyan volcanoes, East African Rift, *Geology*, *37*(11), 979–982. 3, 4.5, 4.6

Biggs, J., I. Bastow, D. Keir, and E. Lewi (2011), Pulses of deformation reveal frequently recurring shallow magmatic activity beneath the Main Ethiopian Rift, *Geochemistry, Geophysics, Geosystems*, *12*(9). 4.5, 4.6, 6.4

Biggs, J., M. Chivers, and M. C. Hutchinson (2013), Surface deformation and stress interactions during the 2007–2010 sequence of earthquake, dyke intrusion and eruption in northern tanzania, *Geophysical Journal International*, *195*(1), 16–26. 6.1.1

Biggs, J., S. Ebmeier, W. Aspinall, Z. Lu, M. Pritchard, R. Sparks, and T. Mather (2014), Global link between deformation and volcanic eruption quantified by satellite imagery, *Nature communications*, *5*. 1.5, 3

Bird, P. (2003), An updated digital model of plate boundaries, *Geochemistry, Geophysics, Geosystems*, *4*(3). 1.1

Bluth, G., and S. Carn (2008), Exceptional sulfur degassing from Nyamuragira volcano, 1979–2005, *International Journal of Remote Sensing*, *29*(22), 6667–6685. 1.3.2

Bluth, G. J., S. D. Doiron, C. C. Schnetzler, A. J. Krueger, and L. S. Walter (1992), Global tracking of the SO_2 clouds from the June, 1991 Mount Pinatubo eruptions, *Geophysical Research Letters*, *19*(2), 151–154. 1.3.2

Bonafede, M., M. Dragoni, and F. Quareni (1986), Displacement and stress fields produced by a centre of dilation and by a pressure source in a viscoelastic half-space: Application to the study of ground deformation and seismic activity at Campi Flegrei, Italy, *Geophysical Journal International*, *87*(2), 455–485. 5.6

Bonforte, A., A. Bonaccorso, F. Guglielmino, M. Palano, and G. Puglisi (2008), Feeding system and magma storage beneath Mt. Etna as revealed by recent inflation/deflation cycles, *Journal of Geophysical Research: Solid Earth (1978–2012)*, *113*(B5). 5.6

Bosworth, W., M. Strecker, and P. Blisniuk (1992), Integration of east African Paleostress and present-day stress data: Implications for continental stress field dynamics, *Journal of Geophysical Research: Solid Earth (1978–2012)*, *97*(B8), 11,851–11,865. 6.1.1

Bosworth, W., P. Huchon, and K. McClay (2005), The Red Sea and Gulf of Aden basins, *Journal of African Earth Sciences*, *43*(1), 334–378. 1.1.1, 6.3

Bown, J. W., and R. S. White (1995), Effect of finite extension rate on melt generation at rifted continental margins, *Journal of Geophysical Research: Solid Earth (1978–2012)*, *100*(B9), 18,011–18,029. 1.1.1

Brandeis, G., and C. Jaupart (1986), On the interaction between convection and crystallization in cooling magma chambers, *Earth and Planetary Science Letters*, *77*(3), 345–361. 5.3

Breit, H., T. Fritz, U. Balss, M. Lachaise, A. Niedermeier, and M. Vonavka (2010), TerraSAR-X SAR processing and products, *Geoscience and Remote Sensing, IEEE Transactions on*, *48*(2), 727–740. 3.1.3, 3.1.3

Bridges, D. L., and S. S. Gao (2006), Spatial variation of seismic *b* values beneath Makushin Volcano, Unalaska Island, Alaska, *Earth and Planetary Science Letters*, *245*(1), 408–415. 2.2.2

Buck, W. (2006), The role of magma in the development of the Afro-Arabian Rift System, *Geological Society, London, Special Publications*, *259*(1), 43–54. 1.1.1

Bürgmann, R., P. A. Rosen, and E. J. Fielding (2000), Synthetic aperture radar interferometry to measure Earth's surface topography and its deformation, *Annual Review of Earth and Planetary Sciences*, *28*(1), 169–209. 3, 3.1.3

Burke, K., and J. Dewey (1973), Plume-generated triple junctions: key indicators in applying plate tectonics to old rocks, *The Journal of Geology*, pp. 406–433. 1.1.1

Burton, M. R., C. Oppenheimer, L. A. Horrocks, and P. W. Francis (2000), Remote sensing of co2 and h2o emission rates from masaya volcano, Nicaragua, *Geology*, *28*(10), 915–918. 5.4

Cann, J. (1970), Petrology of basalts dredged from the Gulf of Aden, in *Deep Sea Research and Oceanographic Abstracts*, vol. 17, pp. 477–482, Elsevier. 1.1.1

Caricchi, L., J. Biggs, C. Annen, and S. Ebmeier (2014), The influence of cooling, crystallisation and re-melting on the interpretation of geodetic signals in volcanic systems, *Earth and Planetary Science Letters*, *388*, 166–174. 1.5, 5.3, 6.4

Casagli, N., A. Tibaldi, A. Merri, C. Del Ventisette, T. Apuani, L. Guerri, J. Fortuny-Guasch, and D. Tarchi (2009), Deformation of Stromboli Volcano (Italy) during the 2007 eruption revealed by radar interferometry, numerical modelling and structural geological field data, *Journal of Volcanology and Geothermal Research*, *182*(3), 182–200. 6.4

Cavalié, O., M.-P. Doin, C. Lasserre, and P. Briole (2007), Ground motion measurement in the Lake Mead area, Nevada, by differential synthetic aperture radar interferometry time series analysis: Probing the lithosphere rheological structure, *Journal of Geophysical Research: Solid Earth (1978–2012)*, *112*(B3). 3.2.1

Cayol, V., and F. H. Cornet (1998), Effects of topography on the interpretation of the deformation field of prominent volcanoes: Application to Etna, *Geophysical Research Letters*, *25*(11), 1979–1982. 4.6

Chadwick Jr, W. W., S. Jónsson, D. J. Geist, M. Poland, D. J. Johnson, S. Batt, K. S. Harpp, and A. Ruiz (2011), The May 2005 eruption of Fernandina volcano, Galápagos: The first circumferential dike intrusion observed by GPS and InSAR, *Bulletin of volcanology*, *73*(6), 679–697. 5.6, 6.2

Chang, S.-J., and S. Van der Lee (2011), Mantle plumes and associated flow beneath Arabia and East Africa, *Earth and Planetary Science Letters*, *302*(3), 448–454. 1.2.1

Chapman, D. (1986), Thermal gradients in the continental crust, *Geological Society, London, Special Publications*, *24*(1), 63–70. 5.3

Charlier, B., C. Wilson, J. Lowenstern, S. Blake, P. Van Calsteren, and J. Davidson (2005), Magma generation at a large, hyperactive silicic volcano (taupo, new zealand) revealed by u-th and u-pb systematics in zircons, *Journal of Petrology*, *46*(1), 3–32. 1.4

Chernet, T., W. K. Hart, J. L. Aronson, and R. C. Walter (1998), New age constraints on the timing of volcanism and tectonism in the northern Main Ethiopian Rift–southern Afar transition zone (Ethiopia), *Journal of Volcanology and Geothermal Research*, *80*(3), 267–280. 1.1.1

Chouet, B. (1996), Long-period volcano seismicity: its source and use in eruption forecasting, *Nature*, *380*(6572), 309–316. 1.6, 1.6, 1.6, 1.6

Chouet, B. (2003), Volcano seismology, *Pure and Applied Geophysics*, *160*(3-4), 739–788. 1.6

Christensen, N. I. (1996), Poisson's ratio and crustal seismology, *Journal of Geophysical Research: Solid Earth (1978–2012)*, *101*(B2), 3139–3156. 4.6

Chu, R., D. V. Helmberger, D. Sun, J. M. Jackson, and L. Zhu (2010), Mushy magma beneath yellowstone, *Geophysical Research Letters*, *37*(1). 1.4

Clarke, P. J. (1996), Tectonic motions and earthquake deformation in Greece from GPS measurements, Ph.D. thesis, University of Oxford. 4.7.2

Cochran, J. R., and F. Martinez (1988), Evidence from the northern Red Sea on the transition from continental to oceanic rifting, *Tectonophysics*, *153*(1), 25–53. 1.2.1

Cole, J., D. Milner, and K. Spinks (2005), Calderas and caldera structures: a review, *Earth-Science Reviews*, *69*(1), 1–26. 2.3.1, 2.3.1

Cole, P., V. Bass, T. Christopher, H. Odbert, P. Smith, R. Stewart, A. Stinton, R. Seyers, and P. Williams (2012), MVO scientific report for volcanic activity between 1 November 2011 and 30 April 2012, *Tech. rep.*, Montserrat Volcano Observatory. 6.4

Condie, K. C. (2013), *Plate tectonics & crustal evolution*, Elsevier. 1.1

Cooper, G. F., C. J. Wilson, M.-A. Millet, J. A. Baker, and E. G. Smith (2012), Systematic tapping of independent magma chambers during the 1ma kidnappers supereruption, *Earth and Planetary Science Letters*, *313*, 23–33. 1.4

Cover, T. M., and P. E. Hart (1967), Nearest neighbor pattern classification, *Information Theory, IEEE Transactions on*, *13*(1), 21–27. 4.7.1

Cox, A., and R. B. Hart (2009), *Plate tectonics: how it works*, John Wiley & Sons. 1.1

Crawford, W. C., A. Rai, S. C. Singh, M. Cannat, J. Escartin, H. Wang, R. Daniel, and V. Combier (2013), Hydrothermal seismicity beneath the summit of lucky strike volcano, mid-atlantic ridge, *Earth and Planetary Science Letters*, *373*, 118–128. 6.1

d'Acremont, E., S. Leroy, M. Maia, P. Gente, and J. Autin (2010), Volcanism, jump and propagation on the Sheba ridge, eastern Gulf of Aden: segmentation evolution and implications for oceanic accretion processes, *Geophysical Journal International*, *180*(2), 535–551. 1.1.1

Daly, E., D. Keir, C. Ebinger, G. Stuart, I. Bastow, and A. Ayele (2008), Crustal tomographic imaging of a transitional continental rift: the Ethiopian rift, *Geophysical Journal International*, *172*(3), 1033–1048. 1.1.1

Daniels, K., I. Bastow, D. Keir, R. Sparks, and T. Menand (2014), Thermal models of dyke intrusion during development of continent–ocean transition, *Earth and Planetary Science Letters*, *385*, 145–153. 1.1.1

Davis, J., T. Herring, I. Shapiro, A. Rogers, and G. Elgered (1985), Geodesy by radio interferometry: Effects of atmospheric modeling errors on estimates of baseline length, *Radio science*, *20*(6), 1593–1607. 3.1.3

de Zeeuw-van Dalfsen, E., H. Rymer, F. Sigmundsson, and E. Sturkell (2005), Net gravity decrease at Askja volcano, Iceland: constraints on processes responsible for continuous caldera deflation, 1988–2003, *Journal of Volcanology and Geothermal Research*, *139*(3), 227–239. 5.2, 5.5, 6.4

Dee, D., S. Uppala, A. Simmons, P. Berrisford, P. Poli, S. Kobayashi, U. Andrae, M. Balmaseda, G. Balsamo, P. Bauer, et al. (2011), The ERA-Interim reanalysis: Configuration and performance of the data assimilation system, *Quarterly Journal of the Royal Meteorological Society*, *137*(656), 553–597. 3.2.1

Del Negro, C., G. Currenti, and D. Scandura (2009), Temperature-dependent viscoelastic modeling of ground deformation: Application to Etna volcano during the 1993–1997 inflation period, *Physics of the Earth and Planetary Interiors*, *172*(3), 299–309. 5.6, 5.6

Delaney, P., and D. McTigue (1994), Volume of magma accumulation or withdrawal estimated from surface uplift or subsidence, with application to the 1960 collapse of Kīlauea Volcano, *Bulletin of Volcanology*, *56*(6-7), 417–424. 4.2, 5.2

DLR (2011), Geo1206. 3.3

Doin, M.-P., C. Lasserre, G. Peltzer, O. Cavalié, and C. Doubre (2009), Corrections of stratified tropospheric delays in SAR interferometry: Validation with global atmospheric models, *Journal of Applied Geophysics*, *69*(1), 35–50. 3.1.3, 3.1.3, 3.2.1

Dragoni, M., and C. Magnanensi (1989), Displacement and stress produced by a pressurized, spherical magma chamber, surrounded by a viscoelastic shell, *Physics of the Earth and Planetary Interiors*, *56*(3), 316–328. 5.6

Dvorak, J. J., and D. Dzurisin (1997), Volcano geodesy: The search for magma reservoirs and the formation of eruptive vents, *Reviews of Geophysics*, *35*(3), 343–384. 1.5, 3

Dzurisin, D. (2003), A comprehensive approach to monitoring volcano deformation as a window on the eruption cycle, *Reviews of Geophysics*, *41*(1). 1.5, 3

Dzurisin, D. (2006), *Volcano deformation: new geodetic monitoring techniques*, Springer Science & Business Media. 5

Dzurisin, D., and Y. Mori (2007), *Volcano deformation: geodetic monitoring techniques*, Springer Berlin. 1.5

Dzurisin, D., J. M. Donnelly-Nolan, J. R. Evans, and S. R. Walter (1991), Crustal subsidence, seismicity, and structure near Medicine Lake volcano, California, *Journal of Geophysical Research: Solid Earth (1978–2012)*, *96*(B10), 16,319–16,333. 2.3

Dzurisin, D., M. P. Poland, and R. Bürgmann (2002), Steady subsidence of Medicine Lake volcano, northern California, revealed by repeated leveling surveys, *Journal of Geophysical Research: Solid Earth (1978–2012)*, *107*(B12), ECV–8. 2.3, 5.3

Dzurisin, D., J. W. Vallance, T. M. Gerlach, S. C. Moran, and S. D. Malone (2005), Mount St. Helens reawakens, *Eos, Transactions American Geophysical Union*, *86*(3), 25–29. 5.4

Eagles, G., R. Gloaguen, and C. Ebinger (2002), Kinematics of the Danakil microplate, *Earth and Planetary Science Letters*, *203*(2), 607–620. 1.2.1

Ebinger, C. (1989), Tectonic development of the western branch of the East African rift system, *Geological Society of America Bulletin*, *101*(7), 885–903. 6.3

Ebinger, C., and M. Casey (2001), Continental breakup in magmatic provinces: An Ethiopian example, *Geology*, *29*(6), 527–530. 1.2.1

Ebinger, C., D. Keir, A. Ayele, E. Calais, T. Wright, M. Belachew, J. Hammond, E. Campbell, and W. Buck (2008), Capturing magma intrusion and faulting processes during continental rupture: seismicity of the Dabbahu (Afar) rift, *Geophysical Journal International*, *174*(3), 1138–1152. 1.6, 2.2.3, 5.5

Ebinger, C., A. Ayele, D. Keir, J. Rowland, G. Yirgu, T. Wright, M. Belachew, and I. Hamling (2010), Length and timescales of rift faulting and magma intrusion: the Afar rifting cycle from 2005 to present, *Annual Review of Earth and Planetary Sciences*, *38*, 439–466. 1.2.2

Ebmeier, S., J. Biggs, T. Mather, G. Wadge, and F. Amelung (2010), Steady downslope movement on the western flank of arenal volcano, costa rica, *Geochemistry, Geophysics, Geosystems*, *11*(12). 6.4

Elliott, J. (2009), Strain accumulation & release on the Tibetan Plateau measured using InSAR, Ph.D. thesis, Oxford University. 3.1.4

Elliott, J., J. Biggs, B. Parsons, and T. Wright (2008), InSAR slip rate determination on the Altyn Tagh Fault, northern Tibet, in the presence of topographically correlated atmospheric delays, *Geophysical Research Letters*, *35*(12). 3.1.3, 3.2.1, 3.3.1

Ellis, B. S., and J. A. Wolff (2012), Complex storage of rhyolite in the central snake river plain, *Journal of Volcanology and Geothermal Research*, *211*, 1–11. 1.4

ERDAS, E. R. (2008), ER Mapper User's guide, *Norcross, USA*. 4.7.1

Farr, T. G., P. A. Rosen, E. Caro, R. Crippen, R. Duren, S. Hensley, M. Kobrick, M. Paller, E. Rodriguez, L. Roth, et al. (2007), The shuttle radar topography mission, *Reviews of geophysics*, *45*(2). 3.1.3

Ferguson, D. J., J. Maclennan, I. Bastow, D. Pyle, S. Jones, D. Keir, J. Blundy, T. Plank, and G. Yirgu (2013), Melting during late-stage rifting in Afar is hot and deep, *Nature*, *499*(7456), 70–73. 1.2.1

Fialko, Y., Y. Khazan, and M. Simons (2001), Deformation due to a pressurized horizontal circular crack in an elastic half-space, with applications to volcano geodesy, *Geophysical Journal International*, *146*(1), 181–190. 4.1, 4.5

Field, L., T. Barnie, J. Blundy, R. A. Brooker, D. Keir, E. Lewi, and K. Saunders (2012a), Integrated field, satellite and petrological observations of the November 2010 eruption of Erta Ale, *Bulletin of volcanology*, *74*(10), 2251–2271. 1.2.2

Field, L., J. Blundy, R. Brooker, T. Wright, and G. Yirgu (2012b), Magma storage conditions beneath Dabbahu Volcano (Ethiopia) constrained by petrology, seismicity and satellite geodesy, *Bulletin of volcanology*, *74*(5), 981–1004. 4.9, 6.1

Foster, J., B. Brooks, T. Cherubini, C. Shacat, S. Businger, and C. Werner (2006), Mitigating atmospheric noise for InSAR using a high resolution weather model, *Geophysical Research Letters*, *33*(16). 3.1.3

Foucher, J.-P., X. Le Pichon, J.-C. Sibuet, D. Roberts, P.-Y. Chenet, A. Bally, E. Oxburgh, P. Kent, J. Dewey, M. Bott, et al. (1982), The ocean–continent transition in the uniform lithospheric stretching model: Role of partial melting in the mantle [and discussion], *Philosophical Transactions of the Royal Society of London. Series A, Mathematical and Physical Sciences*, *305*(1489), 27–43. 1.1.1

Fournier, T., M. Pritchard, and S. Riddick (2010), Duration, magnitude, and frequency of subaerial volcano deformation events: New results from Latin America using InSAR and a global synthesis, *Geochemistry, Geophysics, Geosystems*, *11*(1). 6.4

Furlong, K. P., and D. M. Fountain (1986), Continental crustal underplating: Thermal considerations and seismic-petrologic consequences, *Journal of Geophysical Research: Solid Earth (1978–2012)*, *91*(B8), 8285–8294. 1.1.1

Furman, T., J. Bryce, T. Rooney, B. Hanan, G. Yirgu, and D. Ayalew (2006), Heads and tails: 30 million years of the Afar plume, *Geological Society, London, Special Publications*, *259*(1), 95–119. 1.2.1

Garthwaite, M. C. (2011), Deformation of Tibet: InSAR analysis and viscous flow models, Ph.D. thesis, University of Leeds. 3.1, 3.3.1

Gass, I. (1970), The evolution of volcanism in the junction area of the Red Sea, Gulf of Aden and Ethiopian rifts, *Philosophical Transactions of the Royal Society of London. Series A, Mathematical and Physical Sciences*, *267*(1181), 369–381. 2.2.2

Geist, D. J., G. Bergantz, and W. W. Chadwick Jr (2014), Galápagos magma chambers, *The Galapagos: A Natural Laboratory for the Earth Sciences*, *204*, 55. 6.4

Geller, R. J., and C. S. Mueller (1980), Four similar earthquakes in central California, *Geophysical research letters*, *7*(10), 821–824. 2.2.4

Genco, R., and M. Ripepe (2010), Inflation-deflation cycles revealed by tilt and seismic records at Stromboli volcano, *Geophysical Research Letters*, *37*(12). 6.4

Gerlach, T. M. (1986), Exsolution of h2o, co2, and s during eruptive episodes at kilauea volcano, hawaii, *Journal of Geophysical Research: Solid Earth (1978–2012)*, *91*(B12), 12,177–12,185. 5.4

Gerlach, T. M., K. A. McGee, and M. P. Doukas (2008), Emission rates of CO_2, SO_2, and H_2S, scrubbing, and pre-eruption excess volatiles at Mount St. Helens, 2004-2005, *US Geological Survey professional paper*, (1750), 543–571. 5.4

Geshi, N., T. Shimano, T. Chiba, and S. Nakada (2002), Caldera collapse during the 2000 eruption of Miyakejima Volcano, Japan, *Bulletin of Volcanology*, *64*(1), 55–68. 6.1.2

Ghiglia, D. C., and M. D. Pritt (1998), *Two-dimensional phase unwrapping: theory, algorithms, and software*, vol. 4, Wiley New York:. 3.1.3

Girona, T., F. Costa, C. Newhall, and B. Taisne (2014), On depressurization of volcanic magma reservoirs by passive degassing, *Journal of Geophysical Research: Solid Earth*, *119*(12), 8667–8687. 5.2, 5.3, 5.4, 6.4

Gislason, S. R., D. Wolff-Boenisch, A. Stefansson, E. H. Oelkers, E. Gunnlaugsson, H. Sigurdardottir, B. Sigfusson, W. S. Broecker, J. M. Matter, M. Stute, et al. (2010), Mineral sequestration of carbon dioxide in basalt: A pre-injection overview of the CarbFix project, *International Journal of Greenhouse Gas Control*, *4*(3), 537–545. 5.4

Goitom, B., C. Oppenheimer, J. O. Hammond, R. Grandin, T. Barnie, A. Donovan, G. Ogubazghi, E. Yohannes, G. Kibrom, J.-M. Kendall, et al. (2015), First recorded eruption of nabro volcano, eritrea, 2011, *Bulletin of volcanology*, *77*(10), 1–21. 1.3.1, 1.3.2, 1.3.2, 1.3.2, 4.2.1, 5.2, 6.2, E

Goldstein, P., and A. Snoke (2005), SAC availability for the IRIS community, *Incorporated Institutions for Seismology Data Management Center Electronic Newsletter*, *7*. 2.2.1

Goldstein, R. M., H. A. Zebker, and C. L. Werner (1988), Satellite radar interferometry-two-dimensional phase unwrapping, *Radio science*, *23*(4), 713–720. 3.1.3

González, P. J., S. V. Samsonov, S. Pepe, K. F. Tiampo, P. Tizzani, F. Casu, J. Fernández, A. G. Camacho, and E. Sansosti (2013), Magma storage and migration associated with the 2011–2012 El Hierro eruption: Implications for crustal magmatic systems at oceanic island volcanoes, *Journal of Geophysical Research: Solid Earth*, *118*(8), 4361–4377. 6.1.2

Grandin, R., A. Socquet, M.-P. Doin, E. Jacques, J.-B. de Chabalier, and G. King (2010), Transient rift opening in response to multiple dike injections in the Manda Hararo rift (Afar, Ethiopia) imaged by time-dependent elastic inversion of interferometric synthetic aperture radar data, *Journal of Geophysical Research: Solid Earth (1978–2012)*, *115*(B9). 6.4

Grapenthin, R., J. T. Freymueller, and A. M. Kaufman (2013), Geodetic observations during the 2009 eruption of redoubt volcano, alaska, *Journal of Volcanology and Geothermal Research*, *259*, 115–132. 6.4

Gregg, P. M., J. Lin, M. D. Behn, and L. G. Montési (2007), Spreading rate dependence of gravity anomalies along oceanic transform faults, *Nature*, *448*(7150), 183–187. 6.3

Gualda, G. A., and M. S. Ghiorso (2013), The bishop tuff giant magma body: an alternative to the standard model, *Contributions to Mineralogy and Petrology*, *166*(3), 755–775. 1.4

Gupta, H. (2011), *Encyclopedia of Solid Earth Geophysics*, vol. 1, Springer Verlag. 1.6, 1.6

Gutenberg, B., and C. F. Richter (1944), Frequency of earthquakes in California, *Bulletin of the Seismological Society of America*, *34*(4), 185–188. 2.2.2

Hamiel, Y., R. Grandin, G. Baer, T. Wright, C. Doubre, J. Hamlyn, C. Pagli, and G. Peltzer (2013), InSAR investigation of crustal deformation associated with the 2011 eruption of the Nabro volcano, Eritrea, in *AGU Fall Meeting Abstracts*, vol. 1, p. 0955. 6.2

Hamling, I. J., A. Ayele, L. Bennati, E. Calais, C. J. Ebinger, D. Keir, E. Lewi, T. J. Wright, and G. Yirgu (2009), Geodetic observations of the ongoing Dabbahu rifting episode: new dyke intrusions in 2006 and 2007, *Geophysical Journal International*, *178*(2), 989–1003. 1.2.2

Hamling, I. J., T. J. Wright, E. Calais, L. Bennati, and E. Lewi (2010), Stress transfer between thirteen successive dyke intrusions in Ethiopia, *Nature Geoscience*, *3*(10), 713–717. 6.1.2

Hamlyn, J. E., D. Keir, T. J. Wright, J. W. Neuberg, B. Goitom, J. O. Hammond, C. Pagli, C. Oppenheimer, J. Kendall, R. Grandin, et al. (2014), Seismicity and subsidence following the 2011 Nabro eruption, Eritrea: Insights into the plumbing system of an off-rift volcano, *Journal of Geophysical Research: Solid Earth*, *119*(11), 8267–8282. 2, E

Hammond, J., J.-M. Kendall, G. Stuart, D. Keir, C. Ebinger, A. Ayele, and M. Belachew (2011), The nature of the crust beneath the Afar triple junction: Evidence from receiver functions, *Geochemistry, Geophysics, Geosystems*, *12*(12). 1.2.1

Hammond, J., J.-M. Kendall, G. Stuart, C. Ebinger, I. Bastow, D. Keir, A. Ayele, M. Belachew, B. Goitom, G. Ogubazghi, et al. (2013), Mantle upwelling and initiation of rift segmentation beneath the Afar Depression, *Geology*, *41*(6), 635–638. 1.2.1, 1.3, 6.3, 6.3

Hansen, S. E., and A. A. Nyblade (2013), The deep seismic structure of the Ethiopia/Afar hotspot and the African superplume, *Geophysical Journal International*, p. ggt116. 1.2.1

Hansen, S. E., A. A. Nyblade, and M. H. Benoit (2012), Mantle structure beneath Africa and Arabia from adaptively parameterized P-wave tomography: Implications for the origin of Cenozoic Afro-Arabian tectonism, *Earth and Planetary Science Letters*, *319*, 23–34. 1.2.1

Hanssen, R. F. (2001), *Radar interferometry: data interpretation and error analysis*, vol. 2, Springer. 3, 3.1.3, 3.1.3

Hayward, N., and C. Ebinger (1996), Variations in the along-axis segmentation of the Afar Rift system, *Tectonics*, *15*(2), 244–257. 1.1.1

Hey, R. N., and K. Deffeyes (1972), The Galapagos triple junction and plate motions in the East Pacific, *Nature*, *237*, 20–22. 1.1.1

Hildreth, W. (1979), The bishop tuff: evidence for the origin of compositional zonation in silicic magma chambers, *Geological Society of America Special Papers*, *180*, 43–76. 1.4

Hildreth, W., and C. J. Wilson (2007), Compositional zoning of the bishop tuff, *Journal of Petrology*, *48*(5), 951–999. 1.4

Hill, D. P. (1977), A model for earthquake swarms, *Journal of Geophysical Research*, *82*(8), 1347–1352. 2

Hodge, D. S. (1974), Thermal model for origin of granitic batholiths. 5.6

Hofmann, C., V. Courtillot, G. Feraud, P. Rochette, G. Yirgu, E. Ketefo, and R. Pik (1997), Timing of the Ethiopian flood basalt event and implications for plume birth and global change, *Nature*, *389*(6653), 838–841. 1.2.1

Holohan, E., M. Schöpfer, and J. Walsh (2011), Mechanical and geometric controls on the structural evolution of pit crater and caldera subsidence, *Journal of Geophysical Research*, *116*(B7), B07,202. 2.3.1, 2.3.1

Holohan, E. P., B. v. W. de Vries, and V. R. Troll (2008), Analogue models of caldera collapse in strike-slip tectonic regimes, *Bulletin of volcanology*, *70*(7), 773–796. 6.3

Holohan, E. P., T. R. Walter, M. P. Schöpfer, J. J. Walsh, B. Wyk de Vries, and V. R. Troll (2013), Origins of oblique-slip faulting during caldera subsidence, *Journal of Geophysical Research: Solid Earth*, *118*(4), 1778–1794. 6.3

Holtzman, B. K., J. Kendall, et al. (2010), Organized melt, seismic anisotropy, and plate boundary lubrication, *Geochemistry, Geophysics, Geosystems*, *11*(12). 1.1.1, 6.3

Hooper, A., H. Zebker, P. Segall, and B. Kampes (2004), A new method for measuring deformation on volcanoes and other natural terrains using insar persistent scatterers, *Geophysical research letters*, *31*(23). 3.1.3

Hooper, A., P. Segall, and H. Zebker (2007), Persistent scatterer interferometric synthetic aperture radar for crustal deformation analysis, with application to Volcán Alcedo, Galápagos, *Journal of Geophysical Research: Solid Earth (1978–2012)*, *112*(B7). 5.3

Huppert, H. E., and R. S. J. Sparks (1981), The fluid dynamics of a basaltic magma chamber replenished by influx of hot, dense ultrabasic magma, *Contributions to Mineralogy and Petrology*, *75*(3), 279–289. 5.3

Illies, J. H. (1981), Mechanism of graben formation, *Tectonophysics*, *73*(1), 249–266. 6.1.1

Johnson, D. J., F. Sigmundsson, and P. T. Delaney (2000), Comment on "Volume of magma accumulation or withdrawal estimated from surface uplift or subsidence, with application to the 1960 collapse of Kīlauea volcano" by PT Delaney and DF McTigue, *Bulletin of Volcanology*, *61*(7), 491–493. 4.2.1

Jolivet, R., R. Grandin, C. Lasserre, M.-P. Doin, and G. Peltzer (2011), Systematic InSAR tropospheric phase delay corrections from global meteorological reanalysis data, *Geophysical Research Letters*, *38*(17). 3.2.1

Jones, R., and R. Stewart (1997), A method for determining significant structures in a cloud of earthquakes, *Journal of Geophysical Research*, *102*(B4), 8245–8254. 2.2.1

Kanamori, H. (1977), The energy release in great earthquakes, *Journal of Geophysical Research*, *82*(20), 2981–2987. 2.2.2

Kanamori, H., and P. C. Jennings (1978), Determination of local magnitude, ML, from strong-motion accelerograms, *Bulletin of the Seismological Society of America*, *68*(2), 471–485. 2.2.2

Keir, D., C. Ebinger, G. Stuart, E. Daly, and A. Ayele (2006a), Strain accommodation by magmatism and faulting as rifting proceeds to breakup: Seismicity of the northern Ethiopian rift, *Journal of Geophysical Research: Solid Earth (1978–2012)*, *111*(B5). 1.1.1

Keir, D., G. Stuart, A. Jackson, and A. Ayele (2006b), Local earthquake magnitude scale and seismicity rate for the Ethiopian rift, *Bulletin of the Seismological Society of America*, *96*(6), 2221–2230. 2.2.2

Keir, D., C. Pagli, I. D. Bastow, and A. Ayele (2011), The magma-assisted removal of Arabia in Afar: Evidence from dike injection in the Ethiopian rift captured using InSAR and seismicity, *Tectonics*, *30*(2). 2.2.2

Kennedy, B., J. Stix, J. W. Vallance, Y. Lavallée, and M.-A. Longpré (2004), Controls on caldera structure: Results from analogue sandbox modeling, *Geological Society of America Bulletin*, *116*(5-6), 515–524. 2.3.1, 2.3.1

Keranen, K., S. Klemperer, R. Gloaguen, E. W. Group, et al. (2004), Three-dimensional seismic imaging of a protoridge axis in the Main Ethiopian rift, *Geology*, *32*(11), 949–952. 1.1.1

Kiselev, A. (1987), Volcanism of the Baikal rift zone, *Tectonophysics*, *143*(1), 235–244. 6.3

Klein, F. (2002), *User's Guide to HYPOINVERSE-2000: A Fortran Program to Solve for Earthquake Locations and Magnitudes*, US Geological Survey. 2.2.1, A.2, A.2.1

Klein, F. W. (1982), Patterns of historical eruptions at Hawaiian volcanoes, *Journal of Volcanology and Geothermal Research*, *12*(1), 1–35. 3.4

Lahr, J. (1989), *HYPOELLIPSE/VERSION 2.0*, a Computer Program for Determining Local Earthquake Hypocentral Parameters, Magnitude, and First Motion Pattern*, US Geological Survey. 2.2.1

Lahr, J., B. Chouet, C. Stephens, J. Power, and R. Page (1994), Earthquake classification, location, and error analysis in a volcanic environment: implications for the magmatic system of the 1989-1990 eruptions at Redoubt Volcano, Alaska, *Journal of Volcanology and Geothermal Research*, *62*(1), 137–152. 2.2.1

Lanari, R., P. Lundgren, and E. Sansosti (1998), Dynamic deformation of Etna volcano observed by satellite radar interferometry, *Geophysical Research Letters*, *25*(10), 1541–1544. 1.5

Lavallée, Y., J. Stix, B. Kennedy, M. Richer, and M.-A. Longpré (2004), Caldera subsidence in areas of variable topographic relief: results from analogue modeling, *Journal of volcanology and geothermal research*, *129*(1), 219–236. 2.3.1

Lavallée, Y., P. Meredith, D. Dingwell, K.-U. Hess, J. Wassermann, B. Cordonnier, A. Gerik, and J. Kruhl (2008), Seismogenic lavas and explosive eruption forecasting, *Nature*, *453*(7194), 507–510. 6.1

Le Pichon, X., and J. Francheteau (1978), A plate-tectonic analysis of the Red Sea-Gulf of Aden area, *Tectonophysics*, *46*(3), 369–406. 1.1

Lehto, H. L., D. C. Roman, and S. C. Moran (2010), Temporal changes in stress preceding the 2004–2008 eruption of Mount St. Helens, Washington, *Journal of Volcanology and Geothermal Research*, *198*(1), 129–142. 6.1.1

Leroy, S., P. Gente, M. Fournier, E. d'Acremont, P. Patriat, M.-O. Beslier, N. Bellahsen, M. Maia, A. Blais, J. Perrot, et al. (2004), From rifting to spreading in the eastern Gulf of Aden: a geophysical survey of a young oceanic basin from margin to margin, *Terra Nova*, *16*(4), 185–192. 1.2.1

Leroy, S., E. d'Acremont, C. Tiberi, C. Basuyau, J. Autin, F. Lucazeau, and H. Sloan (2010), Recent off-axis volcanism in the eastern Gulf of Aden: implications for plume–ridge interaction, *Earth and Planetary Science Letters*, *293*(1), 140–153. 1.1.1

Leroy, S., P. Razin, J. Autin, F. Bache, E. d'Acremont, L. Watremez, J. Robinet, C. Baurion, Y. Denèle, N. Bellahsen, et al. (2013), From rifting to oceanic spreading in the Gulf of Aden: a synthesis, in *Lithosphere Dynamics and Sedimentary Basins: The Arabian Plate and Analogues*, pp. 385–427, Springer. 1.2.1

Li, Z., J.-P. Muller, P. Cross, and E. J. Fielding (2005), Interferometric synthetic aperture radar (InSAR) atmospheric correction: GPS, Moderate Resolution Imaging Spectroradiometer (MODIS), and InSAR integration, *Journal of Geophysical Research: Solid Earth (1978–2012)*, *110*(B3). 3.1.3

Li, Z., J.-P. Muller, P. Cross, P. Albert, J. Fischer, and R. Bennartz (2006), Assessment of the potential of MERIS near-infrared water vapour products to correct ASAR interferometric measurements, *International Journal of Remote Sensing*, *27*(2), 349–365. 3.1.3

Lipman, P. W. (2007), Incremental assembly and prolonged consolidation of cordilleran magma chambers: Evidence from the southern rocky mountain volcanic field, *Geosphere*, *3*(1), 42–70. 1.4

Lisowski, M. (2006), Analytical volcano deformation source models, in *Volcano Deformation*, pp. 279–304, Springer. 4.1, 4.3, 4.4

Lu, Z., T. Masterlark, J. Power, D. Dzurisin, and C. Wicks (2002), Subsidence at Kiska volcano, western Aleutians, detected by satellite radar interferometry, *Geophysical Research Letters*, *29*(18), 2–1. 6.4

Lu, Z., T. Masterlark, D. Dzurisin, R. Rykhus, and C. Wicks (2003), Magma supply dynamics at Westdahl volcano, Alaska, modeled from satellite radar interferometry, *Journal of Geophysical Research: Solid Earth (1978–2012)*, *108*(B7). 1.5

Lu, Z., D. Dzurisin, J. Biggs, C. Wicks, and S. McNutt (2010), Ground surface deformation patterns, magma supply, and magma storage at Okmok volcano, Alaska, from InSAR analysis: 1. Intereruption deformation, 1997–2008, *Journal of Geophysical Research: Solid Earth (1978–2012)*, *115*(B5). 4.3, 5.2, 6.2, 6.4

Maccaferri, F., E. Rivalta, D. Keir, and V. Acocella (2014), Off-rift volcanism in rift zones determined by crustal unloading, *Nature Geoscience*. 1.1.1

Macdonald, R., G. Davies, B. Upton, P. Dunkley, M. Smith, and P. Leat (1995), Petrogenesis of Silali volcano, Gregory Rift, Kenya, *Journal of the Geological Society*, *152*(4), 703–720. 6.1

Maguire, P., G. Keller, S. Klemperer, G. Mackenzie, K. Keranen, S. Harder, B. O Reilly, H. Thybo, L. Asfaw, M. Khan, et al. (2006), Crustal structure of the northern Main Ethiopian Rift from the EAGLE controlled-source survey; a snapshot of incipient lithospheric break-up, *Special Publication-Geological Society Of London*, *259*, 269. 1.1.1

Makris, J., and A. Ginzburg (1987), The Afar depression: transition between continental rifting and sea-floor spreading, *Tectonophysics*, *141*(1), 199–214. 2.2.1

Mann, D., J. Freymueller, and Z. Lu (2002), Deformation associated with the 1997 eruption of Okmok volcano, Alaska, *Journal of Geophysical Research: Solid Earth (1978–2012)*, *107*(B4), ETG–7. 4.1, 4.6

Marti, J., G. Ablay, L. t. Redshaw, and R. Sparks (1994), Experimental studies of collapse calderas, *Journal of the Geological Society*, *151*(6), 919–929. 2.3.1

Martin, D., R. W. Griffiths, and I. H. Campbell (1987), Compositional and thermal convection in magma chambers, *Contributions to Mineralogy and Petrology*, *96*(4), 465–475. 5.3

Massonnet, D., and K. L. Feigl (1998), Radar interferometry and its application to changes in the Earth's surface, *Reviews of geophysics*, *36*(4), 441–500. 3, 3.1.1

Masterlark, T. (2007), Magma intrusion and deformation predictions: Sensitivities to the Mogi assumptions, *Journal of Geophysical Research: Solid Earth (1978–2012)*, *112*(B6). 4.6

McClusky, S., R. Reilinger, G. Ogubazghi, A. Amleson, B. Healeb, P. Vernant, J. Sholan, S. Fisseha, L. Asfaw, R. Bendick, et al. (2010), Kinematics of the southern Red Sea–Afar Triple Junction and implications for plate dynamics, *Geophysical Research Letters*, *37*(5). 1.2.1, 6.3

McKenzie, D. (1978), Some remarks on the development of sedimentary basins, *Earth and Planetary science letters*, *40*(1), 25–32. 1.1

McKenzie, D., and M. Bickle (1988), The volume and composition of melt generated by extension of the lithosphere, *Journal of petrology*, *29*(3), 625–679. 1.1.1

McKenzie, D., and W. Morgan (1969a), Evolution of triple junctions, *Nature*, *224*, 125–133. 1.1

McKenzie, D., and W. Morgan (1969b), Evolution of triple junctions, *Nature*, *224*, 125–133. 1.1.1, 1.2, 1.2.1

McKenzie, D., and J. G. Sclater (1971), The evolution of the Indian Ocean since the Late Cretaceous, *Geophysical Journal International*, *24*(5), 437–528. 1.1.1

McKenzie, D., D. Davies, and P. Molnar (1970), Plate tectonics of the Red Sea and East Africa., *Nature*, *226*(5242), 243–248. 1.1, 1.1.1, 1.2.1

McNutt, S. R. (2002), Volcano seismology and monitoring for eruptions, *International Geophysics Series*, *81*(A), 383–406. 1.6

McTigue, D. (1987), Elastic stress and deformation near a finite spherical magma body: resolution of the point source paradox, *Journal of Geophysical Research: Solid Earth (1978–2012)*, *92*(B12), 12,931–12,940. 4.7.3

Métrich, N., A. Bertagnini, and A. Di Muro (2010), Conditions of magma storage, degassing and ascent at stromboli: new insights into the volcano plumbing system with inferences on the eruptive dynamics, *Journal of Petrology*, *51*(3), 603–626. 6.2

Meyer, F. J. (2011), Performance requirements for ionospheric correction of low-frequency SAR data, *Geoscience and Remote Sensing, IEEE Transactions on*, *49*(10), 3694–3702. 3.1.3

Meyer, F. J., and J. Nicoll (2008), The impact of the ionosphere on interferometric SAR processing, in *Geoscience and Remote Sensing Symposium, 2008. IGARSS 2008. IEEE International*, vol. 2, pp. II–391, IEEE. 3.1.3

Mogi, K. (1958), Relations between the eruptions of various volcanoes and the deformations of the ground surfaces around them. 4.1, 4.2

Mohr, P. (1968), Transcurrent faulting in the Ethiopian rift system. 1.3

Moran, S., O. Kwoun, T. Masterlark, and Z. Lu (2006), On the absence of InSAR-detected volcano deformation spanning the 1995–1996 and 1999 eruptions of Shishaldin Volcano, Alaska, *Journal of Volcanology and Geothermal Research*, *150*(1), 119–131. 6.4

Moran, S. C. (1994), Seismicity at Mount St. Helens, 1987–1992: Evidence for repressurization of an active magmatic system, *Journal of Geophysical Research: Solid Earth (1978–2012)*, *99*(B3), 4341–4354. 5.2, 6.4

Morgan, W. J. (1972), Plate motions and deep mantle convection, *Geological Society of America Memoirs*, *132*, 7–22. 1.1.1

Mori, J., R. A. White, D. H. Harlow, P. Okubo, J. A. Power, R. P. Hoblitt, E. P. Laguerta, A. Lanuza, and B. C. Bautista (1996), Volcanic earthquakes following the 1991 climactic eruption of Mount Pinatubo: Strong seismicity during a waning eruption, *Fire and Mud: Eruptions and Lahars of Mount Pinatubo, Philippines*, pp. 339–350. 2

Nakada, S., H. Shimizu, and K. Ohta (1999), Overview of the 1990–1995 eruption at Unzen Volcano, *Journal of Volcanology and Geothermal Research*, *89*(1), 1–22. 5.2, 6.4

Neuberg, J. (2000), Characteristics and causes of shallow seismicity in andesite volcanoes, *Philosophical Transactions of the Royal Society of London. Series A: Mathematical, Physical and Engineering Sciences*, *358*(1770), 1533–1546. 1.6, 1.6

Neuberg, J., R. Luckett, B. Baptie, and K. Olsen (2000), Models of tremor and low-frequency earthquake swarms on Montserrat, *Journal of Volcanology and Geothermal Research*, *101*(1), 83–104. 1.6

Neuberg, J., H. Tuffen, L. Collier, D. Green, T. Powell, and D. Dingwell (2006), The trigger mechanism of low-frequency earthquakes on Montserrat, *Journal of volcanology and geothermal research*, *153*(1-2), 37–50. 1.6, 1.6

Newman, A., T. H. Dixon, G. Ofoegbu, and J. Dixon (2001), Geodetic and seismic constraints on recent activity at Long Valley Caldera, California: evidence for viscoelastic rheology, *Journal of Volcanology and Geothermal Research*, *105*(3), 183–206. 5.2, 5.6

Nishi, K., H. Ono, and H. Mori (1999), Global positioning system measurements of ground deformation caused by magma intrusion and lava discharge: the 1990–1995 eruption at Unzendake volcano, Kyushu, Japan, *Journal of volcanology and geothermal research*, *89*(1), 23–34. 4.1, 4.6

Nishi, Y., S. Sherburn, B. J. Scott, and M. Sugihara (1996), High-frequency earthquakes at white island volcano, new zealand: insights into the shallow structure of a volcano-hydrothermal system, *Journal of volcanology and geothermal research*, *72*(3), 183–197. 6.1

Nobile, A., C. Pagli, D. Keir, T. J. Wright, A. Ayele, J. Ruch, and V. Acocella (2012), Dike-fault interaction during the 2004 Dallol intrusion at the northern edge of the Erta Ale Ridge (Afar, Ethiopia), *Geophysical Research Letters*, *39*(19). 1.2.2, 1.6, 6.3

Nooner, S. L., and W. W. Chadwick (2009), Volcanic inflation measured in the caldera of Axial Seamount: Implications for magma supply and future eruptions, *Geochemistry, Geophysics, Geosystems*, *10*(2). 5.6

Okada, Y. (1985), Surface deformation due to shear and tensile faults in a half-space, *Bulletin of the seismological society of America*, *75*(4), 1135–1154. 4.1, 4.4, B

Onn, F., and H. Zebker (2006), Correction for interferometric synthetic aperture radar atmospheric phase artifacts using time series of zenith wet delay observations from a GPS network, *Journal of Geophysical Research: Solid Earth (1978–2012)*, *111*(B9). 3.1.3

Owens, J. C. (1967), Optical refractive index of air: dependence on pressure, temperature and composition, *Applied Optics*, *6*(1), 51–59. 3.1.3

Pagli, C., F. Sigmundsson, T. Arnadóttir, P. Einarsson, and E. Sturkell (2006), Deflation of the Askja volcanic system: constraints on the deformation source from combined inversion of satellite radar interferograms and GPS measurements, *Journal of volcanology and geothermal research*, *152*(1), 97–108. 1.5, 5.5, 6.3, 6.4

Pagli, C., T. J. Wright, C. J. Ebinger, S.-H. Yun, J. R. Cann, T. Barnie, and A. Ayele (2012), Shallow axial magma chamber at the slow-spreading Erta Ale Ridge, *Nature Geoscience*, *5*(4), 284–288. 1.2.2, 5.2, 5.2, 6.3, 6.4

Pagli, C., H. Wang, T. J. Wright, E. Calais, and E. Lewi (2014), Current plate boundary deformation of the Afar rift from a 3-D velocity field inversion of InSAR and GPS, *Journal of Geophysical Research: Solid Earth*, *119*(11), 8562–8575. 5.3, 6.4

Parker, A. L., J. Biggs, and Z. Lu (2014), Investigating long-term subsidence at Medicine Lake Volcano, CA, using multitemporal InSAR, *Geophysical Journal International*, *199*(2), 844–859. 1.5, 5.2

Parks, M. M., J. D. Moore, X. Papanikolaou, J. Biggs, T. A. Mather, D. M. Pyle, C. Raptakis, D. Paradissis, A. Hooper, B. Parsons, et al. (2015), From quiescence to unrest: 20 years of satellite geodetic measurements at santorini volcano, greece, *Journal of Geophysical Research: Solid Earth*, *120*(2), 1309–1328. 6.4

Parsons, B., T. Wright, P. Rowe, J. Andrews, J. Jackson, R. Walker, M. Khatib, M. Talebian, E. Bergman, and E. Engdahl (2006), The 1994 Sefidabeh (eastern Iran) earthquakes revisited: new evidence from satellite radar interferometry and carbonate dating about the growth of an active fold above a blind thrust fault, *Geophysical Journal International*, *164*(1), 202–217. 4.8

Patanè, D., G. Di Grazia, A. Cannata, P. Montalto, and E. Boschi (2008), Shallow magma pathway geometry at Mt. Etna volcano, *Geochemistry, Geophysics, Geosystems*, *9*(12). 6.1

Pechmann, J. C., and H. Kanamori (1982), Waveforms and spectra of preshocks and aftershocks of the 1979 Imperial valley, California, earthquake: Evidence for fault heterogeneity?, *Journal of Geophysical Research*, *87*(B13), 10,579–10. 2.2.4

Peyret, M., S. Dominguez, R. Cattin, J. Champenois, M. Leroy, and A. Zajac (2011), Present-day interseismic surface deformation along the Longitudinal Valley, eastern Taiwan, from a PS-InSAR analysis of the ERS satellite archives, *Journal of Geophysical Research: Solid Earth (1978–2012)*, *116*(B3). 3.1

Pietranera, L., L. Cesarano, V. Gentile, F. Britti, F. Strehl, A. Relin, and R. Siegmund (2011), Time and resolution : COSMO-SkyMed VHR data in support to precision farming applications, in *17th GEOCAP Conference*, vol. 1, p. 22. 3.2

Pik, R., B. Marty, and D. Hilton (2006), How many mantle plumes in Africa? The geochemical point of view, *Chemical Geology*, *226*(3), 100–114. 1.3

Pik, R., B. Marty, J. Carignan, G. Yirgu, and T. Ayalew (2008), Timing of East African Rift development in southern Ethiopia: Implication for mantle plume activity and evolution of topography, *Geology*, *36*(2), 167–170. 1.2.1

Pinel, V., M. Poland, and A. Hooper (2014), Volcanology: Lessons learned from Synthetic Aperture Radar imagery, *Journal of Volcanology and Geothermal Research*. 3

Poland, M., R. Bürgmann, D. Dzurisin, M. Lisowski, T. Masterlark, S. Owen, and J. Fink (2006), Constraints on the mechanism of long-term, steady subsidence at Medicine Lake volcano, northern California, from GPS, leveling, and InSAR, *Journal of Volcanology and Geothermal Research*, *150*(1), 55–78. 5.2, 5.3

Puglisi, G., A. Bonforte, and S. R. Maugeri (2001), Ground deformation patterns on Mount Etna, 1992 to 1994, inferred from GPS data, *Bulletin of volcanology*, *62*(6-7), 371–384. 4.1, 4.6

Puysségur, B., R. Michel, and J.-P. Avouac (2007), Tropospheric phase delay in interferometric synthetic aperture radar estimated from meteorological model and multispectral imagery, *Journal of Geophysical Research: Solid Earth (1978–2012)*, *112*(B5). 3.2.1

Rhodes, J., K. Wenz, C. Neal, J. Sparks, and J. Lockwood (1989), Geochemical evidence for invasion of Kilauea's plumbing system by Mauna Loa magma, *Nature*, *337*(6204), 257–260. 3.4

Richter, C. (1935), An instrumental earthquake magnitude scale, *Bull. Seism. Soc. Am*, *25*(1), 1–32. 2.2.2

Richter, C. F. (1958), Elementary seismology. 2.3

Riddick, S., and D. Schmidt (2011), Time-dependent changes in volcanic inflation rate near Three Sisters, Oregon, revealed by InSAR, *Geochemistry, Geophysics, Geosystems*, *12*(12). 4.1, 4.6

Rivalta, E., and P. Segall (2008), Magma compressibility and the missing source for some dike intrusions, *Geophysical Research Letters*, *35*(4). 4.2.1, 4.2.1

Robertson, E., J. Biggs, K. Cashman, M. Floyd, and C. Vye-Brown (2015), Influence of regional tectonics and pre-existing structures on the formation of elliptical calderas in the kenyan rift, *Geological Society, London, Special Publications*, *420*, SP420–12. 6.3

Roche, O., T. Druitt, and O. Merle (2000), Experimental study of caldera formation, *Journal of Geophysical Research: Solid Earth (1978–2012)*, *105*(B1), 395–416. 2.3.1

Rogers, N., R. Macdonald, J. G. Fitton, R. George, M. Smith, and B. Barreiro (2000), Two mantle plumes beneath the East African rift system: Sr, Nd and Pb isotope evidence from Kenya Rift basalts, *Earth and Planetary Science Letters*, *176*(3), 387–400. 1.2.1

Roman, D., and K. Cashman (2006), The origin of volcano-tectonic earthquake swarms, *Geology*, *34*(6), 457. 2, 6.1.1

Roman, D., J. Neuberg, and R. Luckett (2006), Assessing the likelihood of volcanic eruption through analysis of volcanotectonic earthquake fault–plane solutions, *Earth and Planetary Science Letters*, *248*(1), 244–252. 2

Roman, D., S. De Angelis, J. Latchman, and R. White (2008), Patterns of volcanotectonic seismicity and stress during the ongoing eruption of the Soufrière Hills Volcano, Montserrat (1995–2007), *Journal of Volcanology and Geothermal Research*, *173*(3), 230–244. 6.1

Roman, D. C. (2005), Numerical models of volcanotectonic earthquake triggering on non-ideally oriented faults, *Geophysical Research Letters*, *32*(2). 1.6

Roman, D. C., S. C. Moran, J. A. Power, and K. V. Cashman (2004), Temporal and spatial variation of local stress fields before and after the 1992 eruptions of Crater Peak vent, Mount Spurr volcano, Alaska, *Bulletin of the Seismological Society of America*, *94*(6), 2366–2379. 6.1

Rooney, T. O., C. Herzberg, and I. D. Bastow (2012), Elevated mantle temperature beneath East Africa, *Geology*, *40*(1), 27–30. 1.3

Rosen, P. A., S. Hensley, I. R. Joughin, F. K. Li, S. N. Madsen, E. Rodriguez, and R. M. Goldstein (2000), Synthetic aperture radar interferometry, *Proceedings of the IEEE*, *88*(3), 333–382. 3.1.3, 3.1.3, 3.1.3, 3.1.4

Rosen, P. A., S. Hensley, G. Peltzer, and M. Simons (2004), Updated repeat orbit interferometry package released, *Eos, Transactions American Geophysical Union*, *85*(5), 47–47. 3.1.4

Rubinstein, R. Y. (2006), Simulation and the Monte Carlo method, 1981, *New York, W iley*. 4.8

Ruch, J., V. Acocella, N. Geshi, A. Nobile, and F. Corbi (2012), Kinematic analysis of vertical collapse on volcanoes using experimental models time series, *Journal of Geophysical Research: Solid Earth (1978–2012)*, *117*(B7). 2.3.1

Ruiz, A., D. Geist, and W. Chadwick (2007), Inflation of Sierra Negra volcano since the 2005 eruption, in *AGU Fall Meeting Abstracts*, vol. 1, p. 1422. 5.2, 6.4

Rychert, C. A., J. O. Hammond, N. Harmon, J. M. Kendall, D. Keir, C. Ebinger, I. D. Bastow, A. Ayele, M. Belachew, and G. Stuart (2012), Volcanism in the Afar Rift sustained by decompression melting with minimal plume influence, *Nature Geoscience*, *5*(6), 406–409. 1.2.1, 6.3

Sanchez, J., S. McNutt, J. Power, and M. Wyss (2004), Spatial variations in the frequency-magnitude distribution of earthquakes at Mount Pinatubo volcano, *Bulletin of the Seismological Society of America*, *94*(2), 430–438. 2.2.2

Scandone, R., and L. Giacomelli (1998), *Vulcanologia: principi fisici e metodi d'indagine*, Liguori. 5.3

Schepanski, K., T. Wright, and P. Knippertz (2012), Evidence for flash floods over deserts from loss of coherence in InSAR imagery, *Journal of Geophysical Research: Atmospheres (1984–2012)*, *117*(D20). 3.1.3

Schilling, F., and G. Partzsch (2001), Quantifying partial melt fraction in the crust beneath the central andes and the tibetan plateau, *Physics and Chemistry of the Earth, Part A: Solid Earth and Geodesy*, *26*(4), 239–246. 1.4

Segall, P. (2006), Time Dependent Volcano Deformation, in *AGU Fall Meeting Abstracts*, vol. 1, p. 05. 5

Segall, P. (2010), *Earthquake and volcano deformation*, Princeton University Press. 4.2, 4.3, 5.6

Segall, P., and M. Matthews (1997), Time dependent inversion of geodetic data, *Journal of Geophysical Research: Solid Earth (1978–2012)*, *102*(B10), 22,391–22,409. 5

Sengör, A., and K. Burke (1978), Relative timing of rifting and volcanism on Earth and its tectonic implications, *Geophysical Research Letters*, *5*(6), 419–421. 1.1.1

Sigmundsson, F., A. Hooper, S. Hreinsdóttir, K. S. Vogfjörd, B. G. Ófeigsson, E. R. Heimisson, S. Dumont, M. Parks, K. Spaans, G. B. Gudmundsson, et al. (2014), Segmented lateral dyke growth in a rifting event at Bardarbunga volcanic system, Iceland, *Nature*. 1.5

Simon, J. I., D. Weis, D. J. DePaolo, P. R. Renne, R. Mundil, and A. K. Schmitt (2014), Assimilation of preexisting pleistocene intrusions at long valley by periodic magma recharge accelerates rhyolite generation: rethinking the remelting model, *Contributions to Mineralogy and Petrology*, *167*(1), 1–34. 1.4

Simons, M., and P. Rosen (2007), Interferometric synthetic aperture radar geodesy. 3.1.3, 3.1.3

Snoke, J. A. (2003), 85.12 FOCMEC: FOCal MEChanism determinations, *International Geophysics*, *81*, 1629–1630. 2.2.3

Solomon, A. (2012), Summary of activities of the Southern Red Sea Administration during the Nabro eruption., *Department of infrastructure of the Southern Red Sea Administration, Assab*. 1.3.2

Sparks, R. (2003), Forecasting volcanic eruptions, *Earth and Planetary Science Letters*, *210*(1), 1–15. 2

Sparks, R. S. J., and H. E. Huppert (1984), Density changes during the fractional crystallization of basaltic magmas: fluid dynamic implications, *Contributions to Mineralogy and Petrology*, *85*(3), 300–309. 5.3

Sparks, S. R., and H. Sigurdsson (1977), Magma mixing: a mechanism for triggering acid explosive eruptions, *Nature*, *267*, 315–318. 5.3

Spera, F. (1980), Thermal evolution of plutons: a parameterized approach, *Science*, *207*(4428), 299–301. 5.6

Spera, F. J. (2000), Physical properties of magma, *Encyclopedia of volcanoes*, pp. 171–190. 4.2.1

Stuart, G., I. Bastow, and C. Ebinger (2006), Crustal structure of the northern main ethiopian rift from receiver function studies, *Geological Society, London, Special Publications*, *259*(1), 253–267. 2.2.1

Sturkell, E., and F. Sigmundsson (2000), Continuous deflation of the Askja caldera, Iceland, during the 1983–1998 noneruptive period, *Journal of Geophysical Research: Solid Earth (1978–2012)*, *105*(B11), 25,671–25,684. 5.3

Sturkell, E., P. Einarsson, F. Sigmundsson, S. Hreinsdóttir, and H. Geirsson (2003a), Deformation of Grímsvötn volcano, Iceland: 1998 eruption and subsequent inflation, *Geophysical research letters*, *30*(4). 5.6

Sturkell, E., F. Sigmundsson, and P. Einarsson (2003b), Recent unrest and magma movements at Eyjafjallajökull and Katla volcanoes, Iceland, *Journal of Geophysical Research: Solid Earth (1978–2012)*, *108*(B8). 6.3

Tait, S., C. Jaupart, and S. Vergniolle (1989), Pressure, gas content and eruption periodicity of a shallow, crystallising magma chamber, *Earth and Planetary Science Letters*, *92*(1), 107–123. 5.3

Tallarico, A., M. Dragoni, M. Anzidei, and A. Esposito (2003), Modeling long-term ground deformation due to the cooling of a magma chamber: Case of Basiluzzo island, Aeolian Islands, Italy, *Journal of Geophysical Research: Solid Earth (1978–2012)*, *108*(B12). 5.2, 5.3, 5.3, 5.3, 5.3

Tarasewicz, J., B. Brandsdóttir, R. White, M. Hensch, and B. Thorbjarnardóttir (2012), Using microearthquakes to track repeated magma intrusions beneath the Eyjafjallajökull stratovolcano, Iceland, *Journal of Geophysical Research*, *117*(null), B00C06. 1.4, 2.3, 4.9, 6.1

Tazieff, H., and J. Varet (1972), Tectonic significance of the Afar (or Danakil) depression, *Nature*, *235*, 144–147. 1.3

Tesfaye, S., D. J. Harding, and T. M. Kusky (2003), Early continental breakup boundary and migration of the Afar triple junction, Ethiopia, *Geological Society of America Bulletin*, *115*(9), 1053–1067. 1.2.1

Thayer, G. D. (1974), An improved equation for the radio refractive index of air, *Radio Science*, *9*(10), 803–807. 3.1.3

Theys, N., R. Campion, L. Clarisse, H. Brenot, J. Van Gent, B. Dils, S. Corradini, L. Merucci, P.-F. Coheur, M. Van Roozendael, et al. (2013), Volcanic SO_2 fluxes derived from satellite data: a survey using OMI, GOME-2, IASI and MODIS, *Atmospheric Chemistry and Physics*, *13*(12), 5945–5968. 1.3.2, 5.4

Thompson, D., J. Hammond, J.-M. Kendall, G. Stuart, G. Helffrich, D. Keir, A. Ayele, and B. Goitom (2015), Hydrous upwelling across the mantle transition zone beneath the Afar Triple Junction, *Geochemistry, Geophysics, Geosystems*. 1.1.1, 1.2.1

Tomiya, A., and E. Takahashi (1995), Reconstruction of an evolving magma chamber beneath Usu volcano since the 1663 eruption, *Journal of Petrology*, *36*(3), 617–636. 5.3

Toombs, A., and G. Wadge (2012), Co-eruptive and inter-eruptive surface deformation measured by satellite radar interferometry at Nyamuragira volcano, DR Congo, 1996 to 2010, *Journal of Volcanology and Geothermal Research*, *245*, 98–122. 6.3, 6.4

Trasatti, E., C. Giunchi, and M. Bonafede (2003), Effects of topography and rheological layering on ground deformation in volcanic regions, *Journal of Volcanology and Geothermal Research*, *122*(1), 89–110. 4.6

Turcotte, D. L., and S. H. Emerman (1983), Mechanisms of active and passive rifting, *Tectonophysics*, *94*(1), 39–50. 1.1.1

Umakoshi, K., H. Shimizu, and N. Matsuwo (2001), Volcano-tectonic seismicity at Unzen volcano, Japan, 1985–1999, *Journal of Volcanology and Geothermal Research*, *112*(1), 117–131. 2, 6.1

Utsu, T. (1965), A method for determining the value of *b* in a formula log n=a-*b*M showing the magnitude-frequency relation for earthquakes, *Geophys. Bull. Hokkaido Univ*, *13*, 99–103. 2.2.2

Vargas-Bracamontes, D., and J. Neuberg (2012), Interaction between regional and magma-induced stresses and their impact on volcano-tectonic seismicity, *Journal of Volcanology and Geothermal Research*, *243*, 91–96. 2, 2.2.3, 6.1.1

Wadge, G., and L. Burt (2011), Stress field control of eruption dynamics at a rift volcano: Nyamuragira, DR Congo, *Journal of Volcanology and Geothermal Research*, *207*(1), 1–15. 6.3

Waldhauser, F. (2001), hypoDD–A program to compute double-difference hypocenter locations (hypoDD version 1.0-03/2001), *US Geol. Surv. Open File Rep., 01*, *113*. 2.2.1

Waldhauser, F., and W. Ellsworth (2000), A double-difference earthquake location algorithm: method and application to the northern Hayward fault, California, *Bulletin of the Seismological Society of America*, *90*(6), 1353–1368. 2.2.1, 2.2.1, A.3

Walker, B. A., C. Miller, L. L. Claiborne, J. Wooden, and J. Miller (2007), Geology and geochronology of the spirit mountain batholith, southern nevada: implications for timescales and physical processes of batholith construction, *Journal of Volcanology and Geothermal Research*, *167*(1), 239–262. 1.4

Walters, R., J. Elliott, Z. Li, and B. Parsons (2013), Rapid strain accumulation on the Ashkabad fault (Turkmenistan) from atmosphere-corrected InSAR, *Journal of Geophysical Research: Solid Earth*, *118*(7), 3674–3690. 3.1.3, 3.2.1

Walters, R. J. (2012), Geodetic observation and modelling of continental deformation in Iran and Turkey, Ph.D. thesis, University of Oxford. 3.1, 3.1.3

Wang, H., T. Wright, and J. Biggs (2009), Interseismic slip rate of the northwestern Xianshuihe fault from InSAR data, *Geophysical Research Letters*, *36*(3). 3.3.1

Wang, H., J. Biggs, and T. J. Wright (2010), π-RATE (V2. 0b2) Poly-Interferogram Rate And Time-series Estimator. 3.3.1

Wang, H. F., and M. P. Anderson (1995), *Introduction to groundwater modeling: finite difference and finite element methods*, Academic Press. 4.6

Warren, N. W., and G. V. Latham (1970), An experimental study of thermally induced microfracturing and its relation to volcanic seismicity, *Journal of Geophysical Research*, *75*(23), 4455–4464. 2.3

Watson, I., C. Oppenheimer, B. Voight, P. Francis, A. Clarke, J. Stix, A. Miller, D. Pyle, M. Burton, S. Young, et al. (2000), The relationship between degassing and ground deformation at Soufriere Hills Volcano, Montserrat, *Journal of Volcanology and Geothermal Research*, *98*(1), 117–126. 1.5

Wauthier, C., D. C. Roman, and M. P. Poland (2013a), Moderate-magnitude earthquakes induced by magma reservoir inflation at Kīlauea Volcano, Hawai'i, *Geophysical Research Letters*, *40*(20), 5366–5370, doi:10.1002/2013GL058082. 2.3, 6.1.1

Wauthier, C., V. Cayol, M. Poland, F. Kervyn, N. d'Oreye, A. Hooper, S. Samsonov, K. Tiampo, and B. Smets (2013b), Nyamulagira's magma plumbing system inferred from 15 years of InSAR, *Geological Society, London, Special Publications*, *380*(1), 39–65. 6.3

Weaver, C. S., W. C. Grant, S. D. Malone, and E. T. Endo (1981), Post-may 18 seismicity: volcanic and tectonic implications, *US Geol. Surv. Profess. Pap*, *1250*, 109–121. 2

Whelley, P. L., J. Jay, E. Calder, M. Pritchard, N. Cassidy, S. Alcaraz, and A. Pavez (2012), Post-depositional fracturing and subsidence of pumice flow deposits: Lascar Volcano, Chile, *Bulletin of volcanology*, *74*(2), 511–531. 6.4

White, R., and D. McKenzie (1989), Magmatism at rift zones: the generation of volcanic continental margins and flood basalts, *Journal of Geophysical Research: Solid Earth (1978–2012)*, *94*(B6), 7685–7729. 1.1.1, 1.2.1, 1.2.2

White, R. A., A. D. Miller, L. Lynch, and J. Power (1998), Observations of hybrid seismic events at soufriere hills volcano, montserrat: July 1995 to september 1996, *Geophysical research letters*, *25*(19), 3657–3660. 6.1

Wiart, P., and C. Oppenheimer (2000), Largest known historical eruption in Africa: Dubbi volcano, Eritrea, 1861, *Geology*, *28*(4), 291–294. 1.2.2

Wiart, P., and C. Oppenheimer (2005), Large magnitude silicic volcanism in north Afar: The Nabro Volcanic Range and Ma'alalta volcano, *Bulletin of volcanology*, *67*(2), 99–115. 1.3, 1.3.1, 1.3.1

Williams, S. N., S. J. Schaefer, V. M. L. Calvache, and D. Lopez (1992), Global carbon dioxide emission to the atmosphere by volcanoes, *Geochimica et Cosmochimica Acta*, *56*(4), 1765–1770. 5.4

Wolfenden, E., C. Ebinger, G. Yirgu, A. Deino, and D. Ayalew (2004), Evolution of the northern Main Ethiopian rift: birth of a triple junction, *Earth and Planetary Science Letters*, *224*(1), 213–228. 1.1.1, 1.2.1

Wotzlaw, J.-F., I. N. Bindeman, K. E. Watts, A. K. Schmitt, L. Caricchi, and U. Schaltegger (2014), Linking rapid magma reservoir assembly and eruption trigger mechanisms at evolved yellowstone-type supervolcanoes, *Geology*, *42*(9), 807–810. 1.4

Wright, T., B. Parsons, J. Jackson, M. Haynes, E. Fielding, P. England, and P. Clarke (1999), Source parameters of the 1 October 1995 Dinar (Turkey) earthquake from SAR interferometry and seismic bodywave modelling, *Earth and Planetary Science Letters*, *172*(1), 23–37. 4.7.2

Wright, T. J., C. Ebinger, J. Biggs, A. Ayele, G. Yirgu, D. Keir, and A. Stork (2006), Magma-maintained rift segmentation at continental rupture in the 2005 Afar dyking episode, *Nature*, *442*(7100), 291–294. 1.2.2, 6.4

Wright, T. J., F. Sigmundsson, C. Pagli, M. Belachew, I. J. Hamling, B. Brandsdóttir, D. Keir, R. Pedersen, A. Ayele, C. Ebinger, et al. (2012), Geophysical constraints on the dynamics of spreading centres from rifting episodes on land, *Nature Geoscience*, *5*(4), 242–250. 1.2.2

Xu, W., and S. Jónsson (2014), The 2007–8 volcanic eruption on jebel at tair island (red sea) observed by satellite radar and optical images, *Bulletin of Volcanology*, *76*(2), 1–14. 6.1.1

Xu, W., J. Ruch, and S. Jónsson (2015), Birth of two volcanic islands in the southern red sea, *Nature communications*, *6*. 1.2.1

Yang, X.-M., P. M. Davis, and J. H. Dieterich (1988), Deformation from inflation of a dipping finite prolate spheroid in an elastic half-space as a model for volcanic stressing, *Journal of Geophysical Research: Solid Earth (1978–2012)*, *93*(B5), 4249–4257. 4.1, 4.3

Yohannes, E. (2012), Geothermal development in Eritrea: A country update, in *African Rift Geothermal Conference*, vol. 1, p. 05. 5.4

Yoon, Y. T., M. Eineder, N. Yague-Martinez, and O. Montenbruck (2009), TerraSAR-X precise trajectory estimation and quality assessment, *Geoscience and Remote Sensing, IEEE Transactions on*, *47*(6), 1859–1868. 3.1.2, 3.1.3

Yun, S., P. Segall, and H. Zebker (2006), Constraints on magma chamber geometry at Sierra Negra Volcano, Galápagos Islands, based on InSAR observations, *Journal of Volcanology and geothermal research*, *150*(1), 232–243. 4.7.3, 6.1

Zebker, H. A., P. A. Rosen, and S. Hensley (1997), Atmospheric effects in interferometric synthetic aperture radar surface deformation and topographic maps, *Journal of Geophysical Research: Solid Earth (1978–2012)*, *102*(B4), 7547–7563. 3.1.3

Zellmer, G. F., and C. Annen (2008), An introduction to magma dynamics, *Geological Society, London, Special Publications*, *304*(1), 1–13. 6.1

Ziebart, M., S. Adhya, A. Sibthorpe, S. Edwards, and P. Cross (2005), Combined radiation pressure and thermal modelling of complex satellites: algorithms and on-orbit tests, *Advances in Space Research*, *36*(3), 424–430. 3.1.3

Zobin, V. M. (2003), *Introduction to volcanic seismology*, Elsevier. 2

Appendix A

Seismology Programs

A.1 Seismic Analysis Code (SAC)

SAC2000 is interactive program often used by seismologists to study seismic events, it can be downloaded from free at: http://ds.iris.edu/ds/nodes/dmc/manuals/ . The SAC manual can be found at http://ds.iris.edu/ds/nodes/dmc/manuals/ there are also many online tutorials for using SAC software. The data used for this study is stored on the SEIS-UK system in 'miniseed' format, I converted into SAC format before exporting the data into my working directory. A standard SAC file is binary format with an ASCII header containing data for one component at a single station. I used SAC to display all three components and to measure the arrival times of the P and S phase onsets. The following command sequence was used:

Step	Command	Detail
1	r*	Read raw data into SAC2000
2	qdp off	Display with full detail
3	ppk perplot N	Display N traces on one screen
4	n,b	Move forward,backward between screens
5	Np,Ns	N Between 0 and 4 to specify the weighting
6	q	Quit interactive screen, return to SAC konsole
7	writehdr	Write picks into header file, one per event
8	ohpf	Open hypo file to record pick times
9	ppk	Display traces with the hpf file open
10	h	Record arrival time values
11	whpf	Write the hpf file
12	chpf	Close the hpf file

This was repeated for each event, for each day of available data. The HPF files created for each event contain the arrival time, weight and phase data. They were then concatenated into a single file which contains the all data for a single day.

A.2 HYPOINVERSE 2000

HYPOINVERSE-2000 is a USGS computer program which computes earthquakes locations and magnitudes from input seismic data such as arrival times and amplitudes. It is freely available at http://earthquake.usgs.gov/research/software/and the manual can be found here: http://www.ipgp.fr/ arnaudl/NanoCD/documentation/3rdParty/hyp2000-1.0.pdf . The software finds the hypocentre location and magnitudes based on seismic station and arrival time data. The program requires station locations, the phase file (created by SAC in this case) and a crustal velocity model (Klein, 2002). HYPOINVERSE-2000 is further parametrised by the input file, outlined in the table below. To execute HYPOINVERSE the commands $inp.ini (execute bacth commands), $LOC (locate earthquakes) and $STO (exit the program) are also required.

Parameter	Value	Detail
h71	1 1 3	Format of output files
200	t 2000 0	Date format
sta	afar.sta	Station location
crh	1 afar.crh	Velocity travel time table
phs	nabro_ps.phs	Date, time& weight of all arrivals on one day
dis	4 500 1 3	Design of the distance weight taper: effectively no taper.
swt	0.5	Weight of S arrivals half of P
pos	1.8	V_P/V_S ratio
rms	4 4 1.5 3	Time residuals are weighted after iteration 4. Cosine taper based on the following parameters.
arc	nabro.arc	Output Archive file
prt	nabro.prt	Output Print file
sum	nabro.sum	Output Summary file
ztr	5	First trial depth for inversion (km)

Following inversion, the program outputs a range of variables to be analysed, which are stored in the archive, print and summary file. These include: the latitude, longitude and depth of each hypocenter, the vertical and horizontal error bars and the arrival time residuals for every pick. For earthquake locating, it is important to check that the travel time residuals at each station are not too large. These residuals are the difference between the observed arrival and the theoretical arrival of a P or S phase, as calculated by the velocity model. For quality control, the picks with a high residual (more than 0.2 s) were reviewed. The pick was either moved to a more appropriate location if a mistake had been made, or left unchanged if the observed arrival time did fit the trace. After all

the picks were checked, HYPOINVERSE-2000 was rerun to acquire final hypocenter locations. The residuals in some instances remained high despite an accurate pick, due to 3D heterogeneities in the subsurface which are not incorporated in the velocity model. As well as the arrival time, HYPOINVERSE-2000 also calculates errors in both vertical and horizontal components, as well as the dimensions and orientation of the error ellipse. Defining the error ellipse helps summarise the error given to a hypocenter. As all of the stations are above the source, the error ellipse is elongated in the Z direction. However due to poor azimuthal coverage of the Mallahle events, the horizontal error and orientation of the error ellipse is skewed for these events.

A.2.1 Travel Time GENerating program (TTGEN)

I used the TTGEN computer program to create a velocity model with linear gradients between fixed layers of fixed velocities. This smoothes out discontinuities between the layers of a 1D velocity model which can result in clustering of hypocentres along refraction boundaries. The TTGEN output model takes the form of a condensed travel time table which can directly input into the HYPOINVERSE program. A brief description of TTGEN is given here, see Klein Klein (2002) for more details.

TTGEN simulates seismic rays from a source, at a user specified depth, to the surface. It calculates the distance, travel time and other parameters for each ray. At each depth of this source, these values are tabulated and for unspecified depth of sources the table values are interpolated.

The independent parameter Q, determines the increment of the angle of the ray leaving the source, the ray parameter and the emergence angle at the surface are a function of Q. This parameter is incremented using the following numerical sequence: It starts at 0 (a vertical ray) then increases by DQ1, NQ1 times. Then it increases by DQ2, NQ2 times. The largest value of Q is therefore, NQ1 $\times$ DQ1 +NQ2 $\times$ DQ2. The default values: NQ1 = 100, DQ1 = 0.08, NQ2 = 100, DQ2 = 0.4, were used for the Nabro data set. The depths at which the Q parameter begins is determined from the same numerical sequence as the Q factor increment; starting at a depth of 0, it then increases by DZ1, NZ1 times. Then it increases by DZ2, NZ2 times. Travel times are also calculated at distances along the ray path at 0, 2DD1, up to ND1 * DD1, and then at ND2 values in increments of DD2.

The numerical sequencing of Q, depth and distances allow for most rays to reach the surface, and a fine grid spacing which becomes coarser with depth. The input file of TTGEN requires the above parameters to be specified as well as the Vp/Vs ratio, the reducing velocity, and the depth and velocity of each point in the model. For this, the homogeneous velocity model was used.

The input file is show below:

nab.prt	nab.		.135
.04	200	0.2	200
1.0	18	4.0	9
1.0	28	4.0	13
nab			
4.1	0.0		
6.1	3.0		
6.8	8.0		
7.4	25.0		

A.3 HypoDD

HypoDD is freely available at http://earthquake.usgs.gov/research/software/ . For details further to those given here, see Waldhauser and Ellsworth Waldhauser and Ellsworth (2000). Double differencing is a technique which uses an iterative least squares method to relate the difference in travel times between the observed and predicted arrivals, for pairs of earthquakes, to changes in the vector containing the hypocenter **?**. HypoDD requires 3 steps: initial formatting, pre-processing (when events are paired) and the relocation inversion.

The initial stage requoires the use of code 'ncsn2pha' to extract the relevent information from the HYPOINVERSE2000 archive file and creates a new file with all hypocentres information and applies unique identifier. This file is input to ph2dt for pairing.

A.3.1 Ph2dt

Ph2dt is a preprocessing program which pairs earthquakes together and forms them into clusters. The aim is to build a network of links between every earthquake recorded. The following table lists the control parameters and the values I used for each.

Parameter	Val. Used	Description
MAXSEP	2	Max distance between a pair
MAXNGH	600	Max No. of events event A is allowed to pair with
MINWGT	0	Min pick weight for an event. Weights are reassigned from 0-4 in HYPOINVERSE to 0-1(best) in HYPODD
MAXDIST	60	Max distance allowed for an event from a station
MINLNK	4	Min No. of links required to define a neighbour
MINOBS	1	Min No. of observations a pair to be used
MAXOBS	7	Max No. of observations a pair to be used

By initially re-weighting the picks and then defining the minimum allowed, the user is able to remove uncertain events within the catalogue from analysis. Ph2dt searches the travel time information stored within the ncsn2pha output to create the earthquake pairs. The program attempts to find the MAXNGH within the MAXSEP defined by the control parameters. This allows pairing of enough events to stabilise the inversion but also only pairs events which are close enough to share common raypaths. The pair is then checked to have enough common links between them i.e. MINLNK is observed. A nearest neighbour approach is used, so MINLNK has to be valid before saving and defining the next event to correspond to event A which lies within MAXSEP. The events have to be within MAXDIST and be recorded at a MINOBS number of seismometers to be saved as a valid pair. After performing ph2dt on the data catalogue, a log file reports important information related to how many earthquakes are paired together and how many of those achieve MINLNK.

A.3.2 HypoDD Input

HYPODD examines each cluster individually, as defined by ph2dt. This ensures connectivity between the events; any event is linked to any other event in the same cluster, the strength of these chains can be defined by OBSCT. Increasing this value will increase connectivity, however it would also split up the cluster further. Lowering the value would allow more events to be defined in one cluster, but it will lower the stability of the solution. Also defining connectivity is the WDCT parameter, lowering the maximum separation distance will result in a smaller cluster with events sharing bigger portions of ray paths, this is very similar to the MAXSEP parameter in ph2dt. HYPODD then relocates using an iterative procedure to minimise double differences, the ISTART command determines whether this begins at the centroid or at the beginning

of the data catalogue. This parameter is important as initial locations will affect the solution. All the parameters that control the inversion and the values I used are listed in the table below.

Parameter	Value	Description
DIST	250	Max distance allowed between the centre of the cluster and the station.
OBSCT	1	Min No. of links an event needs to form a continuous cluster, should be ≤MINLNK.
ISTART	2	Determines initial locations, either from the middle of the cluster or the catalogue locations.
ISOLV	2	Determines the least squared solution used, either singular value decomposition, or LSQR. Both may have to be applied at the error analysis stage.
NSET	3	No. of sets of iterations.
NLAY	4	No. of model layers.
RATIO	1.8	Vp/Vs ratio, constant for all layers.
TOP	0 2 3 8 25	Depth of top layer (km).
VEL	4.1 6.1 6.8 7.4	Specifies homogeneous velocity model
CID	All	Cluster to be relocated
ID	All	ID of events to be relocated

A.4 FOCMEC

FOCMEC (FOCal MEChanism determinations) is a Fortran 77 based computer program available from: http://ds.iris.edu/pub/programs/focmec/ for displaying the focal mechanism of a double couple earthquake. The program requires the polarity of the P, S_{h} and S_{v} phases, it can additionally use the amplitude ratios. It also needs the take-off angles and the station azimuth. An input file for an event is given below as an example. It takes format: Station code, Azimuth, Take-off angle, Polarity. The event identifier is listed at the top.

2011275145635460.ev		
NA5	146.00	134.00C
NA5	146.00	134.00R
NA1	323.00	123.00D
NA1	323.00	123.00L
NA3	66.00	111.00D
NA3	66.00	111.00L
NA2	7.00	107.00D
NA8	96.00	99.00D
NA4	357.00	93.00D
NA7	42.00	116.00D

The FOCMEC inversion uses the above input file and is parametrised with the values in the following table. All measurements were given an equal weight in the inversion, which was allowed to search the full space with a 10° increment. Once the program has found all possible mechanisms or the maximum number of solutions is reached, the inversion is exited and the results written into an ouput file. FOCMEC includes program *focplt* which plots all of the output solutions. I used this program to view the outputs, but used the GMT commands psmeca and pscoupe to plot figures in this thesis and other publications.

Parameter	Value
Output file name	*event*.out
Input filespec	*event*.focmec
Weighting	N
Exit after this many acceptable sols	100
Minimum search value B trend	0
Increment for B trend	10
Maximum B trend	350
Minimum search value B plunge	0
Increment for B plunge	10
Maximum B plunge	90
Minimum search value A angle	0
Increment for A angle	10
Maximum A angle	80

Appendix B

Okada solutions

The full derivation of the surface displacement, strain and tilt for a dislocation on a rectangular plane in a homogeneous halfspace can be found in Okada (1985). Below I give solutions for the horizontal (U_x,U_y) and vertical (U_z) components of ground displacement due to a tensile opening located at (x, y, z) (as described in Chapter 4):

$$U_x = \frac{U_3}{2\pi}\left[\frac{q^2}{R(R+\eta)} - I_3 \sin^2\delta\right] \tag{B.1a}$$

$$U_y = \frac{U_3}{2\pi}\left[\frac{-\tilde{d}q}{R(R+\xi)} - \sin\delta\left\{\frac{\xi q}{R(R+\eta)} - \tan^{-1}\frac{\xi\eta}{qR}\right\} - I_1 \sin^2\delta\right] \tag{B.1b}$$

$$U_z = \frac{U_3}{2\pi}\left[\frac{-\tilde{y}q}{R(R+\xi)} - \cos\delta\left\{\frac{\xi q}{R(R+\eta)} - \tan^{-1}\frac{\xi\eta}{qR}\right\} - I_5 \sin^2\delta\right] \tag{B.1c}$$

$$\tag{B.1d}$$

where,

$$I_1 = \frac{\mu}{(\lambda+\mu)}\left[\frac{-1}{\cos\delta}\frac{\xi}{R+\tilde{d}}\right] - \frac{\sin\delta}{\cos\delta}I_5 \tag{B.2a}$$

$$I_2 = \frac{\mu}{(\lambda+\mu)}\left[-\ln(R+\eta)\right] - I_3 \tag{B.2b}$$

$$I_3 = \frac{\mu}{(\lambda+\mu)}\left[\frac{1}{\cos\delta} + \frac{\tilde{y}}{(R+\tilde{d})} - \ln(R+\eta)\right] + \frac{\sin\delta}{\cos\delta}I_4 \tag{B.2c}$$

$$I_4 = \frac{\mu}{\lambda+\mu}\frac{1}{\cos\delta}\left[\ln(R+\tilde{d}) - \sin\delta\ln(R+\eta)\right] \tag{B.2d}$$

$$I_5 = \frac{\mu}{\lambda+\mu}\frac{2}{\cos\delta}\tan^{-1}\frac{\eta\left(X+q\cos\delta\right) + X(R+X)\sin\delta}{\xi(R+X)cos\delta} \tag{B.2e}$$

and

$$p = y\cos\delta + d\sin\delta \tag{B.3a}$$

$$q = y\sin\delta - d\cos\delta \tag{B.3b}$$

$$\tilde{y} = \eta\cos\delta + q\sin\delta \tag{B.3c}$$

$$\tilde{d} = \eta\sin\delta - q\cos\delta \tag{B.3d}$$

$$R^2 = \xi^2\eta^2 + q^2 = \xi^2 + \tilde{y}^2 + \tilde{d}^2. \tag{B.3e}$$

The parameters are as follows: δ is dip of the rectanglular sill, U_3, U_1, U_2 refer to the type of dislocation (see figure 4.3), μ and λ are Lame's constants, ξ and η refer to the point of dislocation.

Appendix C

InSAR Glossary

Along Track The component of motion of the satellite which is parallel to the trajectory.

Ascending Track The portion of ground covered as the satellite moves from South to North.

Azimuth The along track component of the vector between the ground and the satellite.

Backscatter The portion of the outgoing radar beam that the target redirects back to the satellite.

Baseline Vector separation between the acquisition point on each orbit.

Cross Track The component of motion of the satellite which is perpendicular to the trajectory.

DEM Digital Elevation Model. A 2D matrix of topographic elevations.

Descending Track The portion of ground covered as the satellite moves from North to South.

Epoch The acquisition date of a SAR acquisition.

Geocoded An image which has been resampled from the acquisition geometry (relative to the satellite path) into a geographic projection.

Incidence The cross track component of the vector between the ground and the satellite.

Interfered The net combination of two electromagnetic waves on coincident paths.

Interferometry A technique that uses the differences in the phase of the return signal between two satellite passes to detect slight changes on the Earth's surface.

Footprint The area on the ground illuminated by the radar beam.

Fringe Line on an interferogram corresponding to half a wavelength of range change between the ground and the satellite.

Phase The complex component of a radar image which contains the geometric information on the round-trip travel time between the satellite sensor and the reflector.

Range Distance along the line of sight between the satellite and the ground

Ratemap A geocoded image of ground displacement in terms of linear velocity, often given in mm/yr.

SLC Single Look Complex. A radar image including both phase and amplitude information.

StripMap One of the operational modes of TerraSAR-X, based on the resolution of the image being obtained.

Swath The width of an imaged scene in the range dimension.

Appendix D

Mogi single step Inversion

Initially, I tried to jointly invert the CSK and TSX data sets together. I used Okinv to solve for the location (latitude and longitude), depth and volume decrease of a Mogi source using the ratemaps. The best fit model is situated at 6.66 depth, and located at 13.35°N and 41.70°E, with a volume decrease of 0.05 km^3. For the TSX data this model fits the data well and has a RMS misfit of 1.3 cm/yr and 1.5 cm/yr for the TSX ascending and descending tracks respectively. However, this model does not fit the CSK data equally well, giving an RMS residual of 2.8 cm/yr. The outputs from this one-step Mogi model inversion are shown in Figures D.1 and D.2, and summarsied in Table D.1.

	Latitude	Longitude	Depth (km)	Closing
Mogi	13.35	41.70	6.66	$0.05x10^{-3}km^3$

Table D.1: Best fit Mogi and Sill models following inversion of TSX data acquired on an ascending track between 6 July 2011 and 10 october 2012, and on descending track between 1 July 2011 and 5 october 2012. The source change output from the CSK inversion with was a volume decrease of 0.06 ± 0.006 $x10^{-3}$ km^3 from a Mogi model, or a closing of 76 m $\pm$ 6 m from an Okada model. The CSK data between 6 July 2011 and 19 July 2012 was used. Note this removes the first date of the total CSK acquisition.

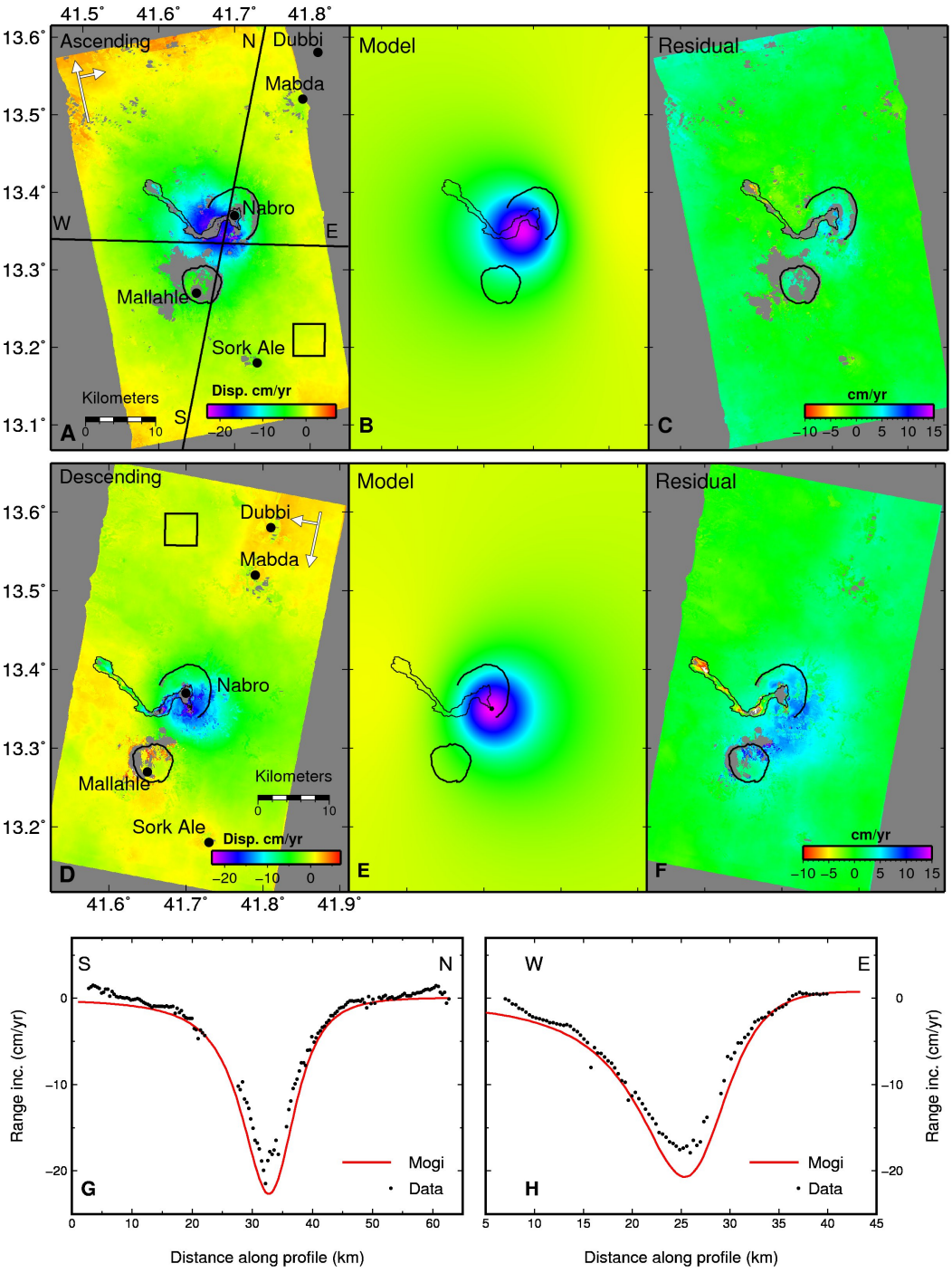

Figure D.1: Best fit model assuming a Mogi source and jointly inverting the TSX and CSK data sets. A) Observed TSX ascending rate map of ground movement, B) Mogi model of deformation for ascending track, C) Residual motion, D) Observed TSX descending ratemap, E) Mogi model of deformation for descending track, F) Residual ground motion, G) Profile of ground displacement along transect N-S on A) and H) Profile of ground displacement along transect E-W on A).

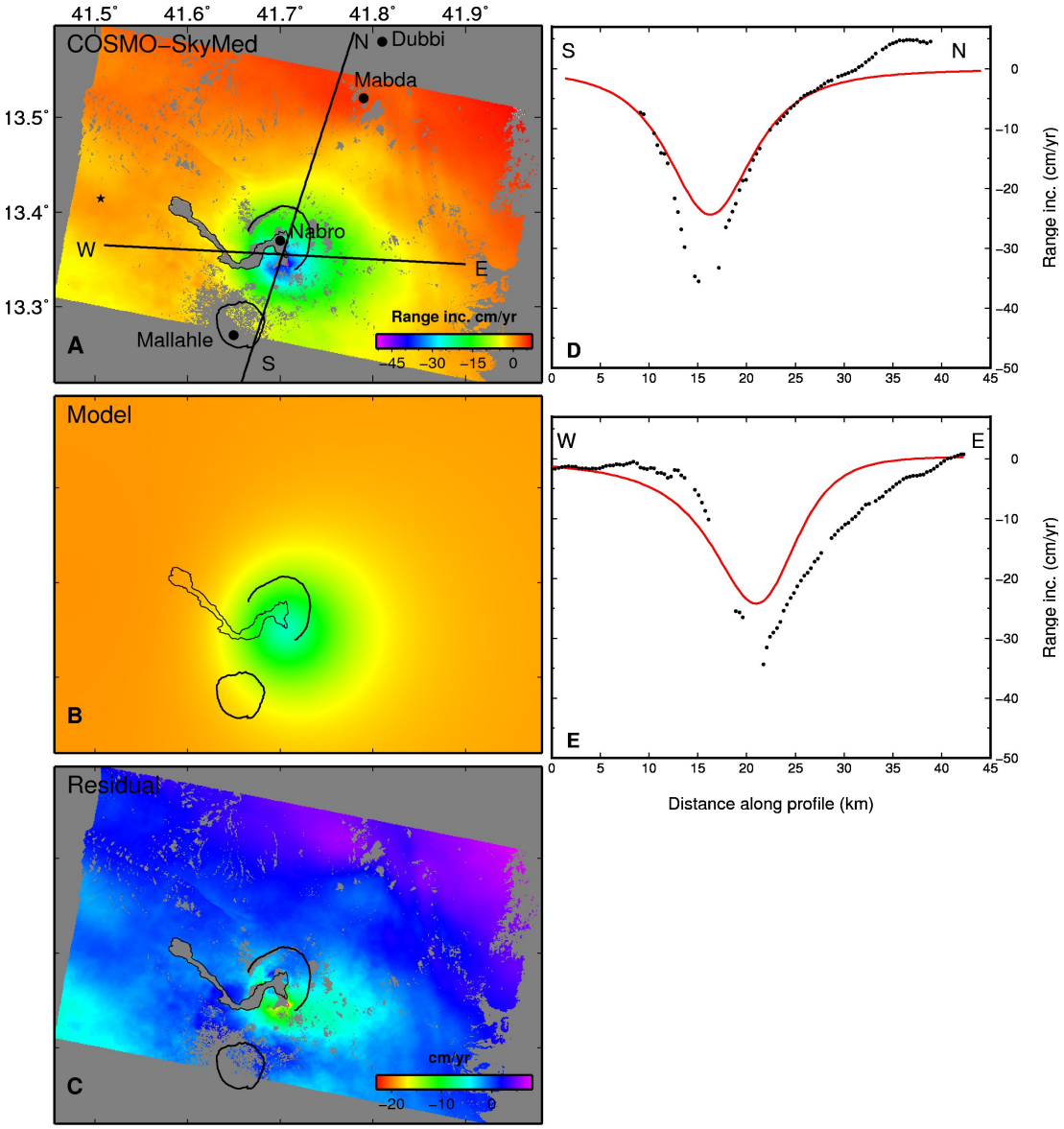

Figure D.2: Best fit model assuming a Mogi source and jointly inverting the TSX and CSK data sets. A) Observed CSK ascending rate map of ground movement, B) Mogi model of deformation, C) Residual motion, D) Profile of ground displacement along transect N-S on A) and E) Profile of ground displacement along transect E-W on A).

Appendix E

Publications

I have presented results from my study PhD at numerous conferences over the last 4 years. These have taken both poster and oral format, some of which are listed below. I have published the seismic results and initial InSAR results in a JGR:Solid Earth article (Hamlyn et al., 2014), and I am a co-author on an overview paper of the Nabro 2011 eruption (Goitom et al., 2015). These articles are printed on the following pages.

Lead author conference contributions and talks

March 2015	High-resolution InSAR time series analysis following the 2011 eruption of Nabro Volcano, Eritrea: implications for the mechanisms of post-eruptive subsidence. Fringe 2015, ESA, Frascati (Oral)
April 2014	InSAR and seismic analysis of the 12th June 2011 eruption of Nabro Volcano EGU, 2014, Vienna (Poster)
February 2014	A conceptual model of caldera subsidence for Nabro Volcano using InSAR & seismic techniques, GNS Science, LSD talk series, 2014, New Zealand (Oral)
December 2012	Earthquake relocations and InSAR time series analysis after the June 2011 eruption of Nabro, Eritrea, AGU Fall Meeting, 2012, San Francisco (Poster)
September 2012	Mechanisms and implications of the 2011 eruption of Nabro volcano, Eritrea, ESC Annual Workshop, 2012, El Hierro (Oral)
April 2012	The 2011 Eruption of Nabro Volcano (Eritrea): Earthquake Locations From a Temporary Broadband Network, EGU, 2012, Vienna (Poster)

AGU PUBLICATIONS

JGR

Journal of Geophysical Research: Solid Earth

RESEARCH ARTICLE
10.1002/2014JB011395

Key Points:
- InSAR and microseismic study following the 2011 eruption at Nabro, Eritrea
- InSAR shows subsidence, best modeled by a Mogi source at 6 km depth
- Seismicity suggests that subsidence is controlled by changes in the magma chamber

Supporting Information:
- Readme
- Figure S1
- Figure S2

Correspondence to:
J. E. Hamlyn,
ee10j2h@leeds.ac.uk

Citation:
Hamlyn, J. E., D. Keir, T. J. Wright, J. W. Neuberg, B. Goitom, J. O. S. Hammond, C. Pagli, C. Oppenheimer, J-M. Kendall, and R. Grandin (2014), Seismicity and subsidence following the 2011 Nabro eruption, Eritrea: Insights into the plumbing system of an off-rift volcano, *J. Geophys. Res. Solid Earth*, *119*, 8267–8282, doi:10.1002/2014JB011395.

Received 19 JUN 2014
Accepted 22 AUG 2014
Accepted article online 2 SEP 2014
Published online 13 NOV 2014

The copyright line for this article was changed on 19 DEC 2014 after original online publication.

This is an open access article under the terms of the Creative Commons Attribution License, which permits use, distribution and reproduction in any medium, provided the original work is properly cited.

Seismicity and subsidence following the 2011 Nabro eruption, Eritrea: Insights into the plumbing system of an off-rift volcano

Joanna E. Hamlyn[1], Derek Keir[2], Tim J. Wright[1], Jürgen W. Neuberg[1], Berhe Goitom[3], James O. S. Hammond[4], Carolina Pagli[5], Clive Oppenheimer[6], J-Michael Kendall[3], and Raphaël Grandin[7]

[1]COMET, School of Earth and Environment, University of Leeds, Leeds, UK, [2]National Oceanography Centre Southampton, University of Southampton, Southampton, UK, [3]School of Earth Sciences, University of Bristol, Bristol, UK, [4]Department of Earth Science and Engineering, Imperial College London, London, UK, [5]Dipartimento di Scienze della Terra, Università di Pisa, Pisa, Italy, [6]Department of Geography, University of Cambridge, Cambridge, UK, [7]IPGP, Paris, France

Abstract Nabro volcano, situated to the east of the Afar Rift Zone, erupted on 12 June 2011. Eruptions at such off-rift volcanoes are infrequent, and consequently, the plumbing systems are poorly understood. We present posteruption Synthetic Aperture Radar (SAR) images from the TerraSAR-X satellite and posteruption continuous seismic activity from a local seismic array. Interferometric analysis of SAR data, reveals a circular, 12 km wide, signal subsiding at ~200 mm/yr. We inverted for the best fit Mogi source finding a $4 \pm 1 \times 10^7$ m^3/yr volume decrease at 7 ± 1 km depth. Between 31 August and 7 October 2011, we located 658 and relocated 456 earthquakes with local magnitudes between −0.4 and 4.5. Seismicity beneath the SE edge of Nabro at 11 km depth is likely associated with high strain rates from deep magma flow into the modeled reservoir. This suggests that magma is supplied through a narrow conduit and then stored at ~7 km depth. We interpret seismicity at 4–6 km depth as brittle fracturing above the inferred magma reservoir. Focal mechanisms delineate a thrust fault striking NE-SW and dipping 45° to the SE across the caldera floor. We propose that the crustal response is to slip on this fault which crosscuts the caldera rather than to deform on ring faults. The NE-SW fault plane is not associated with measurable surface deformation, indicating that it does not contribute much to the caldera deformation. We show that subsidence of the caldera is controlled by magma chamber processes rather than fault slip.

1. Introduction

During continental rifting the majority of active volcanism typically becomes focused in a central rift axis [*Ebinger and Casey*, 2001]. In the Afar region of Ethiopia, this is expressed as laterally stepping en echelon volcanic ranges that accommodate most of the extension [*Hayward and Ebinger*, 1996]. However, volcanic structures are also commonly found offset from the axis of spreading [*Ebinger*, 1989; *Kiselev*, 1987; *Abebe et al.*, 1998; *Sturkell et al.*, 2003; *Bosworth et al.*, 2005]. Termed "off-axis" or "off-rift" volcanoes, their magma supply and their role in accommodating extension remains unclear [e.g., *Maccaferri et al.*, 2014]. Furthermore, eruptions of off-rift volcanoes are infrequent, limiting opportunities to observe them when active. The eruption of Nabro volcano on 12 June 2011 was only the second eruption of an off-rift volcano associated with the Afar Rift Zone (ARZ) in modern times (since Dubbi volcano in 1861 [*Wiart and Oppenheimer*, 2000]). It was also the volcano's first in the historical period [*Wiart and Oppenheimer*, 2005]. Here we analyze posteruption seismicity and Interferometric Synthetic Aperture Radar (InSAR)-derived surface deformation to understand the subsurface magmatic system of this hazardous, off-rift volcano.

Nabro volcano is located on the central part of the Danakil microplate on the southern margin of the Danakil Alps [*Berhe*, 1990] in NE Afar (Figure 1). It is the largest volcano in the ~110 km long Nabro Volcanic Range (NVR), which trends NNE-SSW and extends from Bara' Ale volcano in Ethiopia to the Kod Ali formation in the Red Sea [*Wiart and Oppenheimer*, 2005]. A subsection of the NVR is the Bidu Volcanic Complex (BVC) composed of the Nabro and Mallahle calderas. Nabro comprises a horseshoe-shaped caldera reaching 8 km in diameter, open to the SW and facing the smaller 6 km diameter caldera of Mallahle volcano [*Wiart and Oppenheimer*, 2005]. The summit of Nabro is 2248 m above sea level (asl), making the BVC one of the largest massifs in the Afar region.

 ©2014 Crown copyright. Journal of Geophysical Research: Solid Earth published by Wiley Inc. on behalf of American Geophysical Union.

AGU Journal of Geophysical Research: Solid Earth 10.1002/2014JB011395

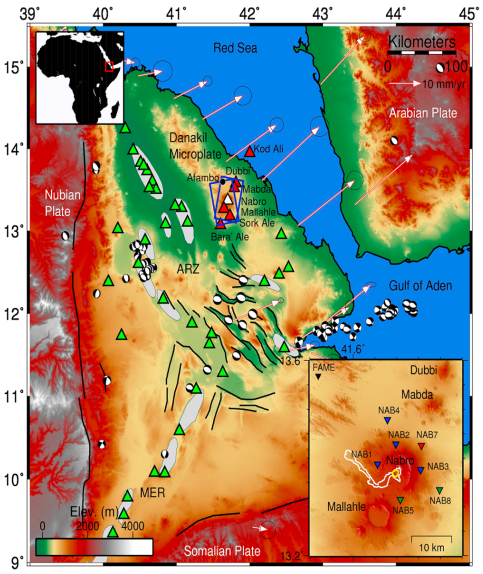

Figure 1. Topographic map (90 m Shuttle Radar Topography Mission) of the Afar Rift Zone (ARZ). Black lines are regional faults, and grey zones indicate volcanic segments. Fault plane solutions determined by the Global CMT project are displayed for earthquakes that occurred between 1979 and 11 June 2011; note the lack of events beneath the Nabro Volcanic Range (NVR). Green triangles indicate regional Holocene volcanoes recorded in the Smithsonian Catalogue "Volcanoes of the World" database, the red triangles constitute the NVR, with Nabro volcano highlighted in white. The white arrows represent measured horizontal GPS displacement relative to the Nubian plate [*McClusky et al.*, 2010]. Blue boxes outline the footprint of TerraSAR-X Tracks 046 and 130. The black dot marks the village of Afambo. (bottom right inset) ASTER G-DEM topographic map of Nabro volcano. Inverted triangles show the configuration of seismic stations used for the analysis. Green: 40 TD Güralp seismic stations. Blue: 6 TD Güralp seismic stations. Red: 6 TD Güralp seismic station used for focal mechanism analysis only. Black: 3ESP seismic station, part of a regional array. White outline: 2011 eruption lava flow. Yellow: 2011 eruption vent region.

Between 23 February and 11 June 2011, nine earthquakes with local magnitudes ranging from 2.6 to 4.8 occurred in the BVC region [*Goitom et al.*, 2014]. These were the first signs of forthcoming volcanic activity at Nabro in modern times. The eruption began between 20:30 and 20:45 UTC on 12 June 2011 from a circular vent region, centered on 41.7°E, 13.4°N and lasted approximately 2 weeks. Explosive phases of the eruption generated ash clouds which reached initial heights of 15–17 km [*Clarisse et al.*, 2014] and disrupted aviation [*Bojanowski*, 2011]. In addition, an estimated 4.3 Tg of SO_2 were emitted to the atmosphere during the eruption [*Theys et al.*, 2013]. This was the largest emission of SO_2 by an African volcano following the release of ~4.11 Tg SO_2 during the 1981–1982 eruption of Nyamulagira [*Bluth and Carn*, 2008]. The 2011 Nabro eruption was one of the most substantial volcanic SO_2 emissions since the 1991 eruption of Mount Pinatubo, which emitted ~20 Tg SO_2 to the atmosphere [*Bluth et al.*, 1992]. A small crater just to the SW of the center of the caldera was the focus of the eruption. By 18 June 2011 this crater infilled with a tephra cone and a 2 km discontinuous alignment of small pits striking NW-SE opened up (Oppenheimer personn.coms). A 17.5 km trachybasalt to trachybasaltic andesite lava flow travelled for ~4 km SW from the vent region, before turning to the NW (Figure 1). In some places, such as near its terminus, the width of the lava flow is as much as 2 km. Flow margins reached 5–10 m in thickness, but the thickness of the interior of the flow could not be judged in the field and may be substantially higher in places. The extent of the eruption required the Southern Red Sea Administration (SRSA) to form response teams to coordinate the disaster [*Solomon*, 2012]. In total, seven people died, three were injured and 12,000 were displaced. The total cost of the eruption was estimated at 3 million USD [*Solomon*, 2012].

In this paper we present observations of the posteruption deformation obtained with high spatial resolution InSAR and microseismicity recorded between 31 August 2011 and 7 October 2011 using a local array. We invert the deformation field revealed by InSAR to model the subsurface change in magma source volume and associated geometry. In addition, we present hypocenters and magnitudes of the earthquakes recorded by the local seismic station network and use them in combination with the deformation data to interpret subsurface magma plumbing. We calculate fault plane solutions to quantify the style and orientation of fault slip in response to magma withdrawal and to study the evolution of the structure of the caldera after the eruption.

 ©2014 Crown copyright. Journal of Geophysical Research: Solid Earth published by Wiley Inc. on behalf of American Geophysical Union.

Journal of Geophysical Research: Solid Earth 10.1002/2014JB011395

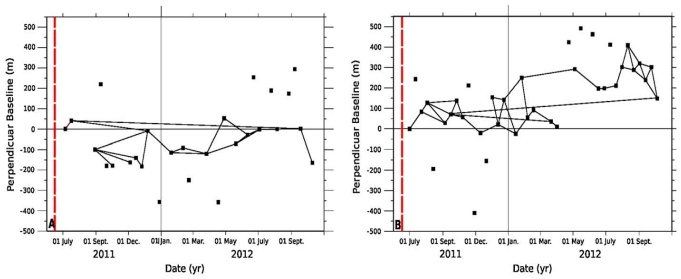

Figure 2. Perpendicular baseline versus time plot for (a) ascending track 130 and (b) descending track 046. Showing acquisitions (black squares) following the eruption. Solid lines represent interferograms where the unwrapping was above 90%. These interferograms are used for this InSAR analysis. Dates not connected were not used for the study. Red dashed line indicates the onset of the eruption.

2. InSAR Analysis

2.1. InSAR Data

The TerraSAR-X (TSX) satellite was tasked to acquire "StripMap" SAR images of the region following the eruption on both ascending and descending orbits. The TSX satellite uses an active X band SAR antenna with a wavelength of 31 mm, the incidence angle of the beam varies across the scene, between 25.1° to 30.5° and 31.7° to 34.8° for the ascending and descending tracks, respectively. Each fringe within an interferogram corresponds to a change in range of ∼15 mm between the ground and the satellite. Each SAR scene is 30 km wide and 50 km long, large enough to cover the BVC and the surrounding area, with a minimum pixel size corresponding to 3 m on the ground. We used a data set of 25 images acquired between 1 July 2011 to 5 October 2012 on descending orbit 046 and complemented these with 19 images from ascending orbit 130 spanning the period between 6 July 2011 and 10 October 2012.

2.2. Method

The potential for spaceborne radar interferometry to monitor long-term deformation over active volcanoes was first demonstrated by *Massonnet et al.* [1995]. Subsequently, it has become an invaluable technique to study the ground displacements caused by magma movements due to the high spatial resolution and synoptic coverage of the data [e.g., *Amelung et al.*, 2000; *Lu et al.*, 2005; *Wright et al.*, 2006; *Biggs et al.*, 2011; *Hooper et al.*, 2012]. We created 34 interferograms from the descending data set and 21 interferograms from the ascending data set. The interferograms have a maximum perpendicular baseline of 200 m and temporal baseline between 11 and 390 days. We used a connected network of interferograms which had at least 90% of the image unwrapped (Figure 2). The interferograms were created using the JPL/Caltech ROI_PAC software [*Rosen et al.*, 2004], and we used the multiinterferogram method of *Biggs et al.* [2007] as implemented in π RATE [*Wang et al.*, 2012] to produce a rate map showing the average Line Of Sight (LOS) displacement rate of each pixel, as well as a time series of this displacement.

2.3. Results

In both ascending and descending data sets, we observe a nearly circular, ∼12 km wide range increase, which is centered on the SW region of Nabro's caldera (Figure 3). As the signal is a range increase in both data sets, the ground surface is moving away from the satellite. Therefore, the volcano is subsiding following the eruption. The caldera region within the descending rate map is incoherent, so we cannot measure the subsidence close to the vent region. In the descending track, the extent of the 17 km long lava flow emplaced by the eruption is also clearly distinguishable as an incoherent region originating from the caldera. There maybe a small localized loading effect within ∼50 m of the lava flow. The ascending track is more coherent within the caldera; the maximum subsidence rate we measure is ∼200 mm/yr. There is a small amount of LOS ground deformation at Mabda, Mallahle and Sork 'Ale volcanoes observable from the ascending rate map (Figure 3); we interpret this as atmospheric noise caused by the topography of the volcanoes, as it is not visible in the descending data set. We have also plotted the subsidence over time (Figure 4) recorded at 1 pixel in the ascending data set. We find that the subsidence over the observation period is altogether quite linear but may have been faster immediately following the eruption. We go on to model the subsidence assuming a linear rate over time.

 ©2014 Crown copyright. Journal of Geophysical Research: Solid Earth published by Wiley Inc. on behalf of American Geophysical Union.

Journal of Geophysical Research: Solid Earth 10.1002/2014JB011395

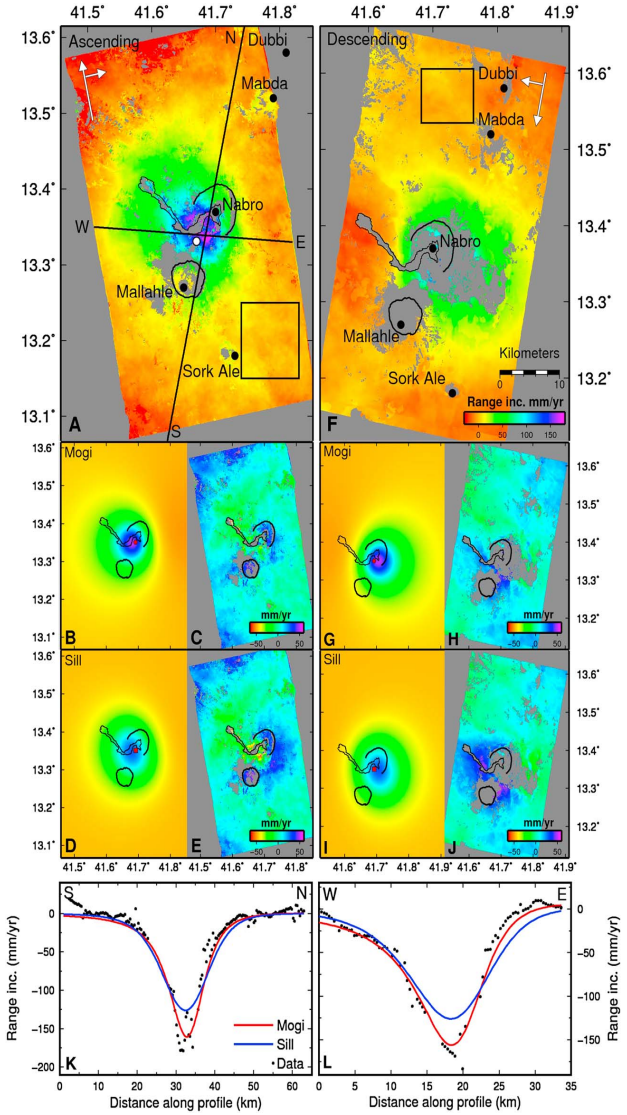

Figure 3. Best-fit model assuming Mogi and sill sources. (a) Observed ascending rate map of ground movement, white point: pixel used for time series. (b) Mogi model of deformation for ascending track. (c) Residual motion following Mogi model. (d) Sill model of deformation for ascending track. (e) Residual motion following sill model. (f) Observed descending rate map of ground movement. (g) Mogi model of deformation for descending track. (h) Residual ground motion. (i) Sill model of deformation for descending track. (j) Residual ground motion. (k) Profile of ground displacement along transect N-S on Figure 3a. (l) Profile of ground displacement along transect W-E on Figure 3a. The black squares in Figures 3a and 3f show the far-field regions used to calculate noise for the Monte Carlo analysis. The red points in Figures 3b, 3d, 3g, and 3i, mark the center of the model at depth. The interferograms span 462 days for both the ascending and descending tracks.

We jointly inverted the ascending and descending ground displacements using a Monte Carlo hybrid downhill simplex inversion technique [*Clarke et al.*, 1997; *Wright et al.*, 1999], which assumes a homogeneous, isotropic, Poisson-solid half space. The rate maps were averaged to 1 km pixels to reduce the inversion time. We first considered a deflating Mogi source in an elastic half space and solved for the depth, location, and volume change of the source (Figure 3). Uncertainties on these parameters were calculated using a Monte

 ©2014 Crown copyright. Journal of Geophysical Research: Solid Earth published by Wiley Inc. on behalf of American Geophysical Union.

Journal of Geophysical Research: Solid Earth 10.1002/2014JB011395

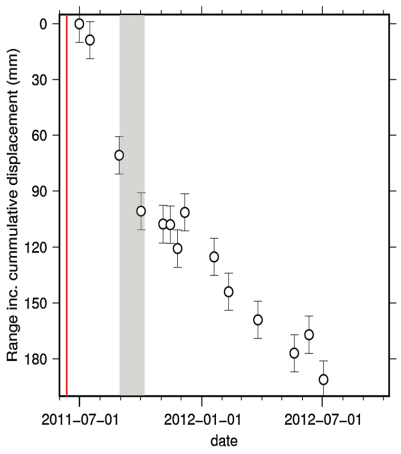

Figure 4. Time series of ground subsidence observed at the pixel marked by the white point on Figure 3a. The red line marks the onset of the eruption. Grey shading is the time period of the seismic data presented in this study.

Carlo simulation by adding correlated noise to the data set [*Wright et al.*, 2003], which was estimated from a background reference region located away from the deformation (Figure 3). We created 100 of such data sets, which were subsequently inverted. The range of the solutions gives the uncertainties of the parameters. We find the best-fitting Mogi source at 7 ± 1 km depth, which reduces in volume by $4 \pm 1 \times 10^7$ m^3/yr, on the surface, the center is located within 0.6 km of 13.35°N and 41.69°E. From the Monte Carlo simulations we find a trade-off between the volume change and the depth of the source. The ground displacement modeled by the Mogi source has an RMS misfit of 13.2 mm/yr and 11 mm/yr for the ascending and descending tracks, respectively. The highest residuals in the ascending track are around the caldera rim, and highest in the descending track between Nabro and Mallahle calderas. This could be due to the loss of coherence in these areas due to the topography and ash cover or due to the model simplifications.

We also considered a sill geometry to model the subsidence. We used the same Monte Carlo hybrid downhill simplex inversion technique, and in the initial inversions, we solved for the location, depth, size (horizontal extent), and closing of a single-square Okada source [*Okada*, 1985]. However, the inversion collapsed to a small source with an unphysically large opening. Effectively, the only constraint on the size of the sill is that the horizontal extent of the sill is much less than the depth of the source. We therefore fix the horizontal extent of the sill to be 1 km in the subsequent inversions and only solve for the amount of closing. This is equivalent to solving for the contraction volume of a point source sill. We find that the best-fit sill is located at a depth of 11 ± 2 km; it has a contraction volume of $4 \pm 1.2 \times 10^7$ m^3/yr, and on the surface, the center is located within 0.9 km of 13.35°N and within 0.6 km 41.69°E. As observed with the Mogi source, due to the nonuniqueness of InSAR modeling, there is still a trade-off between volume change and depth. The sill model underestimates the amount of subsidence at the center of Nabro's caldera, observable from the ascending track. Also, the sill solution does not account for much horizontal movement. This has resulted in higher residuals on the east and west flanks of Nabro in the ascending and descending tracks, respectively. The RMS misfit for the sill model is 13.9 mm/yr and 12.7 mm/yr for the ascending and descending tracks, respectively.

The Mogi model better describes the horizontal ground motions which are implied by the difference between the ascending and descending scenes, suggesting that the surface deformation is best approximated by a deflating point source. The model also captures the maximum surface displacement better than the sill source. Also, the RMS misfit is lower in both tracks and this is emphasized in the transects across the ascending data (Figures 3k and 3l). We have neglected the variation of topography for the inversion, and therefore, we have referenced all depths to 700 m asl, (the seismicity reference elevation). The interferometric analysis and modeling describes the ground displacement and gives an analytical solution to the magma chamber geometry. Using the seismic data we can improve the constraints on the depth of the magma chamber and observe the small scale brittle response to the eruption. These features will further delineate the magma plumbing system and may illuminate faults which accommodate the subsidence. We present the seismic data in the following section and provide a discussion of the integrated results.

3. Seismic Analysis

3.1. Seismic Data

In response to the eruption, we deployed a network of eight broadband Güralp seismic stations (five 6TD and three 40TD, provided by SEIS-UK [*Brisbourne*, 2012]) on the flanks of Nabro. The network was fully operational by 31 August 2011, 79 days after the eruption began. However, the GPS failed at NAB5 (6TD site)

 ©2014 Crown copyright. Journal of Geophysical Research: Solid Earth published by Wiley Inc. on behalf of American Geophysical Union.

AGU Journal of Geophysical Research: Solid Earth 10.1002/2014JB011395

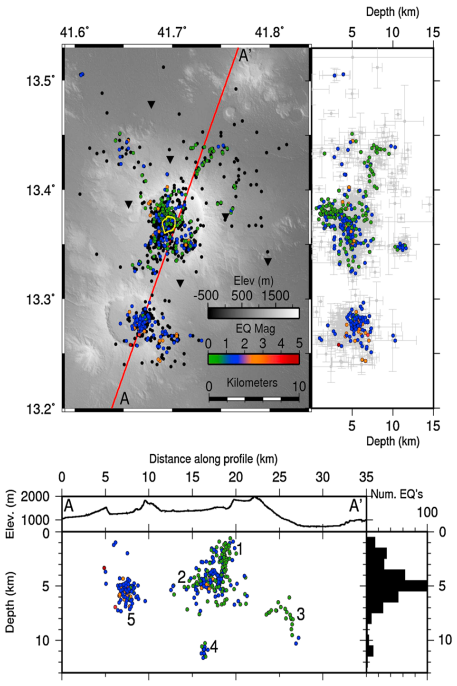

Figure 5. (top) Initial hypocenter locations determined using Hypo2000, for the 658 earthquakes detected during the period 31 August to 7 October 2011, shown as black dots (map view) and grey dots with error bars (N-S depth profile). The position of 456 relocated hypocenters calculated by HypoDD are shown as colored dots, dependent on their local magnitude. Seismic stations used to locate the events are indicated by black triangles. Yellow outline highlights the vent region. (bottom) Topographic profile and hypocenters along transect A-A', determined by HypoDD within 1 km either side of the transect. The depths are given referenced to 700 m asl, the lowest elevation seismometer. The histogram shows numbers of hypocenters at depth per 1 km bin. Numbers indicate clusters as described in text.

and NAB6 (40TD site) was damaged due to flooding; data recorded at these stations were not used in this study; the resulting array configuration is depicted in Figure 1. All local array seismic stations have a natural frequency response of 30 s. In addition to the local network on Nabro, data recorded by FAME a Güralp 3ESP seismometer in the nearby village of Afambo (Figure 1), with a natural frequency response of 60 s, are included in the analysis. This seismometer is located approximately 35 km NW of the caldera and is part of an Eritrean regional array. The first data download was completed on 7 October 2011. These provide the 38 day data set investigated in this study, which covers the posteruption period (the eruption ended by late June–early July 2011). The data have a high signal-to-noise ratio due to a favorable recording environment; the noise levels are low as the equipment was located in small villages, sheltered from the wind and far from ocean noise. The use of a local network is crucial for detecting and accurately locating microseismicity, which can help reveal detailed magma migration pathways and the development of subsurface structures in response to an eruption [e.g., *Aspinall et al.*, 1998; *Roman et al.*, 2006; *Ebinger et al.*, 2008; *Keir et al.*, 2009; *Lehto et al.*, 2010; *Tarasewicz et al.*, 2012a, 2012b; *Roman and Gardine*, 2013]. Furthermore, the focal mechanisms can be tightly constrained due to the spatial distribution of the seismic stations.

3.2. Methods

We manually picked arrival times of the *P* and *S* waves at every seismic station for each distinguishable earthquake using SAC software [*Goldstein and Snoke*, 2005]. We found that the traces did not need to be filtered before analysis due to the high data quality. As part of the process, we assigned a quality value of 0, 1, 2, and 3 to the measurement, based on an estimated *P* wave arrival time error of 0.05, 0.1, 0.015, and 0.2 s, respectively. For *S* waves, the 0 to 3 quality values were assigned to values of 0.1, 0.175, 0.25, and 0.3 s, for the estimated error in arrival time. These values were used as weights in the location inversion performed by the Hypo2000 algorithm [*Klein*, 2002] (Figure 5).

During the 38 day recording period we detected a total of 658 earthquakes on Nabro caldera and in the surrounding area. To locate earthquakes we used a 1-D velocity model with a linear increase in velocity with depth [*Lahr*, 1989]. This avoided clustering of earthquakes at velocity discontinuities, an artefact often observed in velocity models with homogeneous layers. Our velocity model was constrained using crustal scale reflection and refraction seismology across the Danakil blocks [*Makris and Ginzburg*, 1987]. The average location error using this technique is significant; $\pm$ 2 km horizontal, $\pm$ 4 km depth, and obscures detailed observations about the magmatic plumbing of the volcano [*Jones and Stewart*, 1997]. These errors result from a combination of factors including, station locations, available phases, accuracy of the arrival time measurement, and the validity of the velocity model [*Waldhauser and Ellsworth*, 2000].

 ©2014 Crown copyright. Journal of Geophysical Research: Solid Earth published by Wiley Inc. on behalf of American Geophysical Union.

AGU Journal of Geophysical Research: Solid Earth 10.1002/2014JB011395

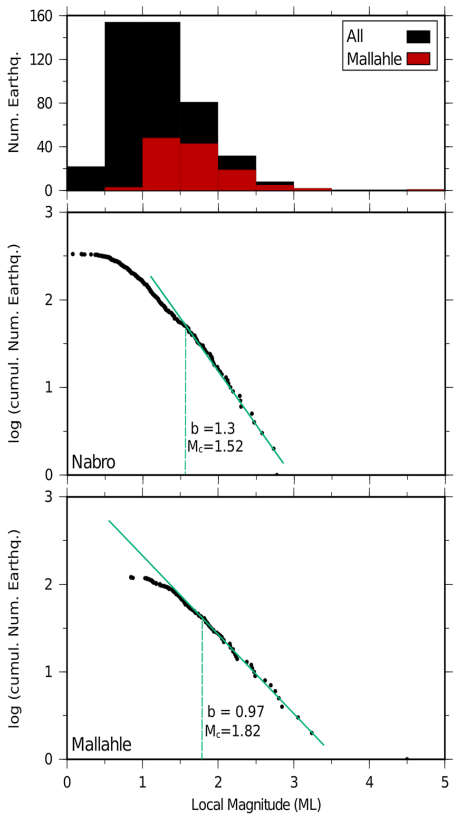

Figure 6. For all 658 events. (top) Distribution of the number of earthquakes at each magnitude. Black shows the distribution for all hypocenters, red shows the distribution for those which occurred on Mallahle caldera. (middle) Gutenberg-Richter distributions of the relocated earthquakes on Nabro. (bottom) Gutenberg-Richter distributions of the relocated earthquakes on Mallahle.

The Hypo2000 algorithm locates hypocenters assuming a 1-D subsurface. However, the velocity of a seismic wave beneath an active volcano will vary in three dimensions due to variations in rock composition and partially molten bodies. In addition, the subsurface velocity structure may also change through time as partial melt bodies evolve. We minimized the dependence of the hypocenter location on the velocity model by proceeding with a double differencing technique, HypoDD [*Waldhauser and Ellsworth*, 2000; *Waldhauser*, 2001], which we applied to the located events determined by Hypo2000, (Figure 5). We parameterized the relocation procedure in order to relocate the maximum number of events while minimizing the allowed separation between the initial hypocenters. In this manner, 456 of the initial 658 earthquakes were relocated.

Local magnitudes (M_L), as originally defined by *Richter* [1935], were computed using the maximum body wave amplitude of the horizontal component seismograms after they are convolved with the standard Wood-Anderson response [*Anderson and Wood*, 1925; *Kanamori and Jennings*, 1978]. The computation also considers the distance between the earthquake and stations in a distance correction term, which allows for decrease in amplitude with distance due to attenuation. We use the correction term derived for the Main Ethiopian Rift (MER) by *Keir et al.* [2006]. This correction is applicable to the high ground motion attenuation conditions, caused by high heat flow due to the presence of partial melt beneath the rift valleys in the region [*Gass*, 1970; *Keir et al.*, 2011]. We use M_L estimates to calculate the seismic moment release using empirical relationships, e.g., *Kanamori* [1977], following the method of *Keir et al.* [2011].

We computed lower hemisphere focal mechanisms to constrain the orientation of crustal strains using FOCMEC [*Snoke*, 2003]. The program uses the station location, take off angles, and *P* and S_H wave polarities to perform a grid search for the best-fit double-couple solution [*Snoke*, 2003; *Ebinger et al.*, 2008]. Using an incremental step of 10°, all fault plane solutions have an error of $\leq \pm 20^o$ in strike and dip of the nodal planes. We were able to estimate 46 robust fault plane solutions beneath Nabro's caldera. We could not determine solutions for events away from the caldera due to the configuration of seismic stations. Data from the seismic station with a failed GPS system (NAB7) were included in the data set as the arrival time of the wave was not relevant for this analysis, but the position of the station was useful for determining the strike of the nodal planes.

3.3. Results

3.3.1. Spatial Variations

All of the events recorded can be defined as volcano-tectonic (VT) earthquakes as they have clear *P* and *S* wave arrivals, with an average peak frequency of 7 Hz [*Lahr et al.*, 1994]. VT earthquakes are commonly recorded at preeruption, coeruption, and posteruption and can indicate changes in the magmatic plumbing

 ©2014 Crown copyright. Journal of Geophysical Research: Solid Earth published by Wiley Inc. on behalf of American Geophysical Union.

AGU Journal of Geophysical Research: Solid Earth 10.1002/2014JB011395

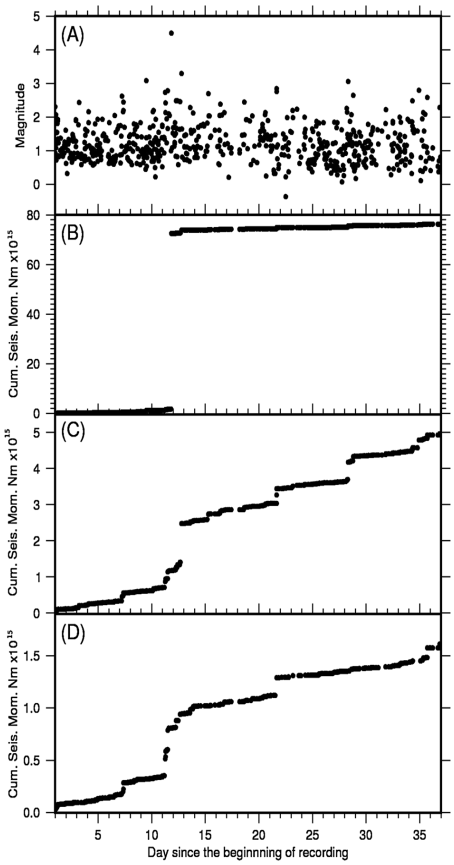

Figure 7. (a) Magnitude of 650 Hypo2000 located earthquakes over the 38 day recording period. (b) Cumulative seismic moment release of all earthquakes over the recording period. (c) Cumulative seismic moment release with the largest event removed. (d) Cumulative seismic moment for earthquakes under Nabro only.

system and emplacement of new intrusions [*Hill*, 1977; *Umakoshi et al.*, 2001; *Roman and Cashman*, 2006; *Roman et al.*, 2006]. Event locations after relocating with HypoDD are overlain on the Hypo2000 results (Figure 5). The relative error of the relocated earthquakes is ± 40 m in depth and ± 16 m in the horizontal coordinate. The depths are referenced to 700 m asl, the lowest elevation seismometer. Five clusters are visible in the spatial distribution of the earthquakes (Figure 5): (1) Directly beneath the vent, there is an elongate, subvertical cluster extending between 1 and 4 km depth. (2) The cluster is located beneath the central and southern part of the caldera, it is subhorizontal with the seismicity deepening to the SW, the cluster is ~5 km long and between 4 and 5 km deep. (3) Beneath the NE flank of Nabro, there is a NE striking cluster which deepens to the north, it is 6–11 km deep. (4) Beneath the SE caldera wall, 16 earthquakes are between 10 and 12 km deep. (5) A cluster lies directly beneath Mallahle, the hypocenters form a spherical cluster ranging between 4 km and 7 km deep. There is a noticeable aseismic zone between Nabro and Mallahle calderas. We will use these clusters to interpret fault slip induced by magma movement, highlighting potential magma pathways, as well as slip on larger scale preexisting faults induced by volume changes in magma reservoirs.

3.3.2. Magnitudes

We determined local magnitudes (M_L) to range between −0.37 and 4.5, for all 658 earthquakes located using Hypo2000. The magnitudes of the relocated earthquakes are shown in Figure 5. The majority of earthquakes beneath Mallahle have a magnitude between 1 and 2, (Figure 6). Most of the events with a magnitude between 0 and 1 are located beneath Nabro, but this can reflect bias caused by the station distribution. In order to see how magnitudes are distributed and how they establish cutoff magnitudes, we used the frequency-magnitude distribution (FMD) [*Gutenberg and Richter*, 1944]:

$$\log N = a - bM_c, \tag{1}$$

where N is the cumulative number of earthquakes with a magnitude equal to or greater than M, a is a constant describing the rate of seismic activity in the study area, and b is the gradient of the FMD plot. M_c, also known as the "cutoff" magnitude, is the smallest magnitude of earthquake to which the catalog is complete; this is determined by the network sensitivity. As equation (1) uses only the maximum observed magnitude, the resulting b value tends to be too low [*Bender*, 1983]. Therefore, as our data only spans a short period, we use the maximum likelihood formula (2) as derived by *Utsu* [1965] to calculate the b value,

$$b = \frac{\log_{10} e}{M_a - M_c}, \tag{2}$$

 ©2014 Crown copyright. Journal of Geophysical Research: Solid Earth published by Wiley Inc. on behalf of American Geophysical Union.

AGU Journal of Geophysical Research: Solid Earth 10.1002/2014JB011395

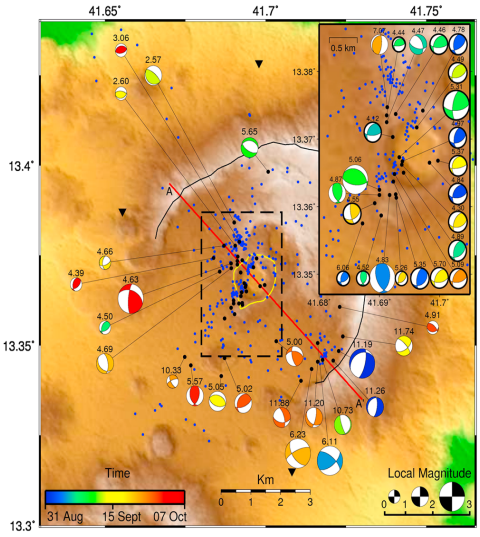

Figure 8. Lower hemisphere fault plane solutions for 46 earthquakes on Nabro; the location of the corresponding hypocenter is shown as a black dot. The size of the fault plane solution is scaled to the local magnitude of the event, and the depth at which it occurred is reported (in km) above the focal mechanism. All other earthquakes in the region are depicted with a blue dot. The color of the compressional quadrant of the solution is related to the time of the event. The 2011 eruption vent region is outlined in yellow, and the caldera rim is outlined in black. (inset) Zoom of the vent region with focal mechanisms. Eighteen thrust mechanisms are outlined in bold.

where M_a is the average magnitude and M_c is the cutoff magnitude. Previous works by *Bridges and Gao* [2006] and *Sanchez et al.* [2004] show how spatial variations in *b* values can provide constraints on the distribution of magma in the subsurface. Therefore, we find separate *b* values for the events on Nabro and those on Mallahle. We plot the FMD for Nabro and Mallahle events separately (Figure 6). The *b* value was determined for Nabro using values of $M_a = 1.86$ and $M_c = 1.52$ and for Mallahle using $M_a = 2.62$ and $M_c = 1.82$. For all detected seismicity on Nabro, $b = 1.3 \pm 0.08$ for the events beneath Mallahle, $b = 0.97 \pm 0.15$ (Figure 6). The difference in cutoff magnitude between the two calderas is due to the siting seismic stations solely on Nabro. The seismic energy release will be compared to the accumulation of the seismic moment as determined by InSAR.

3.3.3. Temporal Variations

The daily number of earthquakes (Figure 7a) varies between 4 and 33 during the 38 day recording period. Figure 7b shows the original 658 earthquakes, which contribute 76×10^{15} N m seismic energy release. The largest release of seismic energy can be attributed to an event with a magnitude > 4. When this event is removed from the analysis (Figure 7c), it can be seen that the seismic moment release increases by between 0.2 and 0.4×10^{15} N m steps every 6–10 days with a linearly increasing moment release between each step. These linear increases with discrete steps are observed on both Nabro and Mallahle calderas. Figure 7d shows the seismic energy release from the events on Nabro only, these show the same trend as that observed in Figure 7c. There appears to be no consistent temporal pattern in the spatial distribution of events.

3.3.4. Focal Mechanisms

We computed 46 focal mechanisms beneath Nabro's caldera of which six were normal, 33 were thrust, and four were largely strike-slip motions (Figure 8). A prominent feature is a series of 18 thrust mechanisms with nodal planes striking NE-SW located in the center of the caldera, under the vent, which occur throughout the recording period at a depth between 4 and 5 km (Figure 8 (highlighted in bold), and Figure 9). In this region, there are three thrust mechanisms with differently orientated nodal planes; one striking northward and two with nodal planes striking ESE-WNW. Also in the center of the caldera, only one solution indicates normal faulting, the nodal planes strike SE-NW. Away from the center of the caldera, only nine of the 46 focal mechanisms have a major normal faulting component, four of which are located within the deep seismic cluster 4 (Figure 5). Due to the seismic network configuration, the focal mechanism of events beneath Mallahle caldera could not be constrained.

3.3.5. Waveforms

In order to test whether different earthquakes located close to each other are generated by the same slip motion in the same fault, we use the criteria of waveform similarities of earthquake pairs. Earthquake waveform pairs that have a significant similarity, expressed by a correlation coefficient greater than 0.7, are produced by the same source mechanism [*Pechmann and Kanamori*, 1982] and located within a distance of a 1/4 wavelength of each other [*Geller and Mueller*, 1980]. We can also use the correlation coefficients to qualitatively highlight changes in the subsurface. We have chosen two pairs of waveforms to perform the cross correlation, whose hypocenters are located within 215 m of each other, which is a 1/4 wavelength

 ©2014 Crown copyright. Journal of Geophysical Research: Solid Earth published by Wiley Inc. on behalf of American Geophysical Union.

Journal of Geophysical Research: Solid Earth 10.1002/2014JB011395

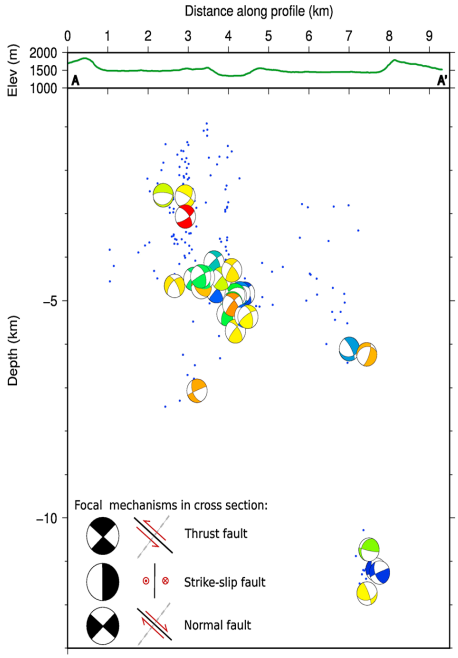

Figure 9. (top) Topography of Nabro along transect A-A'. (bottom) All focal mechanisms have been projected on to transect A-A' (Figure 6), then rotated to a side view, as viewed from south to north.

distance for these waveforms and all have the same focal mechanism. The first waveform pair are separated by 22 days, whereas the second pair occurs almost simultaneously, just 10 min apart. These four seismic waveforms have a peak frequency of approximately 7 Hz and contain some higher-frequency noise, which we filtered by applying a bandpass filter with corner frequencies of 2 and 10 Hz (Figure 10). We determined a cross-correlation coefficient of 0.20 and 0.84 for the first and second pairs, respectively. This discrepancy indicates that despite a close source location and the same focal mechanism, the path effects between the source and the receiver changed significantly between the two earthquakes constituting the first pair. This leads us to suggest that the subsurface evolved over the recording period, due to the ongoing subsidence.

4. Discussion

4.1. Joint Interpretation of InSAR and Seismicity

In this study we have measured the crustal response to the 2011 eruption of Nabro volcano. Using the high-resolution InSAR data in conjunction with seismicity, we are able to create a working model of the magmatic plumbing system and how it interacts with faults (Figure 11). We observe a circular subsidence signal which is offset to the SW of the caldera topography and the vent region, suggesting that the magma reservoir is not located directly beneath the eruption center. The subsidence signal suggests ongoing depressurization of the magma chamber following the eruption. The spatial pattern and sporadic nature of the hypocenters located at shallow depths (less than 6 km) under Nabro, are likely caused by the bending and episodic fracturing of brittle rocks within the volcanic edifice [*Dzurisin et al.*, 1991, 2002], in response to the depletion of the magma chamber. The temporal pattern of earthquake hypocenters has previously been used to show the migration of magma preceding and during eruptions [*Tarasewicz et al.*, 2012a]. However, beneath Nabro the seismicity recorded by the local array does not necessarily show this migration of magma to the surface, rather the constant reactivation of already developed faults, which slip during subsidence.

We find that the depth of the magma body, estimated by inverting the InSAR deformation field, is dependent on whether we chose a Mogi or sill source and the volume change imposed. The Mogi solution suggests a depth of 6.9 ± 1.1 km, whereas the sill solution yields a depth of 11 ± 2 km. Using the spatial distribution of the hypocenters, we suggest that the most applicable geometry of the source resembles the Mogi solution, as we interpret seismic cluster 2 (Figure 5) as the region of brittle failure immediately above the magma chamber, which fractures to accommodate the volume change. Therefore, the residual magma body is situated in the shadow zone immediately below this cluster. However, it is likely that the Mogi approximation is an oversimplification of the geometry of the magma source. A magma plumbing configuration of stacked sills was inferred from joint analysis of seismic, petrological, and geodetic data for Dabbahu volcano [*Field et al.*, 2012]. The magma reservoir under Nabro may also constitute numerous lenses and dykes of partial melt across a depth range of 6 to 10 km, which together approximate a single point source ground deformation signal. The deep cluster of seismicity (cluster 4, Figure 5) directly beneath this region may be related to small-scale fracturing around a constricted part of the plumbing system, potentially linking the shallow sources to a deeper reservoir, similar to an interpretation of lower-midcrustal seismicity at

 ©2014 Crown copyright. Journal of Geophysical Research: Solid Earth published by Wiley Inc. on behalf of American Geophysical Union.

Journal of Geophysical Research: Solid Earth 10.1002/2014JB011395

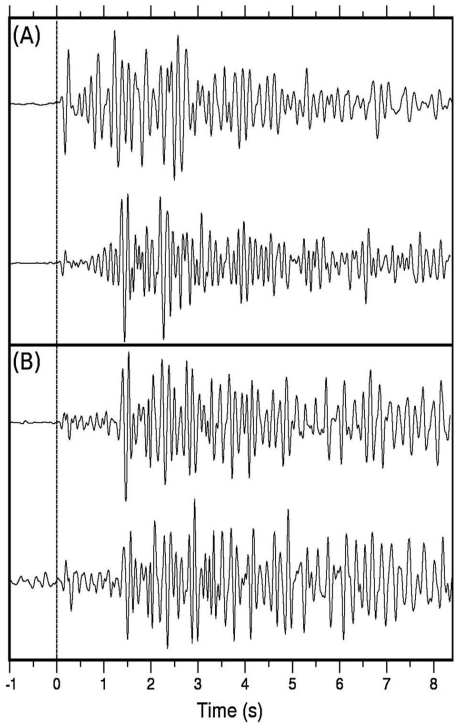

Figure 10. Examples of waveforms with a bandpass filter between 2 and 10 Hz applied. The hypocenters of the pairs are located within 215 m of each other. (a) Waveforms of earthquakes temporally separated by 22 days, with cross correlation of 0.20. (b) Waveforms of earthquakes temporally separated by 10 min, with cross correlation of 0.84.

Eyjafjallajökull volcano [*Tarasewicz et al.*, 2012a]. However, this network of dikes and sills can not be fully constrained using the current data set. Furthermore, the accuracy of the interpretation of our results is based on analytical models which consider a homogeneous, isotropic, Poisson solid, half space with a horizontal free surface. Therefore, our interpretations are subject to the validity of such assumptions. *Masterlark* [2007] found that in the absence of additional geomechanical data regarding the mechanical properties of rock, an analytical model which makes the aforementioned assumptions is best, as the model is simple and fits the observations well. *Masterlark* [2007] also showed that topographic effects are insignificant if an appropriate reference elevation is used.

As the deformation at the vent is incoherent in the InSAR signal, we use the spatial distribution and focal mechanisms of the recorded earthquakes to delineate the small-scale brittle ground response. The vent region and potential conduit are highlighted by seismic cluster 1 (Figure 5). The InSAR subsidence signal is centered on Nabro caldera and does not extend laterally toward

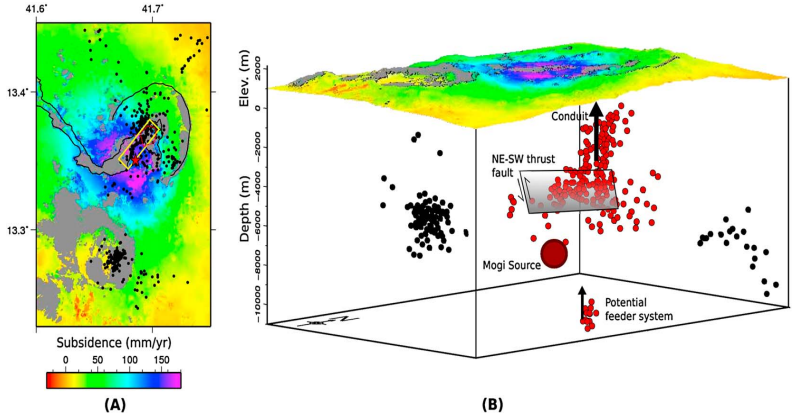

Figure 11. Working model of the magma plumbing system beneath Nabro. (a) Map view of the observed subsidence from the ascending InSAR data. Black outlines: caldera rim and lava flow. Red dashed line: vent region. Black dots: relocated hypocenters. Red star: Mogi model center. Yellow rectangle: NE-SW thrust fault outline at the surface. (b) Three-dimensional view of the proposed working model. Top plane: the observed subsidence from the ascending InSAR data draped on topography. Lower volume: hypocenter locations at depth. Red: earthquakes induced directly by the eruption. Black: regional earthquakes induced by changes to the stress field. The proposed Mogi source (dark red spot), conduit (large black arrow), thrust fault (grey plane), and potential magma supply system (small black arrow) are also highlighted.

 ©2014 Crown copyright. Journal of Geophysical Research: Solid Earth published by Wiley Inc. on behalf of American Geophysical Union.

AGU Journal of Geophysical Research: Solid Earth 10.1002/2014JB011395

Mallahle, which implies that there is no current subsurface magmatic connection between the two calderas. Therefore, the seismicity we observe is due to changes in the stress field resulting from the subsidence at Nabro and not caused by magma movement beneath Mallahle. However, a connection between the two calderas may have existed in the past. Also, the large magnitude (M < 4) VT earthquakes which occurred beneath Mallahle suggest that preexisting faults have been brought closer to failure, due to stress changes following the magma reservoir depressurization [*Wauthier et al.*, 2013a] We interpret seismic cluster 3 to also be a result of the stress change, where the linear structure implies a fault which has been created or reactivated due to the new distribution of stress. We can not constrain the focal mechanisms of these events as they are located outside of the local seismic array. Also, as the earthquakes which highlight the fault have a maximum magnitude of 2 and are at a depth of ~8 km, even if we assume the fault to have a 90° dip and a thrust mechanism, the surface deformation associated with this inferred structure is less than 0.5 mm. Therefore, it is not observable using InSAR techniques despite good coherence in this area. As this fault plane is very speculative we have not included it in the working model (Figure 11).

4.2. Modes of Caldera Subsidence

The structure and evolution of calderas provide information on the behavior magma reservoir, and therefore, understanding their geometries is crucial in predicting future behavior [*Cole et al.*, 2005; *Acocella*, 2007]. We can compare the mode of subsidence implied by the focal mechanisms to models of caldera response. The seismic data reveal fault structures in the shallow subsurface (less than 6 km deep), the magnitudes of the earthquakes which delineate the fault have a maximum magnitude of 3. Earthquakes of this size at ~ 5 km depth cause less than 1 mm of deformation at the surface, which is not resolvable in the InSAR data. We also assess the temporal evolution of these faults through interpretation of the cross-correlated waveforms. In Figure 9, a thrust fault is observed to crosscut the caldera floor 1 km above the center of the magma source. Since the focal mechanisms define a 45° dip along one of the nodal planes (Figure 9), we infer that a fault plane strikes NE-SW, dipping 45° to the SE. We can compare this faulting to both numerical modeling performed by *Holohan et al.* [2011] and analog models [*Lavallée et al.*, 2004; *Kennedy et al.*, 2004; *Roche et al.*, 2000] to provide further insights into the mechanisms of subsidence. *Holohan et al.* [2011] used a two-dimensional finite element method to model the caldera subsidence in a half space with a range of geomechanical properties. If we qualitatively compare Figure 9 to Figure 5c in *Holohan et al.* [2011], we find similarities such as the dip and motion of the fault plane and its position relative to the magmatic body. Using the terminology of *Holohan et al.* [2011], our results could also be described as "reverse fault that separates two inward rotated roof blocks." Quantitatively, the model we refer to would require the ratio between the thickness and diameter of the roof to be less than 0.33. Assuming that the seismicity under Nabro highlights the brittle failure of the roof, we find this ratio is between 0.69 and 0.88. As Nabro's caldera is already well established, the fault plane we observe may have existed prior to the eruption and has been reactivated. This may explain the presence of the fault despite the higher ratio between the thickness and diameter of the roof. Furthermore, we observe a linear increase in the seismic energy release interrupted by discrete steps on a week time scale at Nabro, which is consistent with the findings of *Ruch et al.* [2012] that incremental collapses can occur on mature faults during caldera collapse. In the absence of appropriate measurements for bulk porosity, bulk density, and Youngs modulus for rocks at Nabro, the benefit of further quantitative application models such as that of *Holohan et al.* [2011] is limited.

Ring faults are a common feature of a caldera collapse [*Marti et al.*, 1994; *Cole et al.*, 2005]. However, the hypocenters we located are not concentrated on the caldera walls, implying that these structures may not have been activated during the eruption, which is not uncommon [*Kennedy et al.*, 2004]. In addition, the fault plane solutions of those found in the vicinity of the caldera walls are not tensional (Figure 9). The modelling by *Holohan et al.* [2011] shows an upward migration of faulting; therefore, the hypocenter locations are expected to migrate toward the surface over time. However, as no such pattern is observed within seismic cluster 1, the faults are assumed to have been formed before the local seismic array was deployed, and we only observe their sustained reactivation as the caldera relaxes. By comparing the waveforms of two pairs of earthquakes with adjacent hypocenters on the same fault plane but with each pair having a different temporal separation, we find a distinct decrease in correlation over time. This suggests that subsurface structures were evolving even during the recording period.

4.3. The *b* Values

The *b* values describe a region's ability to accumulate stress, and the average global *b* value is approximately 1.0 [*Richter*, 1958]. However, *b* values can vary between regions as different geomechanical properties

 ©2014 Crown copyright. Journal of Geophysical Research: Solid Earth published by Wiley Inc. on behalf of American Geophysical Union.

AGU Journal of Geophysical Research: Solid Earth 10.1002/2014JB011395

influence the ability of rock to accumulate stress. Low *b* values indicate that a region is capable of accumulating significant stresses, which can result in large earthquakes. Areas with an increased thermal gradient [*Warren and Latham*, 1970] can be associated with a weak rheology, which cause small magnitude stress changes that tend to favor small-magnitude earthquakes. The lower *b* value for Mallahle implies that the earthquakes generated under Mallahle caldera are not dominated by magmatic processes and occur in rock with a stronger rheology. This is consistent with our conclusion that there is no subsurface magmatic link between Nabro and Mallahle calderas. The *b* value we calculated on Nabro is higher, likely due to a relatively weaker rheology, the presence of fluids and melt, the presence of highly fractured rock typical of heavily faulted calderas, and a higher geothermal gradient associated with the magma reservoir.

4.4. Off-Rift Volcanism

Off-rift volcanism is a common phenomenon that has also been observed in the Virunga Volcanic Province [*Ebinger*, 1989], in the Red Sea rift [*Bosworth et al.*, 2005], Iceland [*Sturkell et al.*, 2003], and the Baikal Rift [*Kiselev*, 1987]. Above the rift axis of the ARZ lie large volcanic provinces constructed from magma generated by decompression melting due to lithospheric thinning [*Hammond et al.*, 2013]. *Pagli et al.* [2012] suggest that an elevated magma supply in the rift axis of northern Afar results in shallow magma chamber depths, for example, the < 2.5 km depth chambers determined under Alu-Dalafilla and Dallol volcanoes [*Pagli et al.*, 2012; *Nobile et al.*, 2012]. Our results show that the magma plumbing system of the off-rift, flank volcanoes of the Danakil depression are fundamentally different from those in the rift axis and have deeper magma chamber depths. This is consistent with a lower spreading rate and thicker crust [*Purdy et al.*, 1992; *Morgan and Chen*, 1993; *Chen and Morgan*, 1996].

In rift settings the regional maximum compressive stress is vertical [*Illies*, 1981; *Bosworth et al.*, 1992]. On Nabro we expect the regional stress field to produce a vertical *P* axis and a NE striking *T* axis. However, our posteruption focal mechanisms show a horizontal NW striking *P* axis, revealing a local 90° shift from the expected regional orientation. Studies of VT earthquake swarms have documented a ~90° rotation of the *P* axis on volcanoes prior to and during eruptions, due to the propagation or inflation dikes [*Roman and Cashman*, 2006; *Lehto et al.*, 2010]. However, on Nabro we find that the 90° shift is present during the posteruptive episode, while the volcano is subsiding, the NE-SW striking thrust fault is the geological expression of this stress field. We propose that this posteruption rotation observed on Nabro is due to the stress field induced by magma reservoir depressurization [*Vargas-Bracamontes and Neuberg*, 2012]. However, the fault geometry may also be influenced by the geomechanical structure of the caldera as well as changes to the magmatic plumbing system.

The NVR strikes oblique to the Red Sea rift, bisecting the Danakil microplate which is considered a relatively unrifted, coherent block [*McClusky et al.*, 2010; *Hammond et al.*, 2013]. *Hammond et al.* [2013] suggest that a thermal anomaly may be present, and some argue that increased melt production coincides with steep gradients in the lithosphere-asthenosphere boundary [*Holtzman and Kendall*, 2010; *Rychert et al.*, 2012]. However, these arguments do not explain the strike and extension of the NVR as a near continuous lineament from the ARZ to the Red Sea. *Barberi et al.* [1974] hypothesized that the NVR is a transverse structure, which developed through the rejuvenation of tectonically weak zones that proceeded rift formation. The global CMT catalog shows that the majority of magnitude >4 earthquakes along the NVR have strike-slip and normal fault mechanisms. In addition to fault slip and style, the NEIC catalog of earthquakes shows that the NVR is also well delineated by a NE-SW striking alignment of earthquakes. The combination of fault slip style and earthquake locations on a regional scale show that the NVR has a transtensional motion, somewhat consistent with the previous interpretation in *Barberi et al.* [1974]. In addition, all of our focal mechanisms, which we use to constrain the NE-SW thrust fault crossing the caldera floor, have a strike-slip component. The orientation and strike slip could be due to a preexisting structural grain created by regional transverse motions, which was subsequently exploited during subsidence [*Holohan et al.*, 2008]. At Nyamulagira volcano a crosscutting caldera fault has also been observed during intereruptive periods, and it is considered to be a result of regional stresses [*Wadge and Burt*, 2011; *Toombs and Wadge*, 2012; *Wauthier et al.*, 2013b]. However, on Nabro we cannot differentiate between this cause of strike-slip motion and that produced by the caldera collapse itself. Horizontal motions caused by the interactions of numerous faults on the caldera floor can produce oblique slip faults [*Holohan et al.*, 2013]. The global CMT catalog of normal fault mechanisms and presence of volcanoes along the line suggest that the transform motion is accommodated by opening, partly accommodated by magma intrusion. Joint geological and geophysical data therefore show that the NVR may be analogous to a "leaky" transform fault, common on the magma-rich

 ©2014 Crown copyright. Journal of Geophysical Research: Solid Earth published by Wiley Inc. on behalf of American Geophysical Union.

Journal of Geophysical Research: Solid Earth 10.1002/2014JB011395

ocean ridge system [*Gregg et al.*, 2007]. Our interpretation has the implication that the Danakil block may experience internal deformation and may be better approximated as two microplates either side of the NVR.

5. Conclusions

Our InSAR analysis of ascending and descending images, acquired after the eruption by the TSX satellite between 1 July 2011 and 10 October 2012, shows a concentric subsidence signal centered on Nabro's caldera with a maximum rate of 20 cm/year. The InSAR data can be modelled as a Mogi source at a depth of 6.9 $\pm$ 1.1 km. However, this may be an oversimplified model of magma reservoir geometry. We located 658, and relocated 456 earthquakes recorded over a 38 day period beginning on 31 August 2011. From the distribution of seismicity, we observe fracturing of brittle rock above the magma chamber. In conjunction with focal mechanisms, we delineate a major fault plane with a NE-SW strike which dips 45° to the SE, crosscutting the caldera floor. A deep cluster of seismicity suggests a link to a deeper magma source. The *b* value of the earthquakes beneath neighboring Mallahle volcano and the circular subsidence signal centered on Nabro, suggest that there is no subsurface magmatic link between Nabro and Mallahle calderas.

We observe a reverse fault which cuts through the center of the caldera floor and has the same NE-SW strike as the NVR. This mode of subsidence has been referred to as "snap style" [*Holohan et al.*, 2011]. In addition, this fault contains a strike-slip component, which is probably the result of a regional structural grain. The magma reservoir beneath Nabro is deep and this is only the second eruption of an off-rift volcano associated with the ARZ in modern times. We suggest that this is due to a low magma supply rate beneath Nabro in comparison to the volcanic centers on the rift axis. The majority of the subsidence is accounted for by the Mogi model. The seismicity represents minor deformation and is not required to account for the subsidence. Our results show that the posteruption subsidence of the caldera is controlled by the changes associated with the magma reservoir rather than significant slip on caldera ring faults, which were not activated during the post eruption phase that we have studied.

Acknowledgments

We would like to thank the Southern Red Sea Region Administration, Eritrea for support with the seismic deployments. The facilities of SEIS-UK are supported by the Natural Environment Research Council (NERC) under agreement R8/H10/64. Funding was provided by NERC grant NE/J012297/1 and NERC Fellowship NE/I020342/1 to J.O.S.H., and the NERC Centre for the Observation and Modelling of Earthquakes, volcanoes and Tectonics (COMET). Figures were produced using Generic Mapping Tools (GMT) [*Wessel and Smith*, 1998]. J.E.H. is funded through a NERC studentship at the University of Leeds. The seismic data is currently restricted, but will be uploaded to IRIS in October 2015 where it will be open access. TerraSAR-X data were provided under proposal GEO1206. The ascending and descending rate maps are available in .tif format as supporting information Figures S1 and S2. Raw RADAR data can be obtained by proposal from DLR using the website: http://sss.terrasar-x.dlr.de/.

References

Abebe, T., F. Mazzarini, F. Innocenti, and P. Manetti (1998), The Yerer-Tullu wellel volcanotectonic lineament: A transtensional structure in central Ethiopia and the associated magmatic activity, *J. Afr. Earth Sci.*, *26*(1), 135–150.

Acocella, V. (2007), Understanding caldera structure and development: An overview of analogue models compared to natural calderas, *Earth Sci. Rev.*, *85*(3), 125–160.

Amelung, F., C. Oppenheimer, P. Segall, and H. Zebker (2000), Ground deformation near Gada 'Ale volcano, Afar, observed by radar interferometry, *Geophys. Res. Lett.*, *27*(19), 3093–3096.

Anderson, J., and H. Wood (1925), Description and theory of the torsion seismometer, *Bull. Seismol. Soc. Am.*, *15*(1), 1–72.

Aspinall, W., A. Miller, L. Lynch, J. Latchman, R. Stewart, R. White, and J. Power (1998), Soufrière Hills eruption, Montserrat, 1995–1997: Volcanic earthquake locations and fault plane solutions, *Geophys. Res. Lett.*, *25*(18), 3397–3400.

Barberi, F., E. Bonatti, G. Marinelli, and J. Varet (1974), Transverse tectonics during the split of a continent: Data from the Afar rift, *Tectonophysics*, *23*(1), 17–29.

Bender, B. (1983), Maximum likelihood estimation of *b*-values for magnitude grouped data, *Bull. Seismol. Soc. Am.*, *73*(3), 831–851.

Berhe, S. M. (1990), Ophiolites in Northeast and East Africa: Implications for Proterozoic crustal growth, *J. Geol. Soc.*, *147*(1), 41–57.

Biggs, J., T. Wright, Z. Lu, and B. Parsons (2007), Multi-interferogram method for measuring interseismic deformation: Denali fault, Alaska, *Geophys. J. Int.*, *170*(3), 1165–1179.

Biggs, J., I. Bastow, D. Keir, and E. Lewi (2011), Pulses of deformation reveal frequently recurring shallow magmatic activity beneath the Main Ethiopian Rift, *Geochem. Geophys. Geosyst.*, *12*, Q0AB10, doi:10.1029/2011GC003662.

Bluth, G., and S. Carn (2008), Exceptional sulfur degassing from Nyamuragira volcano, 1979–2005, *Int. J. Remote Sens.*, *29*(22), 6667–6685.

Bluth, G. J., S. D. Doiron, C. C. Schnetzler, A. J. Krueger, and L. S. Walter (1992), Global tracking of the SO_2 clouds from the June, 1991 Mount Pinatubo eruptions, *Geophys. Res. Lett.*, *19*(2), 151–154.

Bojanowski, A. (2011), Volcano mix-up, *Nat. Geosci.*, *4*(8), 495–495.

Bosworth, W., M. Strecker, and P. Blisniuk (1992), Integration of east African paleostress and present-day stress data: Implications for continental stress field dynamics, *J. Geophys. Res.*, *97*(B8), 11,851–11,865.

Bosworth, W., P. Huchon, and K. McClay (2005), The Red Sea and Gulf of Aden basins, *J. Afr. Earth. Sci.*, *43*(1), 334–378.

Bridges, D. L., and S. S. Gao (2006), Spatial variation of seismic *b*-values beneath Makushin Volcano, Unalaska Island, Alaska, *Earth Planet. Sci. Lett.*, *245*(1), 408–415.

Brisbourne, A. (2012), How to store and share geophysical data, *Astron. Geophys.*, *53*(4), 19–20.

Chen, Y. J., and J. P. Morgan (1996), The effects of spreading rate, the magma budget, and the geometry of magma emplacement on the axial heat flux at mid-ocean ridges, *J. Geophys. Res.*, *101*(B5), 11,475–11,482.

Clarisse, L., P.-F. Coheur, N. Theys, D. Hurtmans, and C. Clerbaux (2014), The 2011 Nabro eruption, a SO_2 plume height analysis using IASI measurements, *Atmos. Chem. Phys.*, *14*(6), 3095–3111.

Clarke, P., D. Paradissis, P. Briole, P. England, B. Parsons, H. Billiris, G. Veis, and J.-C. Ruegg (1997), Geodetic investigation of the 13 May 1995 Kozani-Grevena (Greece) earthquake, *Geophys. Res. Lett.*, *24*(6), 707–710.

Cole, J., D. Milner, and K. Spinks (2005), Calderas and caldera structures: A review, *Earth Sci. Rev.*, *69*(1), 1–26.

Dzurisin, D., J. M. Donnelly-Nolan, J. R. Evans, and S. R. Walter (1991), Crustal subsidence, seismicity, and structure near Medicine Lake volcano, California, *J. Geophys. Res.*, *96*(B10), 16,319–16,333.

 ©2014 Crown copyright. Journal of Geophysical Research: Solid Earth published by Wiley Inc. on behalf of American Geophysical Union.

Dzurisin, D., M. P. Poland, and R. Bürgmann (2002), Steady subsidence of Medicine Lake volcano, northern California, revealed by repeated leveling surveys, *J. Geophys. Res.*, *107*(B12), 2372, doi:10.1029/2001JB000893.
Ebinger, C. (1989), Tectonic development of the western branch of the East African rift system, *Geol. Soc. Am. Bull.*, *101*(7), 885–903.
Ebinger, C., and M. Casey (2001), Continental breakup in magmatic provinces: An Ethiopian example, *Geology*, *29*(6), 527–530.
Ebinger, C., D. Keir, A. Ayele, E. Calais, T. Wright, M. Belachew, J. Hammond, E. Campbell, and W. Buck (2008), Capturing magma intrusion and faulting processes during continental rupture: Seismicity of the Dabbahu (Afar) rift, *Geophys. J. Int.*, *174*(3), 1138–1152.
Field, L., J. Blundy, R. Brooker, T. Wright, and G. Yirgu (2012), Magma storage conditions beneath Dabbahu Volcano (Ethiopia) constrained by petrology, seismicity and satellite geodesy, *Bull. Volcanol.*, *74*(5), 981–1004.
Gass, I. (1970), The evolution of volcanism in the junction area of the Red Sea, Gulf of Aden and Ethiopian rifts, *Philos. Trans. R. Soc. London, Ser. A*, *267*(1181), 369–381.
Geller, R. J., and C. S. Mueller (1980), Four similar earthquakes in central California, *Geophys. Res. Lett.*, *7*(10), 821–824.
Goitom, B., J. Hammond, M. Kendall, A. Nowacky, D. Keir, C. Oppenheimer, G. Ogubazghi, A. Ayele, S. Ibrahim, and E. Jacques (2014), Pre-, syn- and post eruptive seismicity of the 2011 eruption of Nabro volcano, Eritrea, *EGU General Assembly Conference Abstracts*, *16*, p. 6856, Vienna, Austria.
Goldstein, P., and A. Snoke (2005), SAC availability for the IRIS community, *Incorporated Institutions for Seismology Data Management Center Electronic Newsletter*, *7*.
Gregg, P. M., J. Lin, M. D. Behn, and L. G. Montési (2007), Spreading rate dependence of gravity anomalies along oceanic transform faults, *Nature*, *448*(7150), 183–187.
Gutenberg, B., and C. F. Richter (1944), Frequency of earthquakes in California, *Bull. Seismol. Soc. Am.*, *34*(4), 185–188.
Hammond, J., et al. (2013), Mantle upwelling and initiation of rift segmentation beneath the Afar Depression, *Geology*, *41*(6), 635–638.
Hayward, N., and C. Ebinger (1996), Variations in the along-axis segmentation of the Afar Rift system, *Tectonics*, *15*(2), 244–257.
Hill, D. P. (1977), A model for earthquake swarms, *J. Geophys. Res.*, *82*(8), 1347–1352.
Holohan, E., M. Schöpfer, and J. Walsh (2011), Mechanical and geometric controls on the structural evolution of pit crater and caldera subsidence, *J. Geophys. Res.*, *116*, B07202, doi:10.1029/2010JB008032.
Holohan, E. P., B. van Wyk de Vries, and V. R. Troll (2008), Analogue models of caldera collapse in strike-slip tectonic regimes, *Bull. Volcanol.*, *70*(7), 773–796.
Holohan, E. P., T. R. Walter, M. P. Schöpfer, J. J. Walsh, B. van Wyk de Vries, and V. R. Troll (2013), Origins of oblique-slip faulting during caldera subsidence, *J. Geophys. Res. Solid Earth*, *118*, 1778–1794, doi:10.1002/jgrb.50057.
Holtzman, B. K., and J.-M. Kendall (2010), Organized melt, seismic anisotropy, and plate boundary lubrication, *Geochem. Geophys. Geosyst.*, *11*, Q0AB06, doi:10.1029/2010GC003296.
Hooper, A., F. Prata, and F. Sigmundsson (2012), Remote sensing of volcanic hazards and their precursors, *Proc. IEEE*, *100*(10), 2908–2930.
Illies, J. H. (1981), Mechanism of graben formation, *Tectonophysics*, *73*(1), 249–266.
Jones, R., and R. Stewart (1997), A method for determining significant structures in a cloud of earthquakes, *J. Geophys. Res.*, *102*(B4), 8245–8254.
Kanamori, H. (1977), The energy release in great earthquakes, *J. Geophys. Res.*, *82*(20), 2981–2987.
Kanamori, H., and P. C. Jennings (1978), Determination of local magnitude, ML, from strong-motion accelerograms, *Bull. Seismol. Soc. Am.*, *68*(2), 471–485.
Keir, D., G. Stuart, A. Jackson, and A. Ayele (2006), Local earthquake magnitude scale and seismicity rate for the Ethiopian rift, *Bull. Seismol. Soc. Am.*, *96*(6), 2221–2230.
Keir, D., I. D. Bastow, K. A. Whaler, E. Daly, D. G. Cornwell, and S. Hautot (2009), Lower crustal earthquakes near the Ethiopian rift induced by magmatic processes, *Geochem. Geophys. Geosyst.*, *10*, Q0AB02, doi:10.1029/2009GC002382.
Keir, D., C. Pagli, I. D. Bastow, and A. Ayele (2011), The magma-assisted removal of Arabia in Afar: Evidence from dike injection in the Ethiopian rift captured using InSAR and seismicity, *Tectonics*, *30*, TC2008, doi:10.1029/2010TC002785.
Kennedy, B., J. Stix, J. W. Vallance, Y. Lavallée, and M.-A. Longpré (2004), Controls on caldera structure: Results from analogue sandbox modeling, *Geol. Soc. Am. Bull.*, *116*(5-6), 515–524.
Kiselev, A. (1987), Volcanism of the Baikal rift zone, *Tectonophysics*, *143*(1), 235–244.
Klein, F. (2002), *User's Guide to HYPOINVERSE-2000: A Fortran Program to Solve for Earthquake Locations and Magnitudes*, U.S. Geol. Surv., Menlo Park, Calif.
Lahr, J. (1989), *HYPOELLIPSE/VERSION 2.0*, A Computer Program for Determining Local Earthquake Hypocentral Parameters, Magnitude, and First Motion Pattern*, U.S. Geol. Surv., Menlo Park, Calif.
Lahr, J., B. Chouet, C. Stephens, J. Power, and R. Page (1994), Earthquake classification, location, and error analysis in a volcanic environment: Implications for the magmatic system of the 1989-1990 eruptions at Redoubt Volcano, Alaska, *J. Volcanol. Geotherm. Res.*, *62*(1), 137–152.
Lavallée, Y., J. Stix, B. Kennedy, M. Richer, and M.-A. Longpré (2004), Caldera subsidence in areas of variable topographic relief: Results from analogue modeling, *J. Volcanol. Geotherm. Res.*, *129*(1), 219–236.
Lehto, H. L., D. C. Roman, and S. C. Moran (2010), Temporal changes in stress preceding the 2004–2008 eruption of Mount St. Helens, Washington, *J. Volcanol. Geotherm. Res.*, *198*(1), 129–142.
Lu, Z., T. Masterlark, and D. Dzurisin (2005), Interferometric synthetic aperture radar study of Okmok Volcano, Alaska, 1992–2003: Magma supply dynamics and postemplacement lava flow deformation, *J. Geophys. Res.*, *110*, B02403, doi:10.1029/2004JB003148.
Maccaferri, F., E. Rivalta, D. Keir, and V. Acocella (2014), Off-rift volcanism in rift zones determined by crustal unloading, *Nat. Geosci.*, *7*, 297–300.
Makris, J., and A. Ginzburg (1987), The Afar depression: Transition between continental rifting and sea-floor spreading, *Tectonophysics*, *141*(1), 199–214.
Marti, J., G. Ablay, L. T. Redshaw, and R. Sparks (1994), Experimental studies of collapse calderas, *J. Geol. Soc.*, *151*(6), 919–929.
Massonnet, D., P. Briole, and A. Arnaud (1995), Deflation of Mount Etna monitored by spaceborne radar interferometry, *Nature*, *375*(6532), 567–570.
Masterlark, T. (2007), Magma intrusion and deformation predictions: Sensitivities to the Mogi assumptions, *J. Geophys. Res.*, *112*, B06419, doi:10.1029/2006JB004860.
McClusky, S., et al. (2010), Kinematics of the southern Red Sea–Afar Triple junction and implications for plate dynamics, *Geophys. Res. Lett.*, *37*, L05301, doi:10.1029/2009GL041127.
Morgan, J. P., and Y. J. Chen (1993), Dependence of ridge-axis morphology on magma supply and spreading rate, *Nature*, *364*(6439), 706–708.

 ©2014 Crown copyright. Journal of Geophysical Research: Solid Earth published by Wiley Inc. on behalf of American Geophysical Union.

Nobile, A., C. Pagli, D. Keir, T. J. Wright, A. Ayele, J. Ruch, and V. Acocella (2012), Dike-fault interaction during the 2004 Dallol intrusion at the northern edge of the Erta Ale ridge (Afar, Ethiopia), *Geophys. Res. Lett.*, *39*, L19305, doi:10.1029/2012GL053152.
Okada, Y. (1985), Surface deformation due to shear and tensile faults in a half-space, *Bull. Seismol. Soc. Am.*, *75*(4), 1135–1154.
Pagli, C., T. J. Wright, C. J. Ebinger, S.-H. Yun, J. R. Cann, T. Barnie, and A. Ayele (2012), Shallow axial magma chamber at the slow-spreading Erta Ale Ridge, *Nat. Geosci.*, *5*(4), 284–288.
Pechmann, J. C., and H. Kanamori (1982), Waveforms and spectra of preshocks and aftershocks of the 1979 Imperial Valley, California, earthquake: Evidence for fault heterogeneity?, *J. Geophys. Res.*, *87*(B13), 10,579–10,597.
Purdy, G., L. Kong, G. Christeson, and S. Solomon (1992), Relationship between spreading rate and the seismic structure of mid-ocean ridges, *Nature, 355*, 815–817.
Richter, C. (1935), An instrumental earthquake magnitude scale, *Bull. Seismol. Soc. Am.*, *25*(1), 1–32.
Richter, C. F. (1958), *Elementary Seismology*, p. 578, W. H. Freeman and Co., San Fransisco, Calif.
Roche, O., T. Druitt, and O. Merle (2000), Experimental study of caldera formation, *J. Geophys. Res.*, *105*(B1), 395–416.
Roman, D., J. Neuberg, and R. Luckett (2006), Assessing the likelihood of volcanic eruption through analysis of volcanotectonic earthquake fault–plane solutions, *Earth Planet. Sci. Lett.*, *248*(1), 244–252.
Roman, D. C., and K. V. Cashman (2006), The origin of volcano-tectonic earthquake swarms, *Geology*, *34*(6), 457–460.
Roman, D. C., and M. D. Gardine (2013), Seismological evidence for long-term and rapidly accelerating magma pressurization preceding the 2009 eruption of Redoubt volcano, Alaska, *Earth Planet. Sci. Lett.*, *371*, 226–234.
Rosen, P. A., S. Hensley, G. Peltzer, and M. Simons (2004), Updated repeat orbit interferometry package released, *Eos Trans. AGU*, *85*(5), 47.
Ruch, J., V. Acocella, N. Geshi, A. Nobile, and F. Corbi (2012), Kinematic analysis of vertical collapse on volcanoes using experimental models time series, *J. Geophys. Res.*, *117*, B07301, doi:10.1029/2012JB009229.
Rychert, C. A., J. O. Hammond, N. Harmon, J. M. Kendall, D. Keir, C. Ebinger, I. D. Bastow, A. Ayele, M. Belachew, and G. Stuart (2012), Volcanism in the Afar Rift sustained by decompression melting with minimal plume influence, *Nat. Geosci.*, *5*(6), 406–409.
Sanchez, J., S. McNutt, J. Power, and M. Wyss (2004), Spatial variations in the frequency-magnitude distribution of earthquakes at Mount Pinatubo volcano, *Bull. Seismol. Soc. Am.*, *94*(2), 430–438.
Snoke, J. A. (2003), 85.12 FOCMEC: FOCal MEChanism determinations, *Int. Geophys.*, *81*, 1629–1630.
Solomon, A. (2012), *Summary of Activities of the Southern Red Sea Administration During the Nabro Eruption*, Dep. of Infrastructure of the Southern Red Sea Admin., Assab, Eritrea.
Sturkell, E., F. Sigmundsson, and P. Einarsson (2003), Recent unrest and magma movements at Eyjafjallajökull and Katla volcanoes, Iceland, *J. Geophys. Res.*, *108*(B8), 2369, doi:10.1029/2001JB000917.
Tarasewicz, J., B. Brandsdóttir, R. White, M. Hensch, and B. Thorbjarnardóttir (2012a), Using microearthquakes to track repeated magma intrusions beneath the Eyjafjallajökull stratovolcano, Iceland, *J. Geophys. Res.*, *117*, B00C06, doi:10.1029/2011JB008751.
Tarasewicz, J., R. S. White, A. W. Woods, B. Brandsdóttir, and M. T. Gudmundsson (2012b), Magma mobilization by downward-propagating decompression of the Eyjafjallajökull volcanic plumbing system, *Geophys. Res. Lett.*, *39*, L19309, doi:10.1029/2012GL053518.
Theys, N., et al. (2013), Volcanic SO2 fluxes derived from satellite data: A survey using OMI, GOME-2, IASI and MODIS, *Atmos. Chem. Phys.*, *13*(12), 5945–5968.
Toombs, A., and G. Wadge (2012), Co-eruptive and inter-eruptive surface deformation measured by satellite radar interferometry at Nyamuragira volcano, DR Congo, 1996 to 2010, *J. Volcanol. Geotherm. Res.*, *245*, 98–122.
Umakoshi, K., H. Shimizu, and N. Matsuwo (2001), Volcano-tectonic seismicity at Unzen volcano, Japan, 1985–1999, *J. Volcanol. Geotherm. Res.*, *112*(1), 117–131.
Utsu, T. (1965), A method for determining the value of b in a formula log n = a - bm showing the magnitude-frequency relation for earthquakes, *Geophys. Bull. Hokkaido Univ.*, *13*, 99–103.
Vargas-Bracamontes, D., and J. Neuberg (2012), Interaction between regional and magma-induced stresses and their impact on volcano-tectonic seismicity, *J. Volcanol. Geotherm. Res.*, *243*, 91–96.
Wadge, G., and L. Burt (2011), Stress field control of eruption dynamics at a rift volcano: Nyamuragira, DR Congo, *J. Volcanol. Geotherm. Res.*, *207*(1), 1–15.
Waldhauser, F. (2001), hypoDD–A program to compute double-difference hypocenter locations (hypoDD version 1.0-03/2001), *U.S. Geol. Surv. Open File Rep.*, *01, 113*.
Waldhauser, F., and W. Ellsworth (2000), A double-difference earthquake location algorithm: Method and application to the northern Hayward fault, California, *Bull. Seismol. Soc. Am.*, *90*(6), 1353–1368.
Wang, H., T. J. Wright, Y. Yu, H. Lin, L. Jiang, C. Li, and G. Qiu (2012), InSAR reveals coastal subsidence in the Pearl River Delta, China, *Geophys. J. Int.*, *191*(3), 1119–1128.
Warren, N. W., and G. V. Latham (1970), An experimental study of thermally induced microfracturing and its relation to volcanic seismicity, *J. Geophys. Res.*, *75*(23), 4455–4464.
Wauthier, C., D. C. Roman, and M. P. Poland (2013a), Moderate-magnitude earthquakes induced by magma reservoir inflation at Kīlauea volcano, Hawai'i, *Geophys. Res. Lett.*, *40*, 5366–5370, doi:10.1002/2013GL058082.
Wauthier, C., V. Cayol, M. Poland, F. Kervyn, N. d'Oreye, A. Hooper, S. Samsonov, K. Tiampo, and B. Smets (2013b), Nyamulagira's magma plumbing system inferred from 15 years of InSAR, *Geol. Soc. London Spec. Publ.*, *380*(1), 39–65.
Wessel, P., and W. H. Smith (1998), New, improved version of Generic Mapping Tools released, *Eos Trans. AGU*, *79*(47), 579.
Wiart, P., and C. Oppenheimer (2000), Largest known historical eruption in Africa: Dubbi volcano, Eritrea, 1861, *Geology*, *28*(4), 291–294.
Wiart, P., and C. Oppenheimer (2005), Large magnitude silicic volcanism in north Afar: The Nabro Volcanic Range and Ma'alalta Volcano, *Bull. Volcanol.*, *67*(2), 99–115.
Wright, T., B. Parsons, J. Jackson, M. Haynes, E. Fielding, P. England, and P. Clarke (1999), Source parameters of the 1 October 1995 Dinar (Turkey) earthquake from SAR interferometry and seismic bodywave modelling, *Earth Planet. Sci. Lett.*, *172*(1), 23–37.
Wright, T. J., Z. Lu, and C. Wicks (2003), Source model for the m_w 6.7, 23 October 2002, Nenana Mountain Earthquake (Alaska) from InSAR, *Geophys. Res. Lett.*, *30*(18), 1974, doi:10.1029/2003GL018014.
Wright, T. J., C. Ebinger, J. Biggs, A. Ayele, G. Yirgu, D. Keir, and A. Stork (2006), Magma-maintained rift segmentation at continental rupture in the 2005 Afar dyking episode, *Nature*, *442*(7100), 291–294.

 ©2014 Crown copyright. Journal of Geophysical Research: Solid Earth published by Wiley Inc. on behalf of American Geophysical Union.

Bull Volcanol (2015) 77: 85
DOI 10.1007/s00445-015-0966-3

RESEARCH ARTICLE

First recorded eruption of Nabro volcano, Eritrea, 2011

Berhe Goitom[1,2] · Clive Oppenheimer[3] · James O. S. Hammond[4] · Raphaël Grandin[5] · Talfan Barnie[6] · Amy Donovan[3] · Ghebrebrhan Ogubazghi[2] · Ermias Yohannes[7] · Goitom Kibrom[7] · J- Michael Kendall[1] · Simon A. Carn[8] · David Fee[9] · Christine Sealing[8] · Derek Keir[10] · Atalay Ayele[11] · Jon Blundy[1] · Joanna Hamlyn[12] · Tim Wright[12] · Seife Berhe[13]

Received: 23 March 2015 / Accepted: 10 August 2015 / Published online: 7 September 2015
© The Author(s) 2015. This article is published with open access at Springerlink.com

Abstract We present a synthesis of diverse observations of the first recorded eruption of Nabro volcano, Eritrea, which began on 12 June 2011. While no monitoring of the volcano was in effect at the time, it has been possible to reconstruct the nature and evolution of the eruption through analysis of regional seismological and infrasound data and satellite remote sensing data, supplemented by petrological analysis of erupted products and brief field surveys. The event is notable for the comparative rarity of recorded historical eruptions in the region and of caldera systems in general, for the prodigious quantity of SO_2 emitted into the atmosphere and the significant human impacts that ensued notwithstanding the low population density of the Afar region. It is also relevant in understanding the broader magmatic and tectonic significance of the volcanic massif of which Nabro forms a part and which strikes obliquely to the principal rifting directions in the Red Sea and northern Afar. The whole-rock compositions of the erupted lavas and tephra range from trachybasaltic to trachybasaltic andesite, and crystal-hosted melt inclusions contain up to 3,000 ppm of sulphur by weight. The eruption was preceded by significant seismicity, detected by regional networks of sensors and accompanied by sustained tremor. Substantial infrasound was recorded at distances of hundreds to thousands of kilometres from the vent, beginning at the onset of the eruption and continuing for weeks. Analysis of ground deformation suggests the eruption was fed by a shallow, NW–SE-trending dike, which is consistent with field and satellite observations of vent distributions. Despite lack of prior planning and preparedness for volcanic events in the country, rapid coordination of the emergency response mitigated the human costs of the eruption.

Keywords Nabro · InSAR · Seismicity · Afar · Danakil · Volcano monitoring · Satellite remote sensing

Editorial responsibility: G. Giordano

✉ Berhe Goitom
bg12363@bristol.ac.uk

[1] School of Earth Sciences, University of Bristol, Queens Road, Bristol BS8 1RJ, UK

[2] Department of Earth Sciences, Eritrea Institute of Technology, PO Box 12676, Asmara, Eritrea

[3] Department of Geography, Downing Place, Cambridge CB2 3EN, UK

[4] Department of Earth Science and Engineering, Imperial College, London SW7 2AZ, UK

[5] Institut de Physique du Globe de Paris, Sorbonne Paris Cité, Univ Paris Diderot CNRS, 75005 Paris, France

[6] Laboratoire Magmas et Volcans, Université Blaise Pascal, Clermont Ferrand, France

[7] Department of Mines, Eritrea Geological Surveys, PO Box 272, Asmara, Eritrea

[8] Department of Geological and Mining Engineering and Sciences, Michigan Technological University, 1400 Townsend Dr, Houghton, MI 49931, USA

[9] Wilson Infrasound Observatories, Alaska Volcano Observatory, Geophysical Institute, University of Alaska Fairbanks, Fairbanks, AK, USA

[10] National Oceanography Centre Southampton, University of Southampton, Southampton SO14 3ZH, UK

[11] Institute of Geophysics, Space Science and Astronomy, Addis Ababa University, Addis Ababa, Ethiopia

[12] COMET, School of Earth and Environment, University of Leeds, Leeds, UK

[13] Global Resources Development Consultants, Asmara, Eritrea

Introduction

On 12 June 2011, Nabro volcano was the site of an eruption that had significant societal and environmental consequences. It is the first eruption of Nabro on record. Previously, the only securely recorded historical eruption in Eritrea was that of Dubbi volcano in 1861, located just over 30 km from the Red Sea coast (Wiart and Oppenheimer 2000; Wiart et al. 2000). That event reportedly claimed 175 lives despite the sparse population of the Southern Red Sea region of Eritrea, likely as a result of inundation of settled areas by pyroclastic density currents (Wiart and Oppenheimer 2000). Ash clouds and tephra fall associated with the 1861 eruption also disrupted navigation in the Red Sea.

Nabro volcano, some 25 km southwest from Dubbi, is part of a much larger massif referred to as the Bidu Volcanic Complex (Wiart and Oppenheimer 2005; Fig. 1), which is comprised of two calderas (Nabro and, just across the international border in Ethiopia, Mallahle). Nabro's 2011 eruption began with very little warning—at the time, there were no seismic or other monitoring networks operating in Eritrea. As we show here, seismometers in Ethiopia, Yemen and Djibouti did record seismicity associated with the volcano, but they did not provide information of operational value at the time of the eruption. However, felt earthquakes on the volcano, occurring over several hours before the eruption, did prompt a rapid evacuation of settlements, notably those within Nabro's caldera. This likely saved many lives. Nevertheless, seven people were killed and three others injured during the eruption. About 12,000 people were ultimately displaced and cared for in temporary camps in the region (Solomon 2012).

In broad terms, Nabro is sited in an extensional setting in the geographical area of Afar, close to the Mesozoic crustal block of the Danakil Alps. It reaches a maximum elevation of over 2,200 m above sea level and has an 8-km-wide summit caldera with associated ignimbrites (Wiart and Oppenheimer 2005). The axis of the Bidu Volcanic Massif, i.e. the alignment of volcanic centres, bears NE–SW, in contrast to the NW–SE trend of the Red Sea and axial volcanic ranges in northern Afar. The Nabro eruption occurred during a period of apparently heightened tectonic and volcanic activity in the Afar/Red Sea region (Yirgu et al. 2014; Jónsson and Xu 2015), which began with the Manda Hararo rifting episode and Dabbahu eruption in Ethiopia (in 2005; e.g. Grandin et al. 2009). Further, there have been eruptions of Dalaffilla (in 2008; Keir et al. 2013) and Erta 'Ale (2010; Field et al. 2012) on the Erta 'Ale range in Ethiopia and Jebel al Tair (2007) and Zubair (2011–13) in the southern Red Sea (Xu et al. 2015).

The 2011 Nabro eruption began shortly before midnight local time on 12 June following several hours of ground shaking. The preceding and accompanying seismicity is the first of note in global catalogues for this part of Afar. Remarkably, the eruption produced the largest stratospheric aerosol perturbation since the 1991 Pinatubo eruption (Fromm et al. 2014). This reflected the substantial SO_2 yield, estimated at around 4.5 Tg for the first 15 days of the eruption by Theys et al. (2013), and penetration of the plume into the lower stratosphere (Fromm et al. 2014; Clarisse et al. 2014). It has been argued that Nabro's is one of a number of eruptions in the twenty-first century to have had a detectable effect on near-global troposphere temperature, sea surface temperature and precipitation, thereby contributing to the apparent 'hiatus' in tropospheric warming since 1998 (Santer et al 2015).

We present here a preliminary synthesis of the nature and mechanisms of the eruption based on multiple observations, obtained via means of satellite remote sensing, regional seismic and infrasound data, fieldwork and petrology. In particular, we aim to reach a first-order characterisation of the eruption in respect of the geometries and kinematics of associated intrusive activity, the compositions of lavas and tephra, the regional context of extensional tectonics and the hazards and humanitarian response. We hope to stimulate further work on the eruption and, more widely, on volcanism in the region. Our study is also relevant to any future work that might consider the geothermal potential of Nabro volcano.

Methods

We outline here the principal datasets and techniques used in this multi-disciplinary study. In addition to those described below, we have incorporated datasets obtained from operational Ozone Monitoring Instrument (OMI) SO_2 retrievals (Yang et al. 2007; Sealing 2013) and a Comprehensive Nuclear Test-Ban Treaty Organisation (CTBTO) infrasound station (IS32) in Nairobi, 1,708 km from Nabro (Fee et al. 2013). Additionally, we report in the Overview of the petrology of the 2011 lavas and tephra section a digest of conventional XRF analyses of the whole-rock compositions of samples of lava and tephra erupted at Nabro in 2011.

Seismology

At the time of the eruption of Nabro in 2011, there were no operational seismometers in Eritrea (triggered permanent stations in the country were out of service) nor was there any routine surveillance of the volcano. The first broadband instruments in the country were deployed (serendipitously) on 23 June 2011, 11 days after the eruption began. This deployment of six sensors was supported by a collaborative project between several of the authors, with the aim of studying regional mantle structure (Hammond et al. 2013). Fortunately, in the months preceding the eruption, seismometers were operating elsewhere in Afar, and we obtained data from ten stations in Ethiopia (Hammond et al. 2013; Barnie et al. 2015b), eight in Djibouti (for which we received arrival time picks) and one in

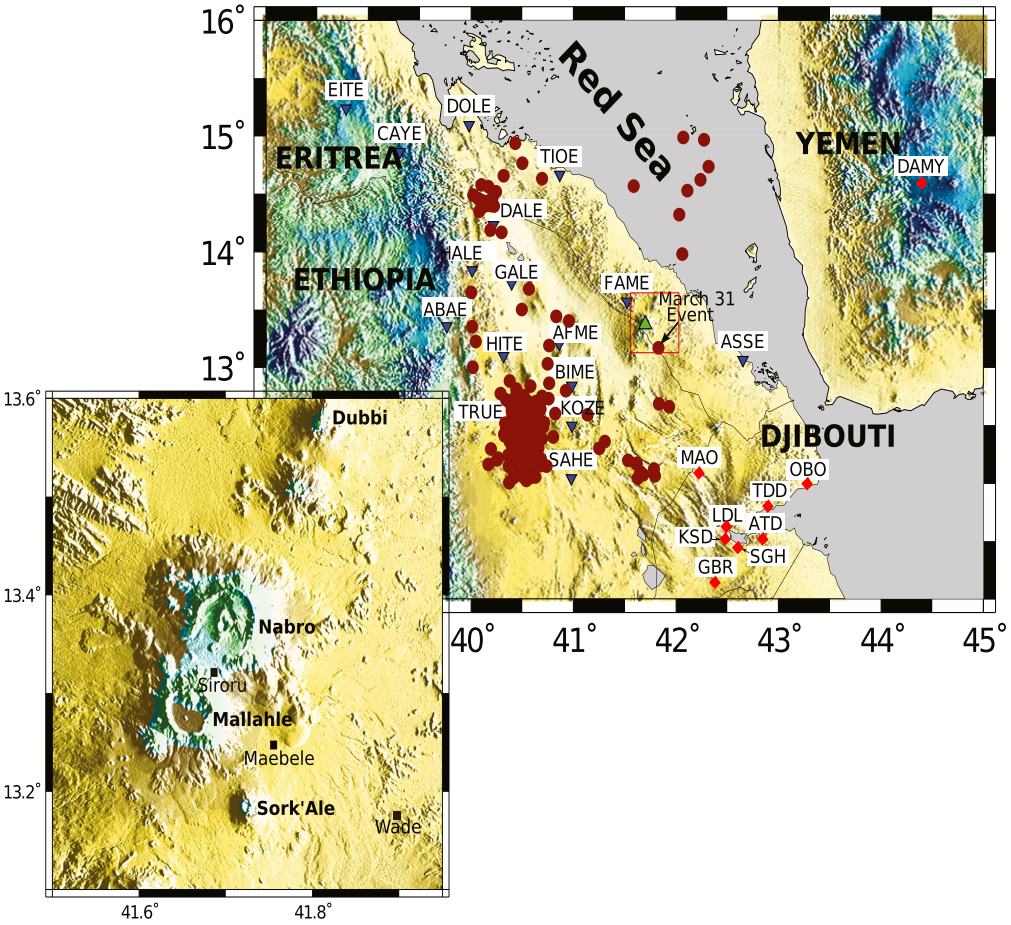

Fig. 1 Seismic stations used in our study (*inverted blue triangles* and *red diamonds* indicate temporary and permanent stations, respectively) and regional seismicity (*red dots*) from the USGS catalogue for the period 1960–2011. The *green triangle* locates Nabro. *Inset map* shows the volcanoes in the Bidu Volcanic Complex (coverage of the *red box* in the larger map)

Yemen. Combined, the data from these networks enable us to characterise the seismicity before, during and after the Nabro eruption (Fig. 1). We focus our analysis on events spanning the period from 23 February to 17 September 2011 (3.5 months before the eruption to 3 months after). We note that in August 2011, eight broadband stations were deployed around the volcano (Hamlyn et al. 2014). These provided a valuable 14-month dataset that is especially suited to studies of the relaxation of the system after the eruption. We did not include these data in the present analysis.

We used HYPOINVERSE-2000 (Klein 2002) to locate events from measurements of P- and S-wave arrival times, drawing on a 1D velocity model previously used for investigations in the Afar region (Keir et al. 2009). This model is based on the crustal structure deduced from wide-angle controlled-source seismology (Makris and Ginzburg 1987). We located earthquakes using a minimum of five stations. Typical horizontal errors are <10 km, but depths are only poorly constrained. When we added data from the more proximal Eritrean stations (available from 23 June 2011), errors are reduced, but locations are systematically shifted ~2 km to the NE. We also relocated events by double-difference methods (Waldhauser and Ellsworth 2000), reducing relative location errors (relative to the master event errors) to between 2 and 50 m, with only six events having relative location errors exceeding 20 m. Local magnitudes were calculated using amplitudes measured on the horizontal components of simulated Wood Anderson displacement seismographs and the distance correction for the Main Ethiopian rift (Keir et al. 2006, 2011). Seismic moment release was estimated using empirical relationships between M_L, m_b and M_o (e.g. Kanamori, 1977; Scordilis 2006) as previously applied in a study of Dallol volcano (Nobile et al. 2012). We used Real-time Seismic Amplitude Measurement (RSAM) to follow

temporal changes in seismicity (Endo and Murray 1991). This was calculated from average amplitude of a 10-min moving window for the vertical component at selected stations.

Spaceborne synthetic aperture radar imagery

Data

We have analysed spaceborne synthetic aperture radar (SAR) imagery to characterise surface changes associated with the Nabro eruption. We examined backscatter images acquired through time to track the evolution of lava flows and tephra deposits, and of large-scale topographic changes, and to measure surface motion based on interferometric processing and image correlation. Data were acquired from the X-band SAR sensors TerraSAR-X (operated by DLR) and COSMO-SkyMed (operated by ASI). The satellites provide SAR images with nominal spatial resolutions of 2 m for TerraSAR-X ('Stripmap mode') and about 1 m for COSMO-SkyMed ('Spotlight' mode).

Our differential analyses require identical acquisition geometry for the SAR images, to avoid geometric distortions and artefacts arising from differences in illumination directions. Pairwise combinations are thus restricted to intervals of 11 days for TerraSAR-X and 9 days for COSMO-SkyMed.

Mapping volcanic deposits

X-band SAR images can map geological structures down to the decametric scale. However, geometric distortions associated with complex topography complicate their interpretation. At large scale (from tens of pixels across), the average amplitude of the SAR images is mostly sensitive to the local illumination angle and therefore to slope. Due to the inclined line-of-sight direction of SAR images (usually about 30° from the vertical), systematic geometric distortions and radiometric variations are evident in scenes with topographic relief: while slopes facing towards the sensor appear bright and compressed, slopes inclined away from the satellite are darker and stretched. SAR amplitude images thus provide a qualitative characterisation of topographic changes (Fig. 2).

At the pixel scale, SAR amplitude also depends on backscattering characteristics of the surface. The latter are determined by the dielectric properties of the surface and surface roughness at the scale of the radar wavelength (about 1 cm in our case). We differentiated the SAR amplitude images acquired before and after the eruption to identify the location and nature of deposits (Fig. 2). The newly emplaced lava flows generally appear bright, likely due to high surface roughness. In contrast, decreased backscattered amplitude indicates 'smoothing' of the topography by tephra deposits. A significant decrease of the SAR amplitude can be seen in a 20×20-km^2 area to the SW of Nabro.

Ground deformation analysis

We have analysed ground deformation associated with the eruption in two ways. First, the line-of-sight component of ground displacement is retrieved via interferometric SAR (InSAR) analysis of pairs of SAR images spanning the eruption. We used the NSBAS software, a modified version of ROI_PAC adapted to processing of time series SAR images (Rosen et al. 2004; Doin et al. 2011). The InSAR method requires preservation of surface properties of the ground—it thus fails where tephra deposits or lava flows have accumulated between image pairs. Thus, we only obtain meaningful InSAR measurements beyond Nabro's caldera rim. InSAR is sensitive only to the component of ground motion that is directed towards or away from the satellite, in the line-of-sight (LOS) direction, about 30° from nadir. Accordingly, we computed interferograms on descending and ascending overpasses (looking from ESE and WSW, respectively) to evaluate the importance of horizontal and vertical components of ground motion (Fig. 3). For SAR data captured after the eruption began, we selected scenes that were acquired within a short time of each other to ensure that the InSAR pairs captured comparable deformation fields. We focus here on two pairs of SAR images acquired by TerraSAR-X: 11 June 2010 and 1 July 2011 for the descending pass and 14 May 2010 and 6 July 2011 for the ascending pass. An analysis of ground deformation spanning the period July 2011 to September 2012 (after the main phase of the eruption) is provided by Hamlyn et al. (2014).

In addition to InSAR, we performed a sub-pixel correlation of SAR amplitude images using the 'ampcor' routine of ROI_PAC (Fig. 3). This resolves two components of the ground motion along the native coordinates of the SAR images: horizontal motion along the satellite track (the 'azimuth offset') and motion towards or away from the satellite LOS, in the slant direction (the 'range offset'). Displacements exceeding around 10 % of the pixel size can be resolved with this method, yielding a detection threshold of 10–20 cm, suitable for measuring large deformation (Grandin et al. 2009). The component of displacement sensed by sub-pixel correlation in the slant range direction is the same as for InSAR but does not saturate in zones of large deformation. Furthermore, in contrast to InSAR, sub-pixel correlation can provide meaningful measurements in tephra-covered areas so long as underlying landforms are still apparent. However, it is difficult to distinguish actual motion from apparent motion due to the addition of material at the surface. Such spurious effects are likely to particularly contaminate the range offsets, as the slant range component is nearly vertical. This should only suggest apparent uplift. In contrast, azimuth (horizontal) offsets, when measurable, should be little biased by resurfacing by tephra deposits.

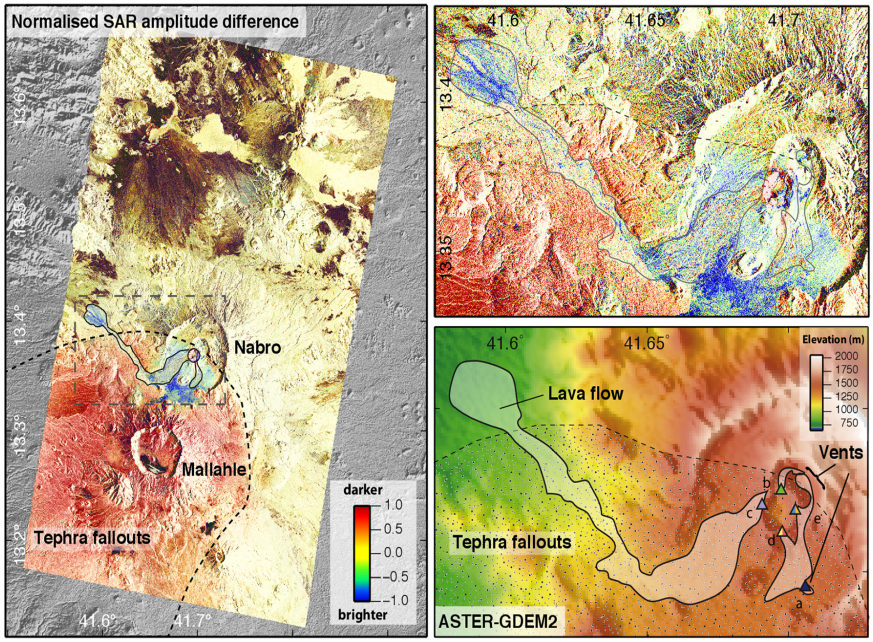

Fig. 2 *Left panel* shows a differential analysis of backscattered SAR amplitude for the Nabro area based on analysis of two TerraSAR-X scenes from 11 June 2010 (pre-eruption) and 1 July 2011. The normalised difference of the amplitude images is computed using the formula: Delta_amp=2×(amp_1−amp_2)/(amp_1+amp_2). *Red areas* indicate decreased SAR amplitude and topographic smoothing (at the cm scale), while *blue areas* correspond to increased SAR amplitude and increased surface roughness. The *upper-right panel* shows the Nabro caldera and 2011 lava flow. The *lower-right panel* shows the corresponding topography. *Coloured triangles* indicate different generations of eruptive vents identified from time series analysis of SAR and thermal imagery (Fig. 10)

Finally, using two satellite overpass directions (ascending and descending), four independent components of the ground motion can be resolved (motion in the slant range direction is determined simultaneously by InSAR and sub-pixel correlation). These four independent components permit, after solving an over-determined set of linear equations for each pixel, retrieval of the east–west, north–south and up–down components of ground displacement (Fig. 4).

Satellite optical imagery

We use satellite images from several sources to track the eruption by its thermal emissions and geomorphologic changes on the ground. These include the following four instruments: the Spinning Enhanced Visible and Infrared Imager (SEVIRI), a multispectral imager aboard Eumetsat's Meteosat geostationary weather satellites; the Moderate-resolution imaging spectroradiometer (MODIS), a multispectral imager aboard NASA's Aqua and Terra satellites; the Advanced Very High-Resolution Radiometer (AVHRR), another multispectral imager aboard various NASA and Eumetsat satellites; and the Advanced Land Imager (ALI), aboard NASA's Earth Observing 1 (EO-1) satellite. SEVIRI has a spatial resolution of about 3 km at nadir, with 96 acquisitions per day; MODIS has a spatial resolution of 1 km at nadir with approximately four acquisitions per day; AVHRR has a spatial resolution of 1 km with a few acquisitions per day; and ALI has a spatial resolution of 30 m with acquisitions typically every few days to weeks when tasked to view an event, either manually or automatically.

We interpret the MODIS, AVHRR and ALI images visually. They contain useful spatial information but are acquired infrequently. In contrast, the SEVIRI images enable near-continuous monitoring albeit at comparatively coarse spatial resolution. We extract the volcanogenic thermal signal from the SEVIRI dataset following Barnie and Oppenheimer (2015a) as follows. Independent component analysis (ICA) is applied to the time series of radiances associated with each non-saturated band 4 (3.9 μm) pixel, in a 9×9 pixel widow surrounding the eruption, to find statistically independent contributing sources. The magnitude of the contribution of each source to each pixel is found, again excluding saturated hotspots. Volcanic sources are identified by a high temperature event (HTE) threshold (the product of the absolute skewness of the source and per-pixel contributions). The per-pixel volcanogenic radiances are then found by summing the outer product of the source and contributions for all sources above the threshold. In this way, the image cube is decomposed into

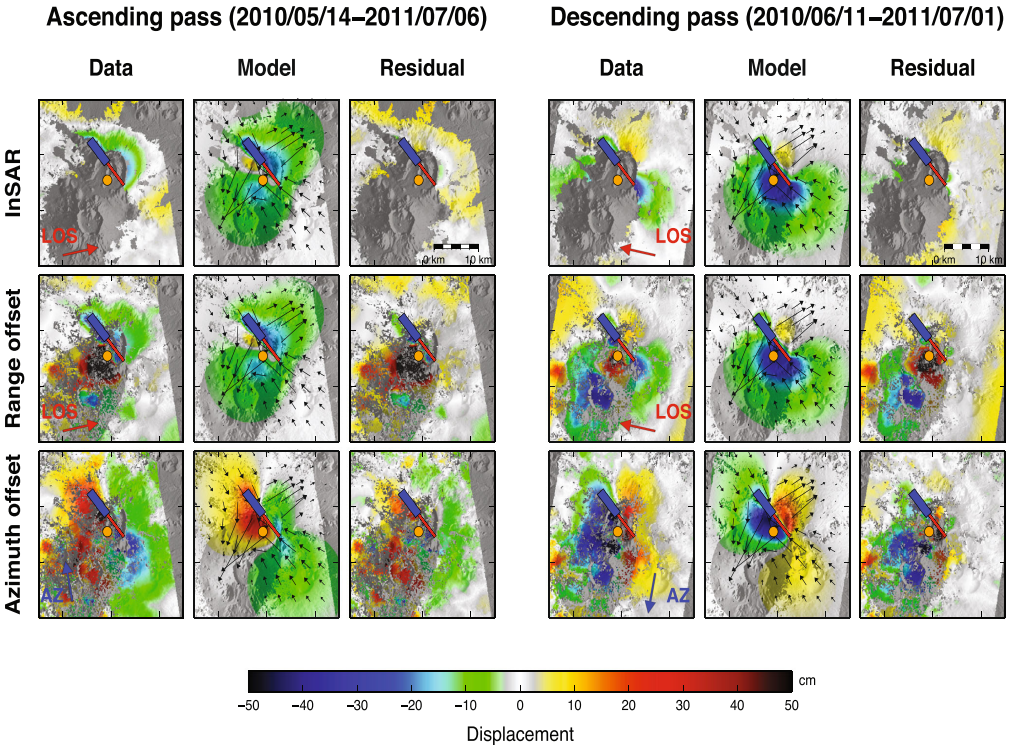

Fig. 3 Comparison of observed (*Data*), predicted (*Model*) and residual (*Residual*) deformation for the various components of ground motion deduced from ascending (*left panel*) and descending (*right panel*) SAR data. The *top row* corresponds to InSAR, the *middle row* to range offsets and the *lower row* to azimuth offsets. The *thick-coloured arrows* show the direction of sensed ground displacement: *red* for line-of-sight (LOS) and *blue* for along-track (AZ). InSAR and range offsets are sensitive to motion only in the LOS direction. The LOS vector makes an angle of 29° with the vertical for the ascending pass (34° for the descending pass). For clarity, only the horizontal component of the LOS vector is shown by the *red arrow*. In contrast, azimuth offsets only provide information on the horizontal component of ground motion in the direction of the satellite track (AZ). In each panel, motion in the direction indicated by the *thick-coloured arrow* has negative sign (*cool hues*), whereas motion in the opposite direction has positive sign (*warm hues*). Note the colour scale is common to all components. *Thin arrows* represent the modelled horizontal component of ground motion derived from the elastic inversion. The *shaded area* SW of Nabro received substantial tephra fallout and was excluded in the inversion. The *blue rectangle* represents the surface projection of the normal fault deduced from the model (Fig. 14). The *red rectangle* shows the surface projection of the dike, and the *orange circle* the surface projection of the pressure source. See Fig. 12 for a perspective view

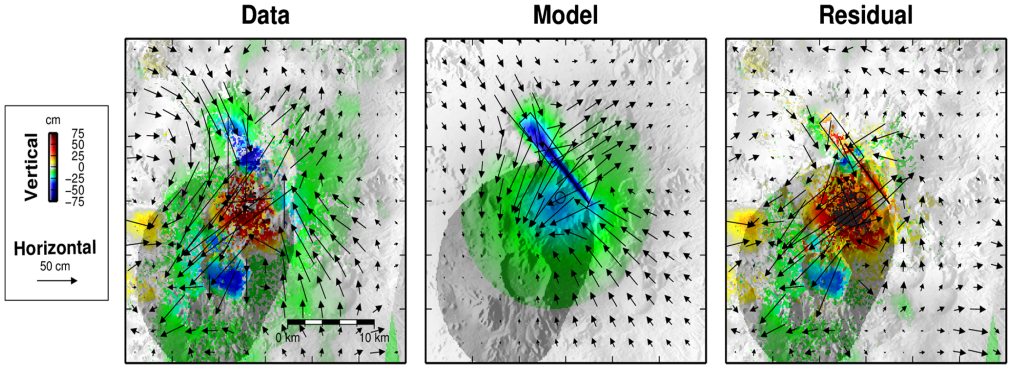

Fig. 4 As preceding figure but for ground motion resolved in east–west, north–south and up–down components. The *left panel* corresponds to a reconstruction of the 3D components of ground motion by combining the six available components of ground motion, among which only four yield independent directions. The *colours* represent the vertical displacement, while *arrows* indicate the horizontal component

a number of radiance sources, the non-volcanic sources excluded, and the image cube reassembled with only non-saturated volcanic sources. For events with many saturated pixels, the correction may underestimate the true radiance but not as substantially as the truncated saturated values. Estimating the contribution of cloud contamination to any given pixel is challenging, and interpretations of the time series are necessarily qualitative: for instance, a drop in radiance could result from either occlusion of hot material or declining lava effusion. We note also that the vent and lava flow were frequently obscured by the volcanic plume.

Fieldwork

Fieldwork was conducted between 8 and 15 October 2011 by a subset of the authors (BG, CO, JOSH, EY and GK), based first at Afambo and later at Wade. Given the limited time, the extent of the lava flow fields and tephra fall, and the proximity of the international border, a comprehensive sampling strategy was impractical. However, lavas and tephra were sampled over a wide area within and beyond the caldera.

Meaningful estimates of lava flow thicknesses were not possible given the dimensions of the flow field. The flow surfaces were well above ambient temperatures in places and were still emitting fumes. The longest flow, which had travelled beyond the caldera, had overrun cultivated and settled areas. It was sampled towards its front. The vent region was approached from the northern part of the caldera. Within the caldera, three shorter flows were sampled.

A second field mission was conducted in October 2012 to decommission the temporary seismic network. It afforded time for a reconnaissance of the vent region from the southern part of the caldera. The two missions provide some relevant observations but were not focused on obtaining specific ground truth with which to validate interpretations based on our analysis of satellite and other monitoring data.

The eruption: observations and models

In this section, we report key observations (seismology, satellite remote sensing and ground surveys) and explanatory models for intrusive and eruptive processes involved in the 2011 eruption.

Seismicity

The area around Nabro has hitherto appeared to be seismically quiet. No major earthquake was reported by international or regional centres (USGS or ISC) prior to the eruption, with the exception of a 4.5-M_W event on 31 March 2011 (i.e. just over 10 weeks before the eruption). This was the first earthquake ever reported by the USGS for the area (Fig. 1). The epicentral coordinates given by the USGS for this event are 13.17° N, 41.83° E (horizontal error>20 km), i.e. about 25 km southeast of Nabro, with an origin time of 18:33:38 UTC.

On 15 May 2011, a scientific team from Asmara visited the area (Ogubazghi et al. 2014) to investigate the effects of this earthquake and to interview eyewitnesses. It was found that most houses within the Nabro caldera were damaged, with the severity ranging from cracked walls to partial collapse (Fig. 5). The event had also induced landslides and, according to local people, killed many domesticated animals including sheep and goats. Small tensional cracks were still present on the ground (Ogubazghi et al. 2014). The length of these cracks reached up to 10 m but, reportedly, they had extended several tens of metres immediately after the event. The cracks trended NNW–SSE, parallel to the direction of plate opening determined from plate kinematic and moment tensor analyses (e.g. McClusky et al. 2010).

While residents of Siroru, a village situated on the southwest floor of Nabro's caldera, clearly felt the shaking, people in the vicinity of Maebele and Wade (close to the USGS-located epicentre) were not awoken by the event. Moreover, damaged houses were observed around Siroru but not in Wade or Maebele. A maximum intensity of VII was estimated for the Siroru area and of less than IV in Wade and Maebele (Ogubazghi et al. 2014). Based on these observations, the epicentre was relocated to 13.33° N, 41.68° E, placing it within the caldera (Ogubazghi et al. 2014). This is close to our relocation of the earthquake, using data from the stations in Ethiopia and Djibouti, to 13.35° N, 41.69° E (horizontal error of ±1.2 km), with a magnitude M_L 4.8 and time of 18:33:37 UTC on 31 March 2011 (yellow star in Fig. 6a).

From analysis of the regional data, we detected just six other events in the Nabro region before 12 June, with M_L ranging between 2.8 and 3.9. We did not identify any earthquakes in the days preceding the eruption (the last one was on 29 May) earthquakes with magnitudes below our detection threshold of $M_L \sim 2.1$ may well have occurred.

The eruption was preceded by 5 h of earthquake swarms, with the first event at 15.37 UTC on 12 June 2011. Two further notable events occurred at 20:32 and 21:03 UTC, the earlier of the two likely very close to the onset of the eruption (Fig. 7).

The most seismically active days were 12 and 17 June, with 79 events (>M_L 2.0) on 12 June and 28 events on 17 June (totalling 55 % of the recorded events). Local magnitudes during this period vary between M_L 2.7 to 5.9, with ten events exceeding M_L 5. The largest event (M_L 5.9) occurred on 17 June; the second largest, at M_L 5.8, took place on 12 June. On 12 June, seismicity occurred beneath both Nabro and Mallahle volcanoes. In contrast, on 17 June, while there was little seismicity at Nabro, Mallahle remained seismically active (Fig. 6b). This suggests a linkage between the two volcanoes, either via their magmatic systems or associated with stress

field changes. This shift in seismicity to the SW precedes the availability of data from the Eritrean stations, so it is not an artefact of changing station coverage. Mallahle remained seismically active in the months after the eruption, as seen from analysis of data from the local seismic network installed in August 2011 (Hamlyn et al. 2014).

While only ten earthquakes were recorded between 12 and 17 June, RSAM analysis of seismograms from the regional stations indicates sustained tremor (Fig. 8a). Spectrograms for the closest stations, KOZE and FAME, reveal a signal dominated by energy at frequency bands <2 Hz (Fig. 8b). The tremor was very high on the first day of the eruption but reduced during the next 2 days. On 16 June, the tremor almost stopped, but it picked up abruptly with the onset of a second period of intense seismicity on 17 June. After this, tremor persisted until 14 July with many fluctuations (Fig. 8c). The tremor was observed at many stations with different azimuths precluding interpretation of the observed signal as a path effect (e.g. Cote et al. 2010). For the period 18 June to 17 September, we located 93 events (43 % of the total events in our analysis). Events were detected on most days, with 3 days marked by earthquakes sized $>M_L$ 4.

Looking at the double-difference relative locations, we identify a NE–SW trend (i.e. parallel to the Nabro-Mallahle axis) in epicentres beneath Mallahle on 17 June (Fig. 6b). In contrast, after 17 June, the distribution of epicentres on Mallahle follows more of a NW–SE (Red Sea) trend (stretching as far as Sork 'Ale volcano; Fig. 6c).

Observations from spaceborne optical and SAR imagers

The Nabro caldera is up to 8 km across (north to south). In its elevated centre, prior to the 2011 eruption, there were two craters, one about 400 m deep and 2 km across and the other, partly recessed into its SW rim, up to 1.4 km across and over 200 m deep. This smaller crater, whose floor was about 100 m deeper than its neighbour and which we refer to as the SW pit, proved to be the main focus of the 2011 eruption. On its floor were the remnants of a small low-aspect-ratio crater about 140 m across. The inner walls of the SW pit, especially on its east side, were draped with what appear from satellite images to have been scoriaceous lavas, perhaps resulting from drain-back of lava. These lavas are less evident on the western wall of the SW pit, which showed signs of substantial hydrothermal alteration.

The time series of SEVIRI images indicates that the eruption started between 20:27 and 20:42 UTC on 12 June, i.e. shortly before midnight local time as confirmed by eyewitnesses. This is evident in Fig. 9a, b, which shows a measure of thermal radiation for two pixels, one representing the final lava flow front and the other the vent region inside the caldera. The signal is 'spiky' due to the intermittent presence of thick plume and cloud that obscure the hot material at the surface. Figure 9c shows the first SEVIRI image to register the eruption, showing an incipient thermal anomaly and plume, placing eruption onset between the time of acquisition of this image and its predecessor (20:42 and 20:27 UTC, respectively). While the SEVIRI images usefully reveal the structure and dispersal of the plume, the thermal anomalies on the ground are obscured until 15 June.

The first high-spatial resolution image we have is an ALI scene acquired at 07:32 UTC on 14 June, i.e. about 35 h after the start of the eruption. A plume rich in condensed steam drifts to the west. It covers most of the caldera, hiding the vent area from view. The next spatially detailed scene, a COSMO-SkyMed SAR image acquired on 18 June, 5 days after the eruption onset, reveals substantial changes compared with a pre-eruption scene—(i) the innermost pit crater has been largely infilled by a tephra cone, (ii) several lava flows have issued from points on and around this cone, (iii) the longest of these flows has breached the open SW margin of the caldera and then travelled NW and (iv) a discontinuous alignment of small pits has opened up along a NW–SE trend, reaching about 2 km from the vent region. Inspection of the pre-eruption topography indicates that the main lava flow (labelled (*c*) in Fig. 10) was sourced at the lowest point on the SW pit rim (about 1,515 m above sea level), on its western side.

To follow events of the first days of the eruption, we have to turn to lower-spatial resolution sensors including MODIS and AVHRR. Figure 9d shows thermal images from these instruments covering the period from 14 to 17 June. The interval can be subdivided into three periods. In period 1, the plume dominates the SEVIRI signal, and the MODIS/AVHRR images show a small thermal anomaly confined to the crater. In period 2, the plume margins develop thermal anomalies at 3.9 μm, which could be due to forward scattering of infrared radiation from the advancing lava flow. Minor

Fig. 5 Building damaged by the 31 March 2011 earthquake. Better constructed walls, as seen in the background, sustained only cracking

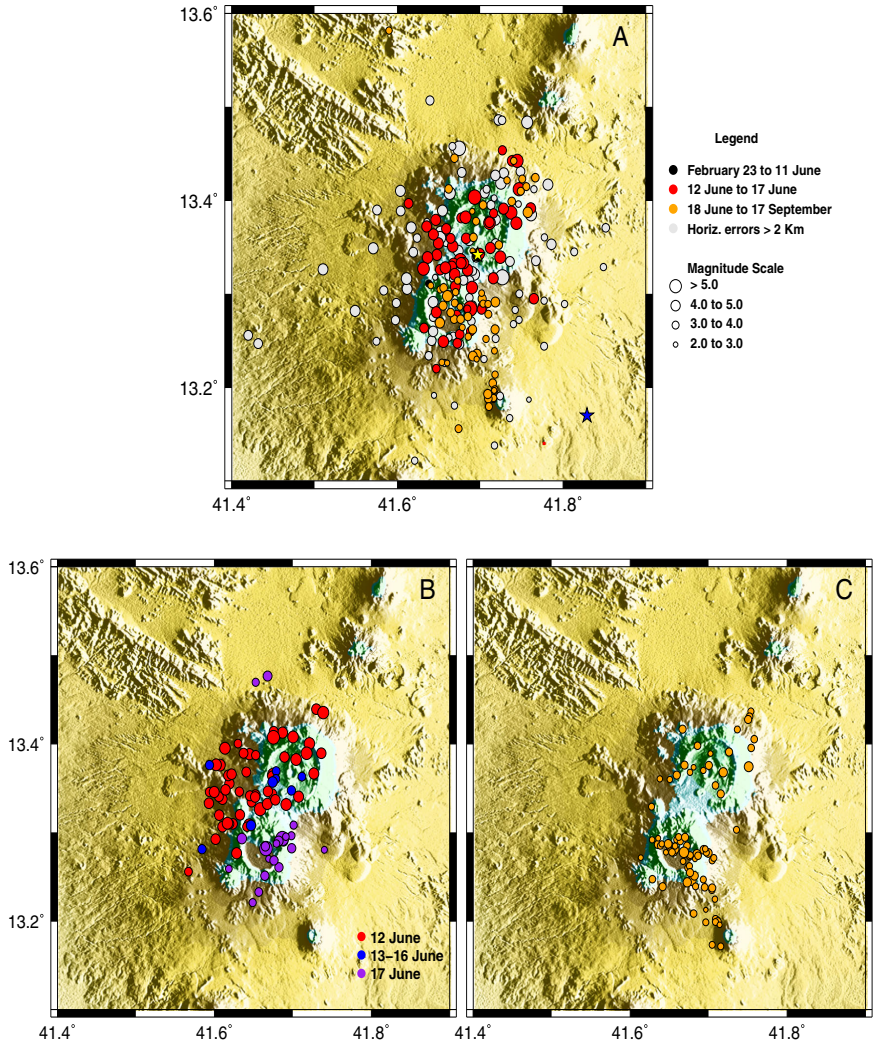

Fig. 6 **a** Seismicity around Nabro for the period 23 February to 17 September 2011. Locations for the 31 March event are shown by the *blue star* (USGS location based on distant stations of the Global Seismic Network) and *yellow star* (our location based on stations in Ethiopia and Djibouti). *Colour codes* display temporal evolution, events with horizontal errors exceeding 2 km are *coloured grey* and symbol size represents magnitude (M_L) classes (see legend). Plots (**b**) and (**c**) show double-difference relative locations for events occurring between 12 and 17 June and between 18 June and 17 September 2011, respectively

thermal anomalies are also registered in the lava flow front pixel indicating that it had covered most of the distance by the evening of 15 June. During period 3 (from the evening of 16 June), the plume has weakened, revealing the thermal anomaly at the vent and showing the lava flow has reached its maximum length by this point.

Returning to the high-spatial resolution imagery, we have two more SAR scenes acquired on 20 and 21 June before the next optical images from ALI were recorded (Fig. 9e). Dramatic topographic changes occurred in the vicinity of Nabro's former SW crater. As a result, images acquired syn- or post-eruption that are geo-coded with a pre-eruption DEM are severely distorted in this area (see Fig. 2). Therefore, we analyse changes in the native geometry of the SAR system. The alternating ascending and descending passes of the satellite further complicate this comparison (successive passes in the same direction are acquired every 11 days by TerraSAR-X). The most prominent change apparent in SAR imagery is the complete filling of the SW crater, already seen in the first image acquired after the eruption onset (20 June). Several new scoria cones are also identified. We calculate that the SW pit was filled from 1,350 m elevation (pre-eruptive crater floor) to

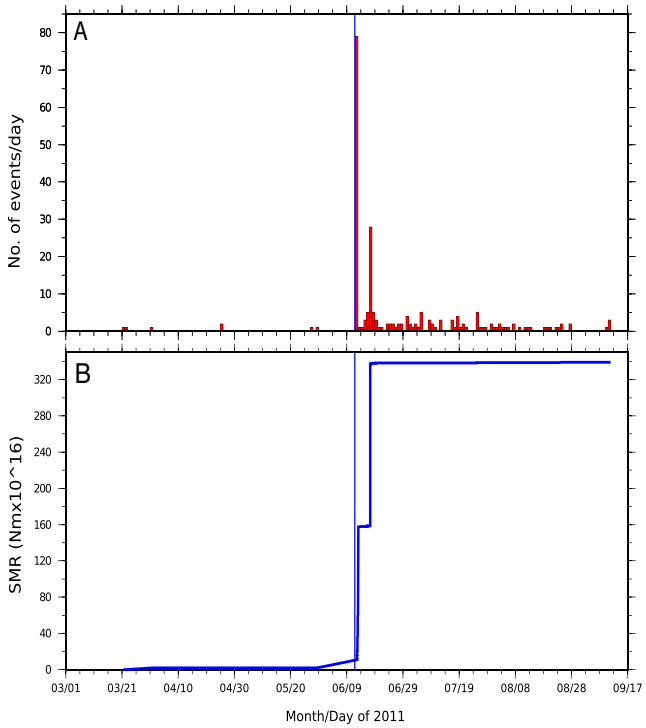

Fig. 7 Time series of **a** daily totals of seismic events located using the Ethiopian and Djibouti stations and **b** corresponding seismic moment release (SMR)

at least 1,550 m elevation (highest altitude of overflow of the crater rim), requiring a volume of lava and tephra exceeding 0.1 km^3.

The ALI scenes acquired between 07:18 UTC on 24 June and 07:27 UTC on 2 July are quite spectacular (Fig. 9e), notably in the shortwave infrared (SWIR) channels. These indicate intense thermal radiation around the vent area located close to the highest point on the SW crater (on its NNE rim) and along a number of lava flows. In all these images, the source of the main lava flow remains 'hot' in SWIR channels, though the intensity of the anomaly has diminished by 29 June. The front of this flow appears still active on 24 June. Video taken by one of us (SB) near the flow front reveals widespread exposure of incandescent lava along the flow margins, in addition to flames leaping from engulfed trees. The strong thermal anomaly centred on the new tephra cone is suggestive of a perched lava lake filling a flared vent.

The main lava flow (labelled (*c*) in Fig. 10) initially travelled SW from the vent region until reaching the breached part of the horseshoe-shaped caldera. At this point, it turned NW, reaching an overall flow length of about 17.5 km. In addition, both SAR images and ALI infrared scenes reveal successive generations of smaller lava flows emplaced to the S, E and N of the vent region. With the exception of a short lava flow fed from a series of aligned vents to the SW of the old crater (flow (*a*) in Fig. 10), all these lava flows appear to originate from four distinct sources at the four cardinal points of the SW pit (flows (*b*), (*c*), (*d*), (*e*) in Fig. 10). The first lava flows were sourced at points around the W (*c*), N (*b*) and S ((*a*) and (*d*)) rims of the SW crater. Vents located to the north of the rim ((*b*) and (*e*)) sourced lava flows that were confined to a pre-existing pit crater. Lava supply from vent (*b*) had ceased by 20 June. In contrast, the flows emitted by vent (*d*) were emplaced in two phases: a short flow was emitted before 20 June and was subsequently covered by a longer flow that remained active until at least 1 July. Finally, onset of effusive activity at vent (*e*) seems to have occurred after 20 June and continued until at least 12 July. We note that vent (*c*), which sourced the main lava flow, marked the lowest point of the pre-existing crater rim (1,515 m elevation). Vent (*e*), the second longest-lived, was located at 1,525 m elevation; vent (*d*), the third longest-lived, at 1,545 m elevation; and vent (*b*) stands at an altitude of 1,585 m. This pattern may suggest a progressive lowering of the magma column.

It is not until 29 June, when there remains only a weak ashy plume drifting to the south, that the ground surface south and southeast of the tephra cone becomes unobscured. A smaller lava flow has advanced east from the SW pit rim and then diverged with one branch heading north where it ponded in the adjacent crater and another moving south down the flank of intracaldera edifice. High temperatures are evident along levées of the main lava flow, where incandescent lava was

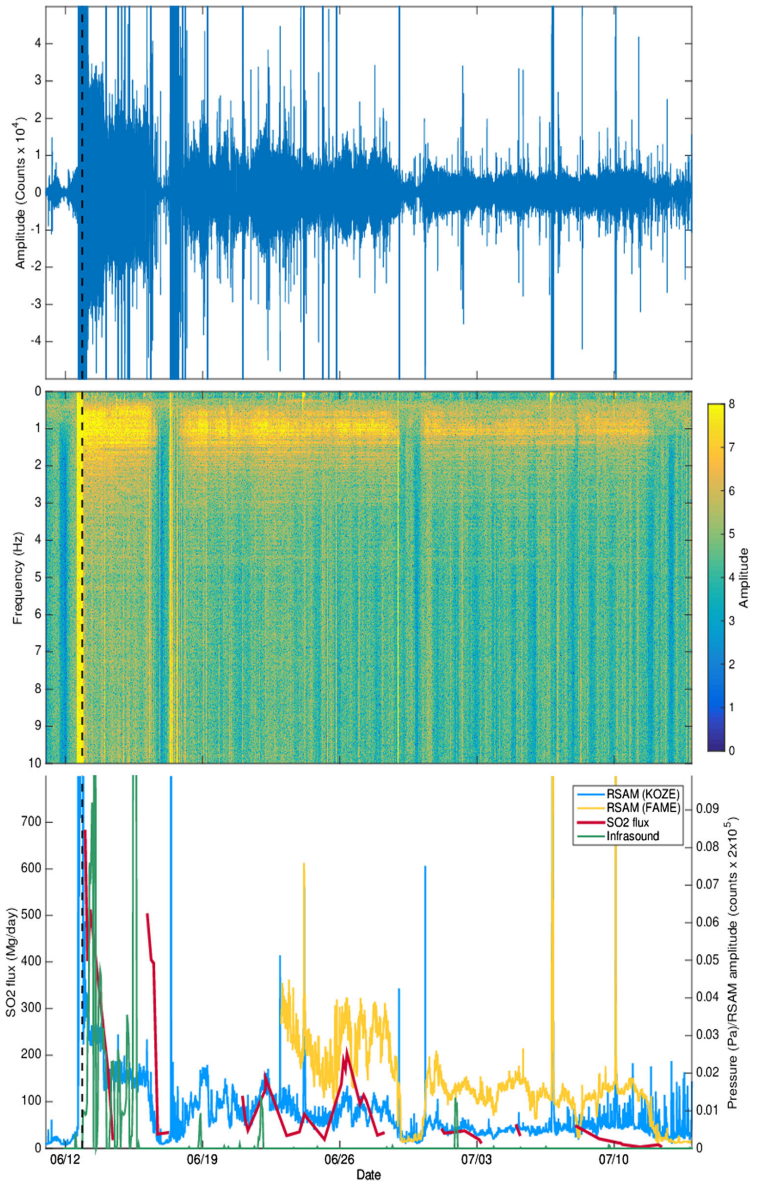

Fig. 8 **a** Raw vertical component seismogram from station KOZE, 120 km from Nabro volcano. **b** Spectrogram from station KOZE. **c** Composite plot showing RSAM at stations KOZE (*blue*) and FAME (*yellow*), SO_2 emission rate computed from OMI data (*red*) and infrasound signal recorded at the Nairobi station (*green*). SO_2 emission rates were derived using a plume traverse technique (e.g. Theys et al. 2013), assuming SO_2 advection in a constant wind field, with wind speed derived from a trajectory model. The magnitude and temporal variation of our OMI-based SO_2 fluxes are broadly consistent with analyses of other satellite SO_2 measurements for Nabro (Theys et al. 2013). The *dashed vertical line* indicates the eruption onset (20:27–20:42) estimated from SEVERI images

likely more exposed. By 2 July, the eastern lava flow had advanced further into the adjacent crater. Particularly striking in the 29 June ALI SWIR bands is the revelation that the aligned cinder cones seen in the SAR images from 18 June onwards coincide with intense thermal anomalies. The location and orientation of these vents suggest the possibility of their source being a NW–SE-striking dike (Fig. 11). These vents do not appear to have contributed significantly to lava eruption after 20 June.

Notably, one of these extends from the SE rim of the SW crater, which appears to have been substantially infilled by lava and tephra. The main flow appears to be at its maximum extent, though the 'spillway' at the vent that sources it remains 'hot', suggesting sustained lava effusion, in the shortwave infrared channels.

Comparing the SAR images acquired on 18 June and 4 July indicates that the main flow only advanced a further 400–500 m in the intervening period, reaching 750 m elevation,

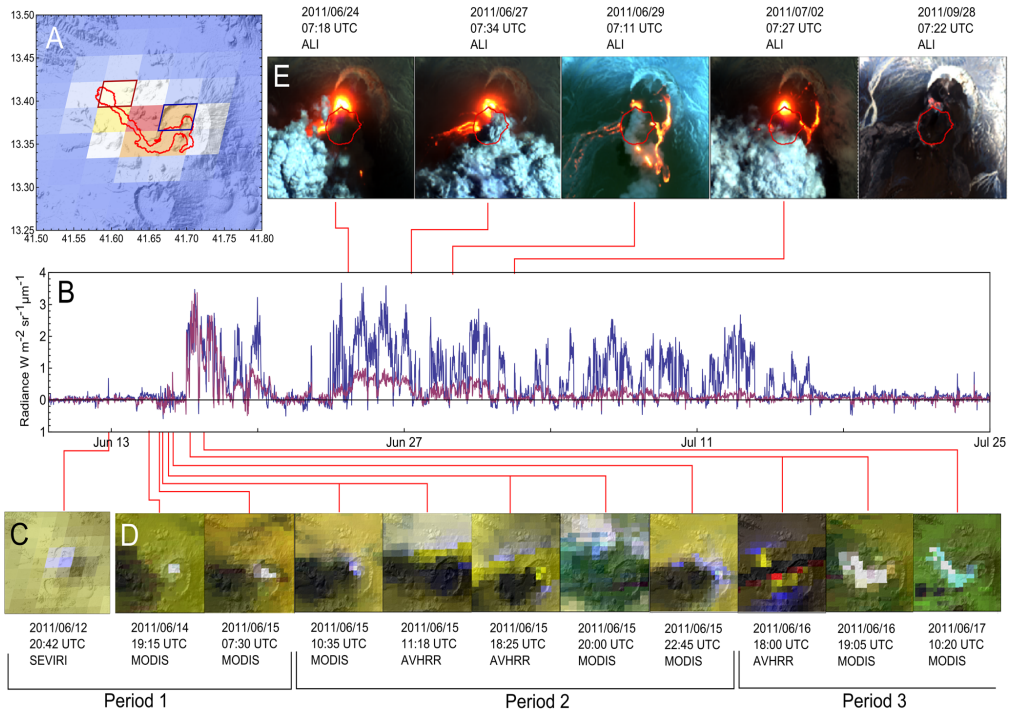

Fig. 9 Spaceborne optical observations of the Nabro eruption. **a** A 3.9-µm image of the saturation-corrected volcanic radiance extracted from SEVIRI at 15:12 UTC on 16 June, superimposed on GDEM topography for comparison. Low-to-high radiance is scaled from *blue-to-red*, and the final extent of the lava flow is outlined in *red*. Pixels covering the vent area and lava flow front are outlined in *blue* and *purple*, respectively. The time series of volcanogenic radiance for these pixels are shown in **b**. Note that the radiance time series are 'spiky' due to presence of cloud and plume. **c** The SEVIRI image that signals the start of the eruption (and providing the isolated spike in radiance seen late on 12 June in **b**, before the vent is obscured by plume). **d** Low-resolution images tracking the eruption onset, with bands around 4, 10 and 12 µm as RGB, respectively, in each case. Saturation of AVHRR channels results in loss of a strip of pixels, leading to the banding effect seen in some images. During period 1, the thermal anomaly is restricted to the SW pit in the Nabro caldera, while during period 2, a weak thermal anomaly around the plume margins may result from forward scattering of thermal emission from the advancing lava flow indicating breaching of the SW pit. Period 2 is associated with weak thermal anomalies in the SEVIRI time series seen in **b**. Period 3 follows the first break in the plume, revealing that lava has reached almost its final extent by this point. **e** High-resolution shortwave infrared images of the vent region during the later stages of the eruption. *Red polygon* marks the outline of the original SW pit

and a total length of approximately 17.5 km. The ALI images show that between 24 June and 2 July, the main lava flow advanced only ~140 m at its front, though it likely continued to thicken and widen in places along its length during this period. Between 17 and 23 July, the SAR images reveal drainage of lava from the main flow's channel, quite close to the source and within the caldera. There has been a minor advance of the intra-caldera flow to the SE. As early as 20 June, scarps are apparent around the tephra cone, where the original rim of the pit crater is being expressed or exposed. Much more of the new tephra cone apparently collapsed later in July, though between 23 July and 8 August, no further substantive changes are evident in the SAR imagery.

By 28 September, the SWIR channels of the ALI image indicate anomalous radiation only in association with hot spots around the vent region and along the rim of the original pit crater. The lava flows appear 'cold' at these wavelengths. This pattern persists in the 6 October ALI scene but, 10 days later, the anomalies around the vent region in the SWIR bands look less intense. This is consistent with observations made by several of us during fieldwork carried out on the volcano between 8 and 15 October. We observed incandescent vents in the vent area from the caldera rim on the night of 12 October and a weak plume drifting across the caldera during the daytime.

A prominent signature of the initial flows emitted from vents (*a*) and (*c*) (Fig. 10) is that their texture appears to be smoother in the first image acquired after the start of the eruption (20 June) than seen subsequently. The smooth texture of early lava flows seen in the SAR images could reflect lower surface roughnesses of the lavas or, more likely, tephra fallout from the early phases of the eruption (the effects of which are readily apparent elsewhere within the caldera; Fig. 2). This would suggest that the output of ash diminished substantially

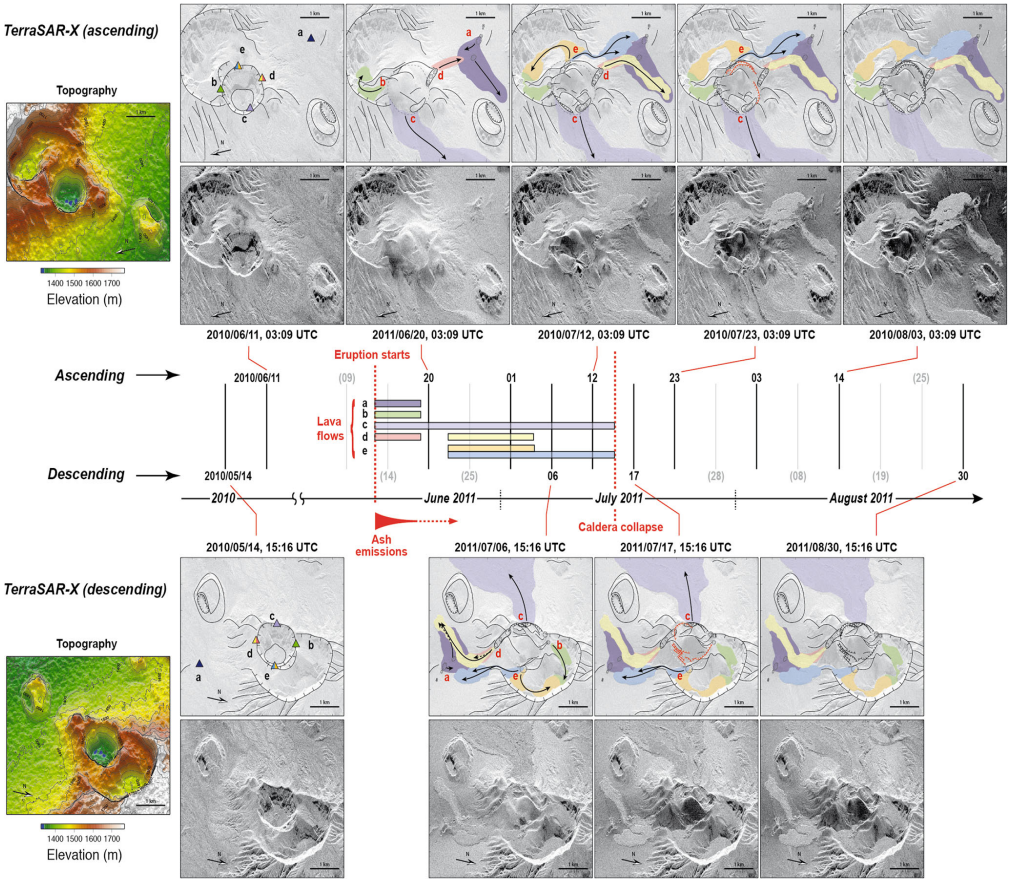

Fig. 10 Time series of SAR images focused on the source region of the flows, with interpretations of lava flow emplacement and topographic changes. *Upper and lower panels* show ascending and descending geometry, respectively (in the native geometry of the sensor to avoid artefacts caused by erroneous orthorectification due to syn-eruptive topographic changes; see Fig. 3). The images have been rotated to facilitate interpretation. In each SAR image, the far range is at the *bottom*, and the near range is at the *top*. Note significant distortions and radiometric changes associated with steep slopes. The *central panel* shows lava flow emplacement through time, with the dates of the images used for interpretations (dates indicated in *grey* were unavailable)

after 20 June, as later lava flows retain their 'blocky' appearance thereafter.

In the SAR images acquired after 20 June, we see that lava eruption from sources (*d*), (*c*) and (*e*) (Fig. 10) continued up to early to mid-July. This is consistent with the volcanic thermal radiance registered in the pixel situated above the vent, which persisted until around midday on 16 July, before decaying rapidly to low values before midnight (Fig. 9b), marking the cessation of intense eruptive activity. The radiant signal from the flow front decayed significantly by early July, suggesting

Fig. 11 Photograph of part of the fissure system taken in 2012. View approximately to the W—a small cone, formed in the 2011 eruption, is apparent on the left and the front of lava effused from vent (*e*) (Fig. 10) apparent on the right. Behind is the modified cone of the SW pit crater

waning advance. Compared with the 12 July SAR image, the 17 July scene reveals a set of ring faults or fractures associated with subsidence of the newly emplaced central cone. The geometries of these fault traces recapitulate the trace of the former SW pit rim, suggesting localisation of brittle deformation along the interface between the previous crater walls and the new infill of tephra and lava. Lava eruption seems to have ceased in conjunction with this substantial collapse of the material, although minor changes prevailed near vent (*c*), possibly arising from drainage of lava already within the channel or slope instability.

Both the SAR and optical images clearly reveal the fallout from the eruption, fanning out in a 130° sector from the vent area (spanning SSE to WNW). In the SAR images, this is apparent from a decrease in backscattered intensity (area in red in Fig. 2). This reflects a smoothing of the topography at the scale of the radar wavelength (about 1 cm) and decrease of the energy backscattered towards the antenna. The most significant change in radar intensity occurred before the first acquisition (20 June), which suggests that the bulk of the ash was deposited in the first 6 days of the eruption. The area of tephra fallout evident in the SAR imagery covers an area of about 700 km^2. It is not possible to assess the thickness of tephra on the ground solely from the available satellite images.

Satellite geodesy

The decomposition of ground displacement into horizontal (east–west and north–south) and vertical components derived from SAR imagery reveals a complex pattern of ground motion (Fig. 4). At the large scale, the horizontal displacement field indicates an overall NE–SW extension, concurrent with NW–SE compression. Maximum horizontal displacements reach 0.75–1 m beyond Nabro's caldera rim. The vertical component of ground displacement indicates widespread subsidence, reaching an average of 0.2 m to the N, E and SE of Nabro. Localised subsidence, reaching up to 0.5 m, is apparent to the NW of the caldera rim within an area elongated along a NW–SE axis. Displacements retrieved within the caldera and to the SW of the vent region are particularly complex. The most prominent feature is localised uplift reaching about 0.75 m within a circular area, 5 km in diameter. The vents lie on the edge of this zone. Further south, apparent subsidence of Mallahle caldera exceeds 0.5 m. Horizontal displacements are directed to the SW and exceeded 1 m. This area of complex deformation coincides with a decorrelation of the InSAR data (Fig. 4) and a decrease of the backscattered SAR amplitude (Fig. 2). This suggests that thick tephra deposits cover the area and that the retrieved ground motion is at least partly an artefact. We therefore neglect this area in the quantitative analysis of ground deformation that follows.

For a first-order interpretation of the deformation source, we performed a series of forward elastic models to reproduce the main features of the ground displacement field in well-resolved sectors of the volcano and its environs. These were based on models from Okada (1985) and Mogi (1958) to predict surface deformation induced by rectangular dislocations or isotropic point sources, respectively. We tested various combinations of faults, dikes and pressure sources. We found three elementary sources sufficient to explain the pattern and amplitude of ground deformation. Our preferred model includes a NW–SE dike, responsible for the NE–SW horizontal dilation pattern observed to the NE of the volcano. This is consistent with the orientation of vents observed within the crater (Observations from spaceborne optical and SAR imagers section). A negative pressure source beneath the vent area explains the overall subsidence signal, as well as NW–SE contraction. The net NE–SW dilation results from the predominance of dike-induced dilation over Mogi-induced contraction in the direction perpendicular to the dike. In contrast, the dike does not produce significant horizontal motion beyond its tips, so that the effect of the negative pressure source accounts for the NW–SE-oriented pattern of contraction observed to the SE and to the NW of the volcano. Finally, a shallow NW–SE-striking, NE-dipping normal fault reproduces the localised subsidence seen to the NW of Nabro.

We then used these three sources of deformation to initialise a nonlinear inversion of the surface deformation that takes the six displacement fields as an input (InSAR, SAR range offset and SAR azimuth offset, for ascending and descending passes). We followed Tarantola and Valette (1982) to optimise the geometry (location, size, dip, depth) and kinematics (slip magnitude and direction or magnitude of pressure change) of the three elementary sources. Not all the parameters could be constrained due to incomplete spatial coverage of the data and various tradeoffs. The best-fit model is shown in perspective view in Fig. 12. This preferred solution includes a negative pressure source equivalent to a volume loss of 0.07 km^3, situated at 6 km depth. This depth coincides with the depth of a deflating pressure source deduced from analysis of ground deformation derived from InSAR time series (spanning 1 July 2011 to 5 October 2012), and with a cluster of micro-earthquake sources 5 km below sea level, located using the local seismic network operating from 31 August 2011 (Hamlyn et al. 2014). The modelled dike is vertical, strikes at 320° N, is 8-km-long and extends from 0.3 km down to 4.3 km depth. It corresponds to a volume inflation of 0.04 km^3, which is comparable to the volume lost from the underlying pressure source. As noted, the strike direction of the dike is roughly parallel to the alignment of the vents identified from high-resolution imagery (Observations from spaceborne optical and SAR imagers section). This trend is perpendicular to the direction of regional spreading associated with motion of the Arabian and Nubian plates.

Lastly, the normal fault strikes at 320° N, slips by 0.7 m, has a dip angle of 55° and extends from 0.8 km down to

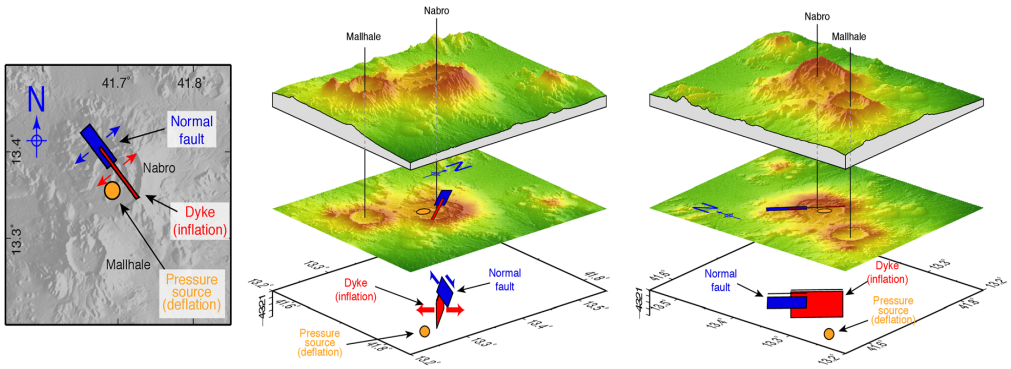

Fig. 12 Model deduced from elastic inversion of the SAR-derived surface displacement field. The *left panel* shows the surface projection of the three elementary sources used in the model in map view. The *centre and right panels* show the same sources in a 3D perspective view, looking from the SE and SW, respectively

3.2 km depth. The seismic moment associated with this fault is 4.3×10^{17} N m, which is equivalent to an M_w 5.8 earthquake (assuming a shear modulus of 3.3×10^{10} Pa). This is comparable to the sum of the two most energetic earthquakes that occurred on the day of peak seismic activity on 12 June, at 20:32 and 21:03 UTC, with magnitudes M_w 5.6 and M_w 5.4, respectively (2.91×10^{17} and 1.42×10^{17} N m according to gCMT). The focal mechanisms of these two earthquakes indicate normal faulting striking 280–290° N, albeit with a substantial non-double-couple component (Fig. 13). Given the uncertainties in the analysis, this is broadly consistent with the 320° N direction determined from our interferometric SAR analysis.

Overall, the elastic modelling suggests that the Nabro eruption was associated with a shallow dike intrusion. This dike may have linked a deeper source to the surface eruption. The onset of seismicity suggests the dike intruded on 12 June. It triggered slip on one or several normal faults running parallel to the dike at shallower depth, as observed elsewhere in regions undergoing local or regional extension (e.g. Rubin and Pollard 1988; Rowland et al. 2007). It is evident from our InSAR analysis that faulting breached the surface on the NW flank of Nabro. Figure 14 shows the co-eruptive displacement along a profile perpendicular to the inferred normal fault. Motion away from the satellite to the NE of the surface trace of the fault clearly points towards a normal fault dipping to the NE with most of the vertical displacement concentrated in the hanging wall. Fault geometry in the vent region cannot be readily identified due to resurfacing by lava flows and tephra deposits.

Dike intrusions are common during volcanic eruptions. However, the broad scale of fringes in the interferograms indicates that the dike opened permanently with some magma retained in the crust (i.e. not all was erupted). This inflation of the dike suggests a response to the regional extensional stress field and a degree of tectonic influence on the eruption. However, the relative importance of tectonics versus magmatic processes in nucleating, feeding and maintaining the inferred dike remains unclear. It is interesting that the initial dike injection beneath Nabro followed a NW–SE, Red Sea trend (Satellite geodesy section), while on 17 June, the seismicity shifted to Mallahle and defined a NE–SW trend (Fig. 6b). Seismicity beneath Mallahle then switched back to more of a NW–SE, Red Sea trend, stretching as far as Sork 'Ale volcano (Fig. 6c). This may indicate a perturbation of the stress regime in which the direction of maximum horizontal stress changed. A closer study of earthquake source mechanisms and seismic anisotropy may provide further evidence and insights.

The residual displacement field determined after subtracting the best-fit model reveals several other notable features. Beyond the masked area (shaded zones in Figs. 3 and 4), the residual horizontal and vertical displacements are generally small. In contrast, a residual uplift, reaching about 1 m, is seen to the SW of the vent region. This is likely the result of tephra accumulation in the first days of the eruption. A distinct negative anomaly, corresponding to subsidence, is also apparent within the caldera of Mallahle volcano. This residual signal might correspond to deflation of a reservoir below Mallahle, induced by activity of the neighbouring magmatic system. This activation of Mallahle is seen also in the seismicity, beginning 17 June (Seismicity section) and continuing in late 2011 (Hamlyn et al. 2014).

While our model captures the main features of the ground deformation field, we emphasise that it is non-unique for several reasons: (i) the retrieved surface displacements do not span exactly the same observation intervals, (ii) spatial coverage of the data is patchy due to the tephra fall deposits, (iii) sub-pixel correlation results are fairly noisy around the volcano, likely due to slope effects and relatively adverse surface conditions for X-band SAR imaging (compared with the Afar plains), (iv) the deformation field is particularly complex and (v) the elastic inversion problem is inherently non-unique. Thus, alternative solutions based on a different set of assumptions could be proposed. For instance, Hamiel et al. (2013)

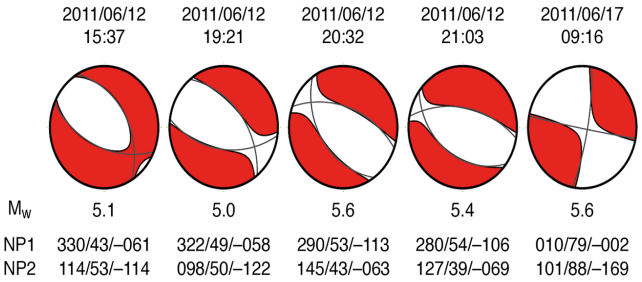

Fig. 13 Moment tensors for all events with moment magnitudes (M_w) exceeding 5.0 and detected near Nabro during June 2011 and recorded in the Global Centroid Moment Tensor (gCMT) catalogue (Dziewonski et al. 1981; Ekström and G.M. and Dziewonski, A.M. 2012). The plots show the full moment tensor of each event, with *grey lines* showing the fault planes of the double-couple component of the moment tensor. Strike, dip and rake of the two nodal planes are indicated

explained the first-order contribution to the observed deformation as a NNE–SSW-trending, left lateral, strike-slip fault located at shallow depth beneath Nabro volcano, consistent with the focal mechanism of one of the most energetic earthquakes of the eruption episode (09:16 UTC, 17 June 2011, M_w 5.6).

Synthesis of observations

Figure 8c integrates observations of the Nairobi infrasound station, RSAM and SO_2 emission rates computed from available OMI satellite data. Several features stand out in the time series: (i) the persistence of seismic tremor and its infrasonic

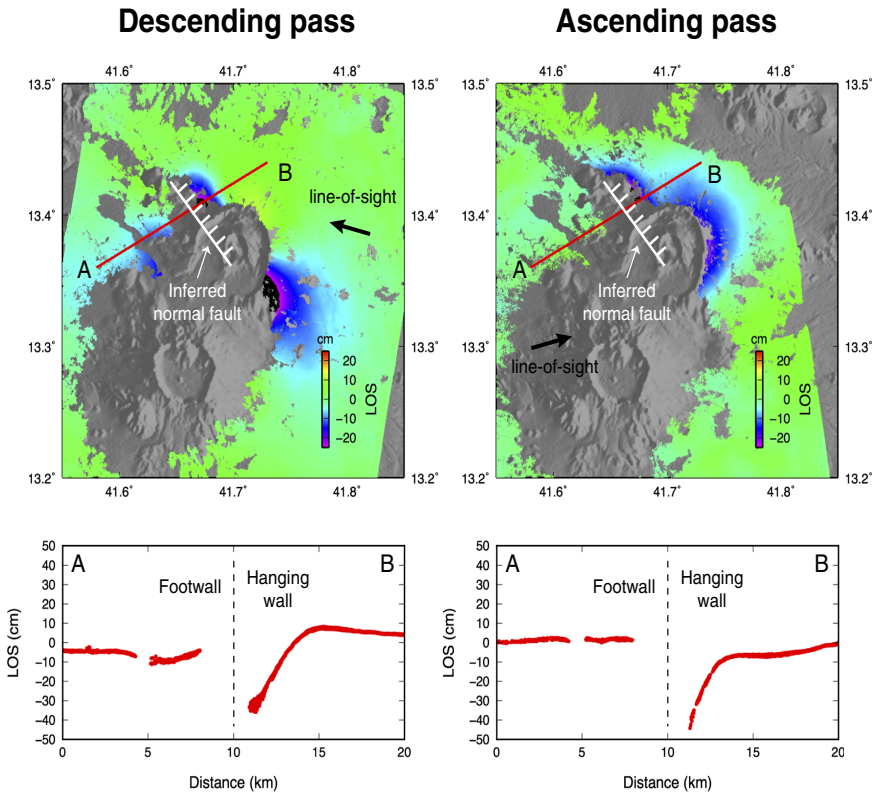

Fig. 14 Descending (*left*) and ascending (*right*) interferograms showing the line-of-sight component of ground displacement around Nabro volcano. *Blue-to-purple* shading corresponds to motion away from the satellite. The *thick black arrows* show the line-of-sight direction. The *red lines* indicate the profiles across an inferred normal fault (surface trace in *white with bars* indicating the hanging wall), shown in the corresponding *lower panels*

equivalent (i.e. continuous vibration of the atmosphere) during and after the main eruptive stage, (ii) approximate correlations between the temporal trends in the three parameters, (iii) a pronounced drop in RSAM to near zero around 17 June and (iv) plateau-like temporal signals in RSAM prior to 17 June but more fluctuating trends afterwards. Most of the located events occurred on 12 and 17 June. The largest earthquakes also occurred on these days.

The SEVIRI images bracket the eruption onset to between approximately 20:27 and 20:42 UTC on 12 June—the later scene shows a pronounced thermal spike over the caldera. The prominent earthquake at 20:32 UTC could signify the final dike advance that breaks the surface. The infrasound recorded at the closest station in Djibouti (264 km from Nabro) picks up abruptly at 21:44 UTC (Fee et al. 2013). For an acoustic travel time of circa 20 min from Nabro, this indicates that explosive activity either began or picked up substantially at 21:24 UTC. This may indicate that the first 50 min or so of the eruption saw predominantly effusive activity at one or more vents, although the SEVIRI images indicate a plume that rapidly gains altitude between 20:42 and 20:57 UTC.

Optical and SAR observations indicate that the main lava flow had advanced to close to its maximum extent within about 3 days of the eruption onset on 12 June. In addition, most of the tephra was emplaced within about 6 days of the onset. The persistent tremor between 12 and 16 June suggests sustained high lava effusion rates during this period. On the other hand, infrasonic signals point to continuous but fluctuating explosive activity, consistent with the evidence for airborne ash and tephra accumulation on the ground. Unique features in the infrasound signal suggest the volcanic jet was gas-rich and supersonic (Fee et al. 2013). SO_2 emissions were strong during this period, likely with efficient decoupling of gas from erupting magma at the vent(s). The comparative quiescence in activity around 16/17 June is puzzling but may correspond to a choking in magma supply to the vent(s).

The abrupt resumption of tremor on 17 June and accompanying seismicity suggests renewed magma supply. Interestingly, most of the seismicity is located beneath Mallahle volcano, suggesting either triggering by changes in the local stress field (e.g. Walter et al. 2014) or potentially interconnection between magma reservoirs (e.g. Albino and Sigmundsson 2014). The former explanation seems more likely based on the observation that post-eruption seismicity (31 August–7 October 2011) beneath Mallahle had significantly lower *b* values than that associated with Nabro (Hamlyn et al. 2014). Optical imagery indicates vigorous activity at the vent region, likely characterised by a lava lake sourcing a steam-rich, low-altitude plume. SO_2 was still detected by OMI but burdens and emission rates were reduced, suggesting lower lava effusion rates and consistent with generally low explosivity at the vent(s). Explosive activity on 18 and 21/22 June is apparent in the Nairobi infrasound data and coincides with a pulse in RSAM and SO_2 output. By 29 June, the optical shortwave infrared images (ALI) indicate diminished lava effusion. While SO_2 emissions persisted, outputs were further reduced.

Overview of the petrology of the 2011 lavas and tephra

The lava erupted is trachybasaltic to trachybasaltic andesite in composition—between 48–53 wt% SiO_2 and 5–7 wt% total alkalis, following a mildly alkali-enriched trend relative to rocks from the axial volcanic ranges in Afar (e.g. Barberi et al. 1972; Fig. 15). Whole-rock MgO contents are low (3–5 wt%). There are abundant phenocrysts of olivine, clinopyroxene, plagioclase and magnetite, with rare ilmenite, chromite and fluorapatite. Microlites of olivine, clinopyroxene, plagioclase and Fe-Ti oxides are present in the ground mass. Some tephra samples are glassy with abundant plagioclase microlites, while others are more crystalline. Phenocrysts show both normal and reverse zoning, indicating a complex plumbing system. This is rare in Afar and may be the result of the presence of thicker crust in the proximity of the Danakil Alps.

Olivine phenocrysts are typically compositionally zoned with fayalite-rich rims and forsteritic cores (Fo about 85). Some contain inclusions of chromite. There are also a few smaller crystals that are reverse-zoned. Clinopyroxenes exhibit diverse textural features. One population has no discernible zoning, while the majority of phenocrysts are normally zoned. A few, however, show slight reverse zoning. Plagioclase is abundant and shows normal zoning, with cores about An_{80} and rims about An_{55}. Magnetite and ilmenite are both present and are relatively homogeneous. There are two apatite populations, one containing very little sulphur and the other exhibiting some zoning in sulphur.

The lava is highly crystalline and shows evidence of along-flow fractionation. The variation in the tephra textures may represent discrete batches of magma from depth. There is localised contamination from lithics of rhyolitic composition, most probably introduced in the upper regions of the conduit. Textural and compositional features suggest that some of the magma was reheated prior to the eruption, while other phenocrysts appear to have been transported rapidly from depth. It is likely that there was at least one recharge event prior to the 2011 eruption, which would be consistent with seismic data.

Clinopyroxene-hosted melt inclusions contain up to ~3,100 ppm S, whereas matrix glass contains very low sulphur. A separate sulphide phase is present in some samples and as inclusions in phenocrysts. It contains up to 3 % Cu and 1.3 % Ni. Taking the SO_2 mass released into the atmosphere as 4.5 Tg (Theys et al. 2013), a crystallinity of 60 % and the aforementioned value as indicative of melt sulphur content, the dense rock volume of the eruption amounts to approximately 0.47 km^3 (magnitude 5.1, given by [$\log_{10}$ (mass in kg)

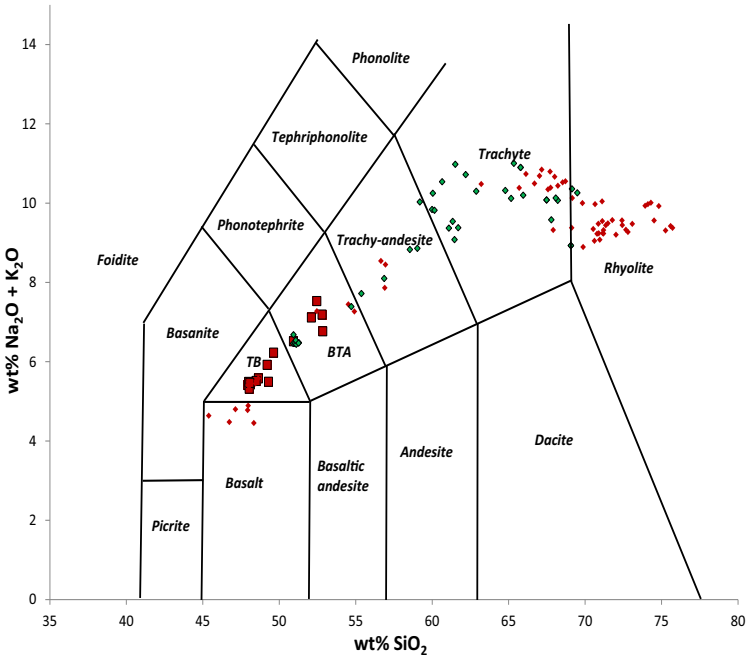

Fig. 15 Total alkalis versus silica plot for eruptive products from the 2011 eruption

−7]). This is roughly compatible with the scale of emplaced lava flows (approximately 18 km^2 in area for an assumed mean thickness of 20 m) and tephra deposits (5 m mean thickness inside the caldera, 0.1 m mean thickness beyond). We hope in the future to be able to obtain further tandem SAR data products to enable a more accurate determination of the lava and tephra volumes. This will be essential for a robust treatment of the volatile budget.

Impacts of the eruption and emergency response

The Danakil region is generally dry and sparsely populated. However, Nabro, which rises to more than 2,200 m above sea level, engenders a microclimate that favours denser settlement. Several villages are, or were, located within the caldera and on the flanks of the volcano. Siroru, the main settlement within the caldera, had a population of around 3,000 prior to the eruption. The inhabitants of the region are mostly pastoralists keeping herds of sheep, goats, camels, donkeys and cattle. Despite the limited number of recorded earthquakes, the seismic hazard in the region had been previously recognised (e.g. Midzi et al. 1999). The eruption of Dubbi in 1861 (Wiart and Oppenheimer 2000) is also a testament to the volcanic hazard and is remembered by communities living in the area today. Nevertheless, prior to the 2011 eruption, a national risk mitigation strategy for geophysical threats was lacking. There was no monitoring of any kind on Nabro nor was there a formalised warning system in place.

We believe that the experience of the 4.5 M_W event on 31 March 2011 may have served to sensitise and increase preparedness of the population in advance of the eruption. Almost all the houses in the affected area that were built with non-mortared stone walls suffered severe damage or collapse; those built with mortared walls suffered varying degrees of cracking (Fig. 5). During the visit of the scientific team in May 2011, village and district administrators and community leaders were briefed on what to do in the event of future earthquakes, namely to vacate their homes and avoid structures that could collapse and areas susceptible to landslides.

Village and district administrators in Eritrea are mostly war veterans well-versed in aspects of emergency management and in coping with situations with limited means at their disposal. Their experience was likely decisive in the immediate local management of the unfolding emergency on 12 June 2011. An army detachment based close to the local administration building in Siroru maintained radio contact with the Southern Red Sea Region Administration (SRSRA) in the regional capital, Assab (about 120 km away, as the crow flies). Together with other nearby units, they helped to evacuate people as the crisis developed on the night of 12/13 June 2011. Clearly, people living within the caldera, on the volcano flanks and in range of the tephra fallout, were most affected by the eruption and its associated seismicity. In

particular, Siroru was destroyed by a combination of seismic shaking, lava flows and burial in tephra. While some people refused to be evacuated, by and large the rescue efforts were conducted with the full cooperation and consent of the affected people.

Another factor that may have contributed to the rapid response is that one of us (JOSH) happened to be in Asmara at the time of the eruption. He received an automated e-mail via the USGS National Earthquake Information Center's 'Preliminary Determination of Epicenters' service concerning the first larger earthquake on 12 June (15:33:12 UTC, i.e. 5 h before the eruption). This information was relayed via another member of our team (GO) to the SRSRA.

The first meeting of the SRSRA committee tasked with coordinating the response to the unfolding humanitarian crisis took place at 08:00 local time on 13 June 2011 in Assab. This resulted in the dispatch of a medical team and provision of emergency relief (food supplies and shelters, Solomon, 2012). Other government agencies provided longer term assistance to displaced people in respect of health care and schooling.

The SRSRA classified the displaced persons into two categories. Those in category 1 came from villages that were destroyed. Those in category 2 were those whose villages were threatened by the eruption including the effects of fumes and tephra fallout. According to Solomon (2012), during the first 2 days of the eruption, the estimated numbers in category 1 were 700–800 families (about 2,500–3,000 individuals). The corresponding values for category 2 were about 2,250 families (about 9,000 individuals). On 17 June 2011, when the eruption intensified, most category 2 evacuees were reclassified as category 1. In total, about 11,780 people were affected. Seven people were killed and three were injured during the eruption (Solomon 2012).

The losses in household goods were substantial (Solomon, 2012). In previously settled areas of the caldera floor south of the vent region, tephra accumulated to depths of several metres, burying or partially burying many structures. Two villages were completely destroyed, and recorded losses include 19,839 goats and sheep, 460 cattle, 834 camels and 142 donkeys. Total economic losses were estimated to be in the region of US$3 million (Solomon 2012). The contamination of water wells in the area, at least on the Eritrean side, appears to have been limited (Solomon 2012).

Many of the people displaced by the eruption were unable to return to their homelands; substantial numbers have been permanently resettled elsewhere. Resettlement can have major consequences for livelihoods, communities and culture and can expose people to new hazards (Usamah and Haynes 2012). Resettlement programmes are arguably most effective when the affected communities are closely involved in decision-making. According to Solomon (2012), this appears to have been the case following the Nabro eruption.

Information on impacts on the Ethiopian side of the border is limited, but the caldera of Mallahle volcano was inhabited and received significant fallout of tephra from the eruption plumes. We were told that the affected communities received assistance in Eritrea (although the two countries do not maintain diplomatic relations). Communications received from staff at a mining operation in Dallol, 170 km to the northwest in Ethiopian Danakil (and below sea level) suggested grounding of a portion of the gas and aerosol emissions, causing discomfort to workers. Respiratory stress may have been exacerbated by the extreme temperatures experienced in this part of northern Afar in the summer.

In terms of civil aviation issues, the region falls under the responsibility of the Toulouse Volcanic Ash Advisory Centre. The volcanic clouds resulted in disruptions to aviation in the region with international flights in East Africa and the Middle East particularly affected. In the first days of the eruption, there was confusion in the outside world as to whether it was Dubbi or Nabro that was erupting.

Concluding remarks and perspectives

The 2011 Nabro eruption offers a valuable opportunity to develop our understanding of unrest and eruptive activity of caldera systems, the local interactions between tectonics and volcanism and between neighbouring volcanoes and the origins and significance of the off-axis volcanic ranges in the wider Afar region. We summarise key observations and preliminary interpretations as follows:

1. The June eruption was preceded by a damaging earthquake (the 31 March 2011 event) and further felt seismicity and earthquake swarms up to 5 h beforehand. (We heard anecdotally from a local guide that the vigour of steam vents inside the caldera had increased in advance of the eruption. These vents were apparently used by people living within the caldera for therapeutic purposes but had heated up to the point where they were no longer comfortable.) These signs indicate that the eruption was presaged by sensible phenomena.
2. The eruption began between 20:27 and 20:42 UTC, according to satellite images, and possibly close to 20:32 UTC, the time of a large earthquake. It may have been predominantly effusive for the first 50 min or so, then sufficiently explosive to be recorded at distant infrasound stations. A 17.5-km-long lava flow was observed on 16 June 2011, exceeding 1 km in width in places. Explosive activity generated significant tephra clouds and a substantial quantity of SO_2 was released to the atmosphere. Compositions of erupted lavas and tephra range from trachybasalt to basaltic trachyandesite. (At present, the eruption magnitude is poorly constrained, but it could be calculated in future if additional SAR data are acquired for construction of pre- and post-eruption digital topography.)

3. Approximately 12,000 people were displaced as a result of the eruption, and seven fatalities were recorded. Considering that more than 3,000 people lived within the Nabro caldera itself, the toll is remarkably low. This reflects a rapid, largely spontaneous evacuation of settlements close to the vent region, prompted by premonitory ground shaking and the first signs of eruption.
4. Our analysis of regional seismic records for the period 23 February–17 September 2011 revealed 217 events within a 25–40 km radius of Nabro. Seven of these events occurred before the eruption. Their local magnitudes range between 2.1 and 5.9, with 76 events exceeding M_L 4 and eight events larger than M_L 5. While the located events identify temporal variation of seismicity beneath Nabro volcano in the lead up to the eruption, we note that our detection threshold is quite high, about M_L 2.1. Double-difference relocations of the events reveal clustering beneath both Nabro and Mallahle volcanoes and hint at alignments of epicentres, along a NE–SW trend, notably on 17 June 2011 (parallel to the Nabro-Mallahle axis), and, subsequently, along a NW–SE trend (parallel to the Red Sea).
5. Geodetic modelling suggests that the eruption was associated with intrusion of a shallow dike that triggered slip on parallel normal faults. The orientation of this dike is roughly NW–SE, parallel to the trend of an eruptive fissure formed during the eruption and to the Red Sea.
6. In general terms, temporal trends in recorded seismicity, SO_2 output and infrasound signals are correlated, with several pulses and fluctuations. The onset of the eruption was marked by high seismicity and infrasound followed by strong SO_2 emissions to the atmosphere. Seismic and infrasonic tremor persisted for about a month. A lull occurred on 16 June, but seismicity increased abruptly on 17 June.

Our study of the Nabro eruption has highlighted the importance of diverse Earth observation techniques for monitoring volcanoes in comparatively remote regions, especially where local ground-based sensor networks are limited or lacking. It also exemplifies the precarious status of risk management where it is not underpinned by operational monitoring.

Acknowledgments This research was funded by the NERC (project no. NE/J012297/1 'Mechanisms and implications of the 2011 eruption of Nabro volcano, Eritrea') with contributions from JOSH's NERC fellowship (NE/I020342/1) and supported with access to the NERC Ion Microprobe Facility. Additional funding was received in the form of grant NE/L013932/1 held by DK and the support of several of the authors by the NERC-funded Centre for Observation and Modelling of Earthquakes, Volcanoes and Tectonics (COMET). We acknowledge funding for BG from the EPSRC and the School of Earth Sciences at the University of Bristol; for AD by the Leverhulme Trust and Isaac Newton Trust; for SAC from NASA through the Aura Science Team (grant NNX11AF42G) and MEaSUREs (grant NNX13AF50G) programmes; and DF from NSF grant EAR-1113294. TerraSAR-X data were provided by DLR under grant award GEO1206. We acknowledge the cooperation we received from the Eritrean government, Southern and Northern Red Sea Administrations, local sub-zones and village administrations. We thank the Department of Mines, Ministry of Energy and Mines for their continued support throughout the project. Special thanks go to Zerai Berhe, Mebrahtu Fisseha, Michael Eyob, Ahmed Mohammed, Kibrom Nerayo, Asresehey Ogbatsien (plausible future presenter of *Top Gear*) Andemichael Solomon and Isaac Tuum. We thank Alem Kibreab for his vital help in facilitating the fieldwork. We are very grateful to the two referees (Cindy Ebinger and John Pallister) and the handling editor (Guido Giordarno) for their beneficial and enthusiastic comments on the original manuscript.

Open Access This article is distributed under the terms of the Creative Commons Attribution 4.0 International License (http://creativecommons.org/licenses/by/4.0/), which permits unrestricted use, distribution, and reproduction in any medium, provided you give appropriate credit to the original author(s) and the source, provide a link to the Creative Commons license, and indicate if changes were made.

References

Albino F, Sigmundsson F (2014) Stress transfer between magma bodies: influence of intrusions prior to 2010 eruptions at Eyjafjallajökull volcano, Iceland. J Geophys Res Solid Earth 119(4):2964–2975

Barberi F, Tazieff H, Varet J (1972) Volcanism in the Afar depression: its tectonic and magmatic significance. In: Girdler RW (ed) East African rifts, vol 15, Tectonophysics., pp 19–29

Barnie T, Oppenheimer C (2015) Extracting high temperature event radiance from satellite images and correcting for saturation using independent component analysis. Remote Sens Environ 158:56–68

Barnie TD, Keir D, Hamling I, Hofmann B, Belachew M, Carn S, Eastwell D, Hammond JOS, Ayele A, Oppenheimer C. and Wright T (2015b) A multidisciplinary study of the final episode of the Manda Hararo dyke sequence, Ethiopia, and implications for trends in volcanism during the rifting cycle. Geological Society London Special Publications, 420 (doi:10.1144/SP420.6)

Clarisse L, Coheur P-F, Theys N, Hurtmans D, Clerbaux C (2014) The 2011 Nabro eruption, a SO_2 plume height analysis using IASI measurements. Atmos Chem Phys 14:3095–3111. doi:10.5194/acp-14-3095-2014

Cote DM, Belachew M, Quillen AC, Ebinger CJ, Keir D, Ayele A, Wright T (2010) Low-frequency hybrid earthquakes near a magma chamber in Afara: quantifying path effects. Bull Seismol Soc Am 100(5A):1892–1903

Doin MP, Guillaso S, Jolivet R, Lasserre C, Lodge F, Ducret G, Grandin R (2011) Presentation of the small baseline NSBAS processing chain on a case example: the Etna deformation monitoring from 2003 to 2010 using Envisat data, In Proceedings of the European Space Agency Symposium "Fringe". Frascati, Italy

Dziewonski AM, Chou T-A, Woodhouse JH (1981) Determination of earthquake source parameters from waveform data for studies of global and regional seismicity. J Geophys Res 86(2825–2852): 1981. doi:10.1029/JB086iB04p02825

Ekström G, Nettles M, Dziewonski AM (2012) The global CMT project 2004-2010: centroid-moment tensors for 13,017 earthquakes. Phys Earth Planet Inter 200–201(1–9):2012. doi:10.1016/j.pepi.2012.04.002

Endo ET, Murray T (1991) Real-time seismic amplitude measurement (RSAM): a volcano monitoring and prediction tool. Bull Volcanol 53(7):533–545

Fee D, Matoza RS, Gee KL, Neilsen TB, Ogden DE (2013) Infrasonic crackle and supersonic jet noise from the eruption of Nabro Volcano, Eritrea. Geophys Res Lett 40:4199–4203. doi:10.1002/grl.50827

Field L, Barnie T, Blundy J, Brooker RA, Keir D, Lewi E, Saunders K (2012) Integrated field, satellite and petrological observations of the November 2010 eruption of Erta Ale. Bull Volcanol 74(10):2251–2271

Fromm M, Kablick G III, Nedoluha G, Carboni E, Grainger R, Campbell J, Lewis J (2014) Correcting the record of volcanic stratospheric aerosol impact: Nabro and Sarychev Peak. J Geophys Res Atmos 119:10,343–10,364. doi:10.1002/2014JD021507

Grandin R et al (2009) September 2005 Manda Hararo-Dabbahu rifting event, Afar (Ethiopia): constraints provided by geodetic data. J Geophys Res 114:B08404. doi:10.1029/2008JB005843

Hamiel Y, Grandin R, Baer G, Wright TJ, Doubre C, Hamlyn J, Peltzer G (2013) InSAR investigation of crustal deformation associated with the 2011 eruption of the Nabro volcano, Eritrea. In AGU Fall Meeting Abstracts (Vol. 1, p. 0955)

Hamlyn J, Keir D, Wright TJ, Neuberg J, Goitom B, Hammond JO, Pagli C, Oppenheimer C, Kendall J-M, Grandin R (2014) Seismicity and subsidence following the 2011 Nabro eruption, Eritrea: insights into the plumbing system of an off-rift volcano. J Geophys Res Solid Earth 119:8267–8282. doi:10.1002/2014JB011395

Hammond JOS, Kendall J-M, Stauart GW, Ebibger CJ, Bastow ID, Keir D, Ayele A, Belachew M, Goitom B, Ogubazghi G, Wright TJ (2013) Mantle upwelling and initiation of rift segmentation beneath the Afar Depression. Geology 41:635–638

Jónsson S, & Xu W (2015). Volcanic eruptions in the southern Red Sea during 2007–2013. In *The Red Sea* (pp. 175-186). Springer Berlin Heidelberg

Kanamori H (1977) The energy release in great earthquakes. J Geophys Res 82:2981–2987. doi:10.1029/JB082i020p02981

Keir D, Stuart GW, Jackson A, Ayele A (2006) Local earthquake magnitude scale and seismicity rate for the Ethiopian rift. Bull Seismol Soc Am 96(6):2221–2230

Keir D, Hamling IJ, Ayele A, Calais E, Ebinger C, Wright TJ, Jacques E, Mohamed K, Hammond JOS, Belachew M, Baker E, Rowland JV, Lewi E, Bennati L (2009) Evidence for focused magmatic accretion at segment centers from lateral dike injections captured beneath the Red Sea rift in Afar. Geology 37(1):59–62. doi:10.1130/G25147A.1

Keir D, Pagli C, Bastow IaI.n D, Ayele A (2011) The magma-assisted removal of Arabia in Afar: evidence from dike injection in the Ethiopian rift captured using InSAR and seismicity. Tectonics, 30, (2), TC2008. (doi:10.1029/2010TC002785)

Keir D, Bastow ID, Pagli C, Chambers EL (2013) The development of extension and magmatism in the Red Sea rift of Afaf. Tectonophysics 607:98–114. doi:10.1016/j.tecto.2012.10.015

Klein, F.W., (2002). User's guide to HYPOINVERSE-2000, a Fortran program to solve for earthquake locations and magnitudes. Open File Report 02-171, US Geological Survey

Makris J, Ginzburg A (1987) The Afar depression—transition between continental rifting and sea-floor spreading. Tectonophysics 141(1–3):199–214

McClusky S et al (2010) Kinematics of the southern Red Sea–Afar Triple Junction and implications for plate dynamics. Geophys Res Lett 37: L05301. doi:10.1029/2009GL041127

Midzi V, Hlatywayo DJ, Chapola LS, Kebede F, Atakan K, Lombe DK, Turyomurugyendo G, Tugume FA (1999) Seismic hazard assessment in eastern and Southern Africa. Ann Geofis 42:1067–1083

Mogi K (1958) Relations between the eruptions of various volcanoes and the deformations of the ground surfaces around them. Bull Earthq Res Inst 36:99–134

Nobile, A., Pagli, C., Keir, D., Wright, T. J., Ayele, A., Ruch, J. and Acocella, V. (2012) Dike-fault interaction during the 2004 Dallol intrusion at the northern edge of the Erta Ale Ridge (Afar, Ethiopia). Geophysical Research Letters, 39, (19), L19305. (doi: 10.1029/2012GL053152).

Ogubazghi G, Goitom B, Kibreab A, King J (2014) Relocation of the 31 March 2011 earthquake in the Nabro Volcanic Range of Southern Eritrea. Eritrean J Sci Eng 1:93–102

Okada Y (1985) Surface deformation due to shear and tensile faults in a half-space. Bull Seismol Soc Am 75(4):1135–1154

Rosen PA, Hensley S, Peltzer G, Simons M (2004) Updated repeat orbit interferometry package released. EOS Trans Am Geophys Union 85(5):47–47

Rowland J, Baker E, Ebinger CJ, Keir D, Kidane T, Biggs J, Wright TJ (2007) Fault growth at a nascent slow-spreading ridge: 2005 Dabbahu rifting episode, Afar. Geophys J Int 171(3):1226–1246

Rubin AM, Pollard DD (1988) Dike-induced faulting in rift zones of Iceland and Afar. Geology 16(5):413–417

Santer, B. D., et al. (2015) Observed multivariable signals of late 20th and early 21st century volcanic activity. *Geophys. Res. Lett.,* 42, 500–509, doi:10.1002/2014GL062366 DOI:10.1002/2014GL062366#_blank#Link to external resource: 10.1002/2014GL062366

Scordilis EM (2006) Empirical global relations converting Ms and mb to moment magnitude. J Seismol 10:225–236. doi:10.1007/s10950-006-9012-4

Sealing, C. R. (2013) Characterizing the first historic eruption of Nabro, Eritrea: insights from thermal and UV remote sensing. MS thesis, Michigan Technological University

Solomon A (2012) Summary of activities of the Southern Red Sea Administration during the Nabro eruption. Department of Infrastructure of the Southern Red Sea Administration, Assab

Tarantola A, Valette B (1982) Generalized nonlinear inverse problems solved using the least squares criterion. Rev Geophys 20(2):219–232

Theys N, Campion R, Clarisse L, Brenot H, van Gent J, Dils B, Corradini S, Merucci L, Coheur P-F, Van Roozendael M, Hurtmans D, Clerbaux C, Tait S, Ferrucci F (2013) Volcanic SO_2 fluxes derived from satellite data: a survey using OMI, GOME-2, IASI and MODIS. Atmos Chem Phys 13:5945–5968. doi:10.5194/acp-13-5945-2013

Usamah M, Haynes K (2012) An examination of the resettlement program at Mayon Volcano: what can we learn for sustainable volcanic risk reduction? Bull Volcanol 74(4):839–859

Waldhauser F, Ellsworth WL (2000) A double difference earthquake location algorithm: method and application to the Northern Hayward Fault, California. Bull Seismol Soc Am 90(6):1353–1368

Walter TR, Shirzaei M, Manconi A, Solaro G, Pepe A, Manzo M, Sansosti E (2014) Possible coupling of Campi Flegrei and Vesuvius as revealed by InSAR time series, correlation analysis and time dependent modeling. J Volcanol Geotherm Res 280:104–110

Wiart PAM, Oppenheimer C (2000) Largest known historic eruption in Africa: Dubbi volcano, Eritrea, 1861. Geology 28:291–294

Wiart P, Oppenheimer C (2005) Large magnitude silicic volcanism in north Afar: the Nabro Volcanic Range and Ma'alalta volcano. Bull Volcanol 67:99–115

Wiart PAM, Oppenheimer C, Francis P (2000) Eruptive history of Dubbi volcano, northeast Afar (Eritrea), revealed by optical and SAR image interpretation. Int J Remote Sens 21:911–936

Xu W, Ruch J, Jonsson S (2015) Birth of two volcanic islands in the southern Red Sea. Nat Commun 6:7104. doi:10.1038/ncomms8104

Yang K, Krotkov NA, Krueger AJ, Carn SA, Bhartia PK, Levelt PF (2007) Retrieval of large volcanic SO2 columns from the Aura Ozone Monitoring Instrument: comparison and limitations. *Journal of Geophysical Research: Atmospheres (1984–2012)*, *112*(D24)

Yirgu G, Ferguson DJ, Barnie TD, Oppenheimer C (2014) Recent volcanic eruptions in the Afar rift, northeastern Africa, and implications for volcanic risk management in the region. In: Ismail-Zadeh A, Fucugauchi JU, Kijko A, Takeuchi K, Zaliapin I (eds) Extreme natural hazards, disaster risks and societal implications. Cambridge University Press, Cambridge, p 200–213